Understanding the Yield Behaviour of Single Crystal Ni-based Superalloys

Yuan Ming Wang-Koh

Nickel-based superalloys are the material of choice for turbine applications due to their superior high-temperature strength capabilities. This has been attributed to the γ' precipitates which have the $L1_2$-ordered crystal structure. Because of the ordered crystal structure, dislocations must travel in pairs, separated by an anti-phase boundary (APB), when moving through the precipitates. The dislocations are known to cross-slip from $\{111\}$ glide planes onto $\{100\}$ planes because the APB energy is lower on $\{100\}$ planes. However, this theory remains unconfirmed. To better understand this unique property in superalloys, high resolution transmission electron microscopy (HRTEM) has been undertaken on tensile specimens of the single crystal Ni-based superalloys CMSX-4 under different deformation conditions. In a two-phase superalloy, during early stages of tensile deformation, dislocations nucleate in the γ matrix phase and glide in the narrow channels between precipitates. The yield point was found to correspond to the entry of dislocations into the γ' precipitates. Of the dislocations which enter into γ', only a small portion were observed to cross-slip. Due to the two-phase microstructure, dislocation loops are able to form which can shrink and annihilate. Atomic resolution of the dislocation pairs show the APB between the pair is on the $\{100\}$ plane. On increasing the temperature, the dislocations in the γ channels are able to climb, and stacking fault shear of the precipitates becomes much more prevalent. Upon changing the strain rate of the tensile tests, deformation mechanisms akin to creep were observed which was associated with a drop in the stress. The stress drop is associated with the formation of stacking fault shear and was dependent on the composition of the alloy. The fault structure is the same as those observed in post-creep samples. Chromium and cobalt were also observed to segregate to the fault. The deformation structure of a fourth-generation superalloy, TMS-138A, was also analysed to understand the effects of additional rhenium and ruthenium. The yield point was lower and the dislocations are more rigidly confined to $\{111\}$ slip planes in the γ channels. The observations and analyses included in this thesis improve the understanding of the tensile deformation process of two-phase, single crystal superalloys.

Understanding the Yield Behaviour of Single Crystal Ni-based Superalloys

Yuan Ming Wang-Koh

Department of Materials Science and Metallurgy
University of Cambridge

This dissertation is submitted for the degree of
Doctor of Philosophy

St Edmund's College July 2018

I dedicate this thesis to my paternal grandparents.

Declaration

I hereby declare that except where specific reference is made to the work of others, the contents of this dissertation are original and have not been submitted in whole or in part for consideration for any other degree or qualification in this, or any other university. This dissertation is my own work and contains nothing which is the outcome of work done in collaboration with others, except as specified in the text and Acknowledgements. This dissertation contains fewer than 60,000 words including summary/abstract, tables, footnotes and appendices, but excluding table of contents, photographs, diagrams, figure captions, list of figures/diagrams, list of abbreviations/acronyms, bibliography and acknowledgements.

Yuan Ming Wang-Koh
July 2018

Acknowledgements

First and foremost, I would like to thank my academic supervisor, Professor Catherine Rae, for academic mentorship. You have helped stretch my mind and push me to conduct research diligently and in a proper manner; values which I will carry with me for a lifetime. Thank you also to my industrial supervisor, Dr Neil Jones (Rolls-Royce plc.), for being so accommodating of my various demands, providing material samples at short notice, industrial data where relevant and the frequent discussions on the best direction to drive the projects to make it industrially relevant. I would also like to acknowledge the financial support provided by the Engineering and Physical Sciences Research Council (EPSRC), St Edmund's College and Rolls-Royce plc. The office has provided an endless source of guidance on lab best practices and academic advice to make this project as productive as possible. Dr Hon-Tong Pang for teaching me the various steps for sample preparation and the basics of transmission electron microscopy, Lori Richardson for providing various parts from stores, both in and out of official office hours, Andrew Rayment for all your help with the mechanical testing work featured in this work, and to the electron microscope team: Dave Nicol, Simon Griggs and Chris Dolan for your patience in teaching me how to use the various microscopes that have allowed me to produce images I am truly proud of. To Olivier, being placed next to you in the office was probably the best thing that ever happened to me. Your work ethic made me push myself that extra 5%. I will forever be indebted to you for the endless hours spent assisting me patiently on the microscopes and helping me make sense of the various results. Thank you for also making me feel less self-conscious about running as a hobby. I really hope you have the successful career that your ambition and drive deserves. You left a hole of knowledge that the group will forever struggle to fill. Every cloud has a silver-lining, and I could not have asked for a better desk partner replacement in Sioned. You made days in the office so much easier and gave me the time and space to be myself. I felt so at home in my quadrant of the office. To Amy and especially Caspar, thank you for providing support as we all battled through our daily woes the PhD provides.

The period since submitting have at times left me feeling isolated and helpless. Through it, I have built friendships that will last a lifetime. I was at breaking point when I messaged Kathy.

Thank you for your empathy and guidance, being the calm voice of reassurance and helping me find the answers when I felt so lost. Thank you Matt and Robbie for helping me become aware I am not alone during a difficult write-up. Thank you for Looi for instilling in me the confidence and courage to involve the Degree Committee and get my thesis corrections finally approved. My time in Cambridge would not be the same without the friendships formed outside of the lab. In the Cambridge University Athletics Club and St Edmund's College, I became a part of two of the most caring and loving communities anyone could wish for. Within CUAC, Daisy, thank you for your endless support over the past year. I will never forget the numerous inspirational quotes that lifted me, as well as time spent indulging over cups of high quality coffee and tea, and meals full of organic produce, helping me reason through my emotions. Thank you Cat for being a constant source of encouragement and perspective. The cake is finally out of the oven! Caroline, your mental resilience and fortitude have been a source of courage for me to battle through the troubles this thesis has produced. Thank you Liv for teaching me the importance of self-love. To Alex, Jia and Omer and Stants, thank you for making GC and Eddies feel like home in the year after I formally left Cambridge; for being so accommodating, allowing me to crash at your place so frequently, being the source of the tastiest food and tolerating my highs and lows as I tried to close out my write up. Marta, thank you for being such an incredible house-mate in my write-up period and in the many years since. Your resilience and kindness are a constant source of inspiration. I will cherish so many positive memories from my final summer in Cambridge. Thank you to Steve, Chris and Ram for being with me every step of my time in Cambridge. Thank you TJ for your company and support both in-person and whilst abroad. Thank you Neil for helping me make sense of myself after returning from the 'Superalloys 2016' conference. To Maanik, thank you for providing academic guidance, wisdom and reassurance in the years since leaving Cambridge, helping me to get this chapter of my life closed out.

I am forever grateful to my paternal grandparents for ingraining within me the value of a good education. Lastly to my sisters and parents, whose love and guidance are with me in whatever I pursue.

Contents

List of Figures

List of Tables

Chapter 1

Introduction

Nickel-based superalloys are the industry standard material for applications in both marine and aerospace turbine engines, where resistance to creep, fatigue deformation, corrosion, and oxidation, is required. This material is extensively used, with 40-50% of the total weight of an aircraft engine coming from Ni-based superalloys, and are most commonly found in the combustor and turbine sections of the engine. The reason for their use is the ability to maintain or have enhanced strength within the high temperature environment during operation.

This property is known as the yield strength anomaly and an unusual characteristic of Ni-based superalloys. The source of this phenomenon is largely attributed to the presence of γ' precipitates. The γ' phase has an $L1_2$ ordered crystal structure. This ordered structure produces energetically unfavourable fault structures when dislocations pass through it, hindering dislocation motion. Because of this association, the yield strength anomaly has been extensively studied in relation to intermetallics with the $L1_2$ crystal structure, and in a select number of cases, also to two-phase superalloys. The introduction of the γ matrix and the interfaces between precipitates and matrix is thought to affect the mechanisms and models applicable for $L1_2$-based intermetallics. By increasing the volume fraction of γ' in the superalloy, the mechanical strength has improved. The γ' volume fraction of single crystal turbine blades is optimised at 70-80%.

A turbine engine is an example of a heat engine, whose efficiency, ν, is given by: ν = 1-(T_2/T_1), where T_1 and T_2 are the initial and final temperatures respectively. The most practical way to increase engine efficiency is to raise T_1, the temperature at which gases enter the turbine, known as the turbine entry temperature (TET). This has placed great demand on the turbine, and it is here that yield properties are critical for high stress applications.

The turbine entry temperature of current civil aerospace engines has increased from 700 °C for the first civil aeroengine to the present day temperatures around 1600 °C.[25] This increase has been achieved through iterative improvements in the manufacturing process of turbine blades and composition changes of superalloys, with particular focus on creep performance. However, as engineers develop ways to push the TET even higher, the yield strength is becoming an increasing important focus, especially where stress concentrations result in low cycle fatigue challenges, such as at the turbine blade root. Furthermore, deformation mechanisms which were thought to be only a feature of turbine blades have begun to appear in the discs. By improving our understanding of the yield strength anomaly in relation to the dislocation behaviour, it is hoped that such challenges encountered at higher operating temperatures can be overcome.

In this work, the yield behaviour of superalloys has been studied by changing the temperature, strain rate and composition against a reference condition: commercial second-generation single crystal superalloy CMSX-4, deformed at 750 °C and a strain rate $10^{-4}\,\mathrm{s}^{-1}$. A general overview of the effect of temperature on tensile behaviour is first covered. This is compared against a first-generation superalloy, SRR99, which has a high diffusivity coefficient, to understand the effect of diffusion on stacking fault formation, and a fourth-generation superalloy, TMS-138A, to understand the effect of compositional changes, in particular ruthenium addition, on the tensile behaviour.

The strain rate is another mechanical testing parameter thought to have an effect on the deformation behaviour of Ni-based superalloys. The Young's modulus, strength, plasticity and ductility would be expected to change with increasing strain rate. As a result, the mechanical properties and deformation behaviour of superalloys used for rotating parts under dynamic loading is not given full consideration during the design with respect to composition and microstructure, even though the load is significantly different compared with that under a static load. Therefore, the study on the deformation behavior of the alloy under different strain rates is useful to improve our understanding of the effect of strain rate in relation to the performance of rotating turbine engine components used under service conditions.

Finally, the underlying cross-slip mechanism which is thought to control yield behaviour in $L1_2$ alloys is investigated in single crystal nickel-based superalloys. Though it is well documented that the yield stress anomaly comes from the γ' phase, the dislocation interactions within the two-phase γ/γ' structure is still not fully understood. Through imaging dislocations at various angles, a mechanism governing cross-slip and in turn yield in single crystal Ni-based superalloys is presented. Following this, directions for future research to confirm the cross-slip mechanism and further investigate the effect of composition and temperature on strain rate variation effects are discussed.

Chapter 2

Literature Review

2.1 How Superalloy Turbine Blades Are Made

Turbine blades for the first gas turbine engine were produced by extrusion and forging operations. These blades tended to be heavy and it was impossible to make them hollow, without significant subsequent machining. They were also prone to cracking and incipient melting due to non-uniform composition, from high working temperatures. Nowadays, superalloy turbine blades are made by a process called investment casting. This produces hollow blades with intricate internal cooling passages, allowing cool air to flow through the blade during operation, to restrict the temperature of the blades.

The Investment Casting Process

A schematic illustration of the investment casting process is shown in Figure 2.1. This is a multi-step process with sub-steps depending on the desired casting.[87, 6, 119] The following explanation is applicable to the manufacturing of superalloys for turbine blades. A similar process exists for other metals. The first step involves producing wax patterns of the blades. Molten wax is injected into a metallic ’master’ mould, containing a ceramic core defining the cooling channels of the blade. Once set, this produces wax patterns of the blade. Multiple blades are then attached together to form a wax tree, enabling several blades to be produced in a single casting.

This wax tree is then dipped into a ceramic slurry mixture of binding agents including zircon ($ZrSiO_4$), alumina (Al_2O_3) and silica (SiO_2) to form an investment shell. These layers are usually built up in two steps: the wax tree is first dipped in fine materials to preserve the fine texture and detail of the mould. A stuccoing process then applies layers of coarser ceramic mixture. Hardening allows the coating to cure. These steps are normally repeated three or four times to ensure the wax tree gains a sufficiently thick coating. The layers formed from cyclic dipping in the ceramic slurry mix of different composition give both a sufficiently strong outer layer and an inert, smooth finish layer.

Once the ceramic moulds are fully cured, the mould is turned upside down and baked in stages at varying temperatures. Initially, the temperature is just high enough to melt the wax. Further steps at higher temperatures fire the ceramic mould. After preheating and degassing, the mould is ready to use. Molten superalloy is poured into the mould under vacuum at a temperature of around 1550 °C. After solidification has occurred, the investment shell is released by shakeout and the internal ceramic core is dissolved by chemical means. The blades are cut off from the tree yielding individual turbine blades.

Producing Single Crystal Turbine Blades

The investment casting process has been used to produce turbine blade since the 1970s. Since then, the process has undergone significant refinement to allow casting techniques to produce materials that can withstand higher combustion temperatures, in turn improving the thrust and thermal efficiency of turbine engines. The first turbine blades produced from investment casting had equiaxed grains. To improve creep performance, transverse grain boundaries were prevented from forming during casting by a process termed directional solidification.[163] This involves slowly drawing the casting from the furnace, producing elongated, columnar grains.

The grain boundaries are areas of mechanical weakness. Therefore, to further improve creep and thermal fatigue resistance, the grain boundaries can be entirely removed, in turn, producing single crystal turbine blades. The removal of grain boundaries also results in a higher incipient melting temperature because elements that provide grain boundary strengthening such as boron and hafnium are no longer required.[164] However, even as a single crystal, the mechanical properties are not isotropic. The low-cycle fatigue life during thermal cycling is maximised when $\langle 001 \rangle$ direction of the single crystal is parallel with the loading direction.[28] To get $\langle 001 \rangle$ as the preferred grain orientation during directional solidification, two approaches are used: grain selection and the seeding technique. These methods vary in cost and accuracy, as explained below.

Grain selection relies on competitive growth between grains through a grain selector until one grain dominates. This dominant grain is then drawn out to form the turbine blade.[22] Various grain selector designs are used for the single crystal form of investment casting, of which the most common type of grain selector is pig-tail-shaped, consisting of a starter block and a spiral passage (see Figure 2.2).[22, 119] The width of the spiral is of similar size to one grain, limiting multiple grains entering the casting cavity.[119] Grain selection is widely used due to convenience and being cost-effective, producing cast components within 15° of the primary $\langle 001 \rangle$ orientation.[165] However, this low accuracy for primary grain control and the inability to control secondary orientation limits use to applications where a high degree of orientation accuracy is not required.[85, 174]

The alternative approach, called the seeding method, involves placing a specific orientation seed at the bottom of the casting shell. The seed partially melts and transfers its orientation to a new single grain, which is drawn out to produce a single crystal structure.[26] The seeding method allows for more accurate control of both the primary and secondary grain orientation compared to the grain selection method. However, there are two downsides: this method is more expensive than the grain selection method because the seed has only a single use, and the success rate of production of single crystal superalloy components is low because stray grains often form at the seed surface.[174] At present, these two processes are the most commonly used to produce single crystal Ni-based superalloy components although active work is being done to further improve these processes.

2.2 The Structure of a Superalloy

The essential solutes in Ni-based superalloys are aluminium or titanium, with a total concentration typically less than 10 at.%. This generates a two-phase equilibrium microstructure, consisting of a gamma (γ) phase and a gamma-prime (γ') phase. Figure 2.3 shows the Ni-Al-Ti ternary phase diagram and the γ and γ' phase fields, at two different temperatures: 973 K and 1573 K. For a given chemical composition, the fraction of γ' decreases as the temperature is increased. This allows the γ' to dissolve at a sufficiently high temperature, followed by ageing at a lower temperature to generate the desired shape and dispersion of strengthening precipitates. The γ phase, which forms the matrix, has a face-centred cubic (FCC) structure and a random distribution of different species of nickel and aluminum atoms (Figure 2.4(a)). The γ' phase has a primitive-cubic, ordered crystal structure, with nickel atoms on the faces and aluminium or titanium atoms at the corners (Figure 2.4(b)). This atomic arrangement has the the $L1_2$ crystal structure and chemical formula Ni_3Al.

Within a single crystal Ni-based superalloy, the γ phase forms a matrix phase around the γ' precipitates. The shape of these precipitates is independent on the lattice misfit; the precipitates are spheroidal in shape, and become more cuboidal as coarsening is promoted by

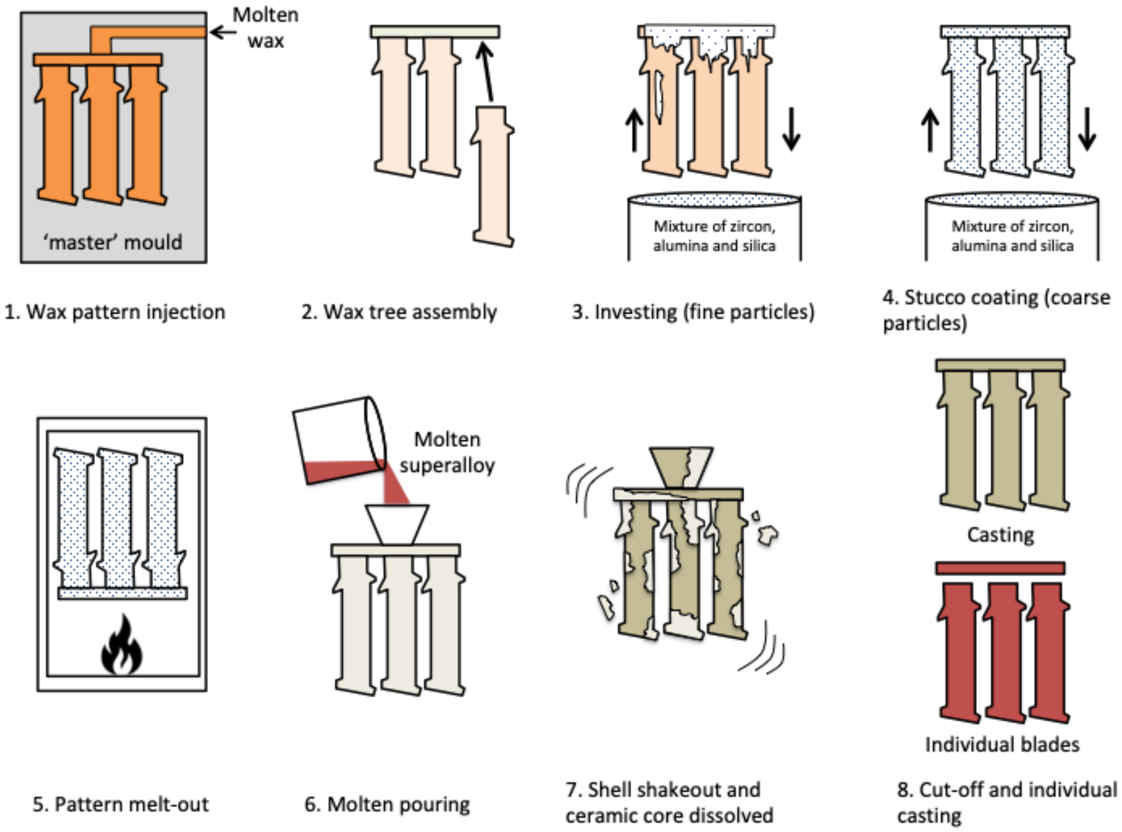

Figure 2.1 A schematic illustration of the various stages of the investment casting process. Adapted from [119].

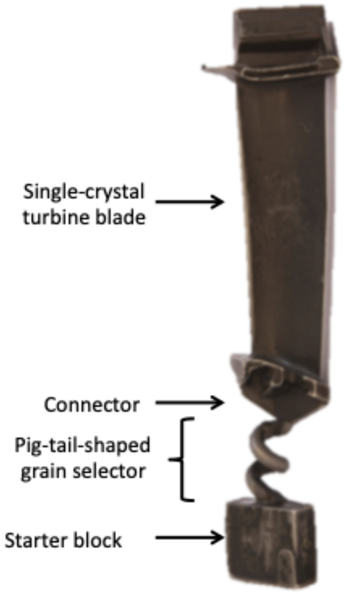

Figure 2.2 A investment cast single crystal turbine blade showing the starter block, pig-tail-shaped grain selector and connector in relation to the turbine blade. Image from Institute of Making.

ageing. The onset of the transition from spheres to cuboidal form is reported to be delayed for alloys with a low misfit.[119] Figure 2.5 is a transmission electron micrograph showing cuboid γ' precipitates within the γ matrix. The optimum microstructure consists of many fine γ' precipitates with thin channels of the γ matrix separating them but the ideal volume fraction is dependent on which mechanical properties need to be optimised under operating conditions. For example, the creep rupture life for third generation Ni-based single crystal superalloy TMS-75 was longest at measured γ' volume fraction of 70% and 55% at 900 °C and 1100 °C respectively.[100] The tensile strength however is reported to peak at 55% volume fraction.[40]

To understand the optimum chemistry of the Ni_3Al γ' phase, it is useful to consider the Ni-Al binary phase diagram, shown in Figure 2.6. At 700 °C, the solubility of Al in Ni is about 10 at.%. The Ni_3Al has an Al content of 25 at.%. Therefore, in a binary system, a composition, c, is needed that satisfies $(c - 10)/(25\text{-}10) = 0.75$. Hence $c = 21.25$ at.% Al. This corresponds to roughly 11 wt.% Al. A modern single crystal superalloy would have about 6 wt.% Al.

The Ni-Al binary phase diagram shows that stable γ' phase of Ni_3Al appears up to 1395 °C. To optimise the γ' volume fraction, the γ' is put into solution by holding the alloy at a temperature below the melting temperature, where γ is the only stable phase. Subsequent ageing heat treatments after solidification are then required at two different, lower temperatures within the γ/γ' phase field to remove residual microsegregation and eutectic mixtures rich in γ'. The higher temperature heat treatment precipitates out coarser particles of γ'. The second, lower temperature heat treatment leads to further precipitation of a finer, secondary dispersion of γ'. The overall result is a bi-modal distribution of γ'.

The removal of grain boundary strengthening solutes in single crystal superalloys results in an increase in the localised melting temperature due to chemical segregation.[164] Single crystal alloys can therefore be solution heat treated to a higher temperature, just below the melting temperature, in the range 1240-1330 °C. This allows dissolution of coarse γ' which is a remnant of the solidification process. Subsequent heat treatments then determine the γ' precipitate size, known as precipitation ageing. For a typical single-crystal superalloy such as CMSX-4, the heat treatment would involve solution treatment at 1314 °C to dissolve the γ' phase.[50] This is followed by a primary age of 4h at 1140 °C and a secondary age of 16h at 870 °C. These subsequent steps help to ensure a homogeneous and fine dispersion of γ' precipitates within the γ matrix. Figure 2.7 shows a prediction of the phase stability for CMSX-4 around the melting temperature. The solutioning window is rather small, about 50 °C, emphasising the precise temperature control required during heat treatment.

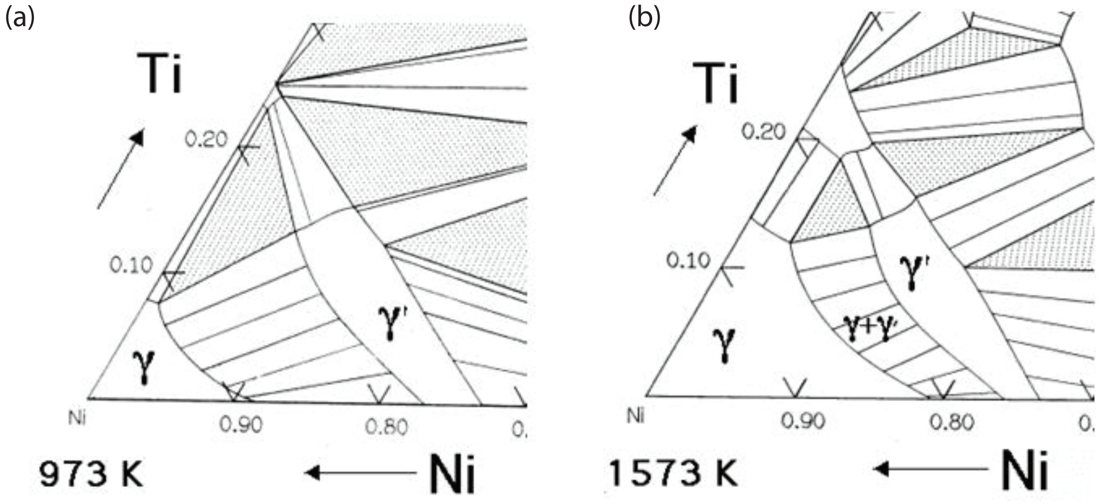

Figure 2.3 The Ni-Al-Ti ternary phase diagram at (a) 973 K and (b) 1573 K. Both show the γ and γ' phase fields. The amount of γ' depends on the chemical composition and temperature.[7]

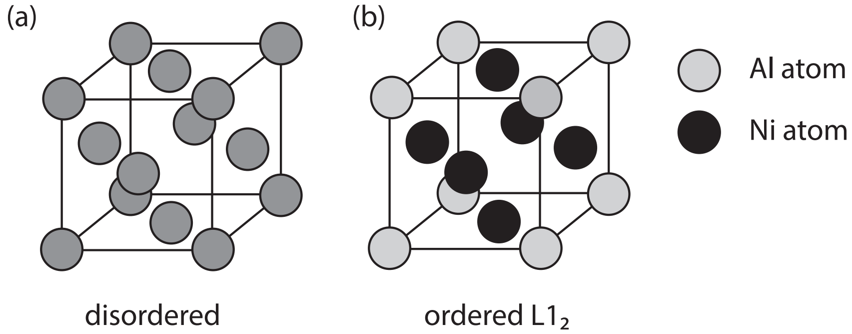

Figure 2.4 (a) The γ-phase has a face-centred cubic (FCC) crystal structure with a random distribution of nickel and aluminium atoms. (b) The L1$_2$ γ'-phase, in contrast, has a primitive cubic, ordered crystal structure with aluminium atoms on the corners and nickel atoms on the faces. Adapted from [119]

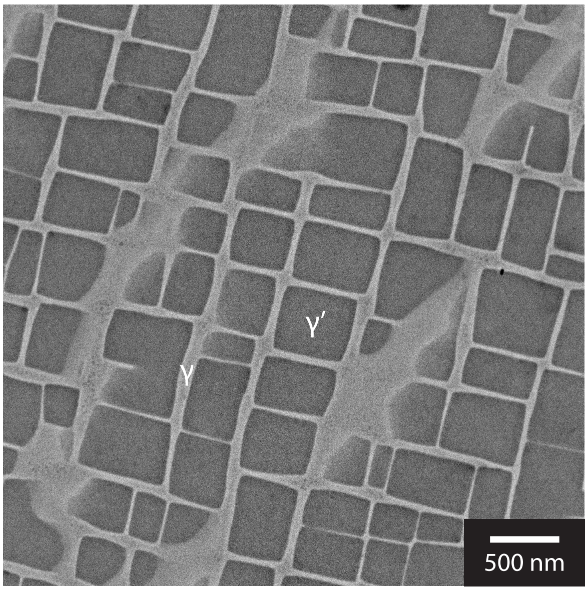

Figure 2.5 The microstructure of a single-crystal superalloy after standard heat treatment showing cubic γ' precipitates encompassed within a Ni-Al solid solution γ-matrix.[129]

2.3 Planar Faults in the $L1_2$ Ordered Structure

The $L1_2$ crystal structure of the γ' phase reduces the symmetry and changes the shortest perfect Burgers vector compared to in the FCC crystal structure of γ phase. The shortest perfect Burgers vector is $a\langle 110\rangle$ within an $L1_2$ crystal structure compared to $\frac{a}{2}\langle 1\bar{1}0\rangle$ for an FCC crystal structure. As a result, a perfect $\frac{a}{2}\langle 1\bar{1}0\rangle\{111\}$ dislocation that forms in the γ phase cannot enter the γ' phase without creating a planar defect such as an antiphase boundary.[77] This is one example of the distinct faults that form as a result of dislocation configurations originating in the matrix phase and moving into the γ' phase. The γ' phase is thought to increase the strength of a γ/γ' material through such planar faults that can form depending on the Burgers vector and direction of movement of dislocations from the disordered FCC crystal structure of the γ phase to the $L1_2$ ordered crystal structure of the γ' phase. A review is given below of the possible planar faults that can form within a γ/γ' material.

In a disordered FCC structure, atoms can be approximated as hard spheres held together by attractive forces. Stacking close packed layers of atoms on top of one another generates the structure. With reference to Figure 2.8, we consider layer A, a two-dimensional closed-packed layer of atoms. Close packing can be continued in a third dimension by stacking additional layers. The atoms of a subsequent layer can occupy B or C sites. If the stacking alternates every third layer (e.g. ABCABC...), an FCC structure is produced, where the layers become $\{111\}$ planes of the crystal. If the stacking is every two layers (e.g. ABABAB...), a hexagonal

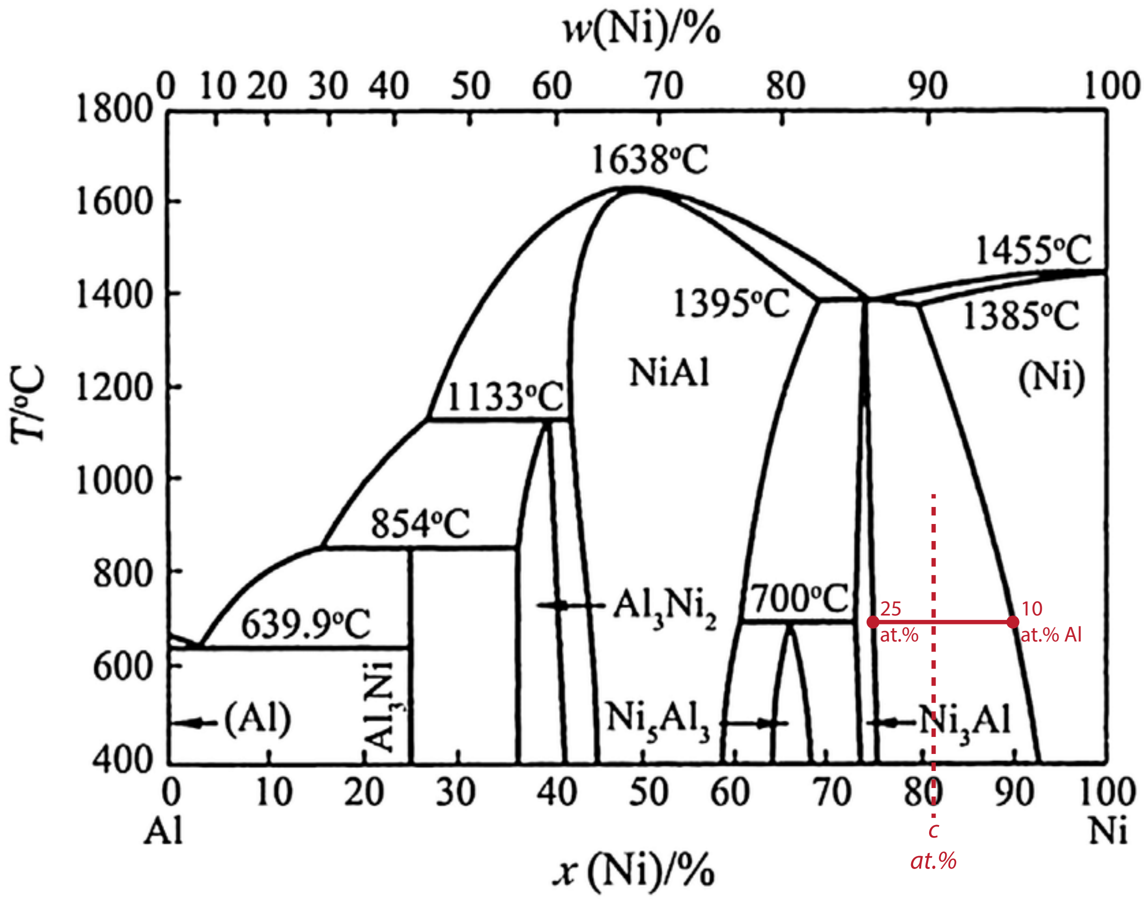

Figure 2.6 The Ni-Al binary phase diagram. As shown in red, the the solubility of Al in Ni is about 10 at.%. The Ni_3Al has an Al content of 25 at.%. To produce an alloy with 75% γ' volume fraction, a composition, c, is needed that satisfies (c - 10)/(25-10) = 0.75. Adapted from [58]

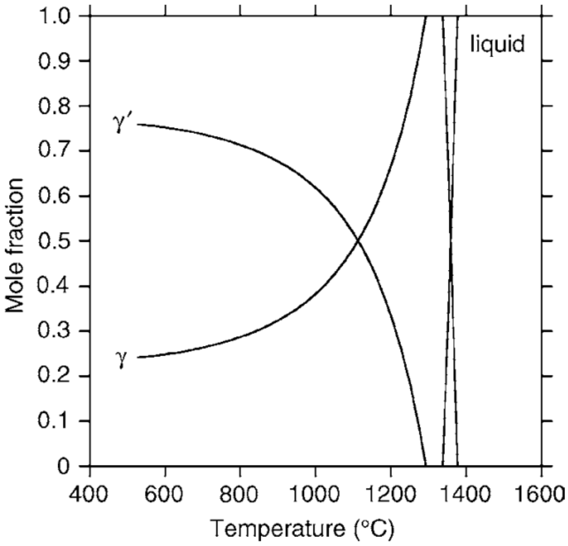

Figure 2.7 Variation of the fraction of the liquid, γ and γ' phases with temperature for the single-crystal superalloy CMSX-4. The solutioning window lies between 1300 °C and 1350 °C.[119]

close-packed (HCP) structure is produced. The passing of dislocations through the crystal structure shifts these layers with respect to each other, introducing defects, as outlined below. Slip in FCC crystals occurs predominantly by the motion of $\frac{a}{2}\langle 110\rangle$ type of dislocations on $\{111\}$ planes. In an $L1_2$ crystal, the passing of a single $\frac{a}{2}\langle 110\rangle\{111\}$ dislocation leaves an anti-phase boundary (APB) in its wake. Although $\frac{a}{2}\langle 110\rangle\{111\}$ is a primitive Burgers vector in an FCC lattice restoring atomic positions, in Ni_3Al it introduces high energy bonds. Al-Al bonds have the highest energy, compared to Ni-Ni and Ni-Al bonds, due to the relatively large size of the aluminium atoms.[101] The structure of the APB can be compared against that of a perfect crystal in Figure 2.9(a) and (b). Although the FCC stacking sequence remains unchanged in an APB, the shift causes layers, represented by *, to have an alternate chemistry to the perfect crystal.

An APB is one of a number of planar defects possible in Ni_3Al, including a number of stacking faults that can be classed as intrinsic, extrinsic or high energy (complex). The $L1_2$ ordering results in a total of seven possibilities, which are variants of the three faults that may form in a disordered FCC crystal.

An intrinsic stacking fault (ISF) can be produced by a shearing operation, which displaces close packed layers by a $\frac{a}{6}\langle 112\rangle$ vector so that their atoms occupy the next available sites (A→B, B→C, C→A). This shear effectively removes a single layer from the stacking sequence and creates two twin planes separated by one atomic layer. When this operation is performed on a perfect Ni_3Al crystal, undesirable bonds are again created and a complex fault is created (Figure 2.9(c)). This fault has been described as a combination of an intrinsic fault and an APB, with a fault energy slightly higher than the APB energy.[84]

When this shear operation is performed at an APB, high energy bonds are removed and a superlattice intrinsic stacking fault (SISF) is created (see Figure 2.9(d)). An SISF can also be produced by displacement of a close-packed plane by $\frac{a}{3}\langle 112\rangle$ which allow the Al atoms to maintain their separation. The removal of nearest neighbour violations supports a number of studies that show the SISF has a low fault energy when compared to the other faults.[36, 120, 66, 162, 151]

A high-energy fault is created when a further shearing operation is carried out on one side of the intrinsic fault plane. This operation is the equivalent of insertion of an extra plane into the stacking sequence:

$$\mathrm{ABCABC} \mid \mathrm{CABCABC} \tag{2.1}$$

A similar operation on a SISF produces the same high-energy fault.

$$\mathrm{ABCABC} \mid \mathrm{C^*A^*B^*C^*A^*B^*C^*} \tag{2.2}$$

In these faults, the atoms in adjacent layers are directly above one another, which violates close packing. When this shear operation is carried out on a CISF, aluminium atoms end up directly above those in the adjacent layer. Since Al-Al have the highest energy, this type of fault has the highest energy per unit area of all {111} faults.[125, 162]

To avoid the high-energy stacking, the first layer after the defect plane in an intrinsic fault is not subjected to the shearing operation. Thus an extrinsic fault is formed, which features two stacking fault planes separated by two twin planes. This high-energy fault is transformed into an extrinsic fault that has the structure SISF/CISF. Since this is a complex extrinsic fault, which has high-energy Al-Al bonding on one side of the fault, it is abbreviated as CESF-1 (see Figure 2.9(g)). Formation of this fault was first considered by Kear *et al.*[162] Subsequently, this fault has been observed in atomistic calculations of Ni_3Al and its energy was found to be substantially larger than that of the APB and CISF.

A different kind of complex extrinsic fault is formed when the same is done to the CISF. The resultant fault consists of two CISFs on adjacent planes and has high-energy Al-Al on both sides of the fault plane. It has exceptionally high energy and is termed the CESF-2 (see Figure 2.9(h)). Kear *et al.*[68, 69] also consider the formation of this fault, and suggested that its formation would be unfavourable due to high fault energy.

The Al-Al bonding in the CESF-2 can be removed, replaced by lower energy bonds by

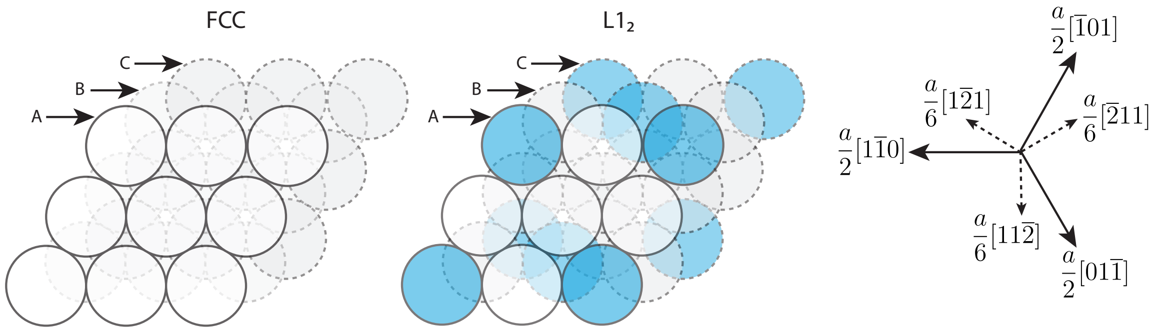

Figure 2.8 Stacking of close packed layers in the disordered FCC and $L1_2$ structures. Blue atoms are aluminium. Adapted from [77, 157].

one of two shearing operations of the single close packed layer in the middle of the fault: either a vector $\frac{a}{6}\langle 112\rangle$ or by $\frac{a}{2}\langle 110\rangle$ vector that lies normal to the former. The resultant fault is known as a superlattice extrinsic stacking fault (SESF), shown in Figure 2.9(i). The SESF fault energy is expected to be comparable to that of an SISF. This shift is essential for the passage of the propagation of partial dislocations through the $L1_2$ crystal structure. However, it is currently unclear how it happens. Mechanisms involving cooperative shear[68] or vacancy-mediated atomic shuffling and reordering[74, 73] have been proposed and are elaborated later in this section.

The γ-surface provides a good graphical representation of the possible fault structures within a crystal structure. The effective γ-surface in the crystallographic $\{111\}$ plane in $L1_2$ Ni_3Al is shown in Figure 2.10.[162] It shows that Ni_3Al can have five metastable stacking faults in this plane. Namely, an intrinsic superlattice stacking fault, extrinsic superlattice stacking fault, a complex stacking fault, an anti-phase boundary stacking fault and a complex extrinsic stacking fault.

The APB created upon the passage of a solitary $\frac{a}{2}\langle 110\rangle\{111\}$ dislocation makes slip on such a system highly unfavourable. Inter-atomic forces oppose the force exerted by the applied stress on this leading dislocation. However, these inter-atomic forces assist the force on the second, trailing $\frac{a}{2}\langle 110\rangle\{111\}$ dislocation, which annihilates the APB, returning the crystal to a perfect state upon passing. The shearing of an $L1_2$ lattice is accomplished by the passage of dislocations moving in closely-spaced pairs, producing an overall lattice displacement of a$\langle 110\rangle$. Such assemblies of dislocations that pass through the superlattice, leaving behind a perfect crystal, are termed ‘superdislocations’.

Depending on the magnitude of the APB energy, the $a\langle 110\rangle$ superdislocation can undergo one of two main dissociation schemes in Ni_3Al. If the APB energy is low, it would dissociate into two identical $\frac{a}{2}\langle 110\rangle$ dislocations. Each of these would consist of two Shockley partials

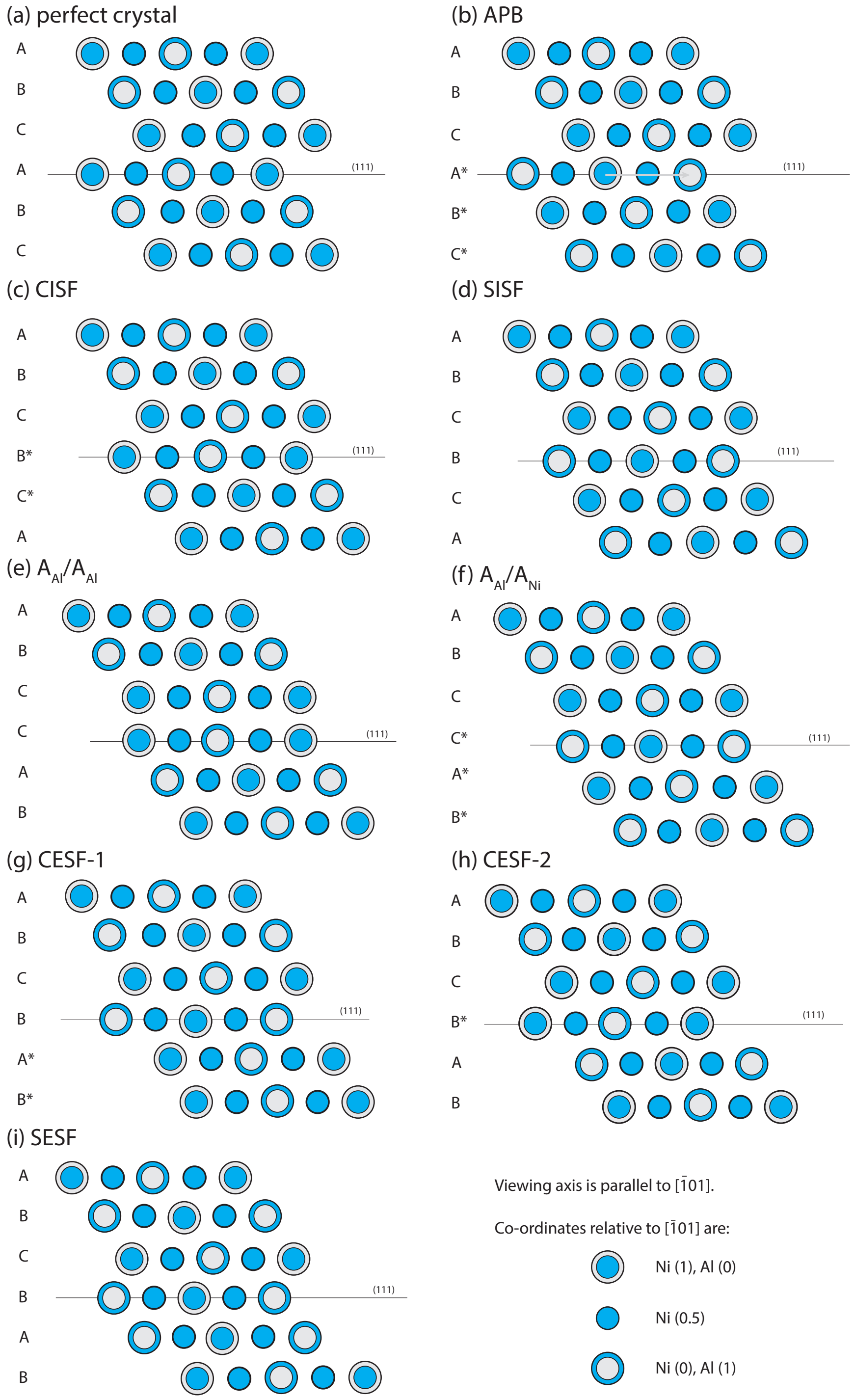

Figure 2.9 Various planar structures that can be produced parallel to {111} in Ni_3Al. Adapted from [77, 157].

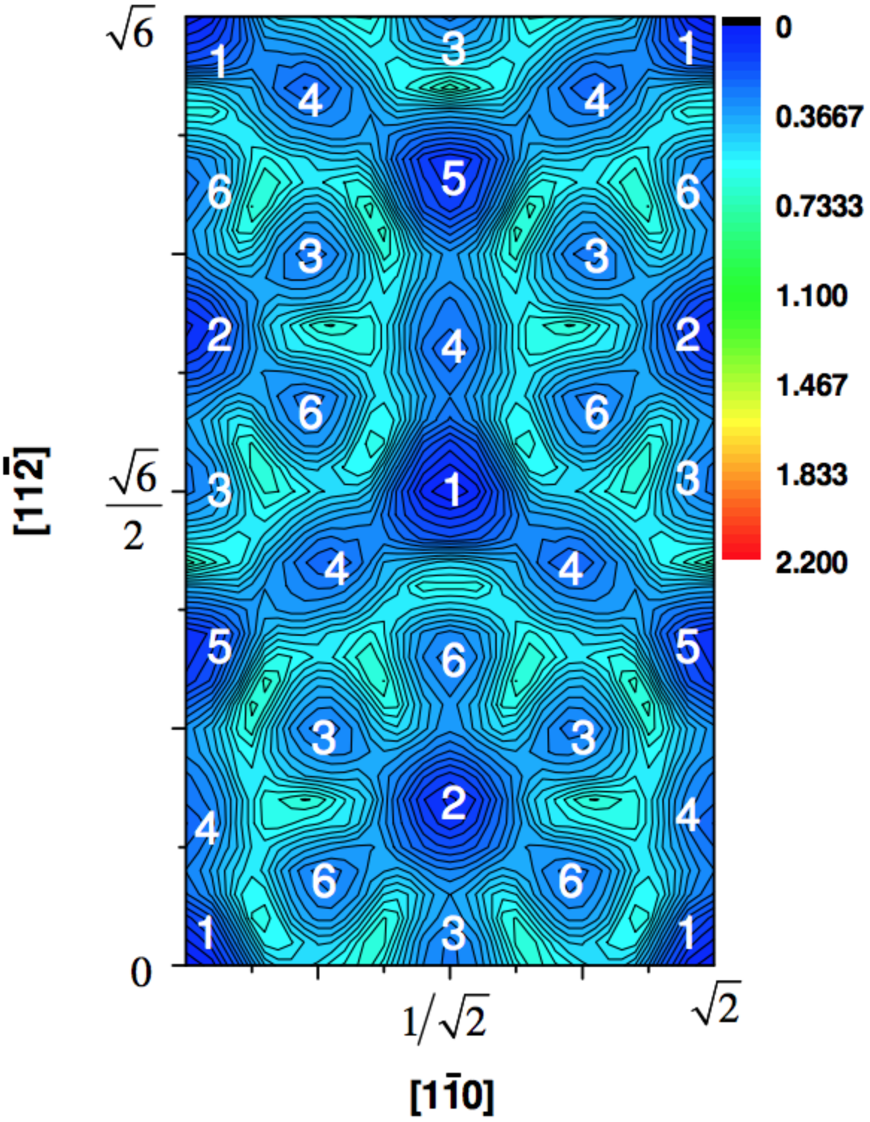

Figure 2.10 The contour plot of the effective γ-surface in the $\{111\}$ crystallographic plane in $L1_2$ Ni_3Al after accounting for the shift of one part of the crystal with respect to another in two adjacent $\{111\}$ planes. 1 denotes the local minima corresponding to the perfect crystal, 2- SISF, 3-APB, 4-CSF, 5-SESF and 6-CESF.[162]

bounding a CISF, shown in Figure 2.11(a):

$$2\mathrm{BA} \rightarrow \mathrm{BA} + \mathrm{APB} + \mathrm{BA} \rightarrow (\delta\mathrm{A} + \mathrm{CISF} + \mathrm{B}\delta) + \mathrm{APB} + (\delta\mathrm{A} + \mathrm{CISF} + \mathrm{B}\delta) \tag{2.3}$$

In contrast, a$\langle 110\rangle$ dislocations separated by a higher energy APB would dissociate into two $\frac{a}{3}\langle 112\rangle$ superpartials coupled by a superlattice intrinsic (or extrinsic) stacking fault. When this type of dissociation is confined to only one plane, the superpartials would dissociate into three Shockley partials forming a CISF and APB, separated by an SISF (as shown in Figure 2.11(b). This six-fold dissociation is as follows:

$$\begin{aligned} 2\mathrm{BA} &\rightarrow 2\mathrm{B}\delta + \mathrm{SISF} + 2\delta\mathrm{A} \\ &\rightarrow [\delta\mathrm{C} + \mathrm{CISF} + \mathrm{B}\delta + \mathrm{APB} + \delta\mathrm{A}] + \mathrm{SISF} + [\mathrm{B}\delta + \mathrm{APB} + \delta\mathrm{A} + \mathrm{CISF} + \mathrm{C}\delta] \end{aligned} \tag{2.4}$$

Despite the relatively low energy of the SISF, the larger Burger's vector of the superpartials makes this configuration unfavourable.

A further dissociation reaction is possible for dislocations with a net translation vector 2BA, that has a lower core energy than both of the cases (2.3) and (2.4). This alternative four-fold dissociation is schematised in Figure 2.11(d). The $\frac{a}{3}\langle 112\rangle$ dislocations could dissociate in a reaction that involves a dipole displacement so that the partial dislocations are on parallel planes, coupled by a low energy superlattice intrinsic fault. This is shown in Figure 2.11(c). Such a dissociation reaction, given by:

$$2\mathrm{BA} \rightarrow [2\mathrm{B}\delta + \mathrm{SISF} + 2\delta\mathrm{A}] \rightarrow [(\overline{\mathrm{B}\delta} + \text{CESF-1} + \mathrm{B}\delta) + \mathrm{SISF} + (\delta\mathrm{A} + \text{CESF-1} + \overline{\delta\mathrm{A}}] \tag{2.5}$$

is prevalent when the APB energy is high and if preferred over equation 2.3[173] The $a\langle 110\rangle$ can also dissociate so that the order of the two $\frac{a}{3}\langle 112\rangle$ superpartials is reversed. This would result in an SESF:

$$2\mathrm{BA} \rightarrow [2\delta\mathrm{A} + \mathrm{SESF} + 2\mathrm{B}\delta] \rightarrow [(\delta\mathrm{A} + \mathrm{CISF} + \overline{\delta\mathrm{A}}) + \mathrm{SESF} + (\overline{\mathrm{B}\delta} + \mathrm{CISF} + \mathrm{B}\delta)] \tag{2.6}$$

and has been illustrated in Figure 2.11(d).

Another superdislocation with net Burgers vector $a\langle 112\rangle$ (6Bδ) can exist in an $L1_2$ structure. Like the passing of $a\langle 110\rangle$ dislocations, it leaves a perfect crystal in its wake.

When the SESF/SISF energy is much lower than the APB energy, dislocations are arranged to form a superlattice intrinsic/extrinsic fault pair, which promotes the shearing of a precipitate. Under these conditions, two dissociations are possible, each with $6B\delta$ Burgers vector. These are termed ‘cooperative slip’ and ‘viscous slip’. This process creates leading Shockley partials of the same Burgers vector that cooperatively shear larger γ' precipitates. Viscous slip is slower because it is limited by diffusion.

For cooperative slip, the $a\langle 112\rangle$ dislocation consists of two $a\langle 110\rangle$ superdislocations gliding on adjacent $\{111\}$ planes. The resultant configuration is shown in Figure 2.11(e). Although the scheme promotes the shearing of a precipitate by the creation of SISF and SESF, this configuration also requires a high-energy CESF-2 and a double APB to be created. These high energy faults would result in dislocation constrictions at the γ/γ' interface during shearing. The second possibility, viscous slip, allows for such dislocation constrictions to be avoided, in turn allowing the 3Bδ dislocations to pass through the γ' in a more relaxed array. If one considers the L1_2 structure and the displacements caused by all the Shockley partials in the viscous slip equation, it becomes apparent that there should be an undesirable CESF-2 in place of the SESF. This dissociation reaction is able to avoid such a high-energy fault by dipole displacement occurring at the partial that creates the extrinsic fault, converting the CESF-2 to a SESF:

$$\begin{aligned}
&6\mathrm{B}\delta \rightarrow 2\times[3\mathrm{B}\delta+\mathrm{APB}+3\mathrm{B}\delta]\\
&\rightarrow(\mathrm{A}\delta+\text{CESF-1}+\mathrm{A}\delta+\mathrm{SISF}+\mathrm{A}\delta)+\mathrm{APB}+(\mathrm{A}\delta+\mathrm{SESF}+\mathrm{A}\delta+CISF+\mathrm{A}\delta) \quad (2.7)
\end{aligned}$$

Another displacement would also be needed at the trailing partial, to give the desired configuration above. Displacement of the whole layer by shear would produce this conversion, but is energetically unfavourable.

Kear *et al.*[68, 69] proposed that the required dipole displacements could be obtained by vacancy migration through a process termed shuffling. This is a diffusion mediated exchange of Ni and Al atoms. Such a mechanism would therefore be favourable at elevated temperatures and low strain rates such as during creep deformation. Kear *et al.*[78] subsequently found evidence of viscous slip in superalloy specimens that had been subjected to primary creep.

The reordering process has been analysed by Kovarik.[73] The dislocation configuration is complex, composed of a series of partial dislocations gliding on adjacent planes. The detailed depiction of Figure 2.11(f) is shown in Figure 2.13. In the compact notation, the leading $\frac{a}{3}[112]$ dislocation is represented as $\overline{\mathrm{B}\delta}$+B$\delta$. $\overline{\mathrm{B}\delta}$ implies that the dislocation is spread on two atomic planes, composed of a δC partial on one plane and a δA partial on the adjacent plane. The dipole displacements, represented by ’□’ provide the necessarily shift of atoms in the central plane by $\frac{a}{2}\langle 110\rangle$ to obtain the low-energy Al-Al nearest neighbour free configuration in the wake of the gliding dislocations.

The reordering process to convert a two-layer CESF-1 into an SISF requires a switch of atoms in the row of anti-sites along the AB or BA direction. Reordering is required at two further separate locations at the trailing half of the fault: one location at the core or after passage of the $\frac{a}{6}[112]$, converting the two-layer CSF into a SESF, the other location is at the core of the $\frac{a}{3}[112]$, converting the APB into a perfect crystal. The energetic aspect of the vacancy exchanges allowing for reordering of nickel and aluminium sites has been studied with *ab-initio* calculations.[74] There exists a variety of pathways that accomplish an exchange of the nickel and aluminium anti-sites. The reordering pathways considered below assume that the starting point is such that the vacancy is on a nickel site adjacent to the anti-site column. The other possible scenario with the vacancy on an aluminium site is not considered here. This assumption stems from the fact that a significantly higher concentration of vacancies exists on nickel sites in the model system, Ni_3Al.[48, 63] Given that the vacancy is on a nickel site, all viable pathways can be considered as a minimum three-step vacancy jump sequence. The first step always involves an exchange of the vacancy with an atom in the anti-site [110] column. The second step involves exchange of the vacancy and the second atom from the anti-site [110] column. This step places the second atom on its proper site. In the third step, the swap between the two anti-sites is accomplished.

Density Functional Theory (DFT) was used to evaluate the energies associated with the various combinations of reordering steps. The more favourable exchange reordering sequence is where the first exchange is V^{Ni}-Ni^{Al} compared to beginning with a V^{Ni}-Al^{Ni} exchange. The simulations also showed that each forward transition in the sequence has a greater probability than a step backward. The ten possible first steps of this sequence are illustrated in Figure 2.12. Of these, only three (I_1, I_2 and I_3) are crystallographically unique. There are nine possibilities for the final step, only five of those sites are unique (only 3 are shown F_1, F_2 and F_3). The pathway I_1, S_1, F_3 was found to be the most favourable energetically.

The planar fault structures within the Ni_3Al structure and γ' phase require energy to form. The strengthening that results from the creation of these planar faults is known as order hardening. Order hardening is thought to be a significant factor to the strength in Ni-based superalloys. Copley and Kear calculated the contribution of APB formation to the critical resolved shear stress of the superalloy Mar-M200 to be approximately two-thirds.[16] The increase in CRSS, $\Delta\tau_{APB}$ was given by:

$$\Delta\tau_{\mathrm{APB}} = \frac{\gamma_{\mathrm{APB}}}{2b} \tag{2.8}$$

where γ_{APB} is the APB energy and b is the Burgers vector.
Order hardening is one of four mechanisms proposed by Ardell *et al.* that contribute towards strengthening of superalloys.[2] The other mechanisms are chemical, modulus and coherency strengthening. Of the remaining mechanisms, only coherency strengthening is thought to have a significant contribution to strength in Ni-based superalloys. The relative contribution of these different strengthening mechanisms to a superalloy also depends on other factors including precipitate volume fraction, distribution of precipitates and precipitate size. What follows is a review of models to understand the effect of precipitate strengthening on a single crystal Ni-based superalloy.

2.4 Precipitate Strengthening in Nickel-based Superalloys

Depending on the size of the precipitate, the response of a dislocation moving in the γ phase after encountering an $\mathrm{L1_2}$ precipitate will vary. The dislocation can bend around, cut through or cross-slip over the precipitate or be stopped by the precipitate. Two cases are commonly considered to determine the effect of precipitate size and volume fraction on the yield strength of a superalloy: the weak pair-coupling and strong pair-coupling. The difference between the two conditions is the relative difference between the paired dislocation spacing and the size of the precipitate. Under the weakly coupled condition, the spacing between two paired dislocations is larger than the precipitate's diameter. As a result, the second, trailing dislocation is some way behind the first, leaving a faulted particle in between the two dislocation lines. This is applicable for small precipitates which can be more easily cut by dislocations. For a microstructure with larger precipitates, the spacing of the dislocation pairs is of similar magnitude to the precipitates' diameter. Therefore, any given precipitate may contain a pair of dislocations which are held together by the anti-phase boundary energy. This condition is termed strong pair-coupling. To further understand what aspects of a Ni-based superalloy have the biggest impact on yield strength, derivations are given below.

Weak Pair-coupling

The weak pair-coupling condition is considered first. Under this condition, the spacing between two paired dislocations is larger than the precipitate's diameter. This results in a faulted particle in between the leading and trailing dislocations. An illustration of this condition is shown in Figure 2.14(a). For simplification, the γ' precipitates are assumed to be spherical and the overall precipitate volume fraction is small.

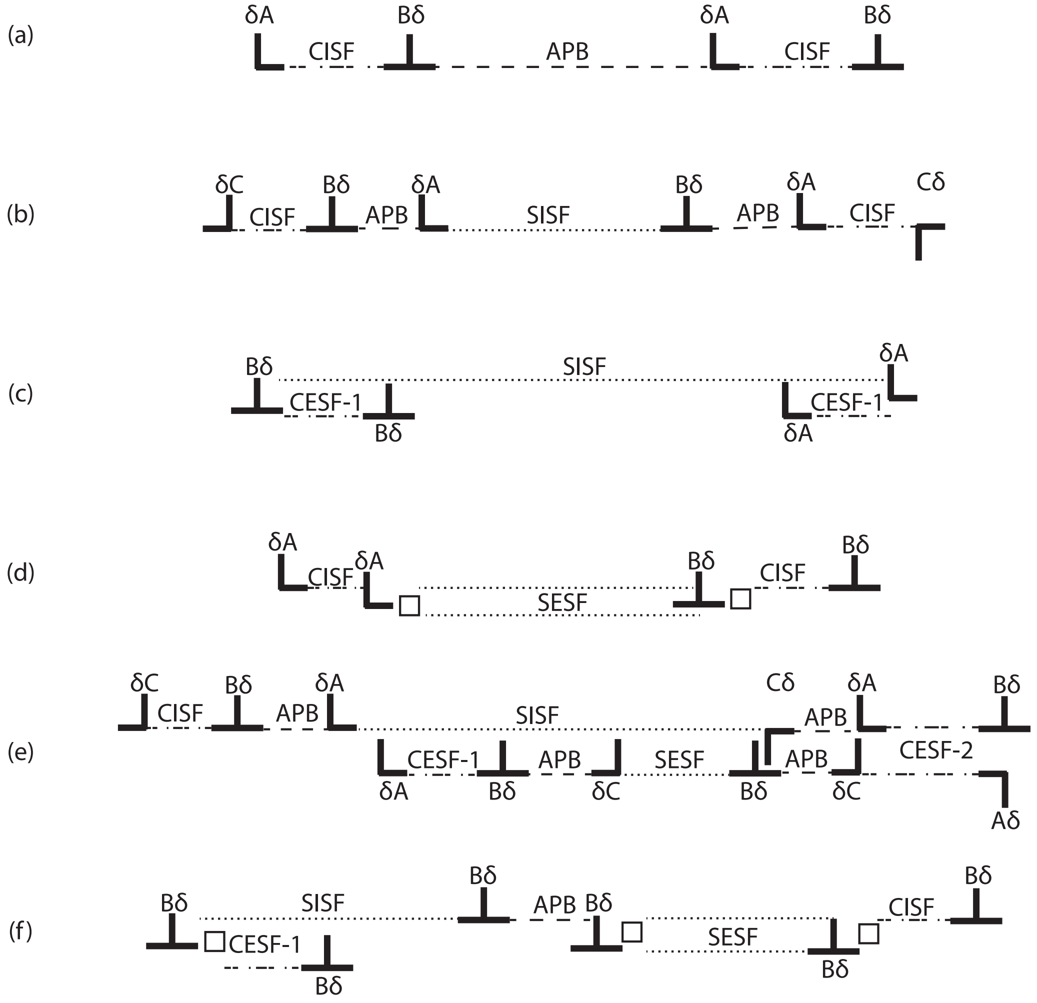

Figure 2.11 Dissociation schemes for $a\langle 110\rangle$ and a$\langle 112\rangle$ superdislocations in the $L1_2$ crystal, (a-d) and (e, f) respectively. The square symbols represent dipole displacement that is necessary to create and remove the SESF in place of the CESF-2. Adapted from Kear *et al.*[68, 69]

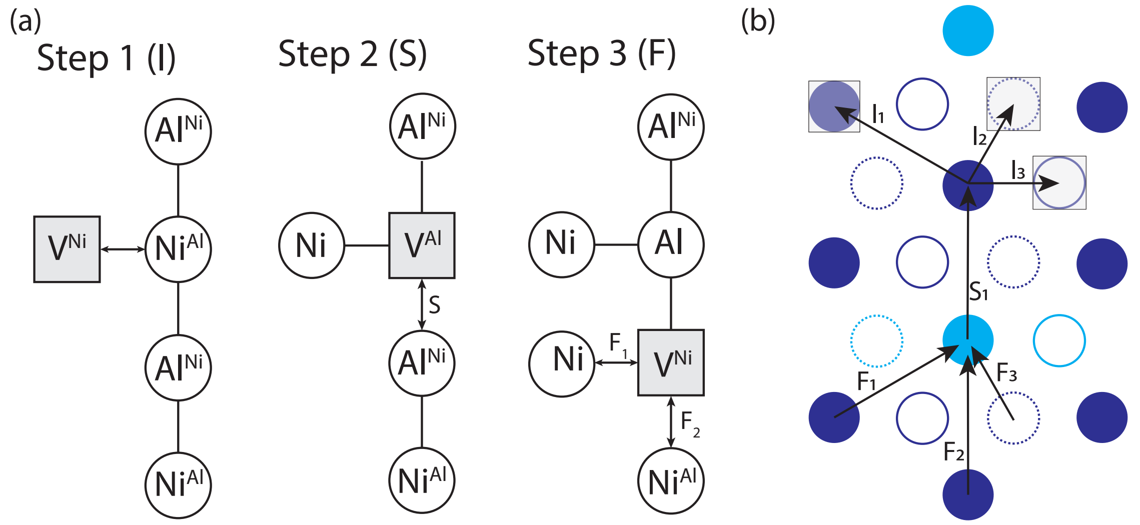

Figure 2.12 (a) A schematic illustration of the reordering sequence initiated by an exchange between Va^{Ni} and Ni^{Al}, (b) The actual representation of the atom configuration and the possible reordering pathways. Dark blue is Ni, light blue is Al. The grey squares are vacancies, empty circles are atoms from the planes above and below. Adapted from [73].

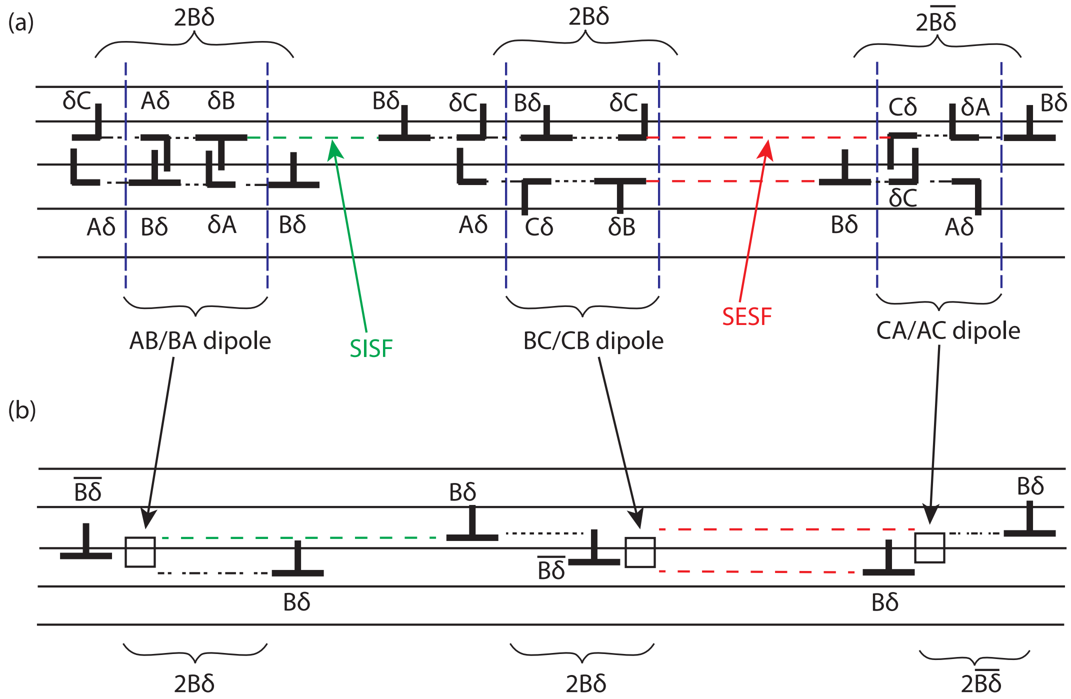

Figure 2.13 The dislocation configuration associated with viscous slip. (a) the detailed dislocation configuration and (b) the simplified notation where □ represents dislocation dipole displacement. Adapted from [69].

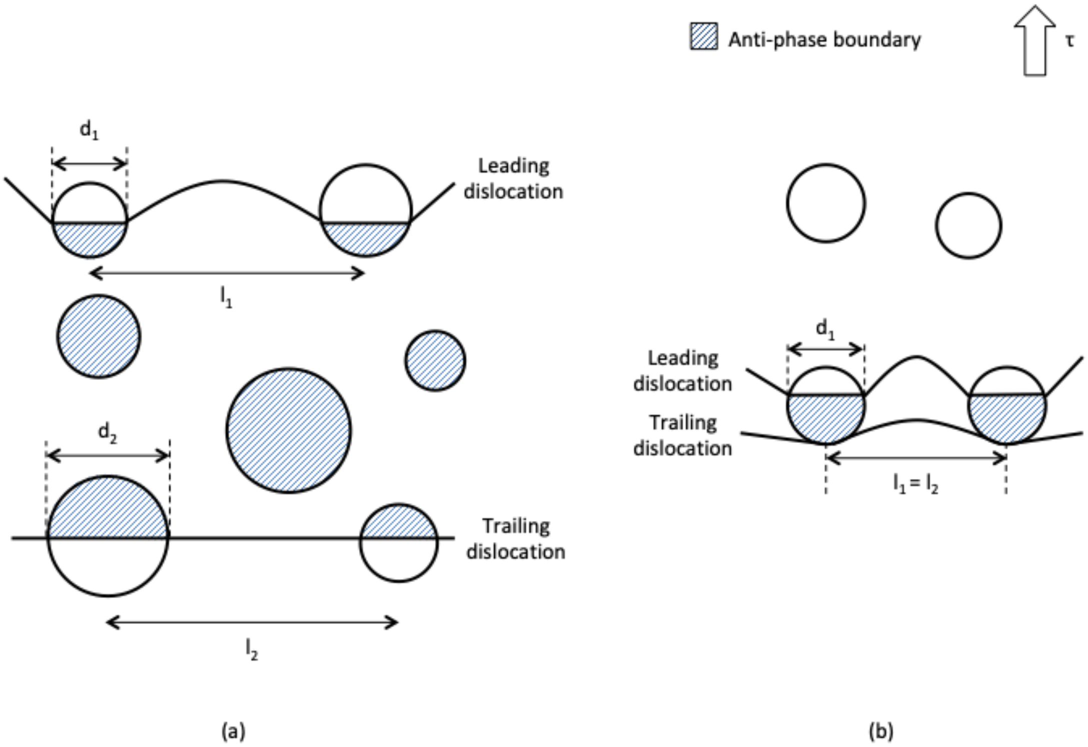

Figure 2.14 Schematic illustration of spherical γ' precipitates being sheared by a pair of dislocations under two conditions: (a) weak pair-coupling and (b) strong pair-coupling. Adapted from [39].

To calculate an expression for the strengthening under this weak pair-coupling condition, the forces on the pair of dislocations is analysed. Three forces act on the pair of dislocations: (i) the applied shear stress which drives the particle shearing process, (ii) a repulsive force, keeping the dislocations separated, because the dislocations are of the same Burgers vector, and (iii) the pinning force caused by the APB energy.

The shear stress exerts a force on each dislocation given by $\tau b l_i$ (i = 1,2) respectively; where τ is the applied shear stress, b is the Burgers vector and l_i is the distance between shearing particles for the leading and trailing dislocations. The elastic repulsive force per unit length is denoted by F_R, the pinning force from the APB, F_p, given by $\gamma_{APB} d_i$ (i = 1,2), where l_i (i = 1,2) is the length of the leading and trailing dislocations, and d_i (i = 1,2) is the length of the dislocations within the precipitates for each superpartial. Doing a force balance on the two dislocations yields the following equations:

$$\tau b l_1 + F_R l_1 - \gamma_{APB} d_1 = 0 \tag{2.9}$$

$$\tau b l_2 - F_R l_2 + \gamma_{APB} d_2 = 0 \tag{2.10}$$

Making τ the subject and eliminating F_R gives:

$$\tau = \frac{\gamma_{APB}}{2b}\left[\frac{d_1}{l_1} - \frac{d_2}{l_2}\right] \tag{2.11}$$

As shown in Figure 2.14, for the weak pair-coupling condition, the trailing dislocation is straight, and therefore, $\frac{d_2}{l_2}$ = v, where v is the precipitate volume fraction.

The leading partial gets pinned back by the particles and must bow between them to overcome the pinning forces. By bowing, a line tension, T, acts in the direction opposite to the pinning force. Under static equilibrium, resolving forces on the particle in the vertical condition gives:

$$F_p = 2T cos\frac{\phi}{2} \tag{2.12}$$

where F_p is the pinning force and ϕ is the angle between the two dislocations lines, each with line tension, T. The amount of bowing is dependant on the particle spacing, known as the Friedel spacing, denoted l_f. The relationship between d_1 and l_f can be derived by modelling a random assortment of particles within a slip plane.[2] The Friedel relationship is given by:

$$l_f = l_1 = \left(\frac{2T}{F_R}\right)^{\frac{1}{2}} \times \left(\frac{2\pi}{3v}\right)^{\frac{1}{2}} \times \frac{d_1}{2} \tag{2.13}$$

To derive an equation for the critical resolved shear stress, τ_c, substitute equation 2.13 into equation 2.11, and replace F_p with $d_1 \gamma_{APB}$ yields the expression:

$$\tau_c = \frac{\gamma_{APB}}{2b} \left[\left(\frac{3F_p v d_1}{T\pi} \right)^{\frac{1}{2}} - v \right] \tag{2.14}$$

Weak pair coupling applies to smaller end of particle size. For large particles, $(3F_p v d_1/T\pi)^{1/2} \gg v$ and a representative value can be expressed as:

$$\tau_c = \frac{\gamma_{APB}}{2b} \left(\frac{3F_p v d_1}{T\pi} \right)^{\frac{1}{2}} \tag{2.15}$$

Therefore the critical resolved shear stress, τ_c can be approximated to $(vd_1)^{1/2}$, i.e. the large particles are expected to have a dominant effect to promote hardening. There is also a strong dependence on the anti-phase boundary energy as the parts of the dislocation line that create an anti-phase boundary are pinned at these locations. Finally, the strength increases as the number of precipitates intercepted by the dislocation increases, hence the dependence on volume fraction.

Strong Pair-coupling

As the γ' precipitate size increases, the point approximation is no longer valid. The precipitate size eventually becomes similar to the spacing of the dislocation pairs. This condition is defined as strong pair-coupling. As shown in Figure 2.14(b), any given precipitate may have two dislocations interacting with it. The forces acting on the two dislocations are the same as in the weak coupling condition, and therefore equation 2.11 holds true. However, under this condition, while the amount of dislocation line in the precipitate varies, the Friedel spacing, l_i, is the same for both dislocations, i.e. l_1=l_2.

Starting from equation 2.11, equating the Friedel spacing for the leading and trailing dislocations reduces the equation down to:

$$\tau = \frac{\gamma_{APB}}{2bl_f} [d_1 - d_2] \tag{2.16}$$

To further understand the source of strength in strong pair-coupling, we need to consider the forces on the leading and trailing dislocations. Figure 2.15 is a schematic diagram of a pair of dislocations interacting with a spherical γ' precipitate. When the leading dislocation enters the precipitate, an anti-phase boundary forms. The area of this anti-phase boundary depends the progress the dislocation makes into the precipitate. The force on the leading dislocation, given by F_1=$d_1\gamma_{APB}$, reaches a maximum when the leading dislocation is halfway through the precipitate, d_1 is equal to the diameter of the spherical precipitate.

The trailing dislocation experiences a force in the opposite direction, F_2=$d_2\gamma_{APB}$. The maximum net force therefore occurs when the trailing dislocation has just touched but not yet entered the precipitate (d_2=0 and therefore F_2=0). The critical shear stress is therefore defined as:

$$\tau_c = \frac{\gamma_{APB}}{2bl_f}d_1 \tag{2.17}$$

The maximum pinning force occurs when the trailing dislocation is just touching the precipitate, d_2=0, and the separation is x_1. Under this condition, the precipitate spacing for the leading and trailing dislocations is the same and equal to the Friedel spacing, i.e. l_1=l_2=l_f and $l_f \neq 0$. A relationship between the precipitate radius, r, the length of the leading dislocation, d_1, and the distance between the leading and trailing dislocations, x_1, can be derived through simple geometry:

$$\frac{d_1}{2} = \left(2rx_1 - x_1^2\right)^{\frac{1}{2}} \tag{2.18}$$

assuming x≫r. The spacing between the two dislocations is also controlled by the anti-phase boundary energy, γ_{APB}:

$$x_1 = \frac{Gb}{\pi\gamma_{APB}} \tag{2.19}$$

where G is the shear modulus, b is the Burgers vector of the dislocations. To understand how the critical shear stress is dependent on the volume fraction and particle size, the expression for the Friedel spacing (equation 2.13), as well as equations 2.18 and 2.19 are substituted into the expression for the critical shear stress for strong pair coupling (equation 2.17):

$$\tau_c = \left(\frac{3}{2}\right)^{\frac{1}{2}} \frac{\gamma_{APB}v^{\frac{1}{2}}}{\pi^{\frac{3}{2}}} \frac{Gb}{r} \left[\frac{2r\pi\gamma_{APB}}{Gb^2} - 1\right]^{\frac{1}{2}} \tag{2.20}$$

This shows τ_c has a $1/r^{\frac{1}{2}}$ dependence as well as a linear dependence on γ_{APB} and a $v^{\frac{1}{2}}$ dependence for the volume fraction.

The $r^{-\frac{1}{2}}$ dependence for strong pair-coupling is in contrast to the $r^{\frac{1}{2}}$ dependence for weak pair-coupling. Plotting the strengthening as a factor of r for the two pair-coupling conditions is shown in Figure 2.16. A transition point occurs between weak and strong pair coupling when the precipitate radius is approximately equal to $2T\gamma_{APB}$ (c. 10-20 nm). At this point, the respective models show the CRSS peaks at a value equal to $\frac{\gamma_{APB}}{2b}$ (c. 300 MPa). When the precipitates increase further in size, deformation occurs by looping around the precipitates instead of cutting through, this is known as Orowan bowing or Orowan looping. The relationship between CRSS to precipitate size associated with Orowan bowing also features in Figure 2.16.

In this state, the equations do not address the transition in the driving force between weak and strong pair coupling. Galindo-Nava *et al.* refined these two models to address the transition between the weak and strong pair-coupling. By deriving a relationship between the length of the leading dislocation as a function of the distance the dislocation has entered into a precipitate, a smooth transition between the two conditions was modelled. This transition resulted in a reduction of around 50 MPa in the CRSS at the transition point.

The model makes further assumptions including a low volume fraction and uniformly sized, spherical precipitates within the microstructure. The model is therefore not necessarily applicable to single crystal Ni-based superalloys, where the precipitate size may be tri-modal, the volume fraction is as high as 75% and the precipitates vary depending on the degree of ageing and lattice misfit.[119] The multimodal precipitate size distribution was accounted for by weighting the contribution of individual particles to the overall strength. The updated multimodal model was found to be a good predictor of yield strength in powder metallurgy superalloys for grain sizes up to 50 μm. A unimodal size distribution was found to have a higher yield stress compared to multi-modal size distribution by up to 100 MPa.

Yield Strength Contribution from γ/γ' Lattice Misfit

The difference in lattice spacing between the γ matrix and γ' precipitates also increases yield strength by impeding dislocations. A distinct cube-cube orientation relationship exists between γ and γ', described as: $\{100\}_{\gamma}//\{100\}_{\gamma'}$ $\langle 010\rangle_{\gamma}//\langle 010\rangle_{\gamma'}$ The small difference in their respective lattice parameters results in a lattice misfit, denoted δ, and defined as:

$$\delta = \frac{2(a_{\gamma'} - a_{\gamma})}{a_{\gamma'} + a_{\gamma}} \tag{2.21}$$

where a_{γ} and $a_{\gamma'}$ are the lattice parameters of the γ and γ' phases respectively. For most commercial single crystal Ni-based superalloys, the misfit value is negative at engine-operating temperature.[97, 113] If the lattice misfit between the γ and γ' phases is not too large, the γ/γ' interface remains coherent, minimising the interfacial energy. The γ' phase will want to deform while remaining geometrically compatible with the γ-phase.

The lattice misfit between matrix and precipitate creates significant internal stresses, which is thought to contribute towards the yield strength of a material through coherency strengthening.

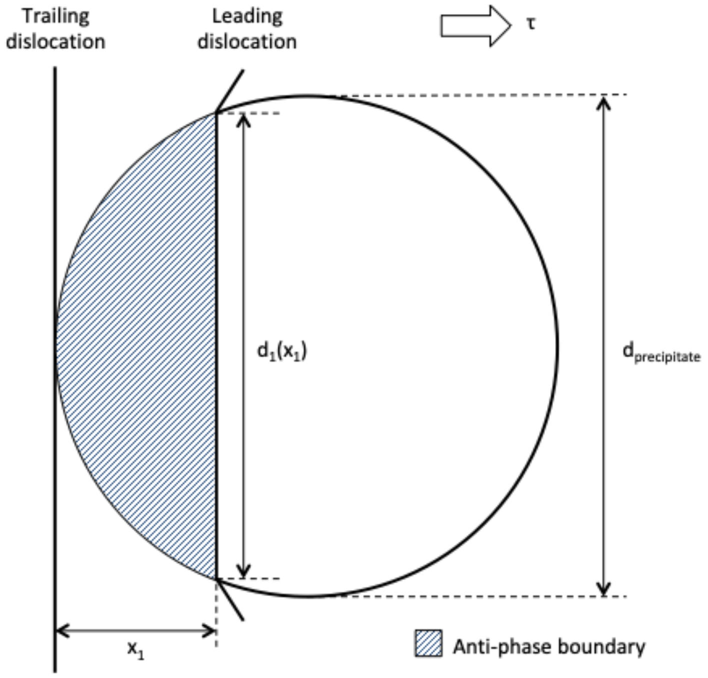

Figure 2.15 A schematic illustration of the strong pair-coupling condition for a pair of dislocations within a spherical γ' precipitate. Adapted from [119].

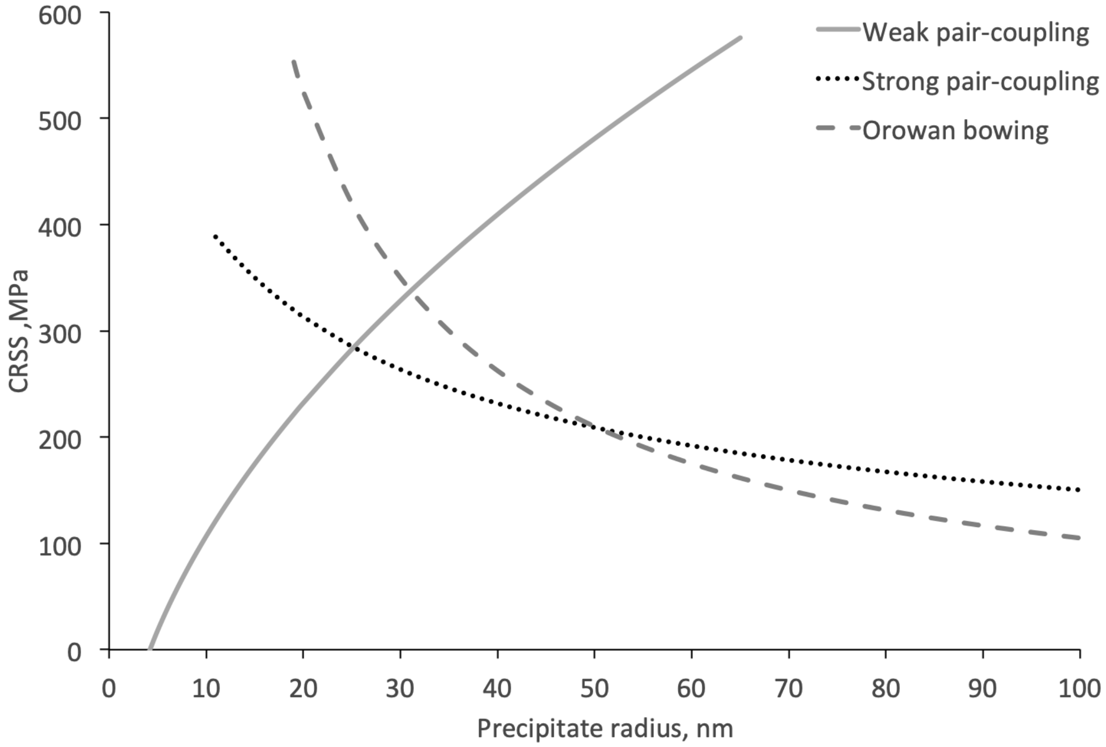

Figure 2.16 Plot of critical shear stress against precipitate size, showing a peak in the CRSS at the transition between weak and strong pair-coupling at a precipitate radius of 10-30 nm.

The incremental effect of increasing lattice misfit to coherency strengthening is reported to be an exponent factor of 1-1.5.[105, 61] In Ni-Cr-Al-Ti-Mo quinary, polycrystalline Ni-based superalloys, the coherency strengthening contribution was predicted to be highest ($\sim 40\,\text{MPa}$) for relatively large magnitudes of lattice misfit.[46] However, how the lattice misfit affects the dislocation behaviour to drive the observed coherency strengthening contribution is debated. There are two main schools of thought: the first suggests keeping lattice misfit as small as possible to minimise the coherency stresses, producing a more stable microstructure.[178] The second suggests a larger lattice misfit favours the formation of denser dislocation networks at the γ/γ' interfaces, inhibiting the shearing of γ' precipitates, in turn stabilising the microstructure.[177]

Experiments attempting to elucidate the effect lattice misfit has on creep strength have shown that a combination of the sign of the lattice misfit and the direction of applied stress are both factors in high temperature creep. For alloys with a negative lattice misfit, the precipitates inhibit deformation in adjacent vertical γ channels, while horizontal γ channels are deformed quite easily. Zhang *et al.*[178] attempted to clarify the effect of lattice misfit on dislocation motion during creep in TMS-75 and TMS-138A. The misfit values were determined by x-ray analysis with TMS-75 found to have a smaller misfit than TMS-138: -0.16 % to -0.33 % respectively. TEM observations during primary creep showed dislocation loops gliding between narrow matrix channels during primary creep.

The preference of elements to segregate to the two phases has an effect of lattice misfit. For example, addition of Mo, which preferentially segregates to the γ phase, displaces atoms of Ni which are smaller, so the γ lattice parameter will increase in size, making the lattice misfit more negative. The opposite also applies, substitution of larger elements for smaller ones makes the misfit more positive. Additions of Re have been shown to make the lattice misfit more negative,[99] while additions of Ru were found to make the lattice misfit more negative by the changes of partitioning ratios of alloying elements via Ru additions.[147]

Effect of Alloying Additions on Yield Strengthening

Superalloys evolved from austenitic stainless steel, where nickel gradually replaced iron as the base element.[130] Chromium was added to provide oxidation and corrosion resistance. Eventually, through empirical trial and error, elements such as aluminium, titanium and niobium were added to give an increased creep life. Only later was the presence of minute, tertiary γ'-phase precipitates identified.[119, 59, 9] Carbon was retained in the earlier alloys, since its addition led to the precipitation of grain boundary strengthening carbides. Molybdenum, tungsten and tantalum were later identified as beneficial for strength, due to solid solution strengthening and carbide formation. Thus, the initial development of a superalloy involved the addition of numerous elements, with the aim of optimising the overall combination of properties. Alloys developed in these early days were either wrought or conventionally cast and all polycrystalline. The focus on creep performance led some of these alloys to be directionally solidified and eventually cast as single crystals. These became known as the first generation of single crystal blade alloys.

Further advancements in metallurgical processing and understanding have allowed for the removal of a number of alloying elements.[130] Removal of grain boundaries has eliminated the requirement for carbon. Similarly, the development of coating technologies has reduced the amount of chromium required because some of the oxidation and corrosion protection functions can be transferred to the coating material.

In the γ-phase, strengthening is achieved through solute pinning of the dislocations.[119] The effectiveness of an element for pinning is found empirically to be roughly proportional to the atomic diameter and also a weaker function of the electron vacancy number, N_V. The electron vacancy number is related to the probability density of electrons per atom. The two are related, increasing from left to right in the d-block of the periodic table. The yield strength was also found to increase per unit change in lattice parameter.

It has recently been shown that the solid solution strengthening effect of the ordered γ' phase is also substantial, and equivalent to that of the matrix phase due to the non-equilibrium phase compositions.[45] The focus on strengthening the γ phase therefore may come at the expense of the contribution from the γ' phase. It has been shown that aluminium is the stronger solid solution hardener, even though its principal is as a precipitation hardener (γ' former). Chromium, tungsten and molybdenum were also found to contribute strongly, while iron, cobalt, titanium and vanadium were identified as weak solute hardeners.[119]

Second and third generation alloys contain up to 3 and 6 wt. % rhenium respectively. Rhenium (Re) addition enhances the high-temperature creep properties and therefore almost all single-crystal superalloys contain a certain amount of Re from the second generation onward. The underlying mechanism for the strengthening phenomenon, termed “the rhenium effect”, is still unclear. It is known that Re is the slowest diffusing element in the single-crystal superalloy.[60, 34, 67] The Re segregates at dislocation core regions and could help to retard the motion of interfacial dislocations.[94] Further quantitative work is required to estimate the strengthening effect of Re. It was previously postulated that the slow diffusion causes Re clusters to form, which act as obstacles for dislocation motion. However, it has been shown that there is repulsion energy between Re-Re nearest neighbours, suggesting Re clusters are unlikely to form in the superalloys and is not the origin of the rhenium effect.[95, 96, 94] With the development of the single crystal Ni-based superalloys, more Re has been added to single-crystal superalloys. A high Re content also leads to a decrease in long-term phase stability of the alloys by promoting the formation of brittle and deleterious topologically closed-packed (TCP) phases.[12, 166, 11] To negate this, ruthenium was later added to the single-crystal superalloys to address the microstructural stability, present in fourth- and fifth-generation single-crystal superalloys.[49, 56, 55] The fourth-generation superalloys are adaptations from the third generation by the addition of 6 wt. % ruthenium. It was found that the addition of ruthenium increased the phase stability of the alloy at high temperatures and improved creep resistance. It has been reported that Ru addition homogenises the distribution of Re between the γ and γ', known as reverse partitioning, in turn slightly reducing the strength of the γ-phase.[107] However, there has been significant disagreement on this effect.[10, 57] The γ/γ' lattice misfit also becomes more negative, increasing the amount of coherency strain. The consequence is poorer performance during primary creep under low temperature high stress conditions. This effect of lattice misfit on yield strengthening in superalloys is elaborated further in the next section.

2.5 Anomalous Yield in Monolithic $L1_2$ Compounds

The Yield Stress Anomaly

The Ni superalloys, and a select group of $L1_2$-based compounds, exhibit an unusual characteristic. Their yield stress, defined here as the stress required to initiate plastic deformation by dislocation glide, increases or shows minimal variation with increasing temperature, from room temperature up to normally around 800 °C, before dropping off rapidly. Nickel, like most materials, exhibits a decrease in yield strength with increasing temperature, suggesting the remarkable mechanical properties stem from the $L1_2$ ordered precipitate phase. However, a comparison between alloyed-γ' and a two-phase Ni superalloy, Mar-M200, shows the increase in strength with temperature is more substantial in alloyed γ' (Figure 2.17).[16] This property is also observed in a variety of single crystal superalloys (Figure 2.18).

From Figure 2.17, it is clear the γ' phase (Ni_3Al) seems to be important for the yield stress anomaly. It was initially hypothesised that the ordered structure and fault structures created through the passage of dislocations causes the yield stress anomaly. As a result, substantial empirical work has been done on monolithic $L1_2$ compounds.[146, 103, 1, 32, 104, 153, 72]

Stoichiometric, single crystals of Ni_3Al are difficult to synthesise due to the peritectic reaction during solidification: liquid + NiAl $\rightarrow$ Ni_3Al, which causes grains to nucleate. In turn it is difficult to suppress these grains sufficiently to produce a single crystal.[86] Only upon the inception and application of float-zone casting was stoichiometric single crystal Ni_3Al producible.[43, 44] Prior to this, elemental additions were added to Ni_3Al or deviations from stoichiometry adopted to avoid the peritectic reaction.[145] As a result, the flow stress behaviour of many $Ni_3(Al, X)$ alloys have been analysed.[145, 123, 32, 76, 118] A summary of the findings of these experiments on $Ni_3(Al, X)$ alloys in relation to the yield stress anomaly are summarised in Table 2.1. It should be noted here that for alloys where the yield stress increase is accompanied by a change on long range order parameter, such as Cu_3Au[115], the following mechanisms and discussion do not apply and have been omitted.

Through experimentation on the various $L1_2$-based alloys, the yield stress anomaly for monolithic $L1_2$ compounds is now principally characterised by the following features:

i. Below the peak temperature, where the yield stress is increasing with increasing temperature, the active slip system is predominantly $\langle 110\rangle\{1\bar{1}1\}$. Beyond the peak temperature, the active slip system becomes $\langle 110\rangle\{0\bar{1}0\}$.[135]

ii. The yield stress usually begins to increase beyond room temperature, though exceptions do exist; the yield stresses of Ni_3Ge[141] and $Ni_3(Si, Ti)$[143, 142] are known to increase from liquid helium temperatures (-269 °C).

iii. The peak position is dependent on load orientation.[138, 123]

iv. The yield stress is strain rate sensitive, though the degree of sensitivity is unclear. Flow stress is almost independent of strain rate.[146, 150] A small but finite strain-rate dependence of flow stress has recently been reported.[134, 31] The sensitivity shows a minimum within the temperature domain of the flow stress anomaly.[148]

v. The work hardening rate is abnormally high, peaking within the temperature range where anomalous yield is observed, and is orientation dependent.[154]

vi. The yield stress anomaly is not a feature of all $L1_2$ alloys.[102, 141]

It makes sense that any mechanism describing the stress anomaly feature for $L1_2$ alloys should include all of the above characteristics. However, to date, only a few characteristics have been attributed to a holistic mechanism. The current commonly agreed theory is the cause of the positive temperature dependence is due to the cross-slip of dislocations from octahedral $\{111\}$ planes onto cubic $\{100\}$ planes, leading to the formation of Kear-Wilsdorf locks.[70] Dislocations cross-slip onto {100} planes because the APB energy is lower on these planes compared to the primary {111} slip plane. Upon increasing the temperature, a greater proportion of dislocations is thought to become immobile by cross-slip, resulting in an increase in strength. Slip activation on the cube planes is thought to lead to the decline in stress past the temperature corresponding to peak stress in $L1_2$ alloys. However, this mechanism does not explain other characteristics thought to be key to the yield stress anomaly listed above. For example, the anomalous increase in stress for some alloys begins as low as -196 °C, far too low for a thermally activated mechanism.[144, 141, 137] In addition, recent experiments have shown that for single crystal Ni_3Al, the yield stress is independent of alloy stoichiometry and orientation-independent.[44, 43, 53, 52, 24]

The hypothesis that the yield stress anomaly is caused by the difference in APB energy has led to a lot of the subsequent research focuses on the anti-phase boundary and the anti-phase boundary energy on the {111} and {100} planes. However, this is further complicated by how difficult it is to calculate APB energies, both theoretically and experimentally. The most common method experimentally is to measure the dissociation widths between partial dislocations by TEM under weak-beam condition; this technique is thought to give the best compromise between adequate resolution and comfortable working conditions. However, sources of error make it difficult to ascertain exact values for APB energies. One problem arises from the fact that any observed dislocation configurations may not be under complete equilibrium. Furthermore, since images are taken under diffracting conditions, a dislocation is shifted with respect to its line and the shift is unique to each partial, the resultant separation does not correlate directly with the actual separation in the crystal.[152] Baluc *et al.*[3] have shown the APB energy ratio is often overestimated prior to considering contributions from elastic anisotropy.

Dislocation Cores

Another potential approach to clarify the yield stress anomaly has been the analysis of dislocation core structures. It is now commonly accepted that low temperature plastic deformation of BCC metals is controlled by screw dislocations which can cross-slip easily but are simultaneously sessile due to the non-planar structure of the dislocation cores.[156, 127] However, prior to this, it was thought that the immobilisation of screw dislocations occurs via a similar mechanism in the $L1_2$ alloys to that in body-centred cubic (BCC) metals.[111, 173] This led to work analysing the nature of dislocation cores in model $L1_2$ ordered alloys by

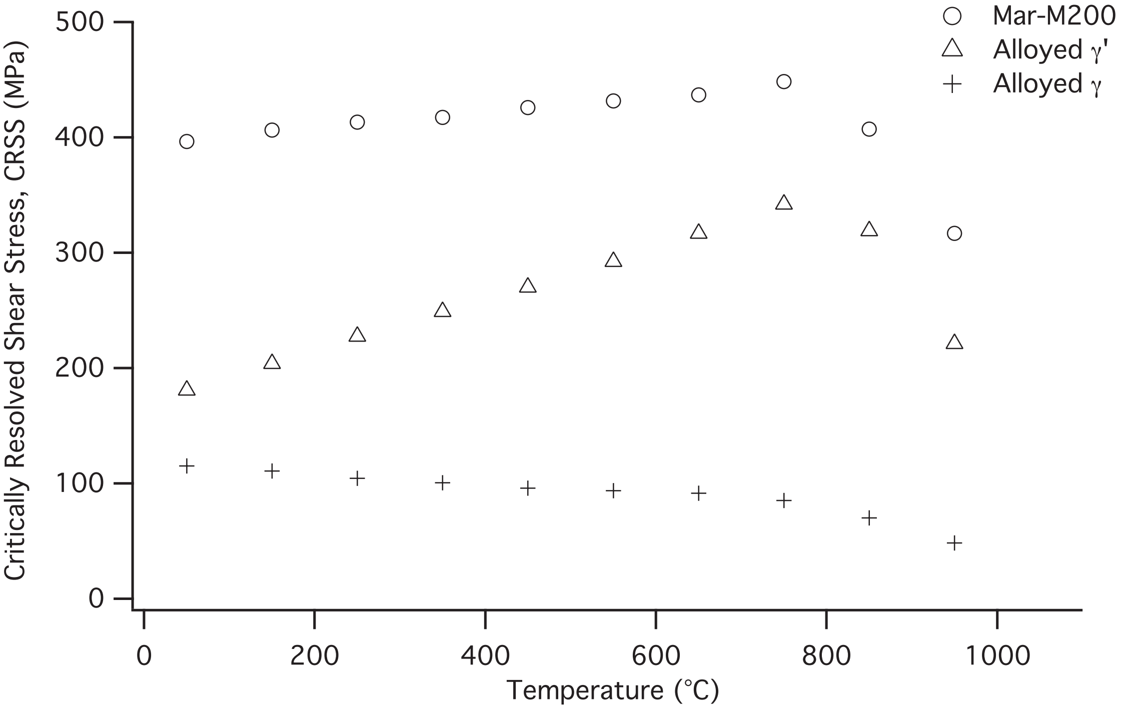

Figure 2.17 A comparison of the critically resolved shear stress of the Ni-based superalloy Mar-M200 and the individual constituent phases of a superalloy.[16]

computer simulation techniques, which is described below.

In the L1$_2$ structure, two $\{111\}$ planes and one $\{010\}$ plane share a common line along any $\langle 110\rangle$ direction, providing an opportunity for screw dislocations to spreads into several non-parallel crystallographic planes. Two dissociation configurations are possible: a glissile one on $\{111\}$ planes and a sessile one on $\{010\}$ planes. When the dislocation core is planar and spread in the plane of the APB, as shown in Figure 2.19, the dislocation is glissile. The core can also be non-planar, extending in both the (111) and $(1\bar{1}1)$ planes; the dislocation possessing this core configuration is sessile. Two further symmetry-related configurations are also possible, where the APB is on the (010) plane with the core spread onto (111) and $(1\bar{1}1)$ planes respectively. Both of these configurations are sessile.

Phase Stability

The phase stability of the L1$_2$ crystal structure with respect to isomorphous crystal structures is also thought to be a factor in the yield stress anomaly. The phase stability theory was first proposed to account for why the yield stress anomaly was not a feature of all L1$_2$-

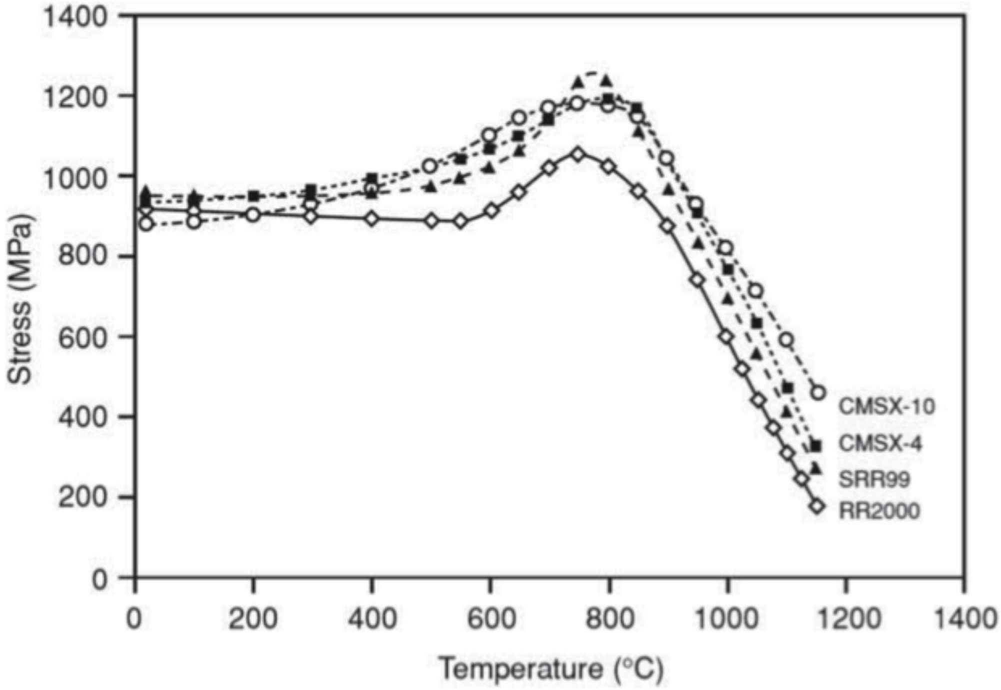

Figure 2.18 Experimental results showing the variation of yield stress with temperature for a variety of single crystal superalloys.[119]

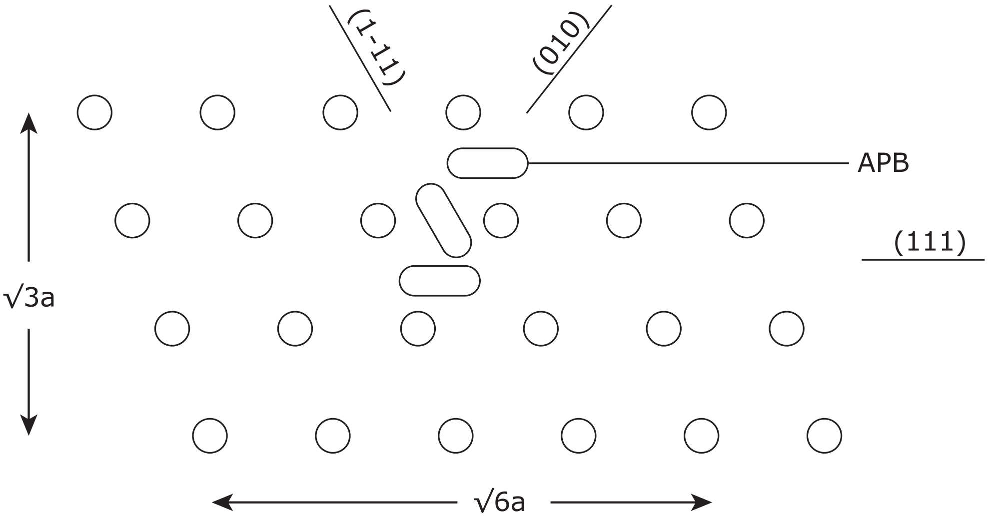

Figure 2.19 A schematic illustration of the possible core configurations viewed down the $[\bar{1}01]$ direction. The oval shape represents the core of the $\frac{a}{2}[\bar{1}01]$ superpartial. When the APB lies on the (111) plane, the core also lies on that plane (top position); here the superpartial is glissile. When the APB lies on the (010) plane, the core spreads onto the $(1\bar{1}1)$ or (111) plane (middle and bottom ovals respectively), depending on the position of the core. In both of these configurations, the superpartial is sessile. Adapted from [110].

Table 2.1 Table detailing the research findings related to the yield stress anomaly for various $L1_2$-based alloys

Alloy	Description of research findings related to the yield stress anomaly	Reference
Ni_3Ga	• The yield stress peaks around 700 K (427 °C) • The ratio between the minimum and peak yield stresses is higher than Ni_3Al	[146, 103]
$Ni_3(Al,W)$	• Yield stress shows a positive temperature dependence; peaking around 800 °C • Peak yield stress is dependent on orientation; orientations close to [111] show a peak at a lower temperature (c. 200 °C)	[123]
$Ni_3(Al,V)$	• Yield stress shows a positive temperature dependence; peaking around 500-600 °C	[118]
$Ni_3(Al,Nb)$	• Yield stress shows a positive temperature dependence, peaking around 800 K (527 °C) for orientations near [001] • The addition of niobium leads to a larger initial yield stress and larger orientation dependence compared to the addition of titanium and tungsten	[76]
Ni_3Ge	• The CRSS shows positive temperature dependence for temperatures below room temperature • The CRSS begins to increase between 200-300 K (-73 - 27 °C) • The steepest increase in CRSS was observed for the $[\bar{1}11]$ orientation	[1, 32]
$Ni_3(Si,Ti)$	• CRSS increased from 77 K (-196 °C), reaching a maximum around 800 K • The peak temperature was orientation dependent, with the orientation closest to [011] exhibiting the highest peak CRSS • The CRSS was almost independent of strain-rate below the peak temperature and strongly positive strain-rate dependent above the peak temperature	[143, 142, 144]
Ni_3Mn	• The CRSS only exhibits a slight positive temperature	[104]
Ni_3Fe	• The yield stress shows a positive temperature dependence with a peak around 200 °C • The magnitude of this anomaly is small compared to Ni_3Al and Cu_3Au	[153, 72]

ordered alloys.[168, 170] It was shown that a lower $L1_2$ phase stability with respect to the isomorphous ordered $D0_{22}$ phase (Figure 2.20) reduced the APB energy on cube planes to almost zero, facilitating cross-slip from $\{111\}$. In general, substitution of ternary elements away from the stoichiometric composition reduced the composition region in which the $L1_2$ structure is stable by reducing the average electron per atom ratio or increasing the atomic radius ratio.[114, 168, 170, 139, 37] The effect of compositional deviations from stoichiometry[103, 140] and ternary additions[75, 92, 106] also fit the predicted behaviour of this concept.

Pt_3Al and Pt_3Ga have the $L1_2$ crystal structure, yet both possess drastically differing flow behaviour.[169, 108, 47] These alloys exhibit an increase in flow stress with decreasing temperature (see Figure 2.21); a phenomenon termed the low temperature anomaly (LTA). In the $L1_2$ structure, Pt atoms form an octahedron within the unit cell, the $D0_c$ structure, as shown in Figure 2.22. The $D0_c$ and $D0_{c'}$ structures are obtained by distorting or rotating this Pt octahedron respectively.[47] Both transformations are accompanied by a tetragonal distortion of the lattice. The $D0_{c'}$ structure was found to be more energetically favourable than the $L1_2$ structure in the temperature region where the LTA is observed, while the $D0_c$ structure was unstable across the whole temperature range.

The instability has electronic origins.[47] A transition from $L1_2$ to $D0_{c'}$ alters the charge distribution in the $D0_{c'}$ phase to become more covalent. Additional electron density bridges form between Pt and Al atoms, enhancing chemical bonding, stabilising the $D0_{c'}$ structure. The stability ratio between the $D0_{c'}$ and $L1_2$ structures is also sensitive to stoichiometry. Iterative additions of Al atoms to $Pt_{3-x}Al_{1+x}$ cause the Pt octahedron to rotate back to the origin position of the $L1_2$ structure. The $L1_2$ structure was found to become stable at compositions in excess of 6 at.% Al.[108] Despite the consistency of argument to justify anomalous yield through phase stability, further calculations based on phase stability for $Ni_3(Al, X)$ single crystals and other $L1_2$-based alloys are yet to be carried out.

2.6 Two-phase Alloys

Though the anomalous flow stress phenomenon of Ni_3Al is an extremely desirable property, this phase alone is known to be brittle and exhibits low ductility at ambient temperatures.[23] However, when embedded within a matrix of Ni solid solution as part of a two-phase structure, the resultant mechanical properties are enhanced, lending themselves to be ideal strengthening components in high temperature applications, especially for the application of

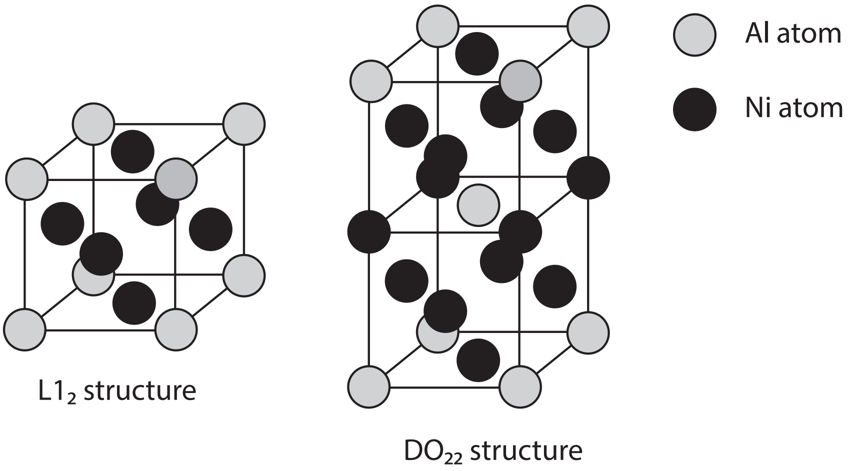

Figure 2.20 The crystal structures of $L1_2$ and $D0_{22}$, showing the relative ordering of Al atoms (grey) and Ni atoms (black).

jet-engine turbine blades.

Two phase Ni-based superalloys only share some of the properties of Ni_3Al. The anomalous flow stress increase is not as steep, and occurs over a much narrower temperature range in a two-phase superalloy. This was shown earlier in a comparison between the constituent phases of a superalloy, γ and γ', and a commercial superalloy Mar-M200 (Figure 2.17). The two-phase superalloys have also been reported to violate Schmid's law and display tension/compression asymmetry.[16, 114] However, the anomalous yield behaviour is not as pronounced, and the tension/compression asymmetry is also dependent on orientation, disappearing for orientations close to $[\bar{1}11]$ where the CRSS for $[\bar{1}01](111)$ slip is lowest in both tension and compression.[128, 51]

Such discrepancies are highlighted from the microstructural differences with $L1_2$-ordered structures. The high γ' volume fraction, which for some alloys exceeds 70 %, confines dislocations at early stages of deformation to the γ channels. Instead of the long lengths of screw dislocations present in monolithic $L1_2$ compounds, in a two-phase superalloy the dislocations grow out from remnant dendritic cores in the γ-phase. Upon application of sufficient stress, the dislocations are able to enter into the γ' precipitates, where they shear as two closely-spaced partial dislocations.

Beyond the peak temperature, the sharp drop-off in yield stress is thought to occur via different mechanisms for two-phase superalloys compared to monolithic $L1_2$ compounds. In Ni_3Al-based alloys, there is a transfer from octahedral slip to cube slip as more cubic slip systems are activated, while in a two-phase superalloy the decrease is attributed to a

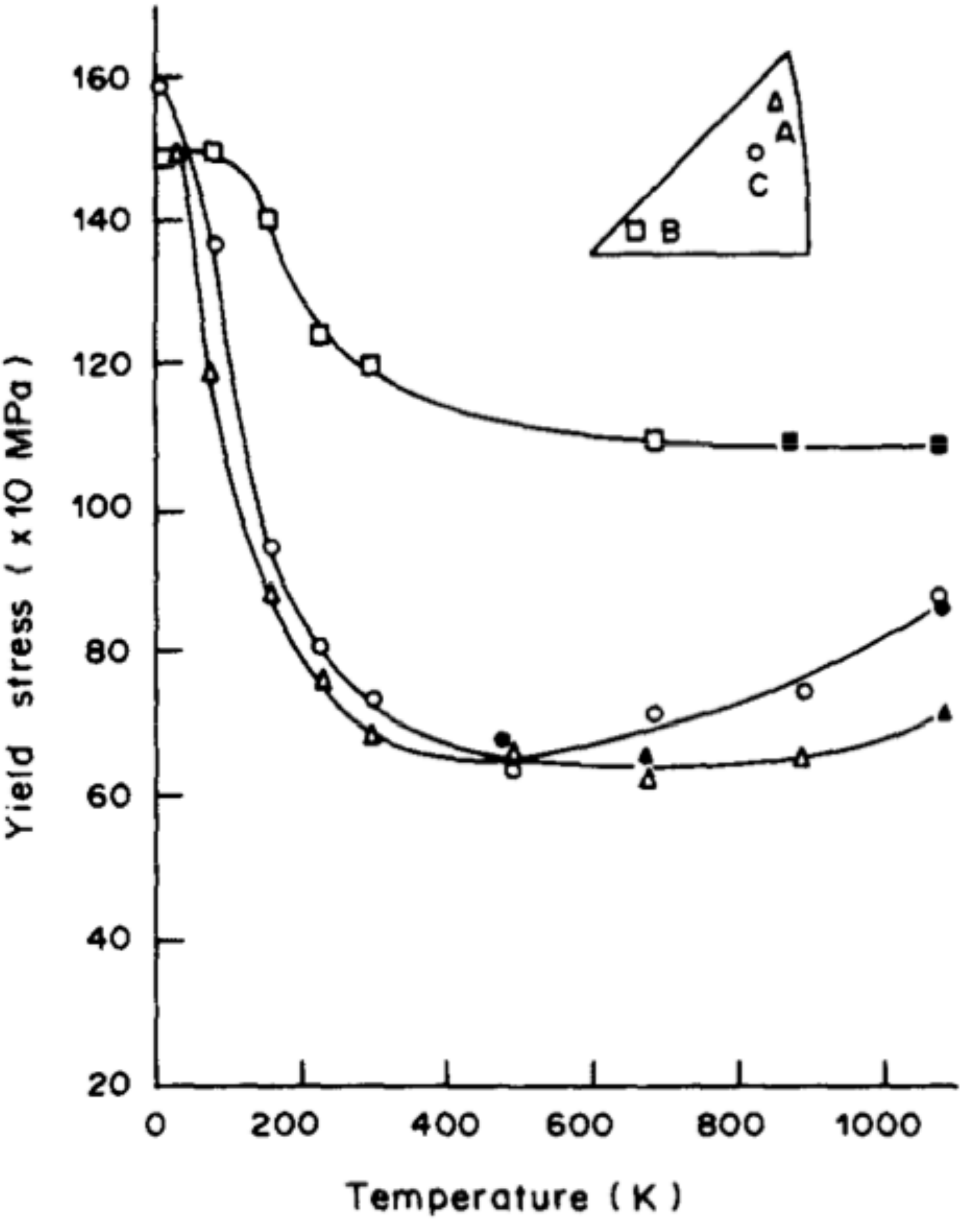

Figure 2.21 The temperature dependence of yield stress for three different orientations under compression for single crystal Pt_3Al. All three orientations show evidence of the low temperature anomaly.[169]

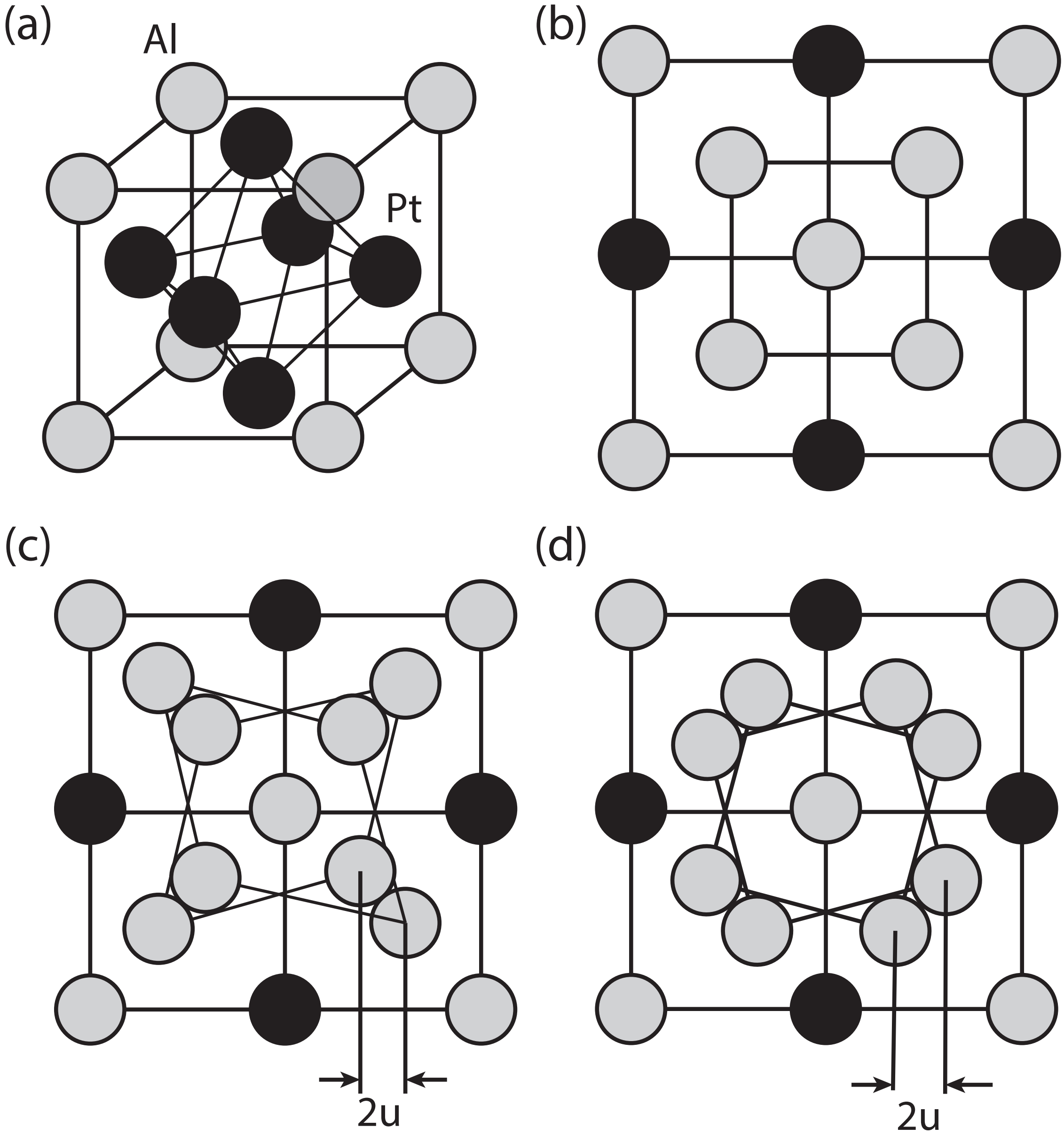

Figure 2.22 The 3-D crystal structure of (a) L1_2 Pt_3Al, and the {001} projection of (b) L1_2, (c) D0_c and (d) D$0'_c$ crystal structures. Key: Al atoms (grey) and Pt atoms (black).Adapted from [47].

decrease in γ' volume fraction though this is yet to be confirmed.[135, 111, 173] Additional factors that result from transitioning to a two-phase alloy also need to be accounted for: misfit between the γ and γ' phases, partitioning preference of elements and the relative fault energies of both the γ' and γ phases.

As a result of these differences, the theories developed through the study of monolithic $L1_2$ compounds are not directly transferable to two-phase single crystal superalloys. Many further questions need to be addressed: what happens to dislocations upon penetration into γ' precipitates? Do dislocation pairs form Kear-Wilsdorf (KW) locks and do they glide on cube planes as they propagate through? An extensive study on the dislocation types and morphologies to answer these questions remains absent.

Sun and Hazzledine investigated the dislocation structure in deformed single crystals of Ni-based superalloy SRR99.[136] The specimens were compression tested and the respective slip planes and geometry of dislocation structures present were deduced. Screw dislocations were observed to dissociate into superpartials on the (010) cross-slip plane, separated by an APB. The superpartials further dissociated into Shockley partials on {111} planes. The screw dislocations glide on the primary (111) slip plane by kink propagation, whose four components all lie on (111).

A study of yielding and deformation behaviour was also conducted on PWA 1480, the first Ni-based single crystal superalloy to enter production.[89, 90] The yield strength was found to be asymmetric in tension and compression following tensile tests interrupted at various temperatures. The resultant microstructures were separated into three temperature regimes: low (<760 °C), intermediate (between 760 and 927 °C) and high (>927 °C). As the temperature increased, the deformation mechanism changed, from γ' shearing to γ' bypass, with the transition occurring within the intermediate temperature range. The yield strength was hypothesised to be controlled by both the distance between cube cross-slip events and γ' precipitate size in PWA 1480 by the relation:

$$\sigma \propto \frac{1}{R} + \frac{1}{\lambda} \tag{2.22}$$

Where σ is the yield strength, R the γ' precipitate size and λ the distance between cube cross-slip events. Between room temperature and peak yield stress temperature, the γ' size was thought to dominate. Around the peak temperature however, the distance between cross-slip events became the dominant factor. It was not clear what controls the specific segment of a shearing dislocation that would cross-slip. Furthermore, the mechanism broke down when stacking faults became the dominant shearing mechanism.

2.7 Modelling Features of Anomalous Yield

Various models have attempted to explain the principal features of anomalous yielding, but to date, none have been able to account for all the principle characteristics and experimental observations. Below details a broad review of the models proposed to date.

Pinning Models

The earliest model hypothesised a mechanism whereby screw dislocations cross-slip from {111} planes, on which they are mobile, to {100} planes, becoming immobile; the driving force being the differential in APB energy between {111} and {100} planes.[148] The positive temperature dependence is attributed to an increased propensity for {010} slip with increasing temperature, causing a transition in the mechanism controlling flow stress: from exhaustion hardening at low temperature, where mobile dislocations are immobilised by interactions with any forest dislocations, debris and solute impurities, to debris hardening at high temperature; dislocations are mobilised by multiplication from old sources and the activation of fresh ones. No transition of mechanisms was found to account for the increase in yield stress and an alternate theory was proposed by Takeuchi and Kuramoto.[146], which is now known as the TK model, and describes segments along the length of a screw dislocation cross-slipping into pinning points (Figure 2.23). The temperature dependence was accounted for by defining the probability of cross-slip as a function of temperature:

$$f = f_0 \exp(\frac{-H_t}{kT}) \tag{2.23}$$

where f is the probability of cross-slip, f_0 is the probability constant, H_t is the activation energy of cross-slip, k is Boltzmann's constant and T is the temperature. This suggests a greater number of pinning points along a dislocation length are generated at decreasing pinning-point spacing as the temperature increases, and a higher level of effective stress is required to keep dislocations in a steady-state motion.

These pinning points are unlocked when forces either side of the kink cause the segments of dislocations adjacent of the pinning point to collapse. At a critical angle, unpinning would occur athermally, with the dislocation free to glide again until further cross-slip occurs.

Paidar *et al.*[110] developed this model further, explaining why the dislocation segments become immobile, proposing that the APB anisotropy originated from the spread of the dislocation core into a non-planar configuration. They were then able to explain the tension/compression asymmetry and orientation dependence, through adapting the unpinning mechanism to a thermally activated process.

The tension-compression asymmetry of the critical resolved shear stress (CRSS) was justified by the Escaig mechanism for cross-slip, shown schematically in Figure 2.24.[29] A pair of partial dislocations is compressed on the primary slip plane. The Escaig mechanism analyses the dislocation core width of this pair before and after cross-slip. If it is energetically favourable for the faulted ribbon between the two partials to expand more widely on the cross-slip plane than the slip plane, the total superpartial pair constricts, before spontaneously cross-slipping and dissociating on the cross-slipped plane. The difference between the normalised stresses on the slip and cross-slip planes gives rise to the tension/compression asymmetry. This asymmetry, a key characteristic of the anomalous yield phenomenon, would had been missed by Takeuchi and Kuramoto since their experiments only involved compression tests.

A further contribution to the energy balance of cross-slip was made by Yoo *et al.*[35] The elastic anisotropy between the dislocation pairs exerts an additional torque. In the case of two parallel screw dislocations, this torque facilitates the cross-slip from the $\{111\}$ onto the $\{001\}$ plane, after which the torque disappears due to symmetry. The tangential force F_t, rotating the pair off a plane at an angle θ from the $\{001\}$ plane was estimated by:

$$F_t = F_r \left(\frac{(A-1)\sin 2\theta}{2(A\sin^2\theta + \cos^2\theta)} \right) \tag{2.24}$$

where F_r is the repulsive force between the two dislocations and A is the anisotropy factor given by $A = 2C_{44}/(C_{11} - C_{12})$. This reaches a maximum of 0.62 F_r for a dislocation pair on a $\{111\}$ plane assuming A=3.3 for Ni_3Al. The Yoo torque is a significant factor, tipping the balance in favour of cross-slip for Ni_3Al. This shows the importance of elasticity to the cross-slip process.

Both the TK and PPV models have been adopted to explain anomalous yield because of their strong agreement with the macroscopic mechanical observations associated with anomalous yield behaviour. However, currently no TEM investigations, neither *in situ* nor post mortem, have succeeded in producing further evidence in support of the pinning process. Instead, the microstructures of $L1_2$-based alloys exhibit long, screw dislocations adopting either incomplete or complete Kear-Wilsdorf (KW) locking configurations.[136] Furthermore, though the PPV model does a good job rationalising the sensitivity of flow stress to crystallographic orientation, it struggles to account for the independence of strain rate to the yield stress. A balance in activation energy between the formation and unlocking of dislocation-locks needs to be established because it is the activation energy of the unlocking mechanism that is responsible for the strain rate sensitivity.[110] Microstructural observations

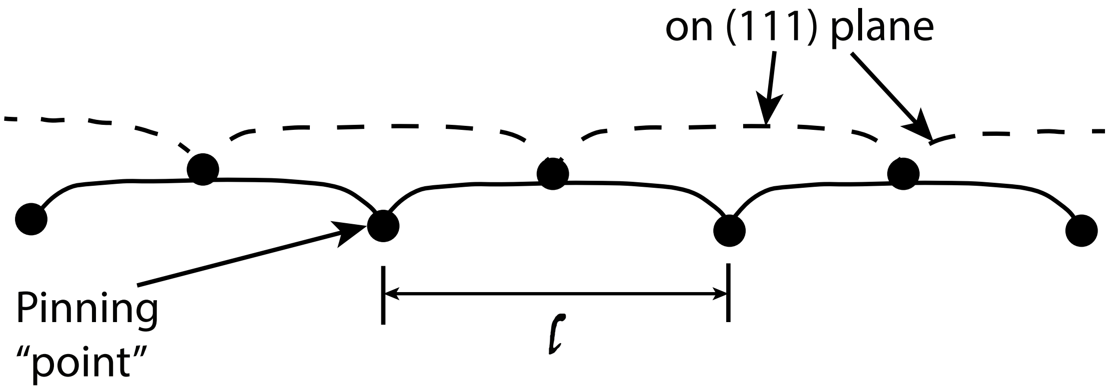

Figure 2.23 A schematic illustration of the successive positions for a dislocation moving on the (111) plane by bowing between pinning points, spaced *l* distance apart.[91]

of dislocation features that are left behind after flow show small elongated dipole loops.[13] It is worth noting that these dipole loops are different from the dipoles described later in two-phase alloys. Explaining their formation led to the development of an alternative unlocking mechanism and a further set of models.

Kink Expansion Models

The presence of long, straight screw superdislocations is one of the most significant microscopic observations in $L1_2$ compounds. Edge dislocations mainly act as links between long screw dislocations and their cross-slipped parts, and are mobile.[54] These step segments are termed 'superkinks'.[136] These superkinks can shuffle along the dislocation, forming long segments of screw orientation cross-slipped on (010) planes, which are locked by KW locks. The steady-state configuration for the unlocking-locking sequence is shown in Figure 2.25. The locks are considered to be stronger and harder to unlock than the pinning points of the PPV model. Unlocking occurs by a process that is thermally activated, but also involves a large athermal component, to account for the small strain rate sensitivity.[91] A sudden increase in strain rate decreases the critical length, producing a large number of mobile superkinks, rapidly increasing the number of mobile superdislocations. These superdislocations would then move rapidly to accommodate the new strain rate level.

Hirsch's model is able to explain the orientation dependence and tension/ compression asymmetry and non-Schmid effects by adopting the activation enthalpy and Escaig mechanisms of the PPV model, despite the differing origins of the locked screws configuration between the two models.[54] Furthermore, the Escaig model fails to quantitatively explain the orientation

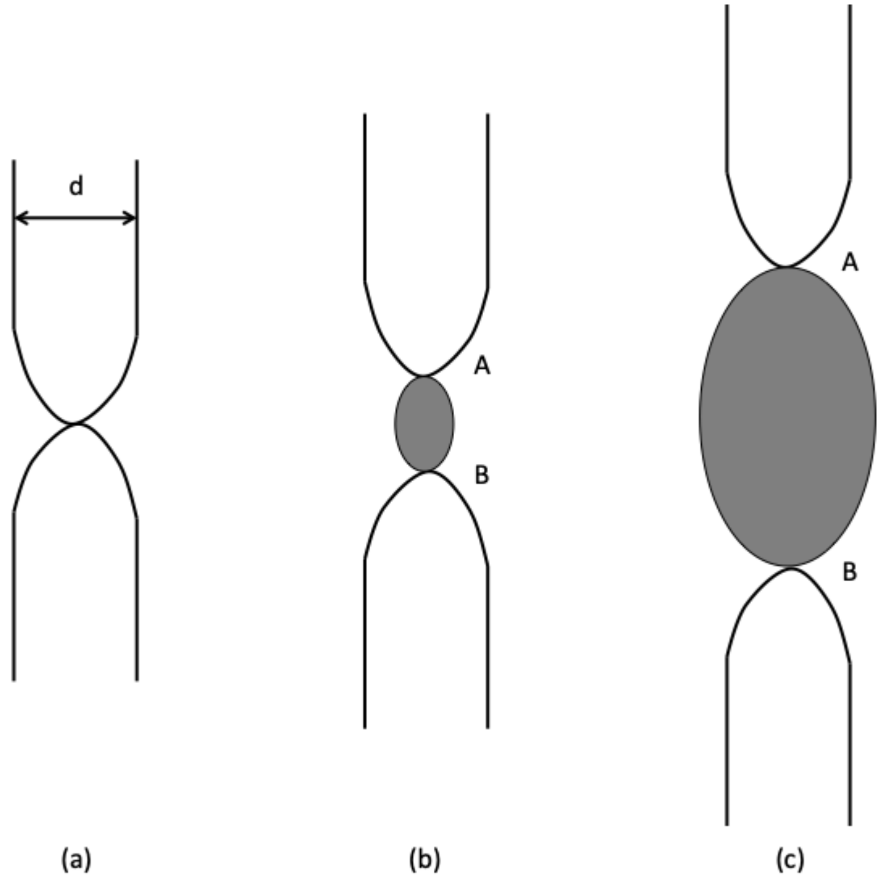

Figure 2.24 A schematic illustration of compact cross-slip mechanism, proposed by Escaig. (a) A pair of partial dislocations on the primary slip plane spaced *d* distance apart have a primary constriction. (b) A length of AB is split and bows out in a cross-slipped plane. (c) A and B are pushed apart due to the stresses on the pair of dislocations.[8]

effects; the author admits the empirical data used to support the model is unreliable.[8] However, this is not the focus of Hirsch's model. Rather, it does a good job of explaining the small strain rate dependence, another key feature of yield behaviour in $L1_2$-based compounds. Hirsch's model is deemed one of the most successful superkink unlocking models, due to the depth of detail describing the locking and unlocking mechanisms. Unlike the PPV model, where unlocking is a purely athermal process, unlocking in the Hirsch model occurs via a hybrid thermal/athermal process. Furthermore, PPV assumed jogs move slowly and screws are pinned only locally; compared to the fast movement of jogs on $\{010\}$ planes, which requires a finite, albeit unknown, amount of activation energy and thus can only occur above a certain temperature.

However, both the PPV pinning model and Hirsch's superkink model possess two underlying assumptions that hinder their ability to account for all empirical features of yield behaviour of $L1_2$-based alloys. First, both models assume a characteristic length for which no basis is explained; for the PPV model, this is the characteristic distance between pinning points, whereas for superkinks, it is the length of the superkinks that is simply assumed to be constant. Secondly, the models are based on a steady state fluctuation. This means the density of obstacles along a superdislocation remains constant, and only upon reaching a critical stress, do these superdislocations become unlocked. Beyond this stress, all obstacles become mobile and are eliminated simultaneously. This would translate to a sharp discontinuity in the flow stress at the yield point. However, yielding in $L1_2$-based compounds occurs gradually. Furthermore, since all the cross-slipped segments dissolve at a critical stress, flow continues indefinitely at a uniform stress. Empirically, single crystals exhibit significant work hardening beyond yield.

As a result, the superkink model was revised.[91][82] The adapted model assumes the superkink height is statistically distributed and must lie between upper and lower bound values to become mobile. Above the upper bound critical height, the superkinks not only become mobile but can also generate new superkinks. Below the lower value, the superdislocation is locked. An increase in temperature shifts these critical values so that a greater portion of dislocations are locked with increasing temperature. The mechanism and causation for the superkink height variation with temperature however is not clear.

The mobility of a screw dislocation is proportional to the average height of the superkinks on it. If the average superkink height falls below a critical value, a mobile dislocation will experience "exhaustion of mobility" and cease. The mobile dislocation density and kink height evolution are dependent on one another as well as temperature and applied stress. Including these revisions, the prediction of $L1_2$ compounds' yield behaviour improves. Some

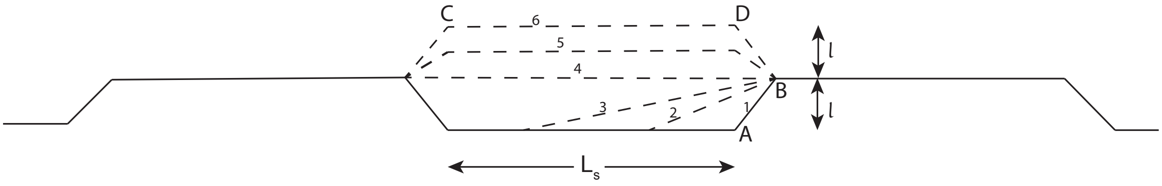

Figure 2.25 The steady-state configuration for the unlocking-locking sequence. Unlocking occurs at A by superkink AB and progresses through the sequence 1 to 6. The screw is eventually locked again along CD. The superkink has progressed a distance of $2l$ and was of width l_s.[54]

discrepancies between experimental and theoretical results still exist. Since the density of mobile superdislocations can change rapidly, the dynamic changes in superdislocation mobility needs to be factored into the model. However, at the time of design, this could not occur due to the limited experimental understanding of the dynamical process of exhaustion in $\mathrm{L1_2}$ compounds.

This section highlights the inconsistencies present within existing models, and the disagreement between models and experimental observations. The origins of the yield stress anomaly remains unclear. In particular, the specific mechanisms and cause of dislocation locking and unlocking. Significant work is required, both experimentally and theoretically before an appropriate model is achieved.

2.8 Empirical Observations of Deformation Mechanisms

Reviewing the microstructures of single crystal Ni-based superalloys that have undergone various deformation help us test the theories and improve our understanding of what controls deformation. This has traditionally been done using Transmission electron microscopy (TEM), to observe the dislocation structures within microstructures. Earlier in this chapter, it was explained how the ordered nature of the γ' crystal structure produces anti-phase boundaries upon shearing of $\frac{a}{2}\langle 110\rangle$ dislocations. APB shearing has been observed in tensile, compression and creep samples of single crystal Ni-based superalloys. A TEM study of single crystal Ni-based superalloy SRR99 deformed under compression at 750 °C showed unit dislocations forming in the γ matrix and cutting γ' cube-shaped precipitates in pairs (see Figure 2.26).[136] Each pair consists of Shockley partial dislocations, separated by an anti-phase boundary on the (001) plane.

In a different piece of research, tensile tests were conducted on the same alloy, single crystals of SRR99 under similar test conditions (750 °C, $\dot{\varepsilon}=10^{-3}\ \mathrm{s}^{-1}$). The deformed microstructure showed shearing of the γ' precipitates by superpartials bound by either APBs or stacking faults (see Figure 2.27).[33] At room temperature and 550 °C, the dual phase microstructure is sheared by slip bands of a/2[$\bar{1}$01] dislocations. In the γ' phase, these dislocations shear as pairs separated by an APB. At higher temperature of 1033 K (760 °C), stacking faults are visible. The dislocation interactions in the γ matrix are reported to lead to build up of dislocation networks at the γ/γ' interface, with the γ' phase sheared by both APB coupled dislocation pairs as well as super stacking faults. However, the resolution was insufficient to resolve the individual dislocations that bind these faulted structures.

A temperature dependence of deformation mechanisms was also observed for single crystal Ni-based superalloy PWA 1480 subjected to tensile deformation ($\dot{\varepsilon}$=10^{-3} s^{-1}).[90] Between 700 and 950 °C, deformation occurred by the shearing of γ' precipitates by single isolated superlattice-intrinsic stacking faults (SISFs). These were produced by the decomposition of $\frac{a}{2}\langle 110\rangle$ matrix dislocations at the γ/γ' interface. At 200 °C and below, deformation occurred by SISF shearing. The temperature dependence was hypothesised to be due to an increase in the SISF energy between 20 and 400 °C.

Similar faulted structures have been observed in creep deformation which can improve our understanding of the faulted structures that form from tensile deformation. Leverant and Kear presented their TEM observations in the single crystal superalloy Mar-M200, that had been subjected to creep at 760 °C and 689.5 MPa.[78] The micrograph showed shearing of the γ/γ' microstructure occurred through glide of $a\langle 112\rangle$ partial dislocations (see Figure 2.28). Similar faulted structures have been observed in single crystal superalloy TMS-82+ deformed under creep conditions at 750 °C and 750 MPa (see Figure 2.29)[117], and single crystal superalloy ME3 subjected to compression creep tests at 750 °C and 552 MPa (see Figure 2.30(a)).[133] For these cases, the faulted structure forms from the dissociation of a pair of $\frac{a}{2}\langle 110\rangle$ dislocation into two $\frac{a}{3}\langle 112\rangle$ and $\frac{a}{6}\langle 112\rangle$ partial pairs. The leading $\frac{a}{3}\langle 112\rangle$ and $\frac{a}{6}\langle 112\rangle$ partial pair is separated by an SISF. The propagation of the $\frac{a}{6}\langle 112\rangle$ leaves an APB. This APB is bound on the other side by the other $\frac{a}{6}\langle 112\rangle$ and $\frac{a}{3}\langle 112\rangle$ partial pair, separated by an SESF. The deformation process outlined is consistent with the viscous slip mechanism.[69, 117]. Due to the high fault energy of the complex faults, the bounding Shockley partial pairs would have such a small separation distance that when observed using conventional TEM, they appear as single $\frac{a}{3}\langle 112\rangle$ dislocations. It was later shown using high resolution scanning electron microscopy (HRSTEM) that these leading and trailing $\frac{a}{3}\langle 112\rangle$ superpartials each dissociate into two $\frac{a}{6}\langle 112\rangle$ Shockley partials, separated by either intrinsic and extrinsic complex stacking faults respectively. Both atomistic simulations and the phase-field model of dislocations (PFMD) have supported these observations.[160, 161]

Other studies have shown a transition between stacking fault shear and APB shear depending on test conditions. In the study of creep deformation in single crystal ME3, the deformation mechanism changed from stacking fault shear to APB shearing, as shown in Figure 2.30. This suggests the creep deformation mechanisms are dependent on temperature. A separate study on single crystal CMSX-4 determined an approximate threshold stress of 500 MPa for stacking fault shear in CMSX-4 during primary creep.[117] In addition, stacking fault shear was prevalent under deformation conditions that favoured multiple slip system activation. This increased the density of dislocations with two different Burgers vectors on two different slip systems interacting to form stacking fault ribbons. This supports the observations made by Feller-Kniepmeier *et al.* that showed prevalence of stacking fault shear in single crystal SRR99 following multiple slip.[33] Microstructures of cast superalloy CM247LC after tensile testing also showed a transition in deformation with increasing temperature.[93] At 650 °C, the predominant deformation mechanism was APB shearing. At higher temperatures, deformation twins and stacking faults were observed.

Two microstructures of two similar superalloys, CMSX-3 and CMSX-4, interrupted under different creep conditions at 850°C are showing in Figure 2.31. Figure 2.31(a) is the dislocation structure of single crystal CMSX-3 interrupted at 0.1% strain. The micrograph shows dislocations within the γ channels.[112] There is limited dislocation interaction with the γ' precipitates. In contrast, single crystal CMSX-4 samples subjected to primary creep at 850 °C and 650 MPa, interrupted at 0.3% strain show stacking faults in the γ' precipitates (Figure 2.31(b)).[124] This further shows activation of stacking fault shear during primary creep may be dependent on the threshold stress and be a time dependent phenomenon.

By amalgamating the deformation mechanisms of polycrystalline ME3, single crystal ME3 and Rene 88DT, a deformation mechanism map was created.[4, 133] This map was adapted to account for the time-dependent nature of deformation modes and shown in Figure 2.32. Creep deformation is observed to be more likely at high temperatures and lower strain rates.[21, 19] The deformation map did not capture effects of grain size, precipitate size/ distribution and alloy chemistry but gives an idea of how the stress and temperature affect the deformation mechanism. Though a similar map is yet to be constructed for tensile deformation mechanisms, it is thought that a similar interplay may exist between strain rate and temperature.

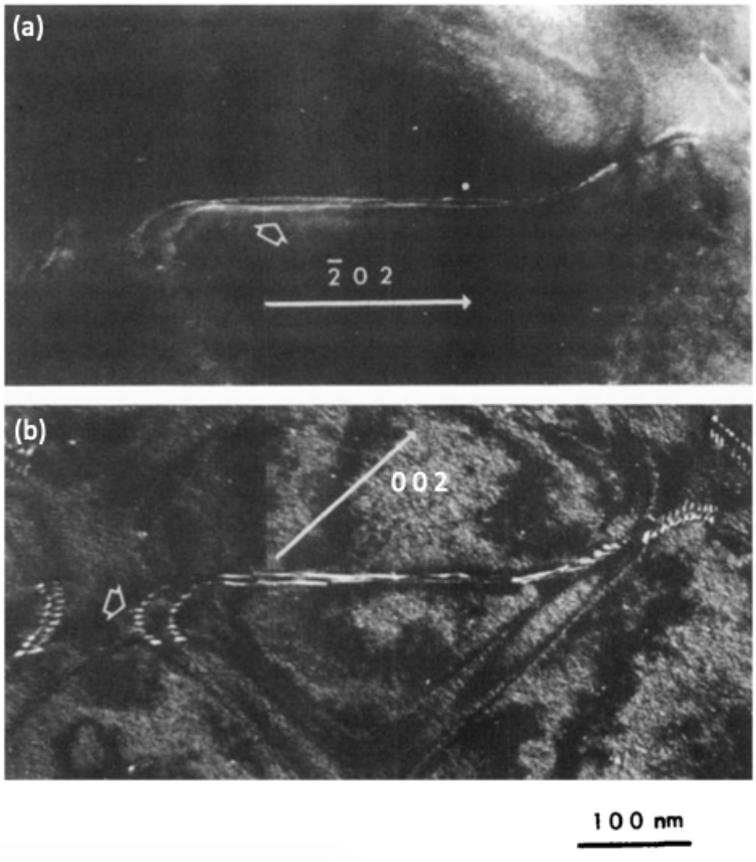

Figure 2.26 Weak beam TEM images, from single crystal Ni-based superalloy SRR99 following compression tests at a strain rate of $\dot{\varepsilon}=10^{-4}$ s^{-1}, showing a pair of unit dislocations, with identical Burgers vector, within the L1$_2$ precipitate under two different beam conditions, (a) **g**=[$\bar{2}$02] and (b) **g**=[022]. The unit dislocations are separated by an anti-phase boundary on the {001} plane. Each unit dislocation visible is a superpartial, dissociating into a pair of Shockley partials, shown by the stacking faults (arrow) in (b).[136]

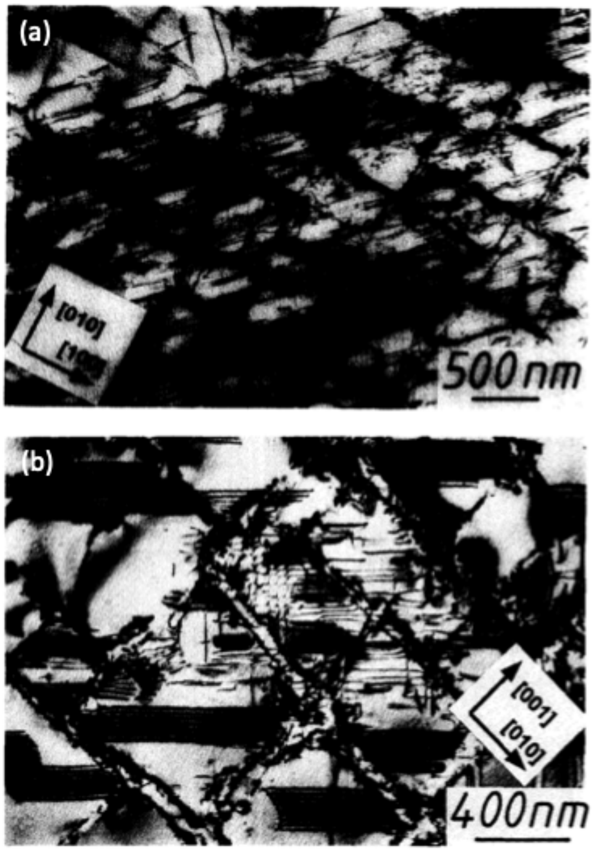

Figure 2.27 Microstructure from bright field TEM of single crystal Ni-based superalloy SRR99 subjected to tensile testing at (a) room temperature, $\dot{\varepsilon}=10^{-3}\,\mathrm{s}^{-1}$, interrupted at $\varepsilon=1.93\%$ and (b) T=1033 K, $\dot{\varepsilon}=10^{-5}\,\mathrm{s}^{-1}$, interrupted at $\varepsilon=1.25\%$. At room temperature, the dual phase microstructure is sheared by slip bands of $\frac{a}{2}[\bar{1}01]$ dislocations. At the higher temperature of 1033 K, stacking faults are also visible.[33]

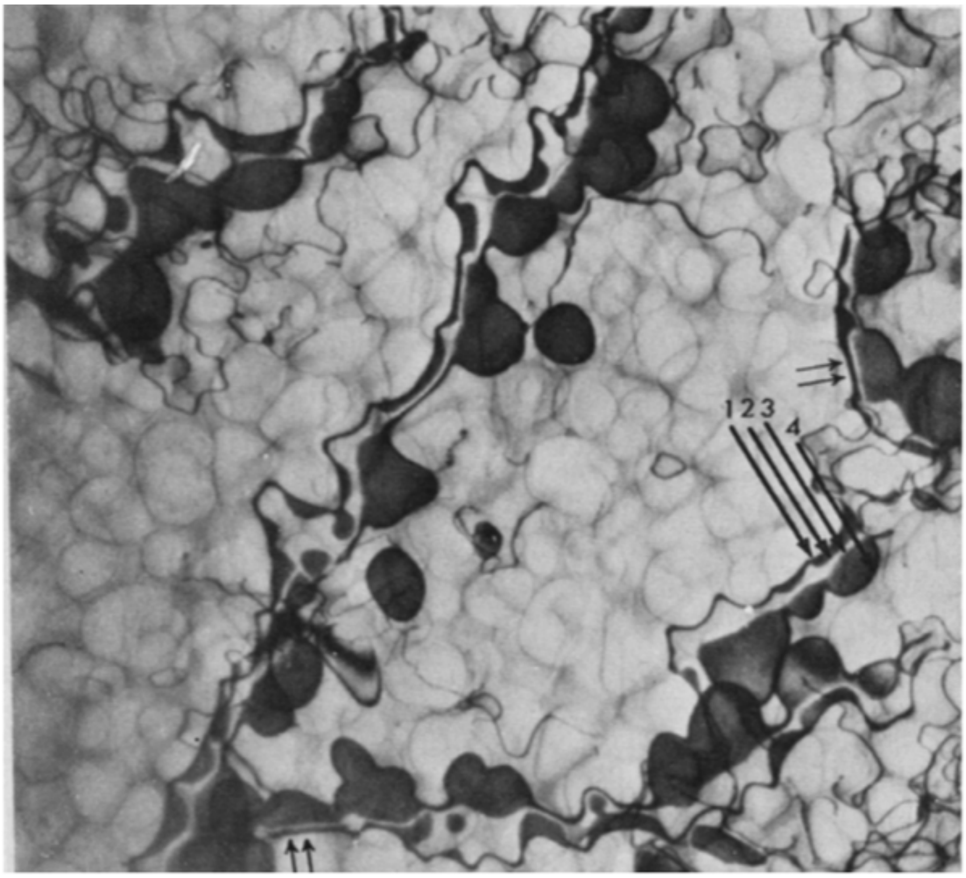

Figure 2.28 TEM micrograph of single crystal Ni-based superalloy Mar-M200 interrupted at 1.4% strain in primary creep on the $(1\bar{1}1)$ plane. The micrograph shows loosely-coupled SISF and SESF fault pairs in the plane of the foil. The dislocations marked 1 and 4 have the Burgers vector $\frac{a}{3}\langle 112\rangle$ and dislocations 2 and 3 have the Burgers vector of $\frac{a}{6}\langle 112\rangle$.[78]

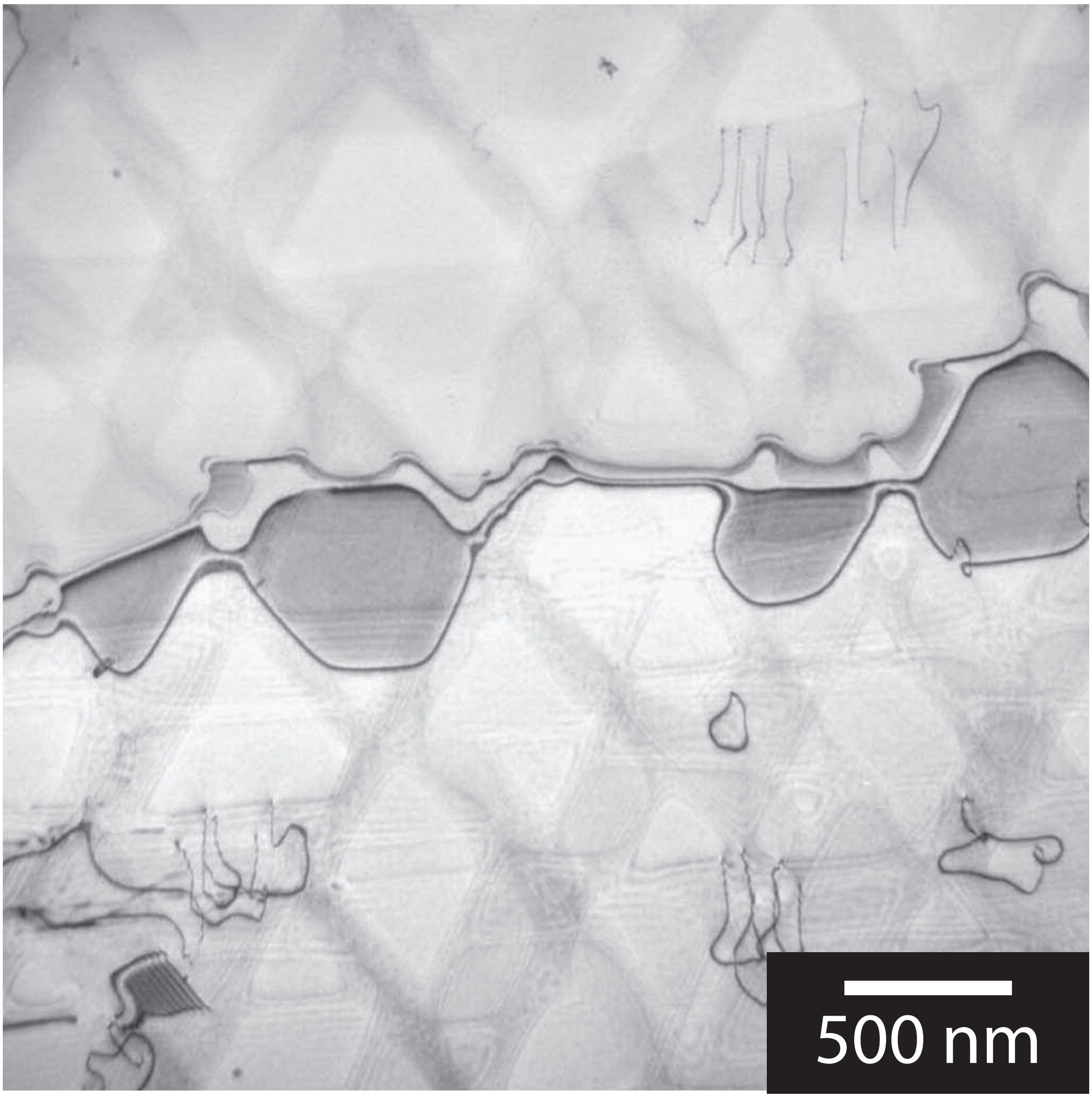

Figure 2.29 TEM micrograph of an $\frac{a}{2}\langle 11\bar{2}\rangle$ in single crystal TMS-82+ deformed in creep at 750 °C and 750 MPa, interrupted at 11% strain. The foil normal is$\{111\}$.[117]

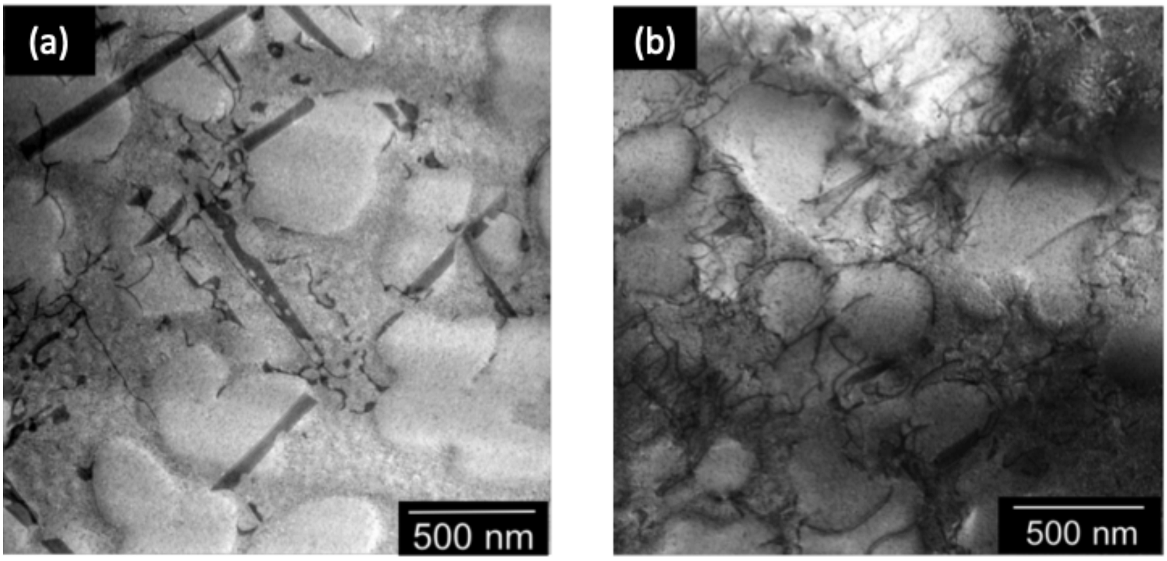

Figure 2.30 Bright field (BF) TEM micrographs of single crystal Ni-based superalloy ME3 under different creep conditions, foil normal = [001]. (a) 700 °C compression creep tests at 552 MPa, (b) 760 °C compression creep tests at 552 MPa. At 700 °C, stacking fault ribbons are visible, shearing γ' precipitates. At the higher temperature of 760 °C, deformation by APB shearing was more commonly observed.[133]

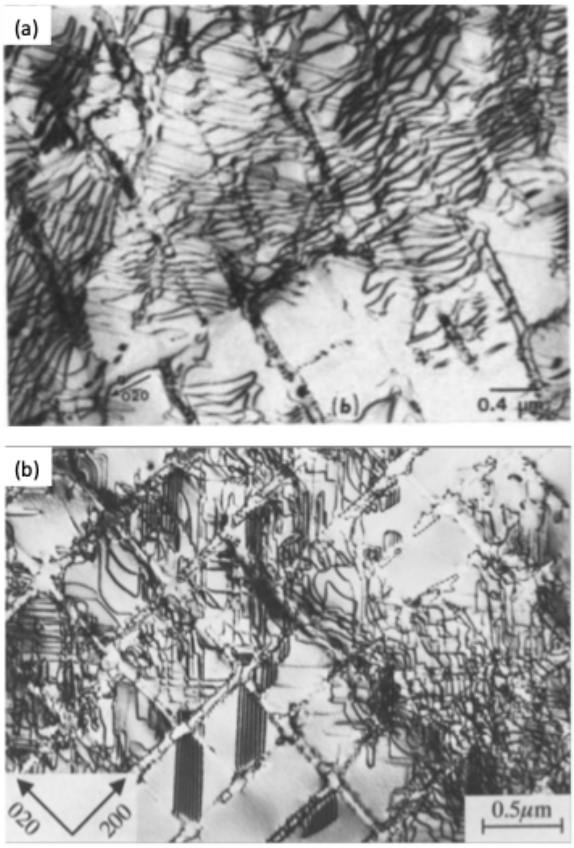

Figure 2.31 Comparison of the dislocation structures of single crystal superalloys subjected to primary creep. (a) CMSX-3 (850°C and 552 MPa, interrupted at 0.1% strain), and (b) CMSX-4 (850°C and 650 MPa, interrupted at 0.3% strain). The foil normal is (001).[112, 124]

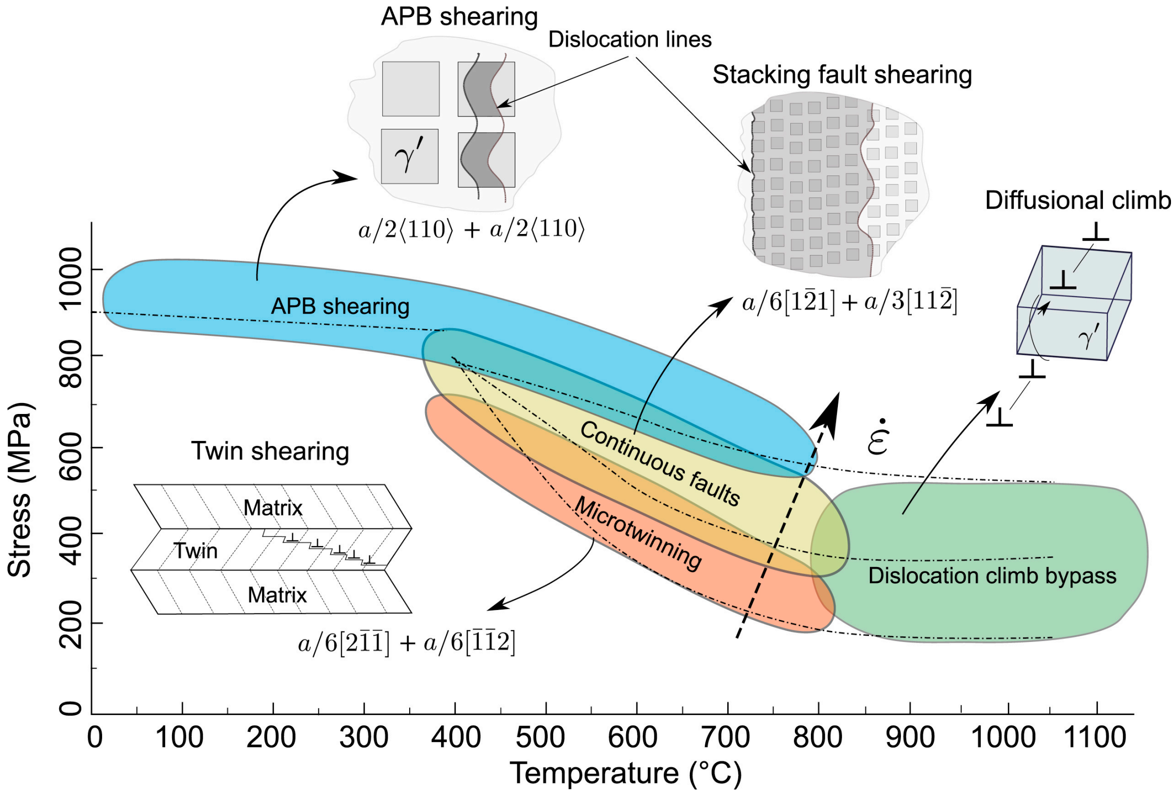

Figure 2.32 A deformation mechanism map for several Ni-based disk alloys illustrating the deformation mechanism's dependence on stress, temperature and strain rate.[4]

2.9 Conclusions

Plastic deformation in Ni-based superalloys is a complex phenomenon. Therefore, the study of yield behaviour has up to now focused predominantly on L1$_2$-ordered alloys and ternary Ni$_3$(Al, X) compounds. It is known that the Ni$_3$Al, L1$_2$-phase imparts strength to a Ni-based superalloy and allows anomalous yield behaviour to be exhibited in addition to numerous other possible planar defects. The mechanisms of plastic deformation are sensitive to strain rate, temperature and stress. These are thought to be independent mechanisms though transitions have been observed during *in situ* testing. The mechanism controlling anomalous yielding is yet to be determined. The most commonly adopted mechanism involves the cross-slip of dislocations from $\{111\}$ planes to $\{100\}$ planes, where they become locked. The locking and unlocking processes and detailed mechanisms that govern such processes are also unclear. Various models have been proposed, with increasing compatibility with the various macroscopic mechanical characteristics observed in L1$_2$-ordered alloys. Both still lack the versatility to explain all characteristics thought to be key features of the anomalous yield behaviour. The anomalous yield effect is not as pronounced in two-phase γ/γ' systems compared to monolithic L1$_2$ compounds. Factors such as volume fraction and size of γ', the misfit between γ and γ' and the relative APB energies in γ' and γ additionally need to be accounted for.

Chapter 3

Methodology

Tensile tests were first run at four different temperatures for three different superalloys to gain an overall understanding of how the microstructure from tensile deformation changes with composition, temperature and strain rate. A reference condition was chosen: the second-generation superalloy CMSX-4 tested at 750 °C at a strain rate $\dot{\varepsilon} = 10^{-4}\,\mathrm{s}^{-1}$. From this reference, the strain rate was increased and decreased by two orders of magnitude. The reference condition was used to image and analyse the dislocations observed in the γ' precipitates.

3.1 Sample Information and Tensile Test Conditions

Tensile tests were conducted under various different conditions to understand the effect of temperature ((Chapter 4), composition (Chapter 4 and 5) and strain rate (Chapter 5) on the deformation structure of single crystal Ni-based superalloys. An in depth analysis of the dislocation structures that form from these tensile tests is the subject of Chapter 6. The tensile specimens were small, and in some cases, it proved necessary to run a second interrupted test to produce enough material for TEM specimens with the desired number of orientations.

Tensile specimens for these tests were machined from widely used single crystal Ni-based superalloys CMSX-4, TMS-138A and SRR99. All superalloy materials were provided by Rolls-Royce plc., Derby, UK. The composition of these superalloys can be found in Table 3.1. Prior to machining, the specimens were homogenised, subjected to a heat treatment and aged: the primary age cycle was 2 hours at 1140 °C and the secondary age was performed for 16 hours at 870 °C. Microstructures of the specimens before testing were composed of cubic γ' precipitates measuring about 350 nm along their edges separated by γ-channels about 50 nm in width, containing small spherical tertiary γ precipitates about 5 nm. The volume

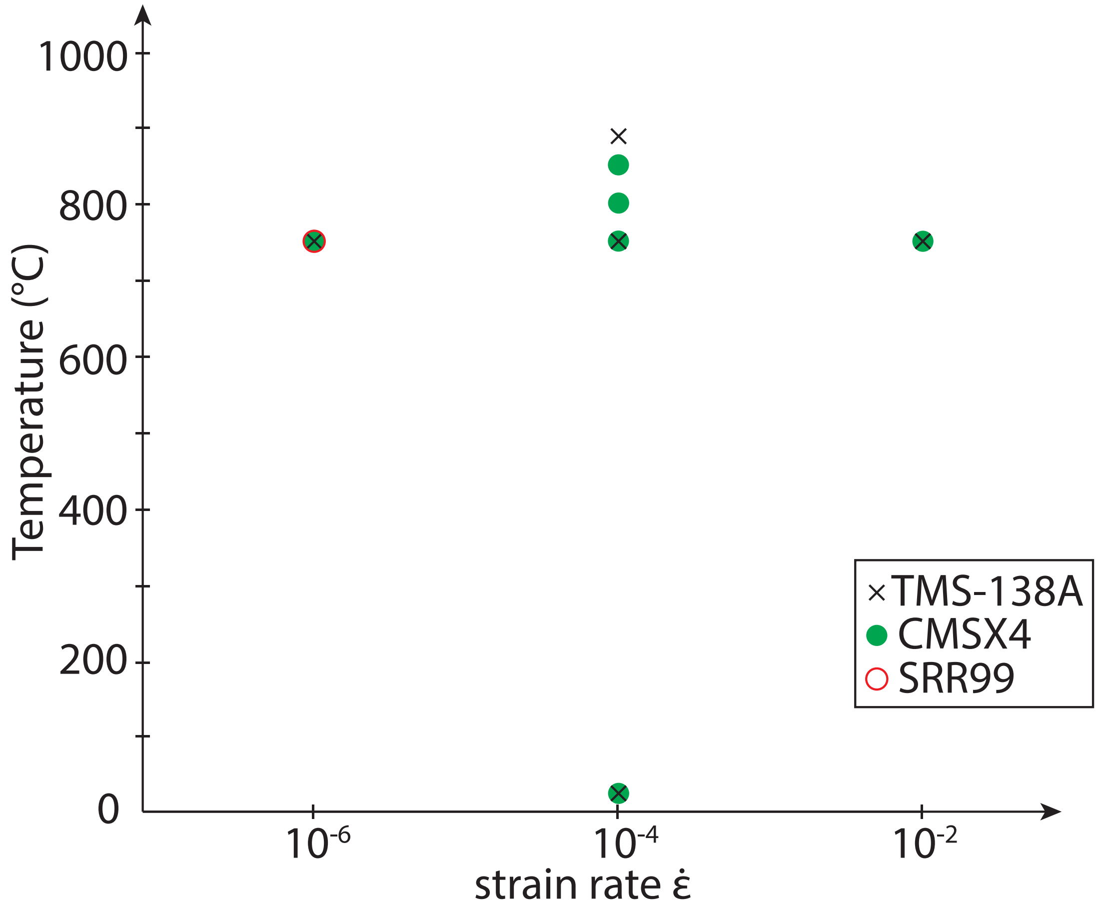

Figure 3.1 A graphical representation of the different test conditions (temperature and strain rate) used during testing of respective alloys throughout this dissertation.

fraction of γ' was roughly 75%.

Threaded tensile samples had a nominal gauge diameter of 3.5 mm and a gauge length of 25 mm. A blue-print of the sample specifications is provided in the Appendix. The specimen orientations were acquired using the SCORPIO system (Single Crystal Orientation Rapid Processing and Interpretation) at Rolls-Royce plc. [64, 131] and detailed in Table 3.3. For all specimen tested, the angles (θ) between the [001] specimen axes and the loading direction was less than 10° to minimise the effect of orientation on results.

Figure 3.1 is a graphical representation of the different test conditions used on the respective alloys throughout this dissertation. Proof stress data were supplied for CMSX-4 and TMS-138A from Rolls-Royce plc. These data were used to find the temperature at which the highest 0.1% proof stress occurred. From this, a temperature either side of the peak stress was chosen to understand the effect temperature has on the yield stress. For CMSX-4, the peak temperature was 800 °C and the two temperatures chosen either side were 750 °C and 850 °C. For TMS-138A, two temperatures were chosen: 750 °C and 900 °C, with the former corresponding to the peak temperature and 900°C as a point at which the proof stress had dropped considerably. All the strain rate variation tests featured in Chapter 5 were run at 750 °C. High temperature, strain-controlled tensile tests were performed using an Instron 8501 - 100 kN servo-hydraulic machine. The tensile tests in Chapters 4 and 6 were performed at a strain rate $\dot{\varepsilon}$=10^{-4} s^{-1}. The tensile tests featured in Chapter 5 were performed at three different strain rates: $\dot{\varepsilon}$=10^{-2} s^{-1}, 10^{-4} s^{-1} and 10^{-6} s^{-1}.

The stress-strain curves obtained in Chapter 4 are different to those featured in Chapters 5 and 6. This is thought to be due to alignment issues of the mechanical testing rig, in addition to contaminants in the oil and the hydraulics system due to an incorrectly fitted water pipe. The stress-strain curves of Chapters 5 and 6 were obtained after the machine was serviced, the grips redesigned and the load train realigned. Nevertheless, the interrupted microstructures featured in Chapter 4 still yield valuable observations.

Table 3.1 Alloy composition of CMSX-4, TMS-138A and SRR99 in at.%

Alloy	Cr	Co	Mo	W	Al	Ti	Ta	Re	Ru	Hf	Ni
CMSX-4	6.5	9.6	0.6	6.4	5.6	1.0	6.5	3	-	0.1	base
TMS-138A	3.2	5.8	2.8	5.6	5.7	-	5.6	5.8	2.8	-	base
SRR99	8.5	5	-	9.5	5.5	2.2	2.8	-	-	-	base

Table 3.2 The interrupted strains of the tensile tests featured in Chapter 5 on three single crystal Ni-based superalloys: CMSX-4, SRR99 and TMS-138A

Alloy	$\dot{\varepsilon}$ (s^{-1})	strain (%)		
		at 1st interruption	at 2nd interruption	at failure
CMSX-4	10^{-2}	3.4	-	10.2
	10^{-4}	4.8	10.7	14.9
	10^{-6}	1.2	2.5	23.1
TMS-138A	10^{-4}	-	-	10.77
	10^{-5}	-	-	17.2
	10^{-6}	-	-	8.77
SRR99	10^{-4}	-	-	12.0
	10^{-6}	-	-	12.6

Table 3.3 Orientation of the various test specimen featured in subsequent chapters and their respective test conditions, given in European convention primary orientation angles.[14]

Alloy	T	$\dot{\varepsilon}$	tensile test status	θ	ρ
CMSX-4	25 °C (RT)	10^{-4} s^{-1}	tested to failure	1	3
CMSX-4	750 °C	10^{-2} s^{-1}	tested to failure	4.8	8.8
CMSX-4	750 °C	10^{-4} s^{-1}	interrupted after yield	6.9	31.3
CMSX-4	750 °C	10^{-4} s^{-1}	tested to failure	7.7	12.2
CMSX-4	750 °C	10^{-6} s^{-1}	interrupted just after yield	5.8	24.2
CMSX-4	750 °C	10^{-6} s^{-1}	interrupted at stress drop after yield	5.4	21.7
CMSX-4	750 °C	10^{-6} s^{-1}	tested to failure	5.6	6.7
CMSX-4	800 °C	10^{-4} s^{-1}	tested to failure	12	2
CMSX-4	850 °C	10^{-4} s^{-1}	tested to failure	2	18
TMS-138A	25 °C (RT)	10^{-4} s^{-1}	tested to failure	3	1
TMS-138A	750 °C	10^{-4} s^{-1}	tested to failure	6	1
TMS-138A	750 °C	10^{-4} s^{-1}	interrupted before yield	4.4	21.3
TMS-138A	750 °C	10^{-4} s^{-1}	interrupted after yield	4.7	20.3
TMS-138A	750 °C	10^{-6} s^{-1}	tested to failure	4.4	21.3
TMS-138A	900 °C	10^{-4} s^{-1}	interrupted after yield	4	7
SRR99	750 °C	10^{-4} s^{-1}	tested to failure	4	22
SRR99	750 °C	10^{-6} s^{-1}	tested to failure	4	22

3.2 Transmission Electron Microscopy (TEM)

To better visualise the dislocation structures associated with the deformation sustained during the mechanical tests, the primary slip plane and respective other crystallographic planes were determined. Back-Laue X-ray diffraction, using a Laue back reflection camera with unfiltered Mo radiation, was employed to determine the orientation of the tensile specimen. This allowed for sectioning of the tensile specimen into transmission electron microscopy (TEM) foils along specific crystallographic planes.

The TEM foils were prepared from 3 mm diameter spark-eroded discs with a thickness of $\sim$150 μm and further electropolished using a Struers Tenupol-5 with a solution of 6 vol%. perchloric acid in methanol, maintained at 20.5 V and -5 °C.

The TEM investigations were performed using a JEOL - 200 CX microscope, as well as a FEI Tecnai Osiris 80-200 equipped with an FEI Super-X EDX system employing four Bruker silicon drift detectors for high collection efficiency ($>$0.9 Steradian) and high count rates ($>$250 kcps). High-resolution TEM investigations were also conducted on an FEI Titan^3 with a CEOS CESCOR hexapole aberration corrector in the probe forming lens.

Complementary to the energy dispersive X-ray spectroscopy (EDS) investigations carried out in the Tecnai Osiris, electron energy loss spectroscopy (EELS) maps were obtained from the FEI Titan microscope following TEM imaging to ascertain local chemical variation within the γ' precipitates where the faults were identified. The EELS maps were collected using a Gatan Tridiem 865 imaging filter and the data were analysed using Digital Micrograph software.

In order to better visualise the faulted structures within the images collected, centre of symmetry (COS) calculations were performed.[88] A MATLAB® routine was employed to identify the atom column positions and then investigate the symmetry of the six nearest neighbour positions. The resulting centre of symmetry contour plot shows the deviation from the symmetry and the identified atom positions as an overlay. More detailed information regarding the procedure can be found below in Section 3.2.1 and the Appendix.

3.2.1 Imaging and Analysis of HAADF Images Through Centre of Symmetry (COS) analysis

It is difficult to identify planar faults in HAADF images. One method that has been used successfully is called Centre of Symmetry (COS) analysis. Each bright spot on a HAADF image represents an atom column viewed directly down a crystallographic direction. The distances to the six nearest, neighbouring atom columns are measured. These are then compared to determine the symmetry of the atom column relative to it's neighbours. At the location of a planar fault, the neighbouring atoms are no longer equidistant from the central atom column, resulting in asymmetry. The varied degrees of asymmetry across a HAADF image will therefore highlight planar faults.

Digital HAADF images were subject to a number of processing steps and numerical analysis in order to enhance and emphasise the observed features. The purpose of this analysis was to locate and identify the symmetry of each atom column and thus any faults in the stacking sequence. All stages of the processing sequence were performed using MATLAB® with the imaging processing toolbox. This is described in more detail in the Appendix.

Chapter 4

The Effect of Temperature and Alloy Composition on Tensile Deformation of Single Crystal Ni-based Superalloys

4.1 Introduction

This chapter focuses on the effect of temperature and composition on the tensile behaviour. The deformation structure of the commonly used, second-generation, single crystal superalloy CMSX-4 was analysed to understand how the dislocation structure affects the macroscopic tensile behaviour. This was compared against a fourth generation single crystal superalloy TMS-138A to understand the effect that additions of Ru and increased quantity of Re have on tensile deformation with temperature. Tensile tests have been interrupted at varying levels of strain. These specimen were then sectioned and prepared for Transmission Electron Microscopy (TEM). Analysis of the microstructural evolution at each temperature and strain interrupton was then carried out.

4.2 Results

Tensile tests were conducted to fixed levels of plastic strain on single crystal tensile samples of Ni-based superalloys CMSX-4 and TMS-138A, all orientated within 2 ° of the [001] crystal axis. All tests were run at a strain rate of $10^{-4}\,\mathrm{s}^{-1}$. Four different test temperatures were used for CMSX-4: room temperature, 750 °C, 800 °C and 850 °C for CMSX-4, compared to three tests temperatures for TMS-138A: room temperature, 750 °C and 900 °C.

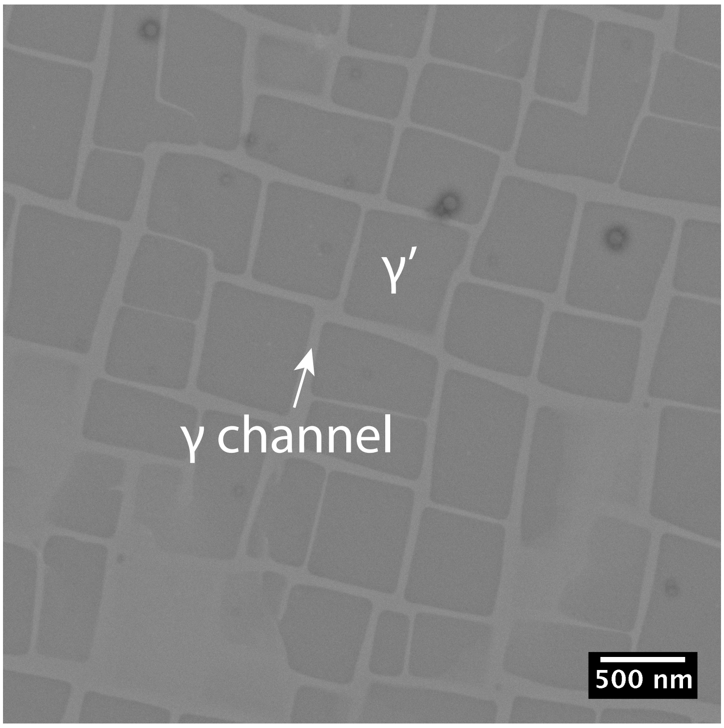

Figure 4.1 An SEM micrograph of the two-phase γ/γ' microstructure of CMSX-4 prior to tensile deformation. The γ' precipitates are cubic in shape, surrounded by the γ matrix.

This section summarises the observations obtained from mechanical tensile tests and microstructures from transmission electron microscopy (TEM) of tensile specimens interrupted at various levels of strain. These strains at all temperatures correspond to the interruption point relative to the yield point: *before yield*, *at yield* and *beyond yield*. The microstructures for specimens tested to failure were too densely filled with dislocations to derive any insight and have thus been omitted from the analysis. The microstructures of the two superalloys contain a fine dispersion of ordered, cubic γ' precipitates, as shown in Figure 4.1. The γ' size was fairly uniform in both superalloys, with an average size of 600 nm and 450 nm for CMSX-4 and TMS-138A respectively. No hyperfine γ' was found. The primary γ' volume fraction was measured to be around 70% (see appendix).[83]

4.2.1 Tensile Test Stress-strain Curves for CMSX-4 and TMS-138A

The stress-strain curves for CMSX-4 tested to failure at various temperatures are shown in Figures 4.2 and 4.3. The interrupted tests traced the failed specimens and can be found in the Appendix. In the elastic regions, the gradient decreases with increasing temperature, with 750 °C and 800 °C possessing similar gradients. A change of gradient occurs in the elastic region of the 750 °C curve suggesting an early onset of plasticity before the yield drop. It is unclear whether this phenomenon occurs at 800 °C and 850 °C, and if so, whether this deviation is more subtle. The stress increases with increasing strain beyond the yield point to failure, showing work hardening at all temperatures. The magnitude of the drop in stress upon the yield point being reached varies with temperature; the largest drop of around 100 MPa was observed for the tensile test conducted at 800 °C, compared to 10 MPa for specimens deformed at room temperature.

The stress-strain curves for TMS-138A are shown in Figure 4.4. As with CMSX-4, the interrupted tests have been placed in the Appendix. The yield point is similar at room temperature and 750 °C, around 875 MPa. The 900 °C curve experienced a much higher yield stress of 1200 MPa. There is a drop in stress after the yield point at room temperature and 900 °C, a feature not present at 750 °C. Furthermore, the tensile curves of 750 °C exhibited rapid work hardening after the yield point, while specimens deformed at room temperature and 900 °C displayed more gradual work hardening to failure. Increasing the temperature also reduced the strain to failure with strain at failure for tests at 750 °C and 900 °C equal to 2.5% and 10% respectively, compared to 22% for room temperature. The 750 °C curve showed serrated flow before failure. This feature was absent in the remaining tests, including the 750 °C tensile test interrupted just before failure (see Appendix).

Comparing the tensile curves from tensile tests on the two superalloys CMSX-4 and TMS-138A, the yield stress is lower for TMS-138A than CMSX-4. At room temperature, the yield point occurs at around 1000 MPa for CMSX4 compared to just above 800 MPa for TMS-138A. All the tensile curves apart from 750 °C for TMS-138A show a drop in stress after the yield point. The strain to failure is significantly lower for the test on TMS-138A at 750 °C compared to the other stress strain curves. The CMSX-4 curve also work hardens more than TMS-138A at room temperature, shown by the slight increase in stress with increasing strain after yield. The CMSX-4 curves at 750 °C and 850 °C even show a slight softening with increasing strain.

4.2.2 Transmission Electron Microscopy (TEM) Observations

The following microstructures have been divided into three groups, corresponding to the stage of each individual stress-strain curve to which they were interrupted relative to the yield point: *before yield*, *at yield* and *beyond yield*. Due to the variation in the stress-strain curves, the absolute interrupted levels of strain differ depending on the test temperature and

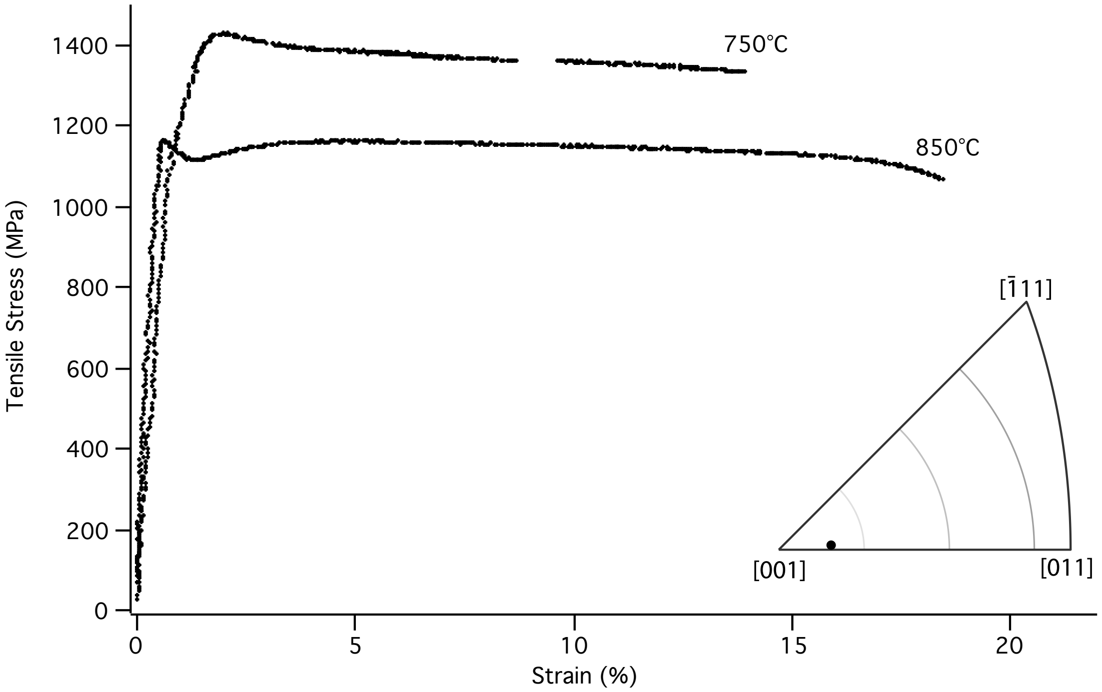

Figure 4.2 The stress-strain curves for CMSX-4 at $\dot{\varepsilon}=10^{-4}\,s^{-1}$ at two temperatures: 750 °C and 850 °C. The stress-strain curves for RT and 800 °C are displayed separately in Figure 4.3 because the strain was not recorded. Inset: an inverse pole figure showing the orientations of the three specimens tested to failure in relation to the [001] tensile direction.

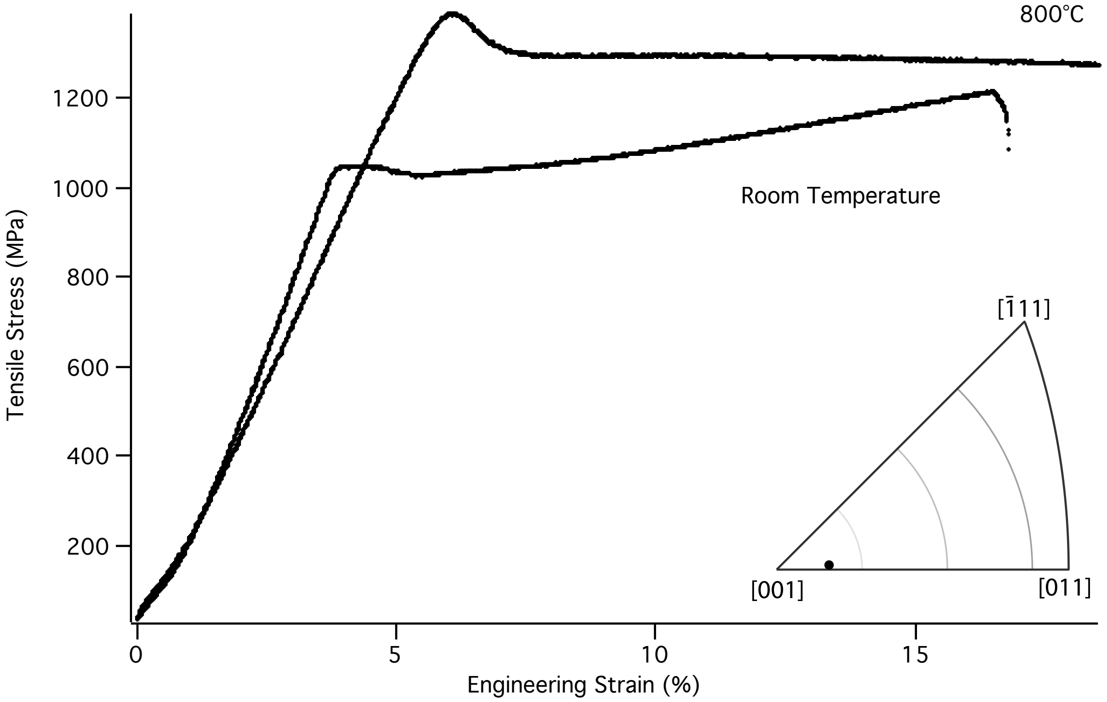

Figure 4.3 Plots of stress against engineering strain curves for CMSX-4 at $\dot{\varepsilon}=10^{-4}\,\mathrm{s}^{-1}$ at room temperature and 800 °C. The absolute strain was not recorded after the extensometer slipped off during testing. Inset: an inverse pole figure showing the orientations of the three specimens tested to failure in relation to the [001] tensile direction.

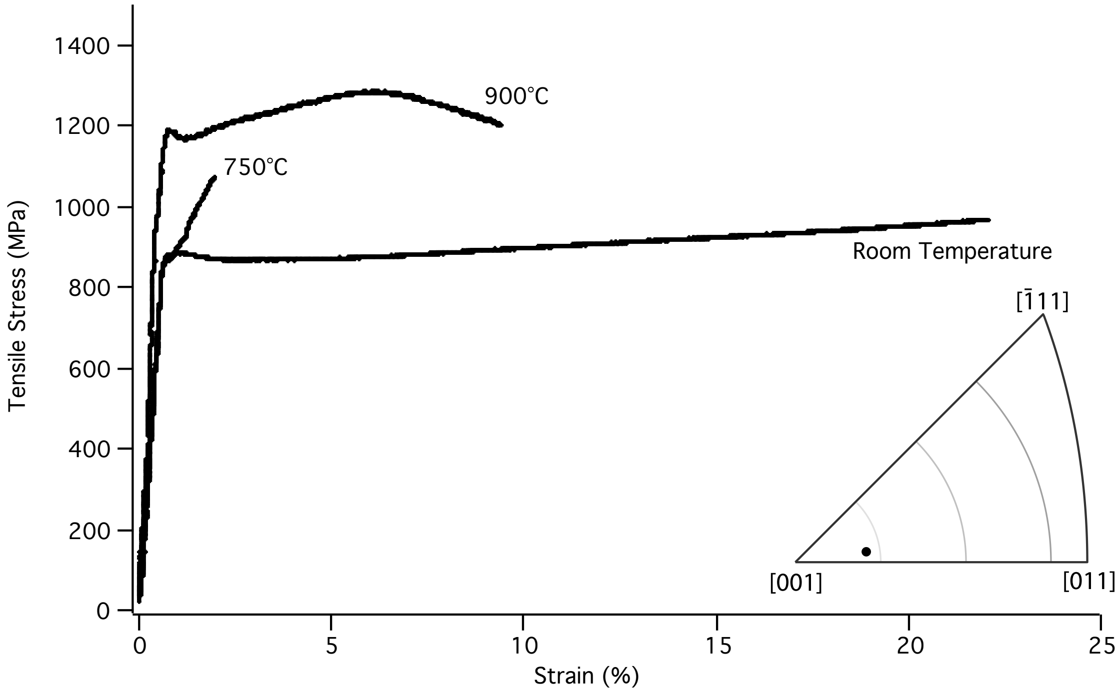

Figure 4.4 Plots of stress-strain curves for TMS-138A at $\dot{\varepsilon}$=10^{-4} s^{-1} at three temperatures: room temperature, 750 °C and 900 °C. The curve for 750 °C is truncated because the extensometer slipped off mid-test. Inset: an inverse pole figure showing the orientations of the three specimens tested to failure in relation to the [001] tensile direction.

alloy, the values for which are listed alongside the respective interrupted condition.
In the early stages of deformation for all samples, dislocation motion is confined to the horizontal matrix channels. This is consistent with the variation of effective stress levels in the three different matrix channels (two horizontal, one vertical) with the orientation of the stress axis, due to the superposition of internal coherency stresses with the external stress. In orientations close to the [001], at early stages of deformation, stress is concentrated within the horizontal matrix channels with a reduced stress level in vertical channels.

4.2.3 TEM Observations of the Deformation Structure of CMSX-4 at Room Temperature, 750°C, 800°C and 850°C

Tensile deformation of CMSX-4 at room temperature

Figure 4.5(a-c) shows the typical features of the dislocation structure for samples interrupted at various stages of tensile deformation at room temperature. Before yield, (see Figure 4.5(a)), dislocations lie in the horizontal γ channels and few dislocations are observed to have penetrated into the γ' precipitates. Some of the dislocations are not on a particular slip plane suggesting they are a result of grown-in dislocations from dendrites. Some appear at a 45 ° angle to the γ' precipitate edges and have specific angles upon changing direction due to cross-slip. These have been highlighted with the letter 'A' in Figure 4.5(a).
By the yield point (Figure 4.5(b)), the number of dislocations in the horizontal γ channels has increased, though due to the sample being cut parallel to the (001) plane, some areas of the horizontal channels are dislocation free, thought to be representative of areas that do not intercept a horizontal γ channel. The matrix dislocations that are visible adopt rigid orientations along the $\{111\}$ slip planes. Dislocations have also penetrated into the γ' precipitates. These appear in a variety of shapes: small, narrow dislocation loops as well as straight and curved dislocations in the γ' precipitates. At the highest level of strain (Figure 4.5(c)), the γ channels are filled with dislocations. These appear as patches as the TEM sample captures areas of the horizontal γ channels. Many dislocations are also observed in the precipitates, in various configurations.

Tensile Deformation of CMSX-4 at 750 °C

At a higher temperature of 750 °C, interrupted before yield (Figure 4.6(a)), dislocations are also mainly present in the horizontal γ channels. Again the dislocations are restricted to glide on the $\{111\}$ slip planes, confined to the γ channels, and oriented at 45° to the γ channels.

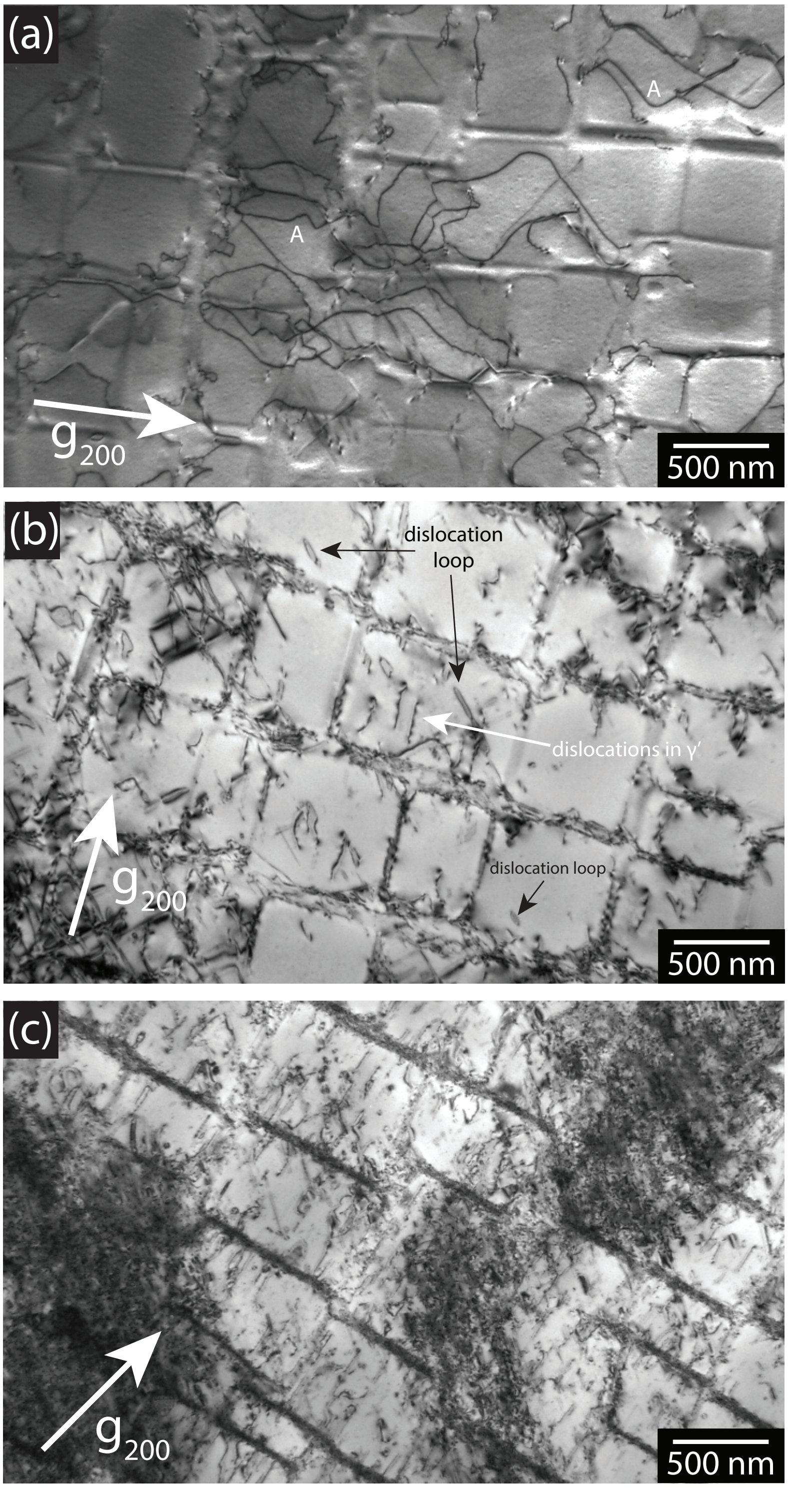

Figure 4.5 The deformation microstructures of CMSX-4 after tensile deformation at $\dot{\varepsilon}=10^{-4}\,\mathrm{s}^{-1}$ at room temperature, interrupted (a) before yield, ε = 3.6% (b) at yield, ε = 4.5% and (c) after yield, ε = 15.3%.

The density is slightly higher than that observed at room temperature, which may be due to the higher strain at which the specimen was interrupted. The γ' precipitates remain relatively devoid of dislocation activity. The deformation structure proceeds by the filling of the narrow γ-matrix channels on $\{111\}$ glide planes with $\frac{a}{2}\langle 110\rangle$ dislocations.

By the yield point (Figure 4.6(b)), dislocations have entered into γ' precipitates in the form of dislocation pairs either closely spaced or separated by stacking faults. The stacking faults glide along $\{111\}$ slip planes, which therefore appear as triangles or parallelograms that span from the corners of the cubic precipitates when viewed down the [001] zone axis. At a strain far beyond the strain at yield (Figure 4.6(c)), the the horizontal matrix channels are filled with dislocations, which appear as dark patches. Significant dislocation activity is observed in the γ' precipitates though the proportion of dislocations seems higher than stacking faults in the precipitates.

Tensile Deformation of CMSX-4 at 800 °C

The development of the deformation structure for tensile deformation at 800 °C is shown in Figure 4.7(a-c). Similar to the microstructure at 750 °C, $\frac{a}{2}\langle 110\rangle$ dislocations are present within the horizontal γ channels on $\{111\}$ slip planes. These are accompanied by stacking faults beginning to shear γ' precipitates. By the yield point (Figure 4.7(b)), the dislocations in the horizontal γ-matrix channels have interacted with each other and climbed, producing a wavier appearance compared to the dislocation structure interrupted at a similar level of strain at 750°C (Figure 4.6(b)). Stacking faults are also observed, now shearing on two slip systems. These are accompanied by dislocation segments and loops within the γ' precipitates. Upon further strain (Figure 4.7(c)), the horizontal γ-channels and vertical γ-channels become heavily saturated with dislocations. Both the horizontal γ-channels and γ' precipitates are filled with dislocations. The microstructure suggests both stacking fault shearing and APB shearing continue as deformation mechanisms. Most precipitates contain stacking faults and dislocations in various configurations.

Tensile deformation at 850 °C for CMSX-4

Figure 4.8(a-c) shows the deformation structure for tensile deformation at 850 °C. $\frac{a}{2}\langle 110\rangle$ dislocations are again present in the horizontal γ-channels before yield has occurred. These, at this early stage of deformation, have a wavier appearance compared to the lower temperatures. No other activity is observed and the γ' precipitates are dislocation free. By the yield point (Figure 4.8(b)), stacking faults are visible within γ' precipitates, shearing along two slip

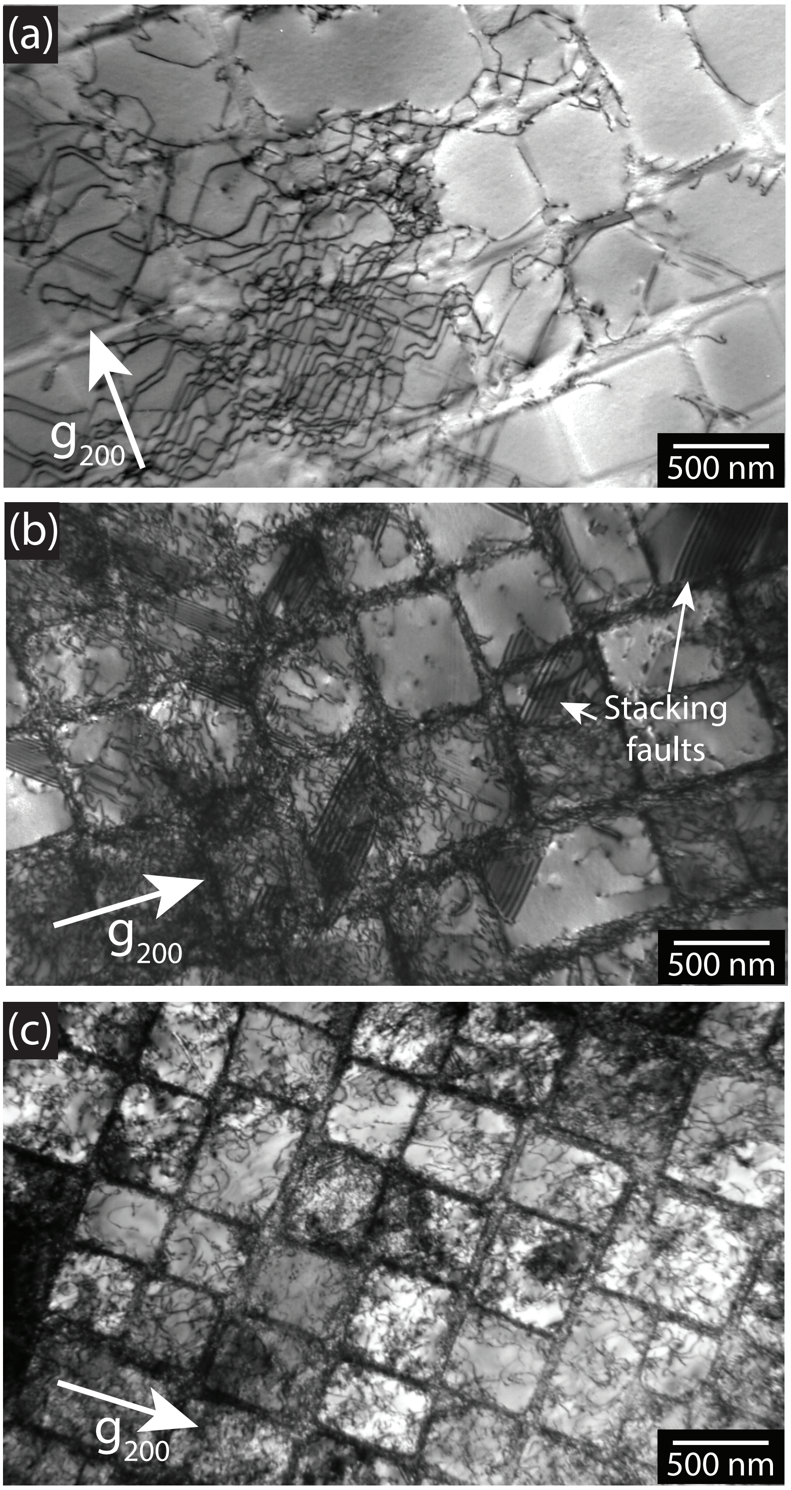

Figure 4.6 The deformation microstructures of CMSX-4 after tensile deformation at $\dot{\varepsilon}=10^{-4}\,\mathrm{s}^{-1}$ at 750 °C, interrupted (a) before yield, $\varepsilon = 4.3\%$ (b) at yield, $\varepsilon = 7.0\%$ and (c) after yield, $\varepsilon = 16.8\%$.

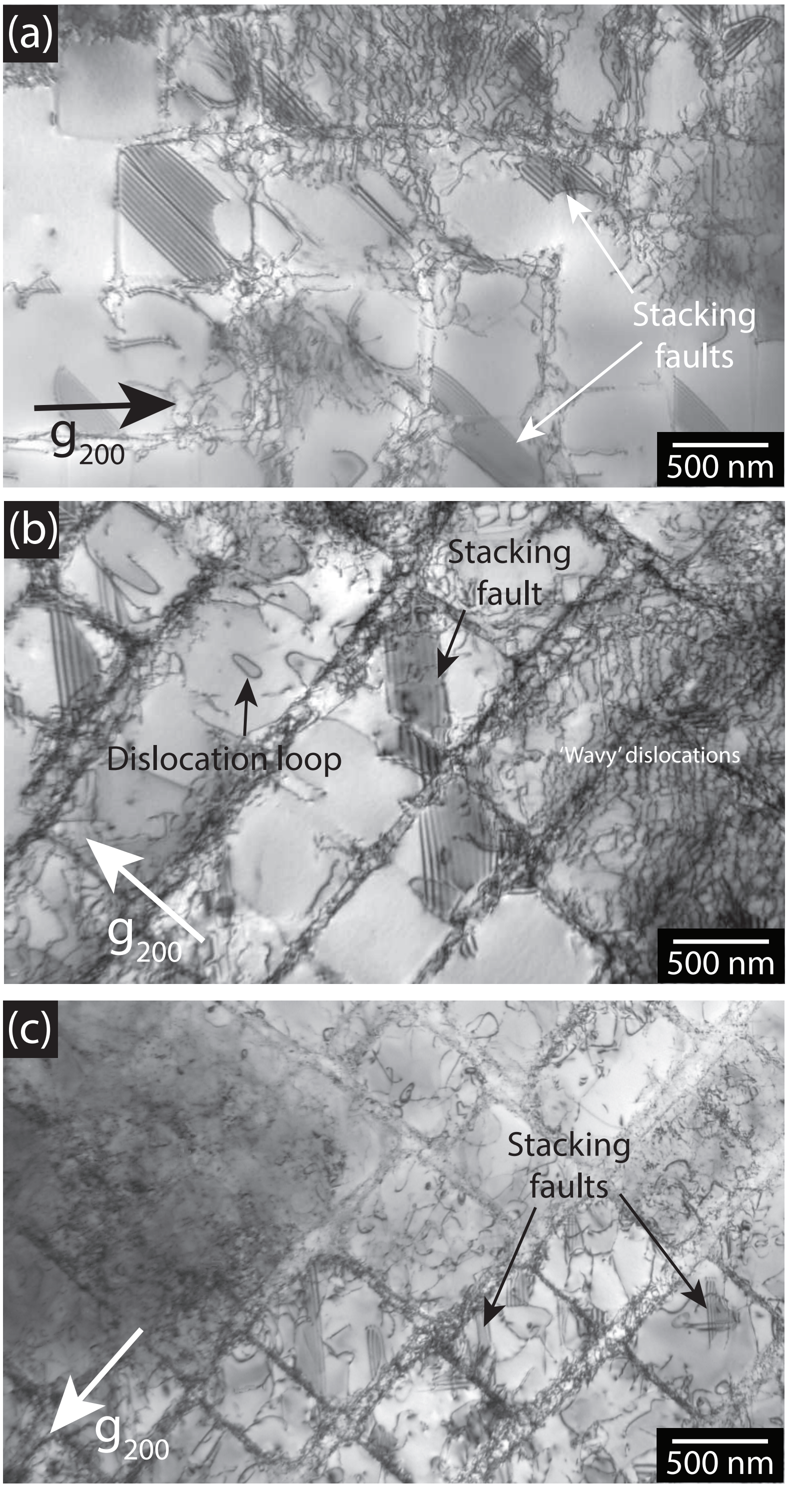

Figure 4.7 The deformation microstructures of CMSX-4 after tensile deformation at $\dot{\varepsilon}$=$10^{-4}\,\mathrm{s}^{-1}$ and 800 °C, interrupted (a) before yield, $\varepsilon = 5.2\%$ (b) at yield, $\varepsilon = 6.5\%$ and (c) after yield, $\varepsilon = 16.8\%$.

directions. Dislocations are also visible in the γ' precipitates though stacking faults are more prevalent. Beyond the yield point (Figure 4.8(c)), there is a significantly higher number of visible dislocations within the γ' precipitates, though a number of stacking faults are also visible.

4.2.4 TEM Observations of the Deformation Structure of TMS-138A at Room Temperature, 750°C and 900°C

Tensile deformation at room temperature

The room temperature deformation microstructure progression is shown in Figure 4.9(a-c). Before yield (Figure 4.9(a)), dislocations are sparse and confined to the horizontal γ channels. The deformation is different in horizontal and vertical channels. The application of a uniaxial tensile stress exaggerates any tensile stress in the vertical direction and reduces stress in the horizontal orientation. This effect is thought to be enhanced in TMS-138A compared to CMSX-4 because TMS-138A has a more negative misfit value (see Figure 4.12).[175, 41, 42] The dislocations appear as right angled segments, because they are confined to the $\{111\}$ slip planes. At the yield point (Figure 4.9(b)), the dislocation segments in the horizontal γ channels are shorter. Some seem to have entered into the γ' precipitates. There is also a lot of activity in the vertical γ channels. The fringes suggest stacking fault formation in the γ or highly ordered and oriented dislocations, packed in, pressing against the γ/γ' interfaces. Beyond the yield point (Figure 4.9(c)), dislocations have penetrated into the γ' precipitates. Both stacking faults and dislocation pairs in the form of dislocations are visible. Given the amount of strain in the sample, the precipitates are quite bare, with much of the strain seemingly accommodated in the vertical γ channels.

Tensile deformation of TMS-138A at 750 °C

The progression of the microstructure during deformation at 750 °C is shown in Figure 4.10. Before yield (Figure 4.10(a)), dislocations are again visible in the horizontal γ channels as well as confined to $\{111\}$ slip planes. Some dislocations have also penetrated into γ' precipitates. By the yield point (Figure 4.10(b)), the matrix dislocations have extended, though still confined rigidly to the glide planes within the channels. The γ' precipitates contain dislocations, though they still appear free from deformation. Beyond the yield point (Figure 4.10(c)), the density of the dislocation network within the γ channels has thickened substantially. Stacking faults now accompany the dislocations within the γ' precipitates.

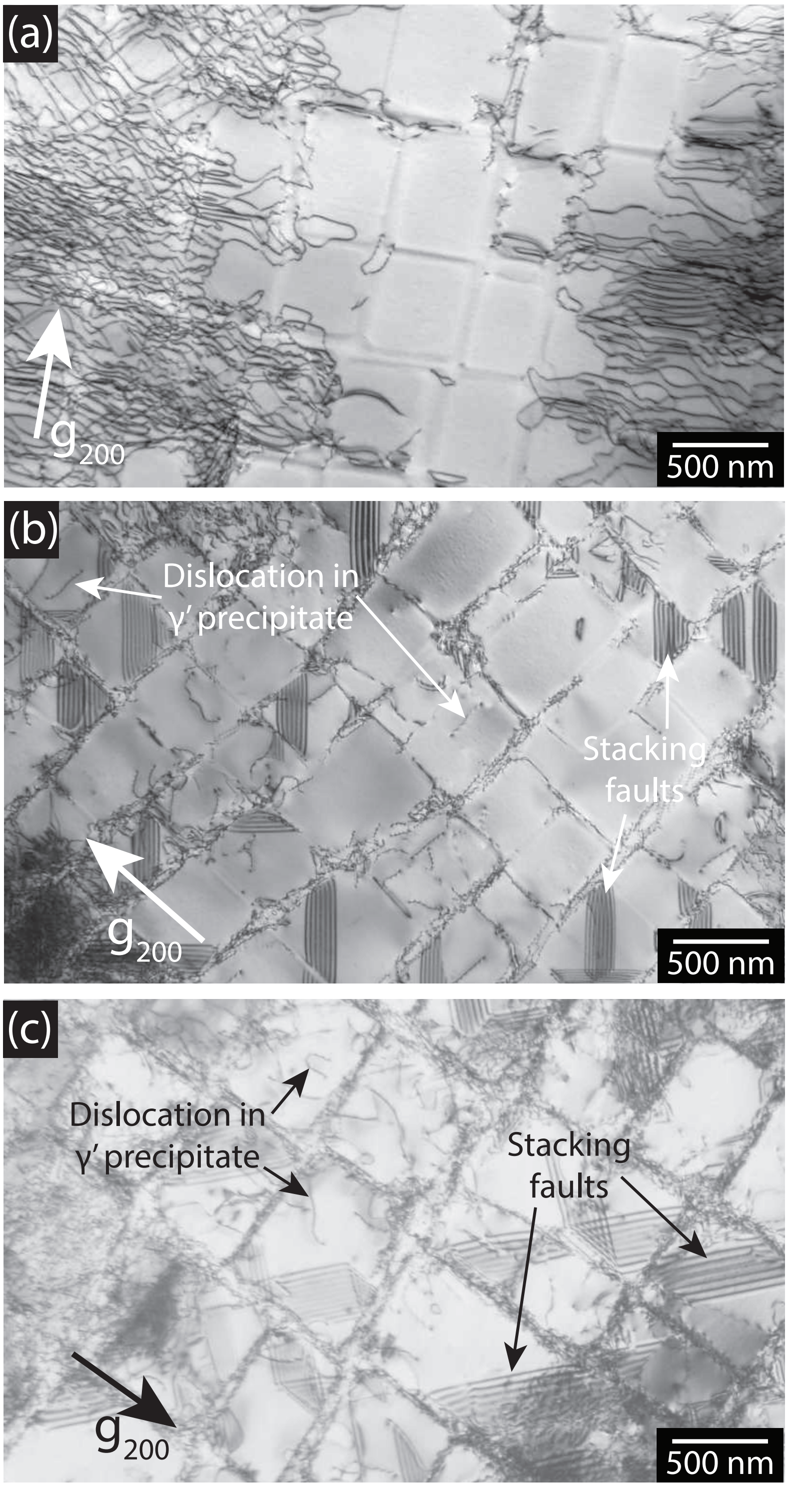

Figure 4.8 The deformation microstructures of CMSX-4 after tensile deformation at $\dot{\varepsilon}=10^{-4}\ \mathrm{s}^{-1}$ and 850 °C, interrupted (a) before yield, $\varepsilon = 4.8\%$ (b) at yield, $\varepsilon = 6.0\%$ and (c) after yield, $\varepsilon = 14.0\%$.

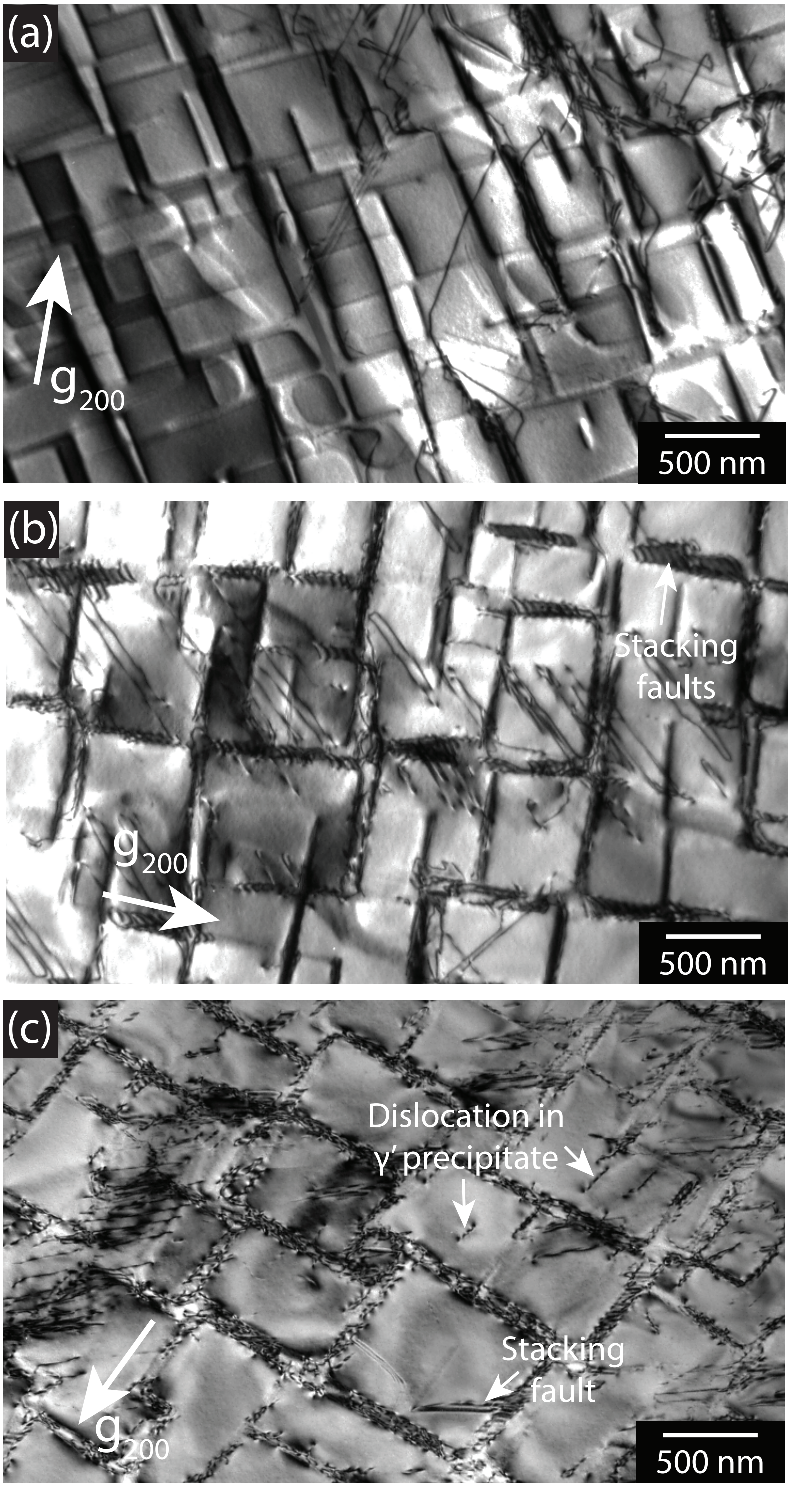

Figure 4.9 The deformation microstructures of TMS-138A after tensile deformation at $\dot{\varepsilon}=10^{-4}\,\mathrm{s}^{-1}$ at room temperature, interrupted (a) before yield, $\varepsilon = 2.6\%$ (b) at yield, $\varepsilon = 5.3\%$ and (c) after yield, $\varepsilon = 10.0\%$.

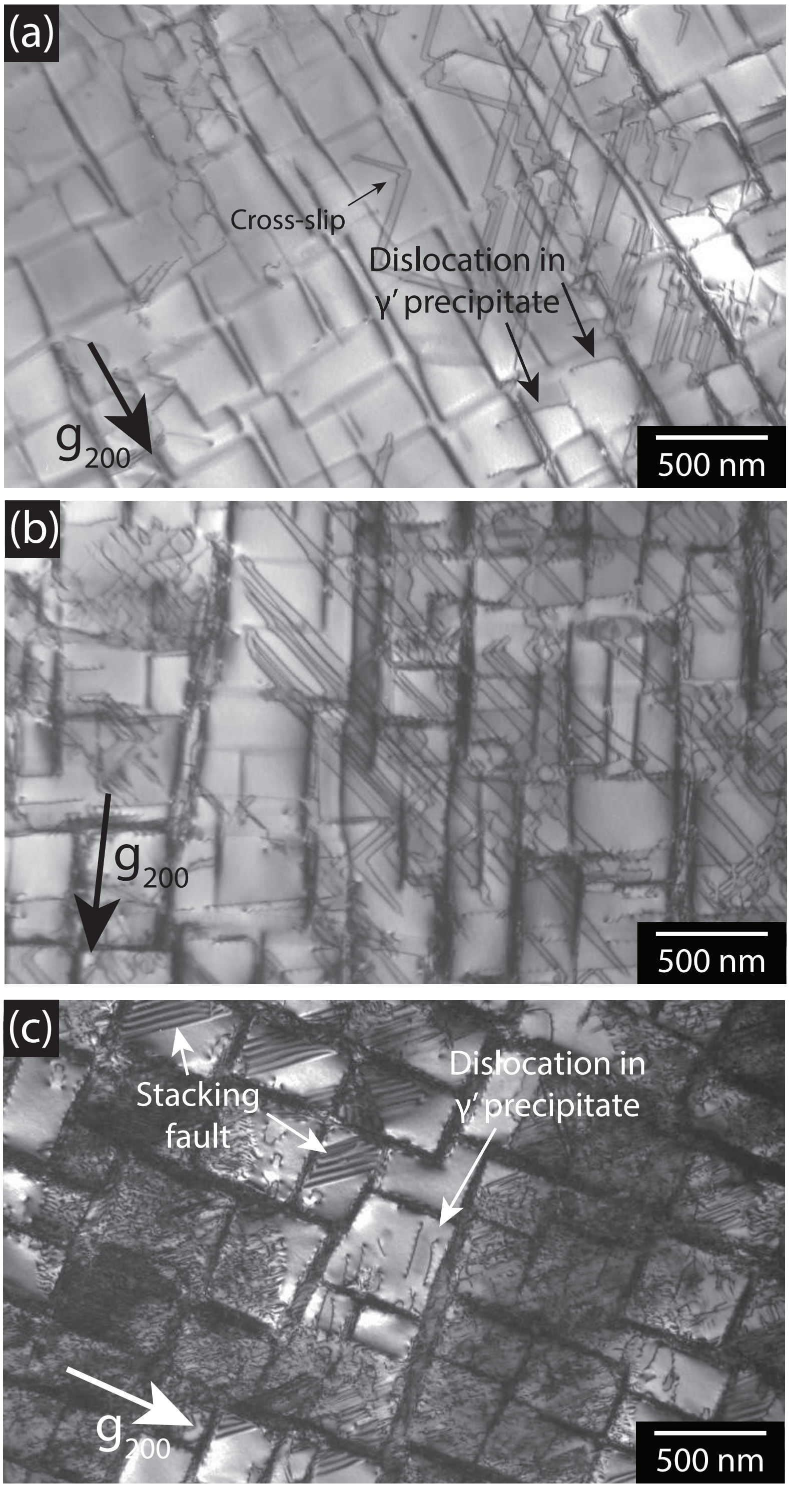

Figure 4.10 The deformation microstructures of TMS-138A after tensile deformation at $\dot{\varepsilon}=10^{-4}\,\mathrm{s}^{-1}$ at 750 °C, interrupted (a) before yield, $\varepsilon = 2.6\%$ (b) at yield, $\varepsilon = 4.1\%$ and (c) after yield, $\varepsilon = 10.0\%$.

Tensile deformation of TMS-138A at 900 °C

The progression of the microstructure during deformation at 900 °C is shown in Figure 4.11(a-c). Before yield (Figure 4.11(a)), the horizontal γ channels are the location of the dislocation activity. The microstructural area captured shows a grown-in dislocation network from which dislocations propagate. The $\frac{a}{2}\langle 110\rangle$ dislocations are still rigidly confined to the $\{111\}$ slip planes in the matrix. The vertical γ channels are mostly void of dislocations. Interrupted at yield (Figure 4.11(b)), the dislocations in the matrix adopt a much wavier appearance due to climb. A high number of stacking faults are also present. These are accompanied by a couple of visible dislocations, which seem to have just entered into γ' precipitates. At higher levels of strain (Figure 4.11(c)), the number of dislocations within the horizontal γ is so great it masks the presence of dislocations within the precipitates. Stacking faults are still present, though not as common as observed in the microstructure of the sample interrupted shortly after yield. Dislocations are also visible in γ' precipitates.

4.3 Discussion

4.3.1 Effect of Temperature on Tensile Deformation

In both alloys, the yield stress was observed to be higher at higher temperatures. For CMSX-4, with reference to the stress strain curves in Figures 4.2 and 4.3, the highest yield stress was observed for the tensile test conducted at 750°C. For all three temperatures above room temperature for tests on CMSX-4, the stress at the yield point is at least 150 MPa higher. For TMS-138A (see Figure 4.4), the yield point is similar for tensile tests at room temperature and 750 °C, and increases by around 250 MPa for 900 °C. The point of yield is thought to correspond to the penetration of dislocations into the γ' precipitates. A higher yield stress therefore means upon increasing temperature, the dislocations in the γ channels require a higher stress to enter the precipitates. The microstructure from the tensile test on TMS-138A at 900 °C at yield (Figure 4.11(b)) show matrix dislocations to be slightly wavier than the same dislocations from tests at room temperature and 750 °C. The wavier dislocations may protect the precipitates from shearing, along the similar school of thought to that favouring high lattice misfit.[177] The theory suggests denser dislocation networks favoured by high lattice misfit protects precipitates from shearing. For CMSX-4, this microstructures provide less conclusive evidence.

The dislocations at higher temperatures are wavier in shape in the CMSX-4 microstructures. This is because the dislocations have more energy to climb. Stacking faults were

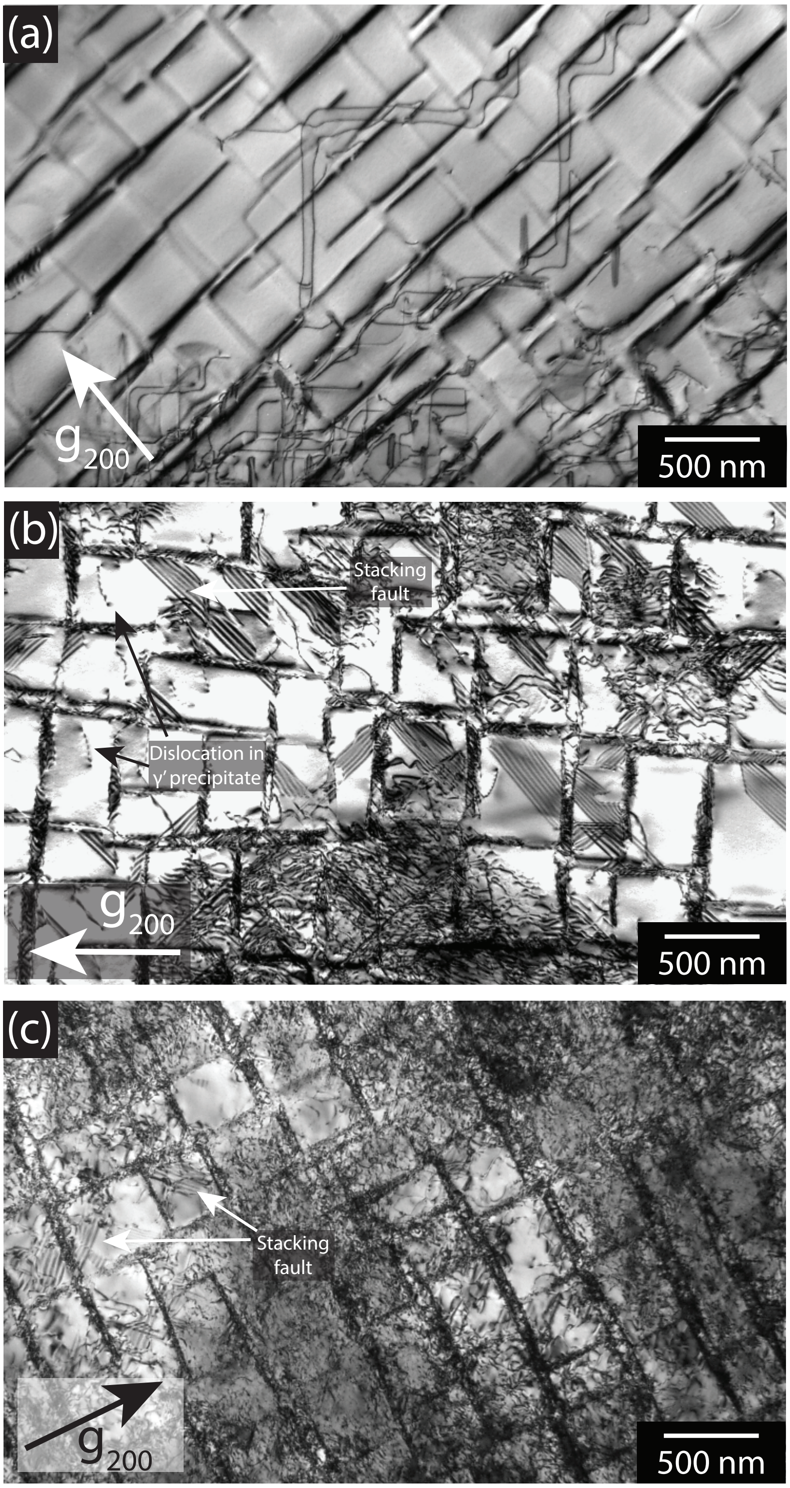

Figure 4.11 The deformation microstructures of TMS-138A after tensile deformation at $\dot{\varepsilon}=10^{-4}\,\mathrm{s}^{-1}$ at 900 °C, interrupted (a) before yield, $\varepsilon = 3.4\%$ (b) at yield, $\varepsilon = 5.6\%$ and (c) after yield, $\varepsilon = 11.6\%$.

also observed in the γ' precipitates of the microstructures from samples interrupted at yield for 750°C and above. At room temperature (Figure 4.5), at all levels of strain, no stacking faults were observed in the precipitates. The formation of stacking faults is a diffusion based mechanism and therefore requires thermal activation to operate. The prevalence of stacking fault shear may also be due to the misalignment of the tensile testing rig. A misalignment may facilitate the activation of multiple slip systems, increasing the chance of the necessary dislocation interactions for stacking fault shear. The formation of stacking faults is thought to occur by a vacancy-mediated reordering process.[73] A higher temperature enables greater vacancy diffusion which would facilitate stacking fault formation.

4.3.2 Effect of Composition on Tensile Deformation

Comparing the stress strain curves of CMSX-4 and TMS-138A, the yield stress is lower for TMS-138A. The difference in yield stress between these two alloys may be due to the difference in lattice misfit as well as the difference in alloy composition changing the energy required to form an APB in the γ' phase. Lattice misfit is covered first. TMS-138A has a higher degree of misfit compared to CMSX-4 ($\delta_{TMS-138A}$ = -0.37% at 1100 °C[175], compared to δ_{CMSX-4} = -0.23% at 1000 °C[41, 42]). A negative lattice misfit means the γ' has a smaller lattice parameter than the γ. This negative misfit forces the γ-phase into compression at the vicinity of the interface with γ', with compensating tensile stresses in the γ' (see Figure 4.12). Upon application of an external tensile stress, the local stresses are modified in the direction of the applied stress. The stress is higher in the horizontal channels than the vertical channels. This is reflected in the micrographs where most of the dislocation activity before yield is in the horizontal channels; the vertical channels remain relatively absent of dislocations. Similar behaviour has been simulated in primary creep deformation.[98]

When dislocations first form in the γ channels, they relieve the misfit stress. These dislocations fill the narrow γ channels and increase the back stress, the long range stress caused by the pile up of geometrically necessary dislocations. Over time, as more dislocations fill the channels, the back stress increases and these dislocations then repel further dislocations of the same Burgers vector from entering. Eventually, the stress becomes sufficiently high for dislocations to penetrate the γ' precipitates. The more negative lattice misfit for TMS-138A would mean the back stress increase is lower perhaps due to a lower number of dislocations packing into the γ channels.

It has also been suggested a more negative lattice misfit changes the dislocation network, which might be the cause of the different dislocation morphologies in the matrix of CMSX-4 versus TMS-138A.[121] Comparison of the two microstructures from specimens interrupted before yield shows the dislocations remain much more rigidly confined to the glide planes in TMS-138A, producing right angled shapes, compared to the wavier appearance of dislocations in CMSX-4. By 850 °C in CMSX-4, the dislocations adopt a wavier appearance, whereas even at 900 °C in TMS-138A, the dislocations continue to adopt more rigid configurations, confined to the $\{111\}$ glide planes. Comparing the composition of CMSX-4 and TMS-138A (see Chapter 3, Table 3.1), the more negative misfit of TMS-138A is thought to be due to the greater quantity of molybdenum. Molybdenum has a larger atomic radius and partitions to the γ phase.[71] TMS-138A also has higher amounts of Re and the addition of Ru. Additions of Re and Ru have been shown to make the lattice misfit more negative by the changes of partitioning ratios of alloying elements.[99, 147] Figure 4.13 shows how the addition of ruthenium changes the composition of the γ' phase in two alloys: PWA 1484 and 1497.[180] Both elemental additions improve the creep properties of superalloys though the actual mechanism from a dislocation dynamics perspective remains unclear. The comparison of the microstructures suggest the addition of Re and Ru may affect the dislocation behaviour within the channels, in turn inhibiting dislocation motion and creep deformation.

The difference in alloy composition may also affect the APB energy in γ' phase. A lower yield stress would suggest the APB energy in γ' is lower in TMS-138A than CMSX-4. Though the interplay between the different elemental composition changes is not analysed, studies have shown the effect of change to the APB energy on individual composition changes. The addition of Ru is reported to have no measurable effect on the APB energy.[122], whereas the addition of Re in γ' phase increaes the APB energy.[172] However, the addition of Mo can decrease the APB energy.[176] Fringes are also observed in the vertical γ channels of the microstructures of TMS-138A interrupted just after the yield point at room temperature and 750 °C. These fringes could be stacking faults, and were not observed in the microstructures produced from the same test conditions in CMSX-4. Similar stacking faults were observed in the γ channels of another fourth-generation superalloy, TMS-138, subject to low cycle fatigue (LCF) at 1073 K.[179] The presence of stacking faults is thought to be due to the higher lattice misfit and lower stacking fault energy in the γ phase for TMS-138A compard to CMSX-4. The higher lattice misfit results in a higher stress state in the horizontal channels, enabling the $\frac{a}{2}\langle 110\rangle$ dislocations to dissociate into two partials. The addition of ruthenium in TMS-138A is also thought to decrease the stacking fault energy in the γ phase.[167]

The yield stress is conventionally defined as the stress at which onset of plastic deformation occurs. However, as observed from Figures 4.2-4.4, the yield stress occurs at around 1% strain. This suggests the two-phase microstructure has undergone some plastic deformation by this point. The definition of 'yield' for single crystal superalloys therefore needs to be changed. Comparison of the microstructure before and after the maximum stress or 'yield point' shows that this corresponds to the penetration of dislocations into the γ', but that dislocation activity in the γ channels is evident before this point. The yield stress in this case corresponds to the stress at which dislocations enter into the γ' precipitates, resulting in a sharp change in gradient of the stress-strain curve. For the stress-strain curves obtained from tests at room temperature, 800 °C, 850 °C for CMSX-4 and 900 °C for TMS-138A, a substantial drop in stress is observed. When this is observed, the first change in gradient has been taken to be the yield point. Following the yield point, a drop in stress is observed. The deformation microstructures from samples interrupted at the yield point show stacking fault shear within γ' precipitates. Stacking fault shear requires a lower stress than APB shear which would explain the drop in stress observed just after the yield point.[117] In the microstructures interrupted at high levels of strain, a lot of dislocation pairs are observed in the γ' precipitates, with a lower proportion of stacking faults. The gradual stress increase due to work hardening after the drop in stress upon yield may result from an increasing proportion of the dislocations in the γ matrix channels shearing precipitates by dislocation pairs separated by an APB.

4.3.3 Drop in Stress After Yield

A drop in stress after yield was observed immediately after the high yield point for 800 °C and 850 °C for CMSX-4 and at 900°C for TMS-138A. This decrease was largest for tests at 850 °C and 800°C for CMSX-4, around 50 MPa at 800 °C and 75 MPa at 850 °C. A similar upper and lower yield stress has been observed in steels, attributed to locking and unlocking of dislocations from the solute atmosphere.[17] However, this mechanism is normally followed by the yield elongation and the formation of Luders bands, which is not observed in the stress strain curves of CMSX-4 or TMS-138A. The microstructures of the samples which exhibit a drop in flow stress upon yield correlate with the appearance of stacking faults within the microstructure at yield. Since the threshold stress to propagate precipitates by stacking fault shear is lower than that of APB shearing, the initiation of stacking fault shear may cause the drop in stress in the stress-strain curves.

The microstructures show that during the early stages of deformation, dislocations pack into the narrow γ channels. Up to the yield point, the stress is a response to the accommodation of

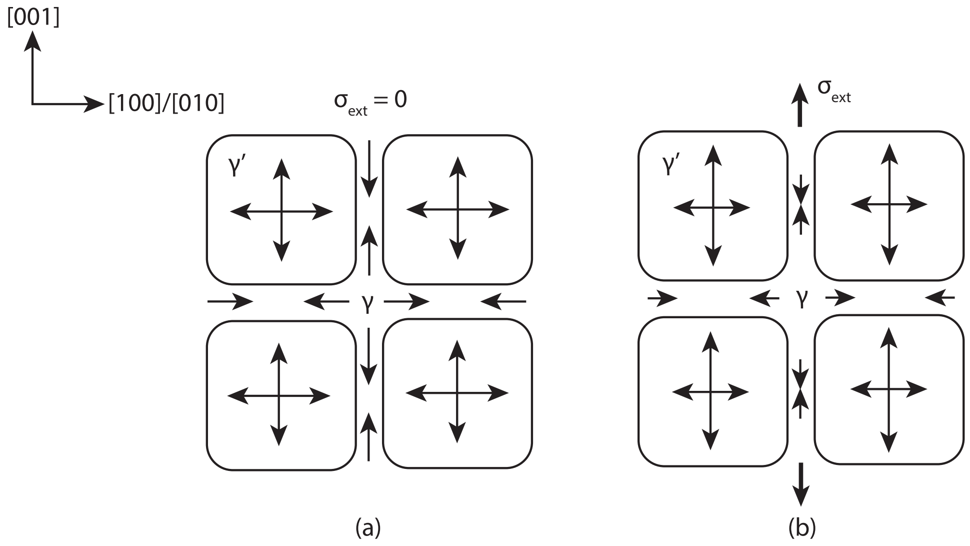

Figure 4.12 A negative misfit means that the γ' has a smaller lattice parameter than that of γ. The latter will therefore be in compression in the vicinity of the interface with γ', and there will be compensating tensile stresses in the γ'. (a) Illustration of the major components of the coherency stresses in the vicinity of the γ/γ' interfaces for a case where the misfit is negative. (b) The modification of the coherency stresses as a consequence of an externally applied tensile stress σ_{ext} in the vertical direction. Adapted from Kamaraj.[65]

further dislocations within the γ channels. When the stress on the γ/γ' interface is sufficiently high, the dislocations are able to penetrate into the γ' precipitates.

The yield point for all four curves for CMSX-4 and at 900 °C for TMS-138A occur above the yield points of samples tested in Chapters 5 and 6, that displayed a lower absolute stress at yield, no upper and lower yield point and a flatter work-hardening phase after the yield point. Before yield, it is hypothesised that dislocations propagate through the narrow γ channels. Upon further dislocations nucleating and being packed into the channels, the back-stress rises. Eventually, once a threshold stress is reached, these dislocations are able to overcome the pinning stress and penetrate into γ' precipitates. Observation of the microstructures of samples interrupted before yield, featured in this chapter, showed deformation associated with dislocations first propagating through the horizontal γ channels. A higher temperature would also result in climb of dislocations, allowing dislocations to reorient themselves within the narrow γ channels to accomodate a greater number of dislocations, resulting in a higher stress being reached before yield.

In CMSX-4, a high dislocation density is observed at all temperatures pre-yield. In contrast, TMS-138A deformed at 750 °C (see Figure 4.4) exhibited rapid work hardening after the yield point, a feature absent in the stress strain curves from tensile tests conducted at room

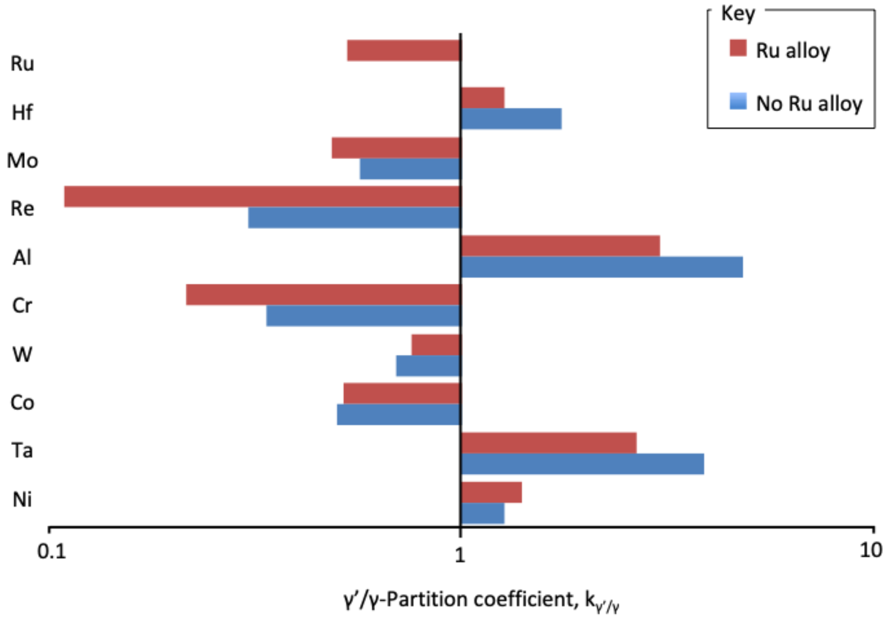

Figure 4.13 Elemental partitioning coefficients of two alloys: PWA 1484 (No Ru alloy) and PWA 1497 (Ru alloy), following creep tests at 982 °C and 248 MPa. The addition of ruthenium, which partitions preferentially to the γ phase, changes the composition of the γ' phase. γ' becomes enriched in W, Ta and Re, at the expense of Ni and Al. Adapted from Zietara[180].

temperature and 900 °C. Wang *et al.* observed similar rapid work hardening after yield at 750 °C and 650 °C for TMS-138A.[38] Comparison of the deformation structures suggest dislocations did not enter the precipitates until higher levels of strain at 900 °C compared to 750 °C. At the yield point, dislocation and precipitate interactions at 750 °C are solely through the formation of dislocations. This contrasts with the deformation structure at 900 °C where stacking faults are much more prevalent. It could be that the threshold temperature for stacking fault shear is higher in TMS-138A, leading to rapid work hardening after yield at 750 °C. The competition between APB shearing and stacking fault shearing is explored further in Chapter 5. The dislocations in the horizontal channels for 750 °C interrupted at the yield point (Figure 4.10(b)) are also quite distinct compared to the convoluted networks that were observed in the 900 °C 'at yield' microstructure (Figure 4.11(b)). This suggests the dislocation interactions with the γ/γ' interface could play a role in the yield point, perhaps governed by the lattice misfit changes with temperature.

4.3.4 Change in Gradient of the Stress-strain Curve

A subtle change is observed in gradient of the stress-strain curve at 750 °C for CMSX-4 and TMS-138A. For CMSX-4, this occurs just below 1200 MPa, compared to around 950 MPa for TMS-138A. This change in gradient was observed for all the interrupted tests though the change was not as severe for the test interrupted '*at yield*' (see Appendix). Tensile tests conducted in later chapters at 750 °C for CMSX-4 displayed a different shaped stress-strain curve. A comparison between the two curves is shown in Figure 4.14. One difference between the tests featured in this chapter versus later chapters is the area over which dislocation activity occurs. The deformation within the microstructure is spread more homogeneously compared to the later tests, which show distinct, narrow slip bands (see Chapter 5). This could be a result of the misalignment of the tensile testing machine. The misalignment would activate multiple slip systems within the specimen. This would also allow for greater strain to be accommodated in the γ channels prior to yielding.

Alignment of the specimen within the grips of the tensile testing machine may also be a factor. If the tensile direction was not directly through the vertical axis of the tensile specimen, slip might become active in other slip systems. Stacking faults were observed within the microstructure shortly after yield. Stacking fault shear is a low stress mechanism and requires the dissociation of $\langle 110 \rangle$ dislocations into $\langle 112 \rangle$ pairs. The threshold stress for this dissociation to occur is lower than shearing by pairs of $\langle 110 \rangle$ dislocations bounding an APB. Misalignment may have caused non-uniform stresses across the specimen in secondary

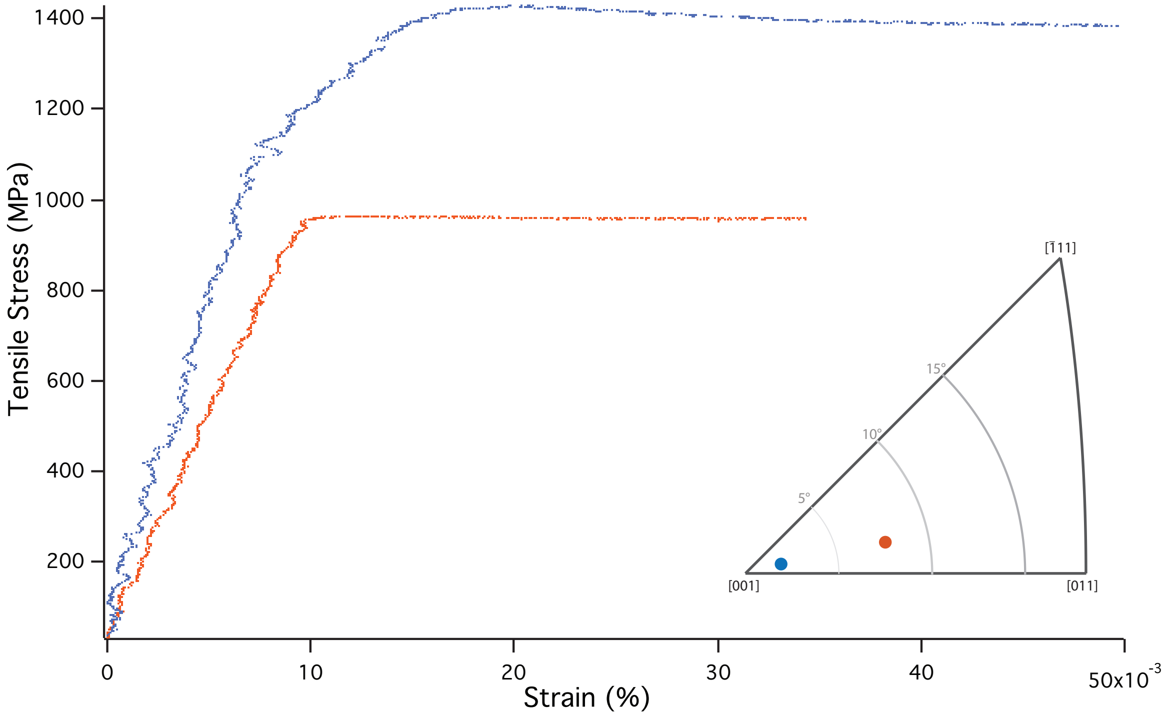

Figure 4.14 The stress-strain curves for two samples of CMSX-4 in two different orientations, deformed at $\dot{\varepsilon} = 10^{-4} s^{-1}$ and 750 °C, showing different stress and strain behaviour.

slip systems, facilitating the formation of stacking faults, or more localised deformation through APB shearing.

4.4 Conclusion

Two superalloys CMSX-4 and TMS-138A were tensile tested at different temperatures and their microstructures analysed to understand the effect temperature and composition have on tensile deformation. For both superalloys, the yield stress was higher at higher temperatures, though for CMSX-4, the highest yield stress occurred at 800 °C and dropped at 850 °C. TMS-138A had a lower yield stress than CMSX-4 at 750 ° but the temperature of peak yield stress seems to be higher. The microstructures showed significant dislocation activity in the γ channels prior to yield. The morphology of these dislocations changed on increasing the temperature, with wavier dislocation networks observed at higher temperatures for CMSX-4. These dislocation networks may act as barrier for dislocations to penetrate γ' precipitates, resulting in higher yield stresses at higher temperatures. The γ-matrix dislocations in TMS-138A were more resistance to climb, thought to be due to the higher lattice misfit, a result of the additional Ru and Re in TMS-138A compared to CMSX-4. The alloy composition difference between TMS-138A and CMSX-4 may also lower the APB energy in TMS-138A, with addition of Ru and the higher at.% of Mo and Re potentially having the most impact. An increase in the prevalence of stacking fault shear was seen at higher temperature in both superalloys. The higher temperature is thought to facilitate vacancy motion and reordering, both diffusion-mediated processes. There were some anomalous features of the stress strain curves, namely a drop in stress after the yield point and a change in gradient within the 'elastic' portion of the curve. Both of these are attributed to misalignment of the tensile testing machine or effect of misorientation away from the [001] tensile axis, leading to multiple slip system activation and irregular deformation features.

Chapter 5

The Effect of Strain Rate on the Tensile Deformation Behaviour of Single Crystal, Ni-based Superalloys

5.1 Introduction

Historically, mechanical tests have been separated into three main categories: creep, tensile and fatigue. From a macroscopic perspective, the deformation associated with each of these tests results in significantly different mechanical behaviour and fracture surfaces. The dislocation-precipitate interactions which govern such macroscopic behaviour is highly dependent upon alloy chemistry, crystal orientation, temperature, stress, γ-channel width and γ' precipitate size and morphology. At low temperature and high stresses, shearing of γ' precipitates occurs via the coupled motion of paired $\frac{a}{2}\langle 110\rangle$ dislocations, known as anti-phase boundary (APB) shearing. At high temperatures ($> 800\,^{\circ}\mathrm{C}$) and low stresses, individual, unpaired $\frac{a}{2}\langle 110\rangle$ dislocations are able to bypass γ' precipitates by thermally activated climb.[126] In between these processes, other precipitate shearing mechanisms have been identified such as microtwinning or formation of superlattice stacking faults.

Despite the number of studies on the specific deformation mechanisms, the transitions have been seldom investigated. It has been shown that changing the strain rate can affect the deformation mechanism for tensile deformation. In a directionally solidified (DS) new Ni-Co superalloy, a drop in strain rate has been shown to induce shearing of the γ' precipitates by stacking faults (SFs) [20]. This was attributed to the low stacking fault energy caused by the addition of high amount of cobalt ($> 20\%$). Smith *et al.* have shown that an increase in titanium, tantalum and niobium content of a superalloy can control the transition between stacking fault shearing and microtwinning.[132] In addition, in polycrystalline Ni-based superalloys and steels, the decrease in strain rate is also accompanied by a transition from stacking fault formation to microtwinning.[74]

However, the transition from tensile deformation to creep-like deformation as well as the presence of a threshold value has not been extensively studied and therefore will be investigated in detail in this chapter. This work aims to show that creep deformation and tensile testing form a continuum. This should in turn improve the understanding of the deformation mechanism as well as the interplay between tensile and creep properties of nickel-based superalloys.

CMSX-4, a second-generation Ni-based superalloy, was used in this chapter's experiments due to its wide use in turbine blade applications. In addition, to further investigate how alloy composition influences the effect of strain rate on tensile deformation, two other single crystal nickel-based superalloys were tested: SRR99 and TMS-138A. SRR99 is a high diffusion first-generation superalloy, TMS-138A is a fourth-generation superalloy. CMSX-4 exhibits a peak yield stress at 750 °C and therefore this was chosen as a benchmark temperature to conduct and compare these tensile tests. Two strain rates were chosen: $10^{-4}\,\mathrm{s}^{-1}$ and $10^{-6}\,\mathrm{s}^{-1}$. The first is the same strain rate as featured in Chapter 4, the second is two orders of magnitude slower and would highlight any features caused by slowing the strain rate.

5.2 Results

5.2.1 Tensile Stress-strain Curves and Corresponding Microstructures

Figure 5.1 shows the stress-strain curves obtained from tensile tests on specimens of CMSX-4, tested to failure at 750°C for three different strain rates, $\dot{\varepsilon}$: $10^{-2}\,\mathrm{s}^{-1}$ (the green curve), $10^{-4}\,\mathrm{s}^{-1}$ (the red curve) and $10^{-6}\,\mathrm{s}^{-1}$ (the blue curve). The orientations of each specimen are shown in the inverse pole figures with corresponding colours.

All curves show a linear progression up to around 950 MPa. The curves then plateau for varying portions of strain. The plastic strain induced at this point is around 1%. Beyond this point, the three curves exhibited different behaviours. The tensile curve from the test at 10^{-2} s^{-1} increased in stress around 4% strain to 1000 MPa before plateauing again to 9% strain, at which point the stress increased at a gradual incline, before failure around 15% strain. The tensile curve produced from the tensile test at $10^{-4}\,\mathrm{s}^{-1}$ maps a similar path to the tensile test at $10^{-2}\,\mathrm{s}^{-1}$, but after increasing in stress around 4% strain to 1000 MPa, the stress doesn't

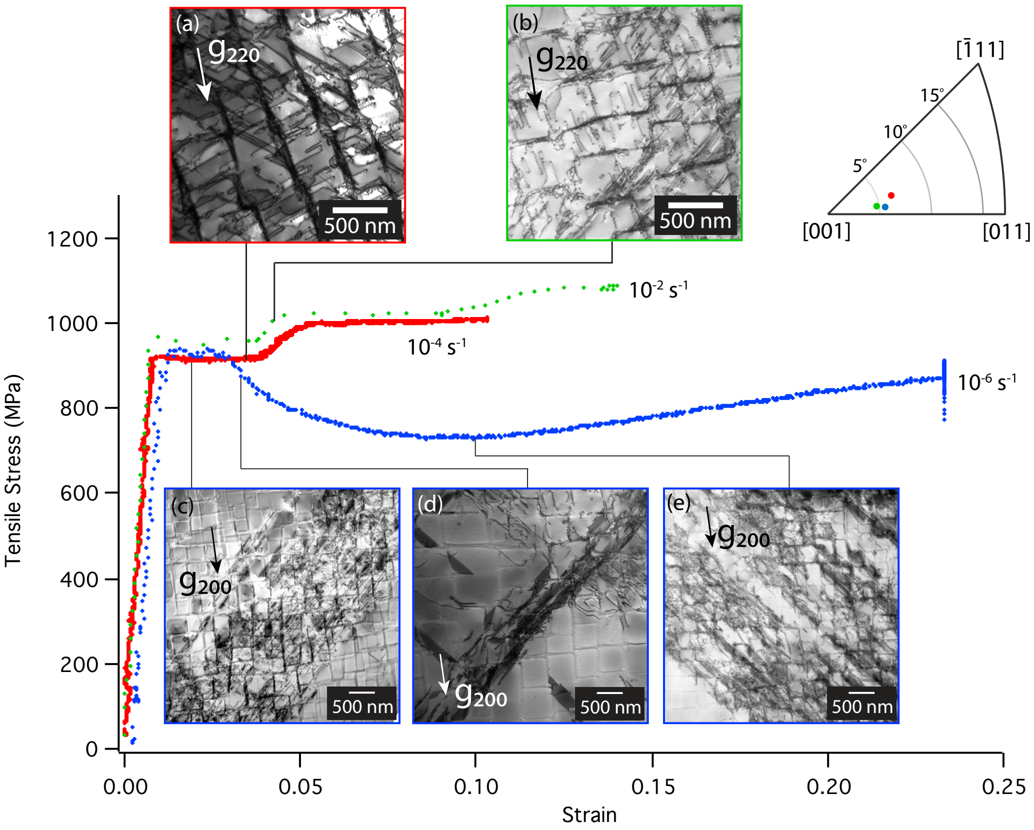

Figure 5.1 Tensile stress-strain curves of CMSX-4 deformed at 750 °C at three different strain rates, $\dot{\varepsilon}$: $10^{-2}\,\mathrm{s}^{-1}$ (the green curve), $10^{-4}\,\mathrm{s}^{-1}$ (the red curve) and $10^{-6}\,\mathrm{s}^{-1}$ (the blue curve). All samples were tested to failure, presented as stress σ vs. strain ε. (a) A TEM micrograph with two beam contrast, **g** = (220) from a tensile specimen tested at a strain rate $\dot{\varepsilon} = 10^{-4}\,\mathrm{s}^{-1}$, interrupted at 3.3% strain. (b) TEM micrograph with two beam contrast, **g** = (220) from a tensile specimen tested at a strain rate $\dot{\varepsilon} = 10^{-2}\,\mathrm{s}^{-1}$ interrupted at 4.8% strain. (c-e) TEM micrographs with two beam contrast, **g** = (200) from a tensile specimen tested at a strain rate $\dot{\varepsilon} = 10^{-6}\,\mathrm{s}^{-1}$. (c) The deformation structure interrupted at 1.2% strain. (d) The deformation structure interrupted at 2.7% strain. (e) The deformation structure interrupted at 10.2% strain. Inset: an inverse pole figure showing the orientations of the three specimen tested to failure in relation to the [001] tensile direction.

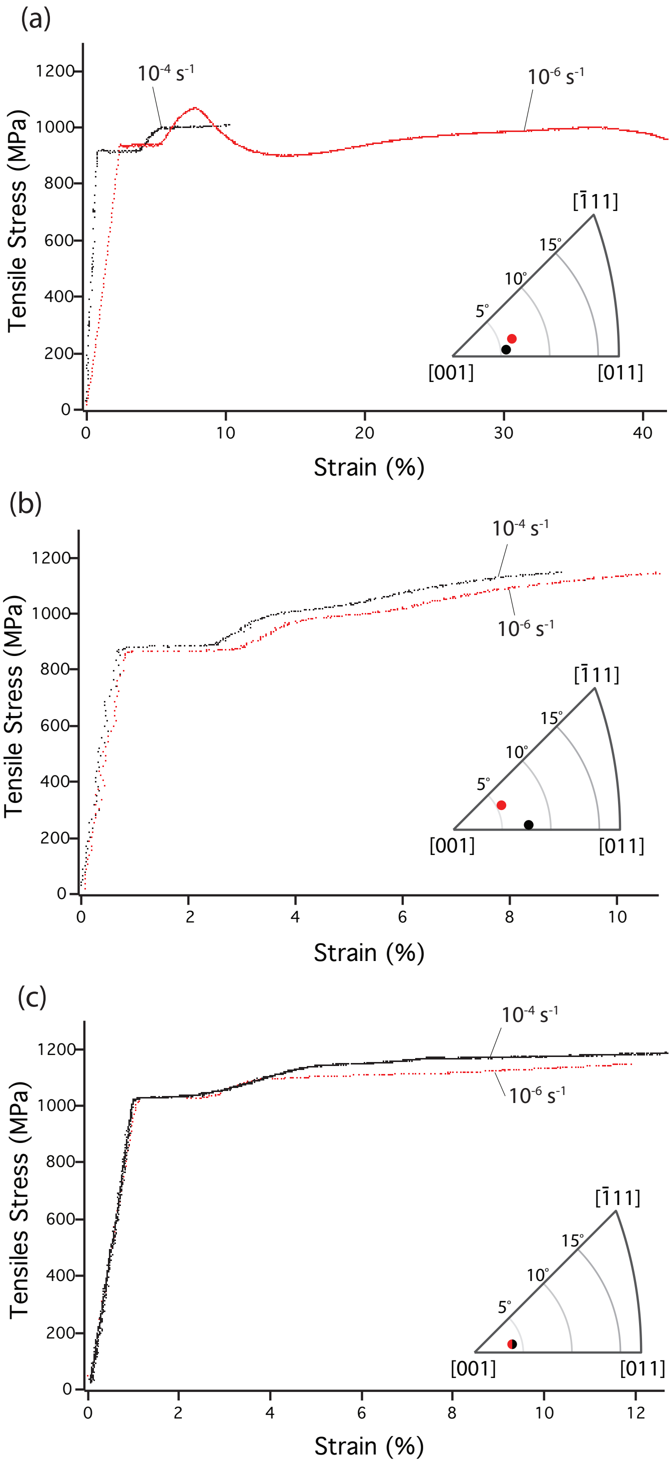

Figure 5.2 Tensile stress-strain curves for (a) CMSX-4, (b) TMS-138A and (c) SRR99, all tested at 750 °C to failure at two strain rates: $10^{-4}\,\mathrm{s}^{-1}$ (black curve) and $10^{-6}\,\mathrm{s}^{-1}$ (red curve). Inset: inverse pole figures showing the orientations of the respective specimens in relation to the [001] tensile direction.

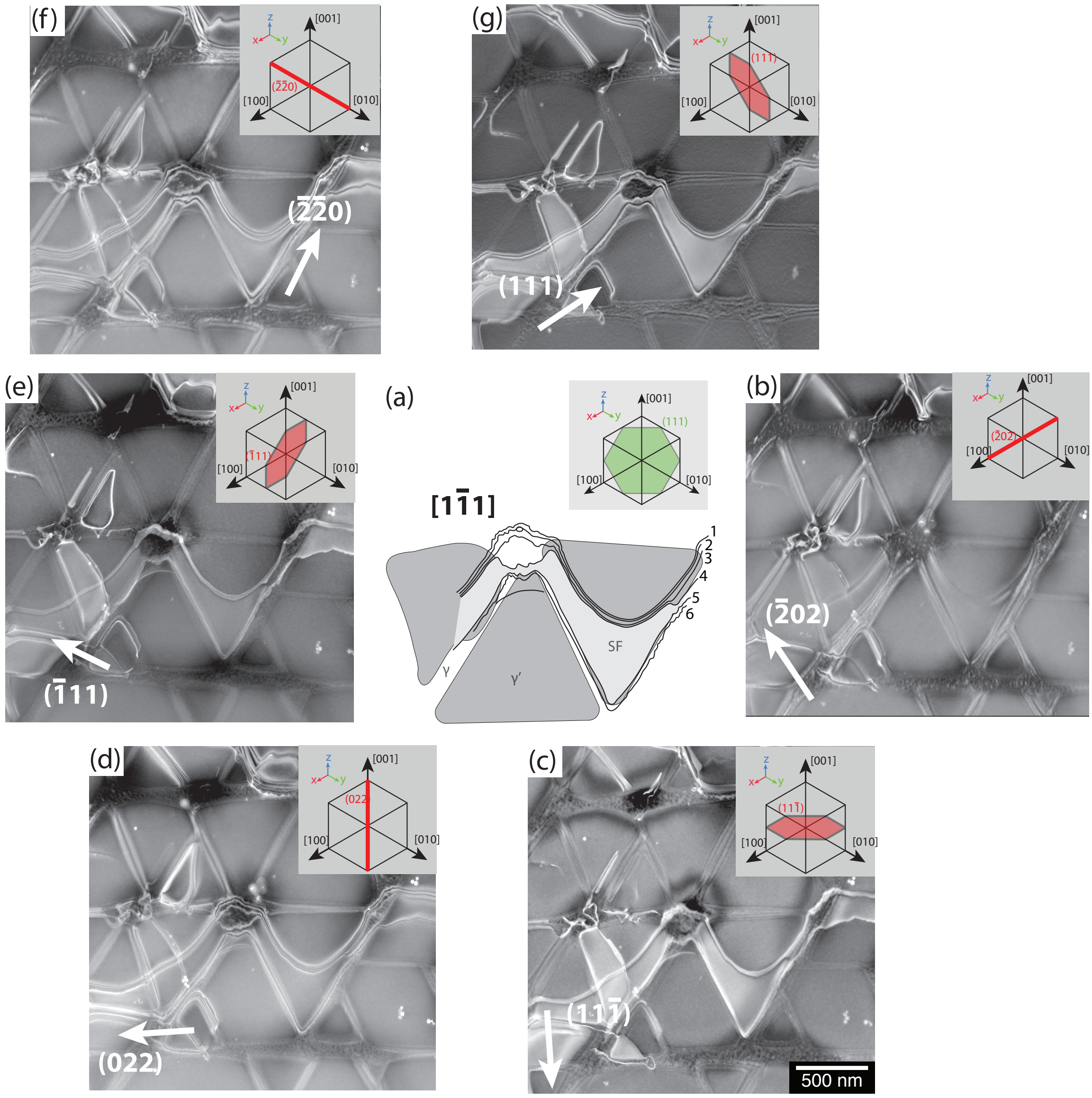

Figure 5.3 STEM micrographs of the microstructure from a CMSX-4 tensile specimen deformed at a strain rate of $10^{-6}\,\mathrm{s}^{-1}$ to 2.7% strain, at 750 °C, cut on the $(1\bar{1}1)$ plane. All sub figures are taken over the same area of the sample. Starting at the centre and then right, going clockwise: (a) A schematic illustration of the dislocation structure, down the $[1\bar{1}1]$ zone axis. (b) Two beam contrast, $\mathbf{g} = (\bar{2}02)$. (c) $\mathbf{g} = (11\bar{1})$. (d) $\mathbf{g} = (022)$. (e) $\mathbf{g} = (\bar{1}11)$. (f) $\mathbf{g} = (\bar{2}\bar{2}0)$. (g) $\mathbf{g} = (111)$. Highlighted planes which are parallel to the electron beam are shown in inset of each subfigure.

increase any further. Failure occurs in comparison at a much lower strain rate of 11.5%.
The tensile curve from the tensile test at $10^{-6}\,\mathrm{s}^{-1}$ exhibited the shortest plateau; the stress remains at 950 MPa to around 3% strain before the stress drops and continues to do so down to 750 MPa at around 8% strain. After this, the stress rises again, at a slower rate, before failing around 23% strain.

Further tests were run at the three different strain rates and interrupted at various points before failure. For the strain rate at $10^{-2}\,\mathrm{s}^{-1}$, another tensile test was run and interrupted at 3.3% strain. Another tensile test was run at $10^{-4}\,\mathrm{s}^{-1}$ to 4.8% strain. Three further tests were run at the strain rate: $10^{-6}\,\mathrm{s}^{-1}$, interrupted at strains of 1.2%, 2.7% and 10.2%. Since the tensile specimens showed varying degrees of orientation away from the [001] direction, available specimen were grouped into similar orientations to minimise the effect of orientation. Tests were interrupted at specific strain levels where the curves exhibited discontinuities. The interrupted stress strain curves overlap consistently with tensile tests run to failure. The tensile curves associated with these interrupted tests can be found in the appendix. A third interrupted test was run to 10.2% but the stress strain curve was not recorded due to instrument failure.

TEM foils were produced from these interrupted test specimens of CMSX-4 and imaged to understand the progression of the deformation structure. Figure 5.1(a) shows a TEM micrograph imaged a couple of degrees tilt away from the [001] zone axis, with two-beam contrast $\mathbf{g} = (220)$. The tensile specimen was tested at a strain rate $10^{-4}\,\mathrm{s}^{-1}$, at 750 °C, interrupted at 3.3% strain. Dislocations are present in both the γ and γ' phases. The dislocations in the γ' precipitates have adopted various configurations. Figure 5.1(b) is a TEM micrograph from a sample deformed at a higher strain rate $10^{-2}\,\mathrm{s}^{-1}$ also at 750 °C. It was interrupted at a slightly higher strain, 4.8%. The dislocation structure is similar to that of Figure 5.1(a), with dislocations present in γ' precipitates and γ channels.

The TEM micrographs for interrupted specimens at the slowest strain rate, $10^{-6}\,\mathrm{s}^{-1}$ are shown in Figure 5.1(c-e). Interrupted at 1.2% strain (Figure 5.1(c)), the tensile specimen has reached a stress plateau. Dislocations are confined to distinct slip bands, with some areas of the microstructure free of any dislocations. At 2.7% strain (Figure 5.1(d)), stacking faults appear in the slip bands. Portions of the microstructure still remain free from dislocations. The stress continues to drop and the TEM micrograph interrupted at 10.2% and around the lowest stress (Figure 5.1(e)) shows these slip bands have widened to cover more of the microstructure.

Tensile tests were also run for two further alloys: TMS-138A and SRR99, across two strain rates: $10^{-4}\,\mathrm{s}^{-1}$ and $10^{-6}\,\mathrm{s}^{-1}$. The tensile curves are shown in Figure 5.2. The respective orientations for each tensile specimen are shown on the inverse pole figure inset of Figures 5.1 and 5.2.

To further investigate the stacking faults observed in the Figure 5.1(d) and (e), Laue back-reflection method was used to determine the primary slip system of the tensile specimens. This allowed for precise sectioning of the specimen; first parallel and then perpendicular to the slip system on which the stacking faults were present. Conventional TEM imaging was performed on specimens cut parallel to the primary slip system, exposing the stacking faults within the plane and dislocations that bound such faults.

Figure 5.3 shows the microstructure of the tensile specimen deformed at a strain rate of $10^{-6}\,\mathrm{s}^{-1}$ to 2.7% strain, cut on the $(1\bar{1}1)$ plane, the active slip system. In the middle, Figure 5.3(a), is a schematic illustration of the dislocation structure. It shows a stacking fault spread on the $(1\bar{1}1)$ plane, bound by a total of six dislocation lines, four on one edge, two on the other, shearing a γ' precipitate. The dislocations cross both γ' precipitates and the γ-channels and seem to progress faster in the channels than the precipitates.

To determine the Burgers vectors of the dislocations that are part of this faulted structure, Burgers vector analysis was conducted, comparing the six different two-beam conditions around the $[1\bar{1}1]$ zone axis. The surrounding six images are STEM micrographs taken under six different two-beam conditions, at different degrees of rotation away from the $[1\bar{1}1]$ zone axis. The white arrows in each of the subfigures are the g-vectors, pointing in the direction of the respective reciprocal lattice planes. Through tilting the sample to varying degrees away from the $[1\bar{1}1]$ zone axis, the red planes in the subfigure can be aligned parallel to the electron beam. Any dislocations on these planes would therefore have no impact on the transmission electron beam ($\mathbf{g}\cdot\mathbf{b}=0$) and appear invisible on the STEM micrograph under that respective two-beam imaging condition. By tilting the sample to the six different two-beam conditions of Figure 5.3, it is possible to deduce the Burgers vectors of the dislocations that bound the stacking fault.

The six dislocations are labelled 1-6. The six dislocations are marked on a 3-point scale of visibility: i (invisible), w (weak, visible but not prominent) and v (visible). Going through each of the six micrographs, it can be deduced that the dislocations have a Burgers vector [121]. The corresponding visibility table is shown in Table 5.1. Under the $\mathbf{g}=(\bar{2}02)$ imaging condition, the dislocations are not visible. Under other conditions, some of the dislocations appear as single dislocations; it is not possible to establish whether they are superpartials or dissociated partials.

Table 5.1 Visibility table for the dislocations labelled in Figure 5.3, from a CMSX-4 tensile specimen deformed at a strain rate of $10^{-6}\,\mathrm{s}^{-1}$ at 750 °C. Dislocations in g-conditions labelled '*' are not clear due to dislocation interactions and strain contrast. [i= invisible, w= weak, v= visible.]

g	$[\bar{1}11]$	$[11\bar{1}]$	$[111]$	$[\bar{2}\bar{2}0]$	$[022]$	$[\bar{2}02]$	Burgers vector
1	w*	v	v	v	v	i	[121]
2	v	v	w	v	v	i	[121]
3	i/w*	i/w*	v	v	v	i	[121]
4	i/w*	i/w*	w	v	v	i	[121]
5	v	v	v	v	v	i	[121]
6	v	v	v	v	v	i	[121]

To understand the atomic structure of these dislocations and stacking faults, the tensile sample was cut on the (110) plane so that the Burgers vectors of the dislocations bound either side of a shearing stacking fault would have its maximum edge component perpendicular to the cut plane. Cutting on this plane would also more accurately establish the magnitude of the Burgers vectors of the dislocations.

Figure 5.4 shows a HAADF-STEM image of a stacking fault captured edge-on, down the [110] zone axis. A fault can be seen propagating from right to left with the leading dislocation highlighted in the HAADF condition. Tertiary γ' precipitates in the γ-channel are also visible. Lattice imaging of the leading dislocation was carried out on the leading dislocation structure and presented in Figure 5.5(a). The stacking fault's location corresponds to the region which has a slightly higher contrast to the background, although to highlight it further, a Centre of Symmetry analysis was performed from the processed image, and is presented in Figure 5.5(b). The imaged stacking fault is propagating from right to left. It shows a two-layered, intrinsic fault (SISF) terminating as a three-layered, constricted extrinsic fault (CESF-2), all within a γ' precipitate.

The Burgers circuit traced around the fault segment requires a displacement vector of **b**=$\frac{a}{4}[\bar{1}12]$ in the observed plane. This is consistent with a dissociated pair of partials in the γ' of $\frac{a}{6}\langle 112\rangle$. The observed configuration shows the leading $\frac{a}{3}\langle 112\rangle$ superpartial dissociated into two identical $\frac{a}{6}\langle 112\rangle$ Shockley partials separated by a complex stacking fault lying on adjacent planes. Calculating the number of atoms at the bottom of the fault, the distance separating these two Shockley partials is approximately 13 lattice spacings.

Figure 5.6(a) shows a stacking fault propagating from right to left. The leading edge of the faulted structure is labelled region 'A', with a portion of the trailing fault labelled region 'B'. EDX maps were collected over regions A and B, in an interval of 2.5 nm with drift correction in place, to check for evidence of chemical variation at and around the stacking faults. The corresponding STEM-HAADF micrographs of regions A and B are shown in Figures 5.6(b) and 5.6(h) respectively. The compositional EDX maps for region A for the elements Cr, Co, Al, W and Ni are shown in Figure 5.6(c-g). The EDX maps for region B are shown in Figures 5.6(i-m).

Figures 5.6(c) and 5.6(d) show segregation of chromium and cobalt at the front-end of the fault. There seems to be a depletion of Al and Ni directly below the fault (Figure 5.6(d) and (f)), and Figure 5.6(e) shows a slight enrichment of W at the fault, though this is not as pronounced as the chromium and cobalt. Chromium and cobalt segregation is also observed along the length of the fault (Figures 5.6(i) and 5.6(j)). There is also a depletion of Al (Figure 5.6(k)). This depletion occurs along the length of the fault despite the HAADF image showing non-uniform brightness across the length of the fault. It is not clear whether W is segregating to or away from the fault. To get a perspective of the relative enhancement of elements at the fault, EDX line scans were taken through the fault region. These are shown in Figure 5.7. It shows chromium and cobalt are enriched by around 2 at.%.

EELS mapping was also conducted in a region containing the middle part of a stacking fault and the adjacent area. Compositional maps were taken corresponding to the Cr $L_{2,3}$, Co $L_{2,3}$ and Ni $L_{2,3}$ edges and are shown with the STEM-HAADF survey image in Figure 5.8. An enrichment of chromium and cobalt and a depletion of Ni along the fault is just about visible, though the segregation to the fault is not as pronounced as in the EDX images. The images nevertheless support the EDX maps of Figure 5.6, that segregation of chromium and cobalt occurs to the stacking fault in this sample.

5.3 Discussion

5.3.1 Features of the Stress-strain Curves

The stress strain curves from specimens tested at strain rates of $10^{-2}\,\mathrm{s}^{-1}$ and $10^{-4}\,\mathrm{s}^{-1}$ show linear deformation up to a yield point around 950 MPa. At the yield point, 1% strain is in the material. Upon yield, the interfacial dislocations, which until this point are packed into the γ channels and pinned up against the γ/γ' interfaces, experience a high enough stress to penetrate into the γ' precipitates. The maximum stress corresponds to the stress needed for

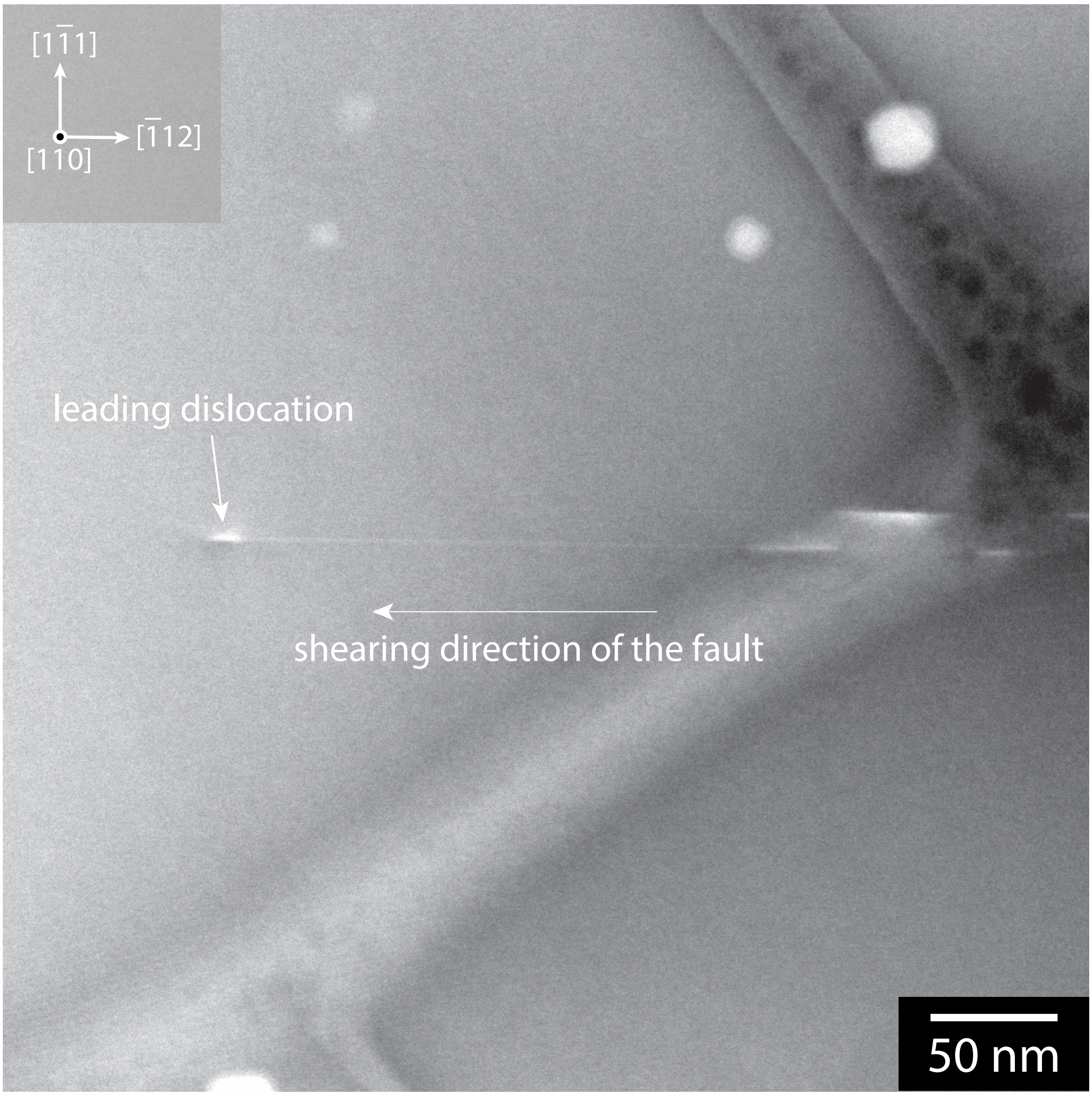

Figure 5.4 A HAADF-STEM micrograph of a stacking fault imaged down the $[110]$ zone axis from a tensile specimen of CMSX-4, deformed at 750 °C at a strain rate of $10^{-6}\,\mathrm{s}^{-1}$ interrupt at 2.7% strain. A stacking fault can be seen propagating from right to left, with the leading dislocations highlighted.

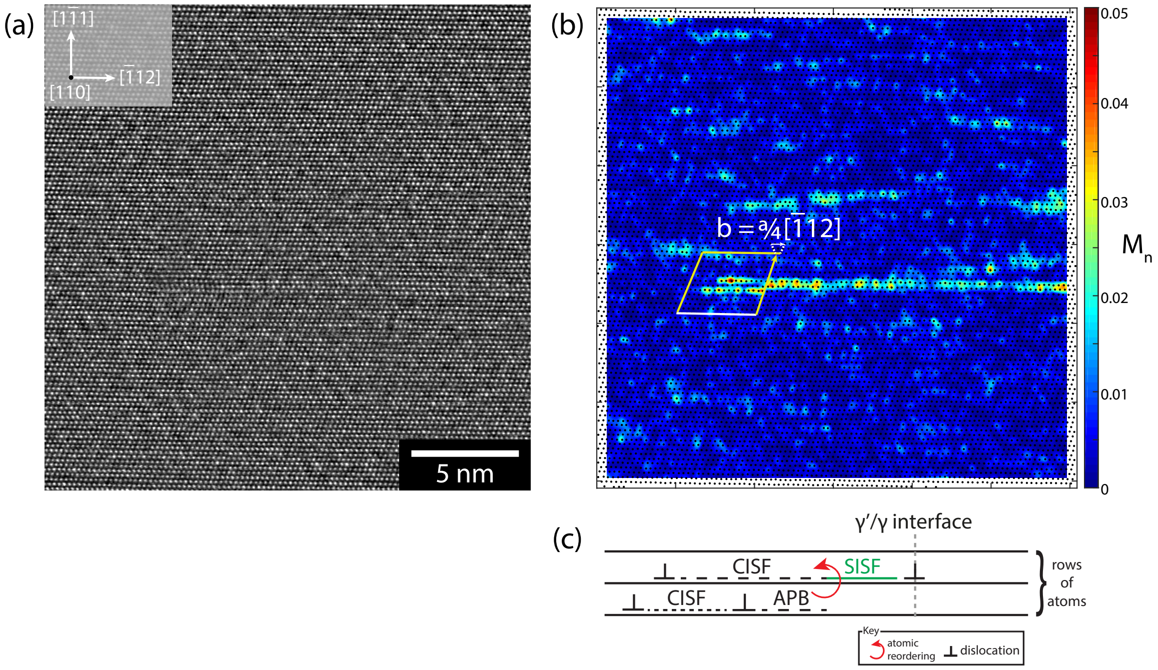

Figure 5.5 (a) A low magnification HRSTEM image of a stacking fault from a tensile sample of CMSX-4 tested at 750 °C at a strain rate $\dot{\varepsilon} = 10^{-6}\,\mathrm{s}^{-1}$, interrupted at 2.7% strain. The sample has been cut on the (110) plane. The stacking fault is viewed edge on and can be seen in both the γ' precipitate and γ channel. (b) The corresponding Centre of Symmetry (CoS) mapping with Burgers circuit shows a fault which is spread over two layers. (c) A schematic illustration of the hypothesised mechanism for the formation of the leading edge of the stacking fault. A CESF-2 converts into a lower energy SISF by a reordering process.

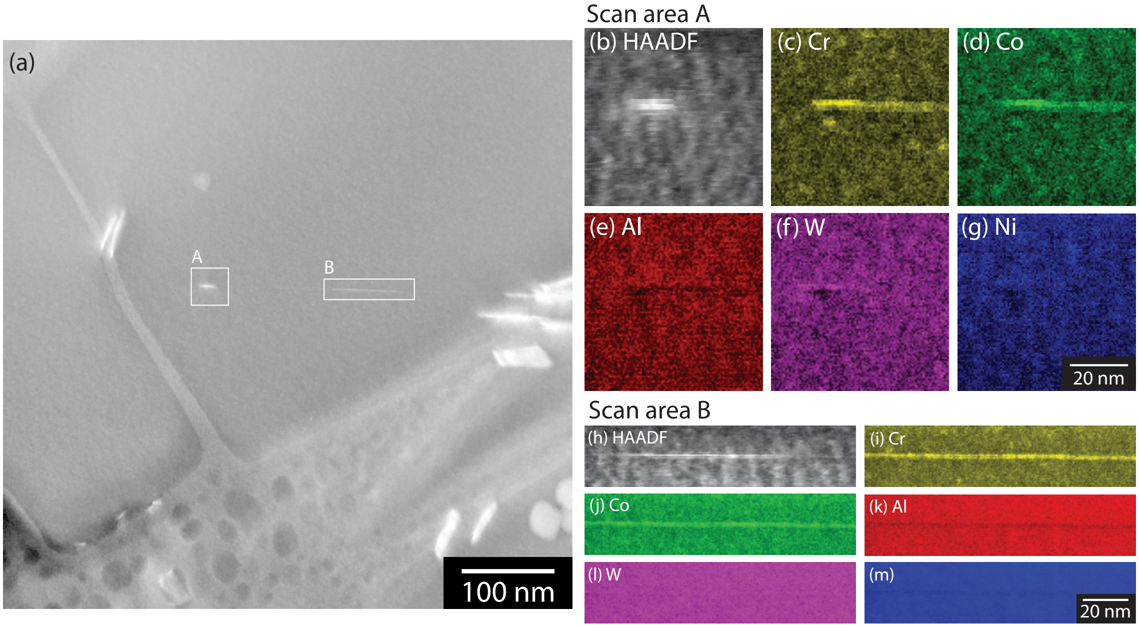

Figure 5.6 EDX maps showing spatial distributions of the elements Cr, Co, Al, W and Ni, taken over two regions of the microstructure from a sample of CMSX-4 deformed at a strain rate of $10^{-6}\,\mathrm{s}^{-1}$ at 750 °C, interrupted at 2.7% strain. (a) A STEM-HAADF micrograph imaged down the [110] zone axis, showing a stacking fault in a γ' precipitate. The EDX scans were taken from the front of the fault and a section midway along the fault, labelled as scan regions ’A’ and ’B’ respectively. (b) A HAADF image of the zoomed-in region ’A’, (c)-(g) show the elemental EDX maps from region A for the elements Cr, Co, Al, W and Ni respectively. (g) shows a HAADF image of the zoomed-in region ’B’, (i)-(m) show the elemental EDX maps for region B for elements Cr, Co, Al, W and Ni respectively.

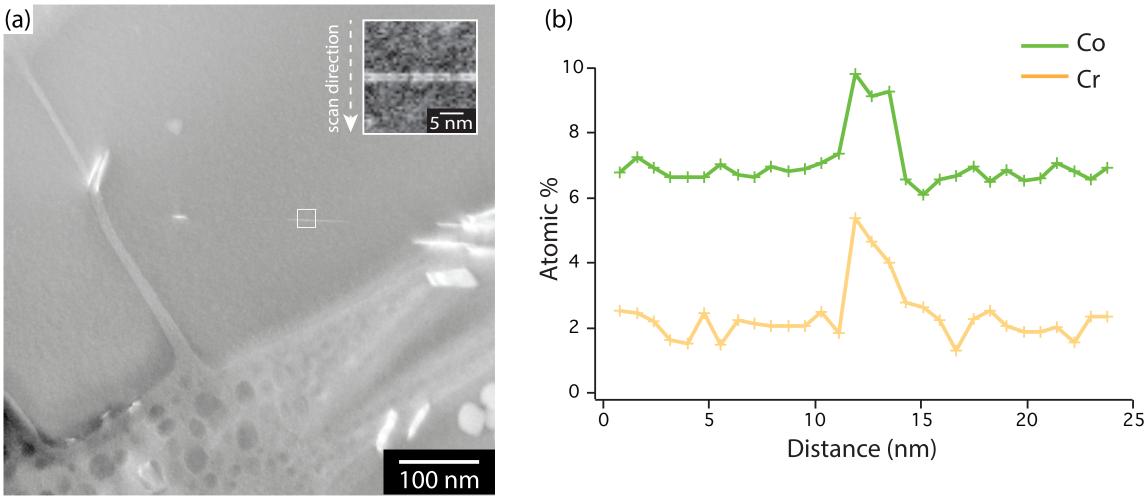

Figure 5.7 EDX line scan of a stacking fault in CMSX-4. (a) A HAADF STEM image viewed down the [110] zone axis shows the position of the line scan relative to the fault and (b) EDX plots show concentration of chromium and cobalt at the fault.

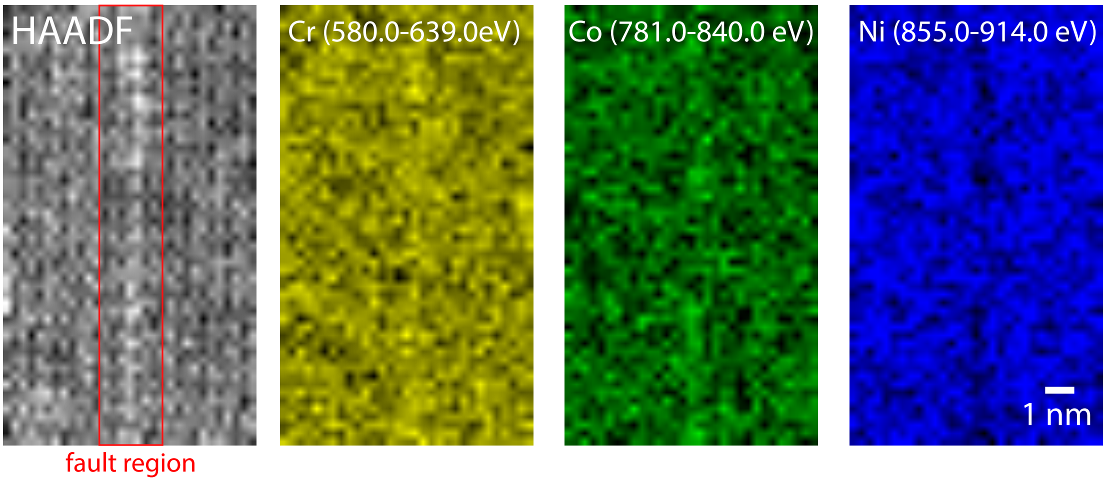

Figure 5.8 STEM-EELS mapping of composition in the vicinity of a stacking fault. (a) STEM-HAADF survey image of the stacking fault and adjacent area used for EELS mapping. (b-d) Compositional maps corresponding to Cr $L_{2,3}$, Co $L_{2,3}$ and Ni $L_{2,3}$ edges respectively.

dislocations to enter into the precipitates. Dislocations flow through the γ channels and γ' precipitates, and some segments of dislocations get locked in a certain configuration in the precipitates. As the proportion of locked dislocations increases, the slip system becomes blocked up and dislocations need to find cleaner areas of the microstructure to slip within. As more slip planes become filled, the slip bands expand.

Figure 5.2 shows the pre-yield behaviour and yield point is almost independent of strain rate. However, the yield point is different depending on the alloy. TMS-138A has a yield point stress slightly lower than CMSX-4. SRR99 had the highest yield stress. As shown in Chapter 4, the yield point corresponds to dislocations entering into γ' precipitates. The lattice misfit between the γ and γ' phases may also affect the yield point.

5.3.2 Stacking Fault Shearing

There are two competing deformation mechanisms for shearing precipitates, and in turn the plastic deformation of single crystal Ni-based superalloys: APB shearing and stacking fault shearing. The stacking fault shear mechanism takes less stress compared to APB shearing but requires diffusion to activate and so at low temperature APB shearing is the default deformation mechanism. At a higher temperature or lower temperature, stacking faults are observed in the γ' precipitates, as shown in both Chapter 4 and in this chapter in Figure 5.1(d) and (e).

The strain rate is related to the dislocation density by Equation 5.1, where ρ is the dislocation density, b is the Burgers vector of the dislocations and v is the average velocity of the dislocations. Since there are two competing processes by which dislocations can shear precipitates, Equation 5.1 can be modified to Equation 5.2:

$$\dot{\varepsilon} = \rho b v \tag{5.1}$$

$$\dot{\varepsilon} = \rho_{APB}\, b_{APB}\, v_{APB} + \rho_{SF}\, b_{SF}\, v_{SF} \tag{5.2}$$

The threshold stress required for APB shearing is higher and this component will dominate at high strain rates and low temperatures. The stacking fault shear portion of the expression will be favoured at slow strain rates and high temperatures.

At the slowest strain rate: $\dot{\varepsilon} = 10^{-6} s^{-1}$ (the blue curve in Figure 5.1), during the elastic region of the curve, dislocations are packing into the γ channels. At yield, the stress is high enough that these dislocations that are pinned up against the γ/γ' interface enter into γ'

precipitates. At this stage, deformation proceeds by APB shearing. Upon further deformation, a second slip system becomes active, as shown by two bands of dislocations in Figure 5.1(d), and these slip bands are perpendicular to each other. The interaction of dislocations in these two slip systems facilitates the formation of stacking faults and stacking fault shearing begins to occur. As strain increases, a greater proportion of the strain is accommodated by stacking fault shear, and the flow stress decreases.

The threshold stress to propagate a stacking fault through the precipitate is lower than the yield stress of 900 MPa for the stress strain curves in Figure 5.1.[116] Therefore, once a proportion of the precipitates is sheared by stacking faults, the flow stress decreases. As strain within the sample increases, more dislocations will shear by the formation of stacking fault ribbons as opposed to APB shearing. In the tensile test conducted at the strain rate $10^{-6}\,\mathrm{s}^{-1}$, the flow stress drops down to around 700 MPa (see the blue curve in Figure 5.1). This is roughly the stress at which primary creep by a stacking fault mechanism would occur.[116] Beyond this point, as these dislocations begin to entangle, gradual work hardening occurs until failure.

5.3.3 Formation of a SESF Terminating in the γ'

The stress-strain curves and associated microstructural analysis show the formation of stacking faults is a strain-rate-dependent phenomenon. Figure 5.5 shows the leading edge of the fault featured in Figure 5.4 consists of a SISF in a γ' precipitate, terminating in a two-layer CESF-2 type fault. The dissociation of the Shockley partials bounding this complex stacking fault is so small that it is not conclusive in Table 5.1, following the Burgers vector analysis of Figure 5.3.

This fault structure has been previously observed in samples deformed under primary creep at intermediate temperatures (750 °C).[158, 159] The structure of these dislocation ribbons has been extensively studied. The a$\langle 112\rangle$ fault ribbons are dissociated into partial dislocations enclosing a low-energy superlattice intrinsic or extrinsic fault (SISF and SESF respectively) as shown in equation 5.3:

$$\begin{aligned}2\times\frac{a}{2}[1\bar{1}\bar{2}] \rightarrow \frac{a}{6}[\bar{1}12] + \textbf{CESF-2} + \frac{a}{6}[\bar{1}12] + \textbf{SISF}\\ + \frac{a}{6}[\bar{1}12] + \textbf{APB} + \frac{a}{6}[\bar{1}12]\\ + \textbf{SESF} + \frac{a}{6}[\bar{1}12] + \textbf{CISF} + \frac{a}{6}[\bar{1}12] \quad (5.3)\end{aligned}$$

where CISF is a complex intrinsic stacking fault and CESF-2 can be treated as an CISF over an CISF in two adjacent $\{111\}$ planes.

This full a$\langle 112\rangle$ dislocation dissociation is rarely observed in a single γ' precipitate. Instead, to avoid the high-energy anti-phase boundary (APB) energy, the dislocation ribbon, either side of the APB, occupies adjacent precipitates where they are separated by perfect crystal in the γ matrix. Due to the high energy of both complex faults, the two $\frac{a}{6}\langle 112\rangle$ Shockley partials are closely spaced and under insufficient resolution are observed as one $\frac{a}{3}\langle 112\rangle$ superpartial.[117]

The fault in Figure 5.5 consists of a $\frac{a}{6}\langle 112\rangle$ zonal partial (δC + δA, which is equivalent to Bδ spread on two adjacent (111) planes), followed by a δB partial on a single (111) plane and finally a two-layer fault consisting of an APB over an SISF.

Figure 5.9 shows the proposed mechanism to form the leading extrinsic fault.[73] It starts with two dislocations reaching adjacent planes (Figure 5.9(a)). The leading partials of the two γ lattice dislocations then enter to form a CESF-2 followed by one of the trailing partials (Figure 5.9(b)); and the fourth partial remains at the interface whilst a reordering process produces an SISF in the γ' (Figure 5.9(c)). This mechanism would explain why this phenomenon was not observed in TMS-138A, where the interfacial dislocations have restricted climb.

The CESF-2 fault forms by the dipole displacement occurring at the second, trailing partial $\frac{a}{6}\langle 112\rangle$. Kear *et al.* suggested such displacements can be achieved through atomic shuffling at the partial dislocations bounding the extrinsic fault.[68, 69, 73] Such mechanisms would be favoured at elevated temperatures and lower strain rates, hence they are observed during creep. The lowering of the strain rate during tensile deformation would allow sufficient time for vacancy migration to occur, facilitating the shearing of γ' precipitates by stacking faults.

5.3.4 Elemental Segregation at the Stacking Fault

The EDX maps in Figure 5.6 show enrichment of chromium and cobalt at the leading edge of the fault. It has been shown in crept microstructures that enrichment of chromium and cobalt lowers the stacking fault energy.[30] This is a precursor to the formation of SISFs and SESFs. This is facilitated by a different segregation environment at the front of the fault (region A) compared to along its length (region B), namely the lack of depletion of aluminium and enrichment of tungsten. Viswanathan *et al.*[155] showed a similar compositional variation exists at SISFs created in the γ' precipitates for CMSX-4. To achieve such compositional

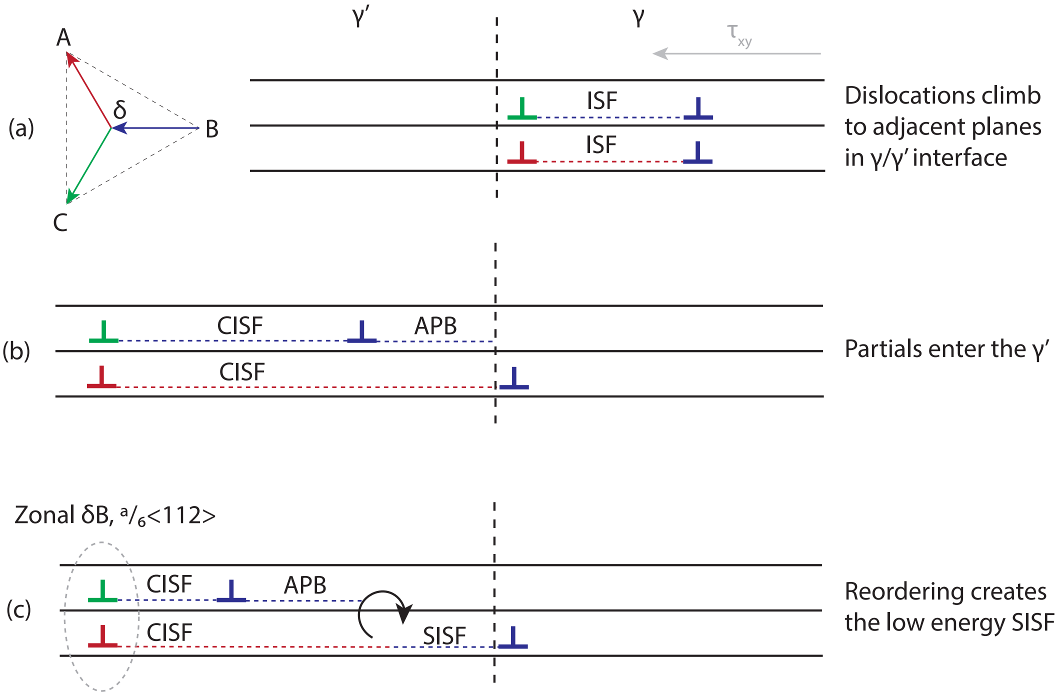

Figure 5.9 Proposed mechanism for the formation of an SISF from two dislocations climbing in the γ/γ' interface. The circular arrow represents reordering.[73]

variations, the authors proposed that diffusion occurs along the cores of the partial dislocations. This is supported by the shape of the leading dislocation lines, as they progress through the γ', as shown in Figure 5.3. The segments of the dislocation line closest to the γ channels had progressed the furthest, creating an arc shape in the precipitate. chromium and cobalt would diffuse to the fault along the dislocation core from the γ-channels since both elements partition strongly to the γ-phase.

5.3.5 The Effect of γ Pockets in γ' Precipitates

The EDX maps of Figure 5.6 show a lack of uniform composition within the γ' precipitate. An alternative mechanism is proposed where the propagating fault is also able to pick up fault-stabilising elements from these micro-pockets of γ formed within the γ' precipitate. Line scans show roughly a 2 at.% increase in chromium and cobalt. These compositional differences may be small enough that it should be possible for elements to readily diffuse to and from the fault from these pockets of γ. Vorontsov *et al.*[160] have shown that both SISF and SESF faults have higher HAADF image intensity in CMSX-4, suggesting diffusion-mediated segregation may be an essential process that controls shearing of the γ' precipitates at intermediate temperatures.

The segregation of chromium and cobalt to the fault suggests that a minimum threshold level of these two elements may be required to form stacking faults. If there is insufficient chromium or cobalt, then the partial dislocations entering into γ' precipitates cannot be stabilised, preventing SF shear. The compositions of the γ and γ' phases of a single crystal Ni-based superalloy are partly controlled by the ageing temperatures and time held at each temperature of the heat treatment cycles during manufacturing. The heat treatment cycles a superalloy is subject to, may therefore affect the ease by which stacking faults can form, and in turn affect the creep resistance of the superalloy.

Chromium and cobalt are known to preferentially partition to the γ phase.[62, 149, 109, 81] In a two-phase superalloy, as precipitates form upon homogenisation, the supersaturated Chromium and cobalt are rejected out into the matrix phase. This process continues upon further ageing. If the heat treatment cycles are not long or hot enough to allow appropriate amounts of chromium and cobalt to partition to the matrix, there would be a deficit within the vicinity of a partial to shear the γ' precipitate, preventing the local chemistry required to stabilise it, which inhibits stacking fault formation. This theory also extends to alloys with lower levels of chromium and cobalt. This would explain why no stacking fault shear was observed in tensile tests at the slowest strain rate for TMS-138A. Compared to CMSX-4, the composition of TMS-138A is depleted of chromium and cobalt. The reduced quantity available in the γ phase may result in a longer diffusion time for sufficient levels of chromium and cobalt to reach and stabilise the fault.

The curves of SRR99 also showed no drop in stress for tensile tests conducted at the slowest strain rate ($10^{-6}\,\mathrm{s}^{-1}$). This alloy was tested because it is a high diffusion alloy. Therefore, it would be expected that vacancy diffusion required for dipole displacement would occur more readily. This would facilitate stacking fault shear. However, the stress strain curve showed no drop in stress, the macroscopic feature associated with stacking fault shear. SRR99 has higher Cr at.% and lower Co at.% compared to CMSX-4. The relative proportion of chromium and cobalt and interplay may therefore affect the ability for the dislocations to deform by stacking fault shear.

In addition to diffusion, the EDX maps of Figure 5.6 reveal the presence of tungsten at the shearing dislocation's core. The diffusion distance is limited for tungsten due to its slightly larger size. It is thought that tungsten may stabilise the dislocation core, getting trapped in its strain field, and displace γ'-former elements during the shearing process. The introduction of tungsten means aluminium and nickel need to be removed to balance the average atomic number, accounting for the depletion of aluminium and nickel within the fault. Furthermore, aluminium and nickel are depleted because they do not contribute towards stabilising the stacking fault and thus get pushed out of the dislocation strain field.

5.4 Conclusions

Changing the strain rate had no effect on the yield stress at 750 °C for CMSX-4, with tensile tests at all three strain rates showing similar values of yield stress. However, it does seem to have an effect on post-yield behavior, where at a sufficiently slow strain rate ($10^{-6}\,\mathrm{s}^{-1}$), a transition in deformation mechanism from APB shearing to stacking fault shearing was observed. This transition was accompanied by a drop in the flow stress, to values typical of primary creep. This transition was not observed in the two other alloys tested: TMS-138A and SRR99. Stacking fault shear was hypothesised to occur due to the activation of a secondary slip system, allowing dislocations on two different slip systems to interact and enter the precipitate. This lowered the flow stress because it requires less stress to propagate a stacking fault compared to APB shearing and over time there are greater number of dislocations propagating by stacking fault shear. EDX and EELS maps of these stacking faults showed segregation of chromium and cobalt at the stacking faults. This suggests alloy composition plays an important role in causing this transition.

Chapter 6

A Transmission Electron Microscopy study of the evolution of dislocations during tensile deformation of the single crystal superalloy CMSX-4

6.1 Introduction

Ni-based superalloys exhibit a yield stress anomaly, which makes this group of materials suitable for high temperature applications such as turbine blades. It is thought that the origin of the yield stress anomaly is dislocations cross-slipping from the $\{111\}$ slip plane to the $\{010\}$ plane, due to the lower APB energy of the $\{010\}$ plane compared to the $\{111\}$ plane. Dislocations that cross-slip become locked, which in turn increases the yield stress. This has been extensively studied in monolithic $L1_2$ compounds, as there is a strong suggestion that the Ni_3Al phase contributes towards this unique property. However, current understanding of the dislocation interactions when this theory is applied to the two phase γ/γ' microstructure of single crystal Ni-based superalloys is not fully understood.

This chapter therefore aims to improve the understanding of how the dislocations interact with the two phase microstructure within a single crystal superalloy, and relate this to the macroscopic yield behaviour. This is done by focusing on the dislocation structures that form upon entry into the γ' precipitates after the yield point. In particular, the morphology of dislocations both in the precipitates and in the γ channels. The dislocation structures that form upon yield are analysed from five different crystallographic orientations relative to the tensile specimen: (a) the (001) plane, perpendicular to the tensile axis, (b) the $(11\bar{1})$ slip plane, (c) the (010) plane, (d) the (100) plane and (e) the (011) plane.

CMSX-4, a second-generation Ni-based superalloy, was used in this set of experiments due to its wide use in turbine blade applications. This alloy exhibits a peak yield stress at 750 °C and therefore this temperature was chosen to conduct and compare these tensile tests.

6.2 Results

Figure 6.1 shows the stress-strain curves obtained from tensile tests on specimens of CMSX-4 tested at 750°C, deformed at a strain rate of $\dot{\varepsilon} = 10^{-4}\,\mathrm{s}^{-1}$. The red curve was interrupted at 1.8% strain, the black curve at 3.3% strain. Two tests were run because one tensile specimen did not have enough material to allow TEM samples to be produced for all the desired crystallographic planes. The interrupted strain levels are different because the tensile tests were interrupted manually. The strain to interrupt the test at was chosen to be shortly after the yield point; a condition where some dislocations will have entered the γ' phase but a low enough number that the micrographs would not be covered completely, making it difficult to discern any mechanisms for dislocation activity. Both stress-strain curves follow a similar path: they rise linearly up to a stress of around 975 MPa. The strain at this point is around 1%. The stress then plateaus upon increasing strain, after which point the tests were interrupted.

Figure 6.2 shows a STEM micrograph of the dislocation structure of CMSX-4 following the tensile test at 750 °C, $\dot{\varepsilon}=10^{-4}\,\mathrm{s}^{-1}$, interrupted at 1.8% strain, viewed down the [001] zone axis, i.e. perpendicular to the tensile axis. Dislocation segments are seen in the precipitates, oriented parallel to the precipitate edges. Some dislocation segments have a darker contrast between them and have been highlighted. There are also two 'U'-shaped dislocation segments, also separated by a darker contrast.

To get a better understanding of the dislocation structures, the tensile specimen was also imaged on this primary slip plane. Through Laue back-reflection, the primary slip plane of the tensile sample was found to be $(11\bar{1})$ plane. Figure 6.3(a) shows a STEM image of the dislocation structure viewed on the $(11\bar{1})$ plane. The γ' precipitates are triangular in shape due to the orientation of the cut plane. Dislocations can be seen gliding through the γ/γ' microstructure in the plane of the paper. Dislocations move within distinct slip bands through the microstructure. Figure 6.3(b) is a magnified image of the highlighted area in Figure 6.3(a). This higher magnification shows dislocations closely spaced when in the γ' precipitates, compared to in the γ channels.

The area of Figure 6.3(b) was imaged under six different two beam conditions, around the

$[11\bar{1}]$ zone axis. The images from the six conditions, taken over the same area, are shown in Figure 6.4. The visibility table corresponding to the six conditions is shown in Table 6.1. Under the **g** = $(1\bar{1}1)$ condition (Figure 6.4(d)), the dislocations become invisible. The dislocation line is broadly parallel to the g_{022} vector and the shearing dislocation is of screw orientation. The Burgers vector of these dislocations is therefore **b**=[011].

The tensile specimen was also cut parallel to the (100) and (010) planes. STEM images of the dislocation structure parallel to the (100) plane is shown in Figure 6.5, while that parallel to the (010) plane is shown in Figure 6.6. The dislocations viewed on the (100) plane (Figure 6.5) are fairly straight, and in closely spaced pairs through the square-shaped γ' precipitates. These dislocations are separated by a high-energy APB. The dislocation pairs run diagonal to the precipitate edges, at an angle of approximately 45°. At the γ/γ' interface, within the γ channels, these two dislocation pairs separate, no longer bound by an APB.

Figure 6.6 shows dislocations lying diagonal within the precipitates, though the separation width is larger and varies along the dislocation line. Some dislocation segments are also observed to be parallel to the precipitate edge. These dislocation segments are thought to have entered the precipitate as dislocation pairs separated by an APB. Their orientation suggests they run effectively into the page at an angle of 45°, with the APB plane on the (001) or (100) cube planes.

In addition to the straight, diagonal dislocation pair segments in the γ' precipitates, dislocation loops were also observed in both STEM micrographs. A dislocation half loop is observed and highlighted in Figure 6.5, while a thin, full dislocation loop is highlighted in Figure 6.6. Figure 6.7 shows STEM images of a full loop imaged under six different two-beam conditions around the $[11\bar{1}]$ zone axis. Two sides of the dislocation loop, the screw segments, become invisible under the **g** = $(1\bar{1}1)$ condition. Under this condition, small segments of the loop are still visible (denoted by the letter 'A' in Figure 6.7(d)). These segments are edge-type dislocation segments.

Figure 6.8 is a STEM micrograph parallel to the (100) plane, showing two dislocation pairs connected in the γ channel. Figure 6.8(a) shows two dislocation pairs which span two precipitates, across the γ channel. A half loop is visible at the top of the image with one edge of the loop segment resting on the γ/γ' interface, and highlighted by a dotted white box. Figure 6.8(b) is a higher magnification of the highlighted region in 6.8(a) and shows the interactions between the two respective dislocations that compose each dislocation pair. The two inner dislocations are linked and lie along opposite γ/γ' interfaces, while the two outer dislocations still connect across to their corresponding segment across the γ channel.

The sample was also cut parallel to the (101) plane to view the diagonal screw dislocations

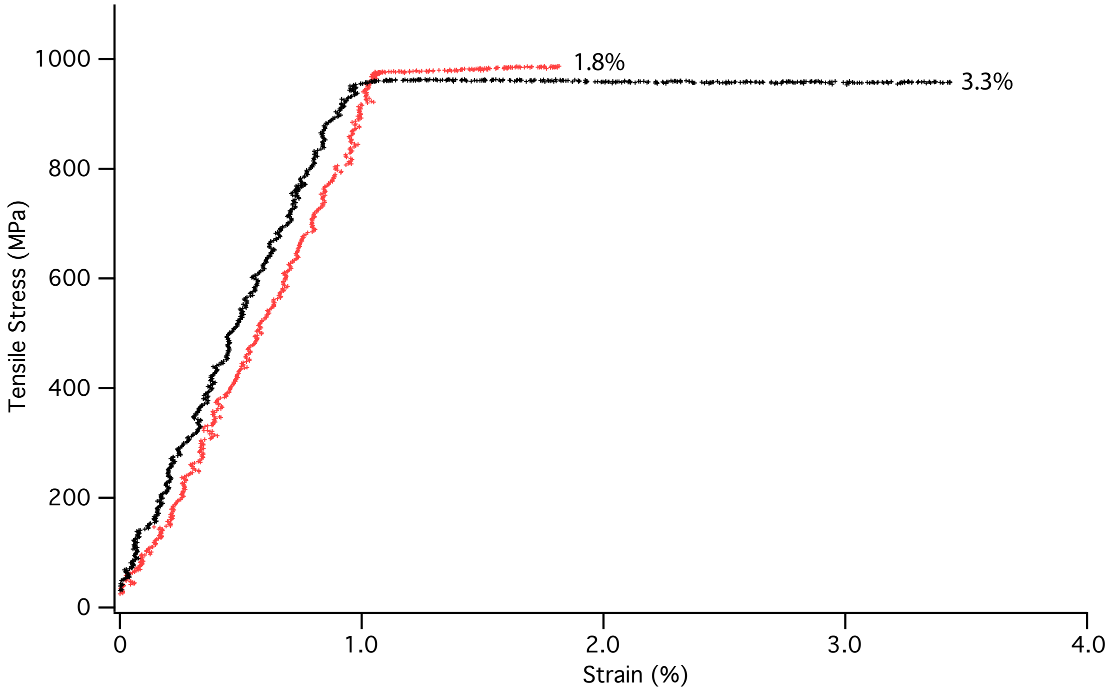

Figure 6.1 Stress strain curves of CMSX-4 tested at 750 °C at a strain rate $\dot{\varepsilon} = 10^{-4}\,\mathrm{s}^{-1}$ interrupted to 1.8% strain (red curve) and 3.3% strain (black curve).

straight down the dislocation line. Figure 6.9(a) shows HAADF STEM images of two dislocation pairs viewed down the [011] zone axis, taken at high resolution using an FEI Titan^3 TEM. Figures 6.9(b) and 6.9(c) show zoomed-in HAADF STEM images of the two dislocations in (a) at greater magnification, also viewed down the [101] zone axis. From this view, it is possible to determine more accurately the separation difference between the dislocation pairs and confirm any segregation.

Figure 6.10 shows a low magnification HRSTEM image of the dislocation pair at high resolution viewed down the [101] zone axis. The dislocation separation is roughly 17 lattice spacings in the $[0\bar{1}1]$ direction, corresponding to an APB separation of 6.2 nm. Streaking is visible along the $(11\bar{1})$ plane in the HRSTEM image (Figure 6.10(a)). However, the corresponding centre of symmetry (COS) mapping shows no strain, implying no dissociation on the octahedral plane. The EDX maps are shown in Figure 6.11. No elemental segregation was observed along the APB between the dislocation pair.

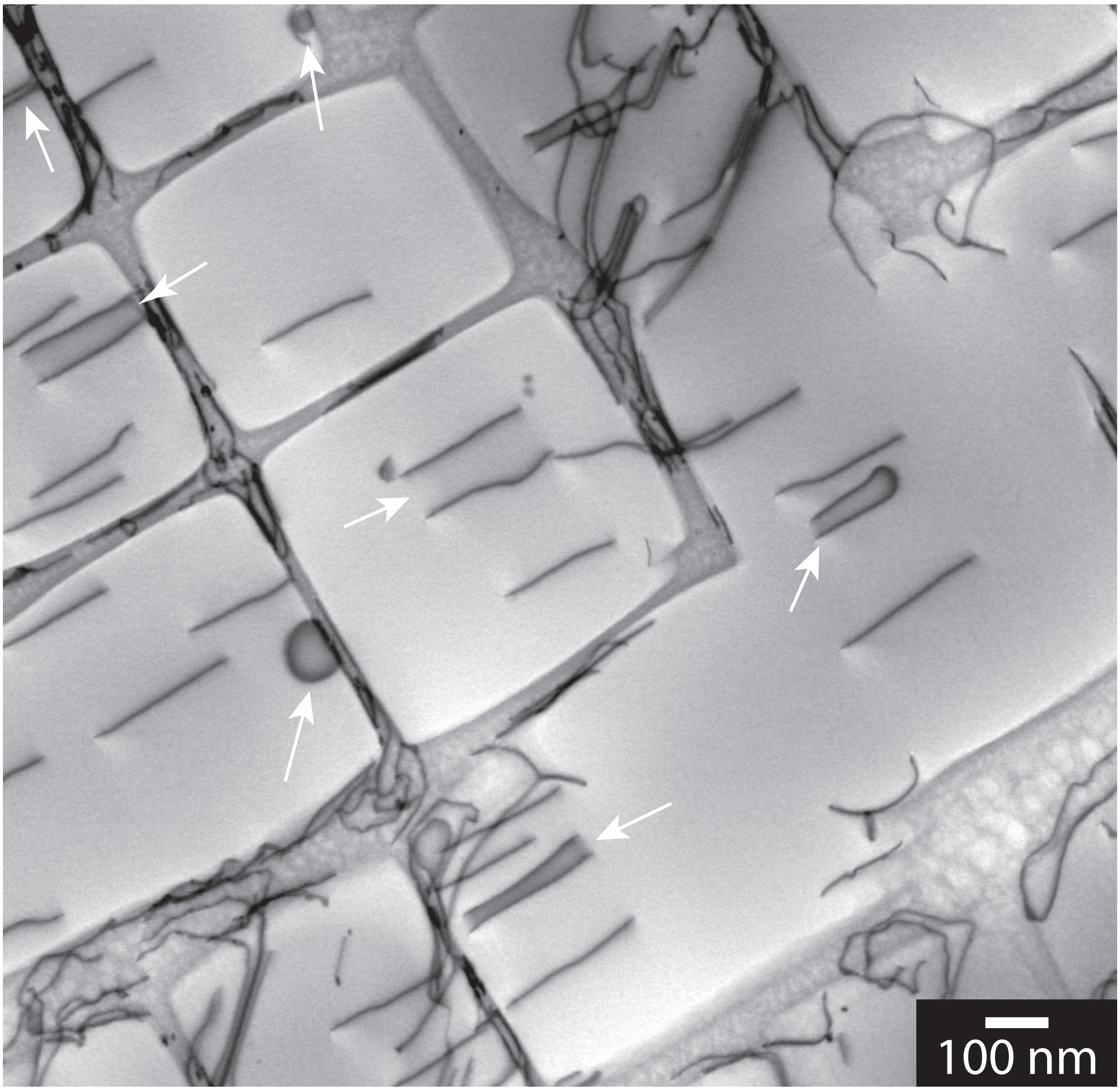

Figure 6.2 A STEM micrograph of the microstructure from a CMSX-4 tensile specimen, deformed at a strain rate of $10^{-4}\,s^{-1}$, interrupted at 1.8% strain, cut and viewed down the [001] zone axis. Areas of darker contrast between some dislocation pairs and 'U'-shaped loops have been highlighted.

Table 6.1 Table of visibility for the dislocations viewed down the $[11\bar{1}]$ zone axis in Figures 6.4 and 6.7.

g:	(022)	$(\bar{2}20)$	(202)	$(1\bar{1}1)$	(111)	$(\bar{1}11)$	Burgers vector
	v	w	w	i	w	v	[011]

i= invisible, w= weak, v= visible

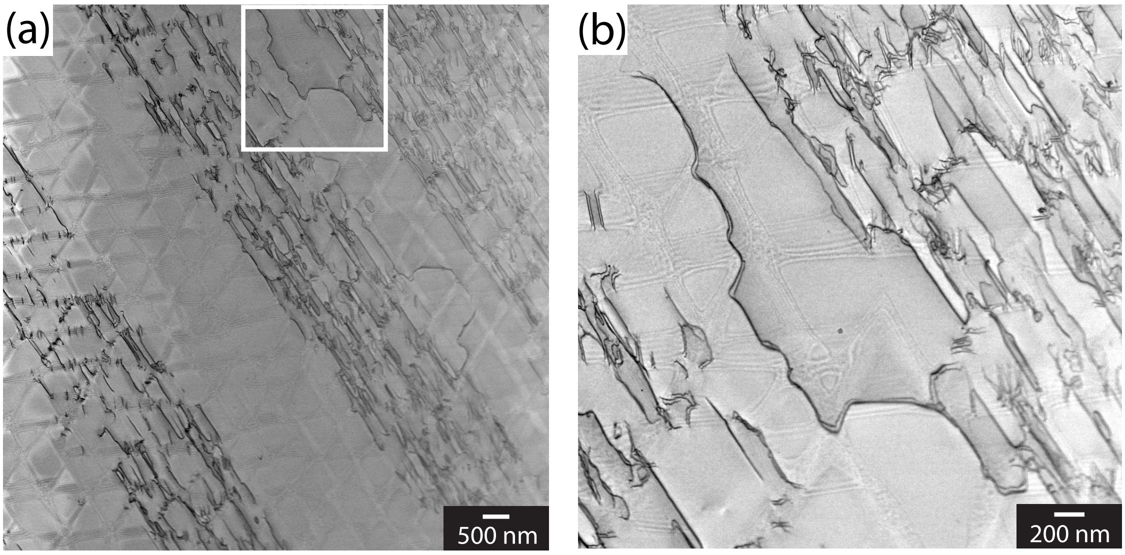

Figure 6.3 (a) A STEM micrograph of the microstructure from a CMSX-4 tensile specimen deformed at a strain rate of $10^{-4}\,\mathrm{s}^{-1}$, interrupted at 1.8% strain, cut and viewed on the $(11\overline{1})$ plane. (b) A higher magnification image of the area highlighted in (a).

6.3 Discussion

6.3.1 The strength contribution from APB hardening in single crystal CMSX-4 at 750 °C

From the stress strain curve in Figure 6.1, the contribution from the γ' precipitates due to APB hardening can be approximated. Copley and Kear expressed the increase in CRSS due to APB hardening, denoted $\Delta\tau_{APB}$, as follows[16]:

$$\Delta\tau_{APB} = \frac{\gamma_{APB}}{2b} \tag{6.1}$$

where γ_{APB} is the APB energy and b is the Burgers vector. As observed in CMSX-4, the dislocations have a Burgers vector, $b = \frac{a}{2}\langle 110\rangle$. Using an estimate of the lattice parameter of γ' at 750 °C[158], the magnitude of the Burgers vector can be found:

$$\begin{aligned} |b| &= \frac{a_{\gamma'}}{\sqrt{2}} \\ &= \frac{0.3627}{\sqrt{2}}\,\mathrm{nm} \\ &= 0.2565\,\mathrm{nm} \end{aligned} \tag{6.2}$$

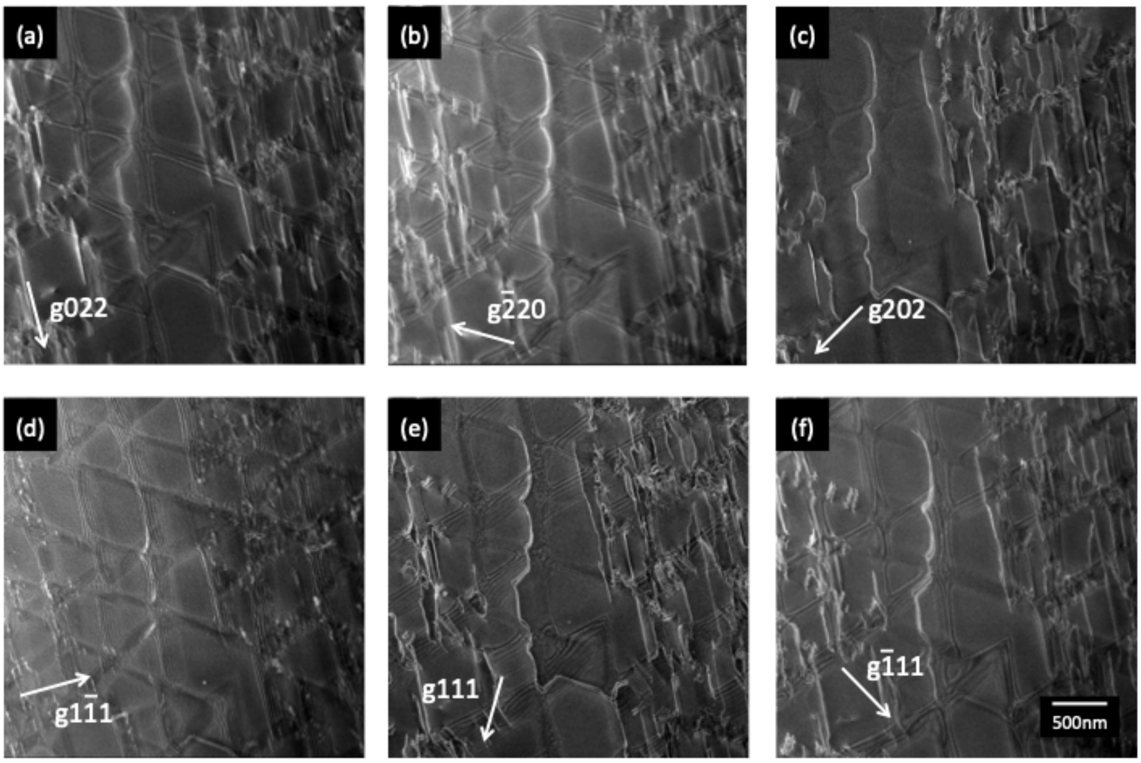

Figure 6.4 STEM micrographs of the microstructure from a CMSX-4 tensile specimen deformed at a strain rate of $10^{-4}\,\mathrm{s}^{-1}$ to 1.8% strain, cut on the $(11\bar{1})$ plane, taken over the same region as that featured in Figure 6.3. All sub figures are taken over the same area of the sample. (a) Two beam condition, **g** = (022), (b) **g** = $(\bar{2}20)$, (c) **g** = (202), (d) **g** = $(1\bar{1}1)$ and (e) **g** = (111) and (f) **g** = $(\bar{1}11)$. Table 6.1 is the corresponding visibility table.

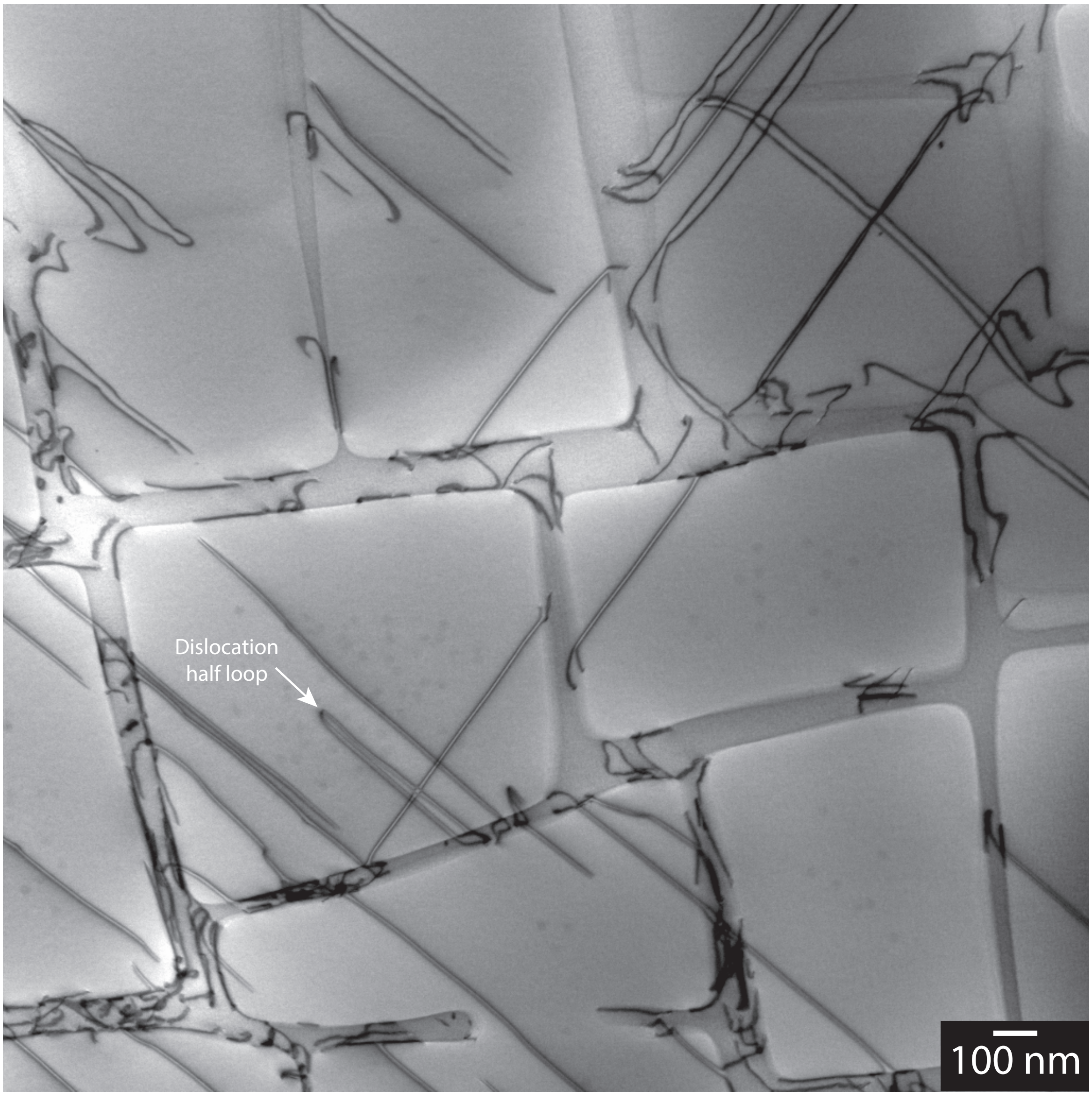

Figure 6.5 A STEM micrograph of the microstructure from a CMSX-4 tensile specimen deformed at a strain rate of $10^{-4}\,s^{-1}$, at 750 °C, interrupted at 1.8% strain, cut and viewed down the [100] zone axis.

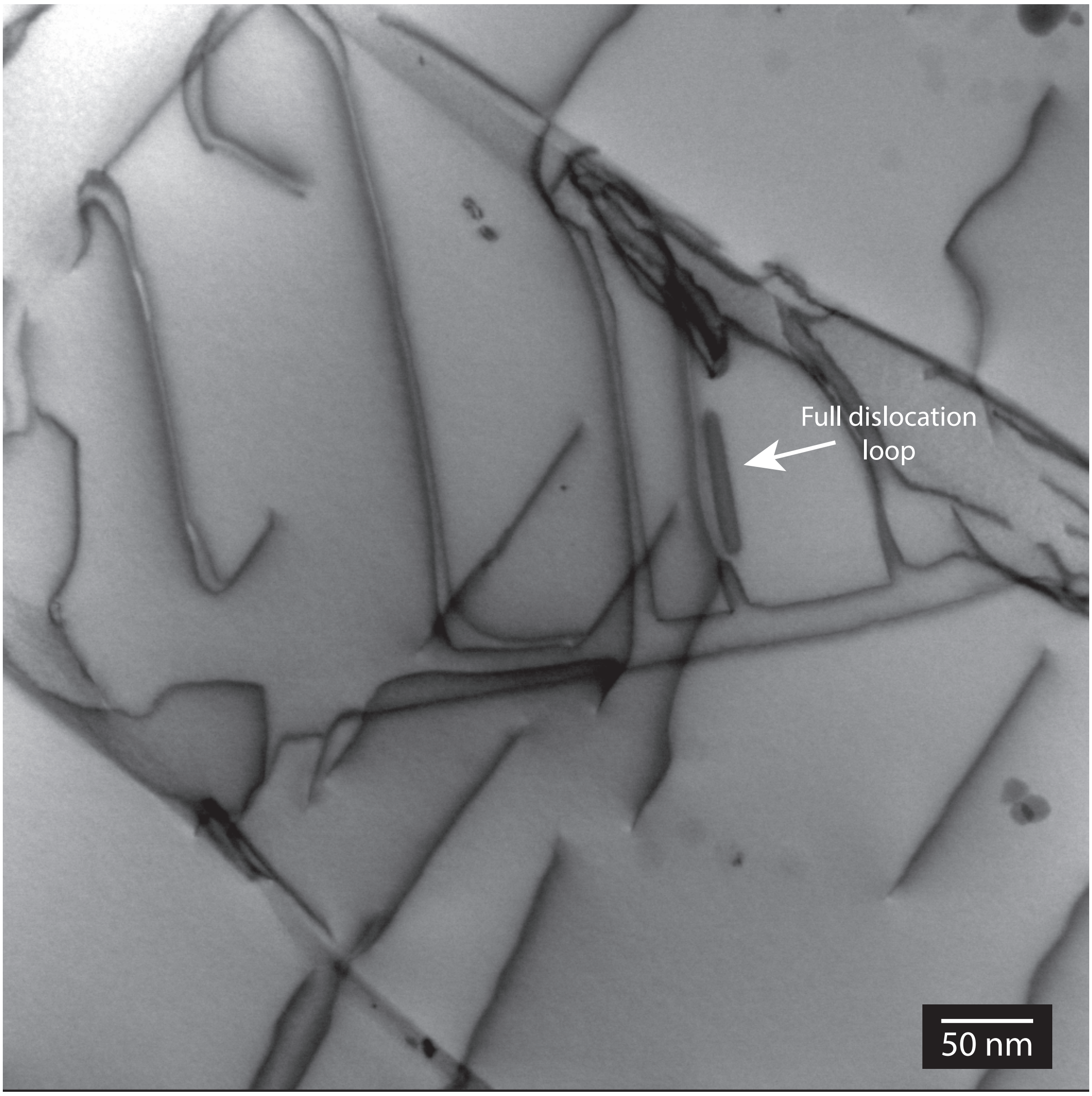

Figure 6.6 A STEM micrograph of the microstructure from a CMSX-4 tensile specimen deformed at a strain rate of $10^{-4}\,\mathrm{s}^{-1}$, at 750 °C, interrupted at 3.3% strain, cut and viewed down the [010] zone axis.

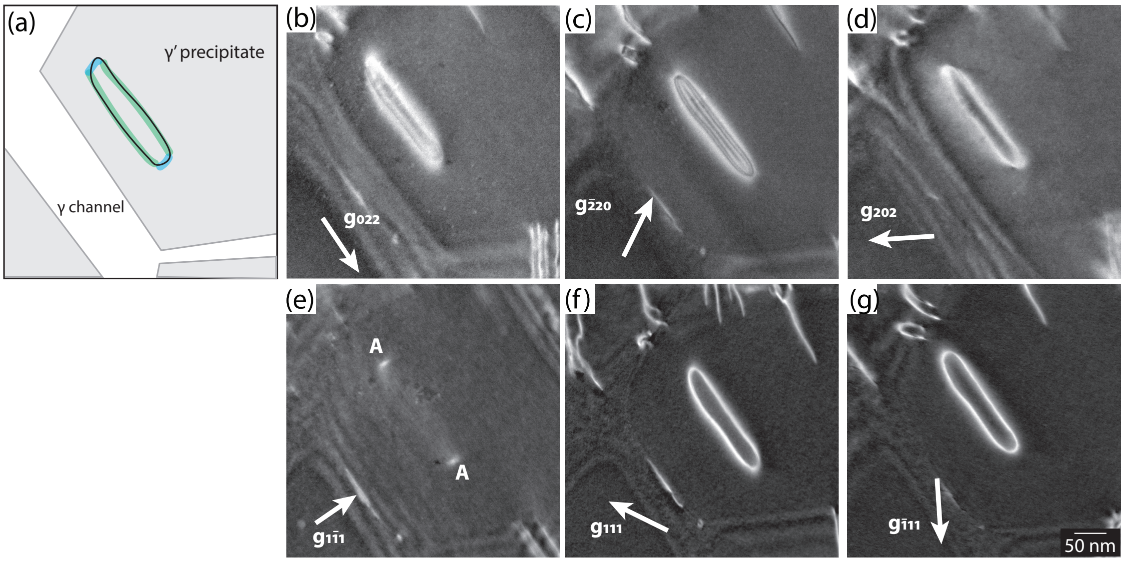

Figure 6.7 STEM images of a full dislocation loop in the γ' precipitate, viewed down the $[11\bar{1}]$ zone axis, from a tensile sample of CMSX-4, deformed at 750 °C and a strain rate of $10^{-4}\,\mathrm{s}^{-1}$, interrupted at 1.8% strain. All sub figures are taken over the same area of the sample. (a) A schematic diagram of the dislocation loop relative to the γ' precipitate and γ channel. The green segments highlighted represent the screw segments, the blue segments highlighted represent the edge segments. (b) Two beam condition, **g** = (022), (c) **g** = $(\bar{2}20)$, (d) **g** = (202), (e) **g** = $(1\bar{1}1)$ and (f) **g** = (111) and (g) **g** = $(\bar{1}11)$. The screw segments of the dislocation loop is invisible under the **g** = $(1\bar{1}1)$ condition. Table 6.1 is the corresponding visibility table.

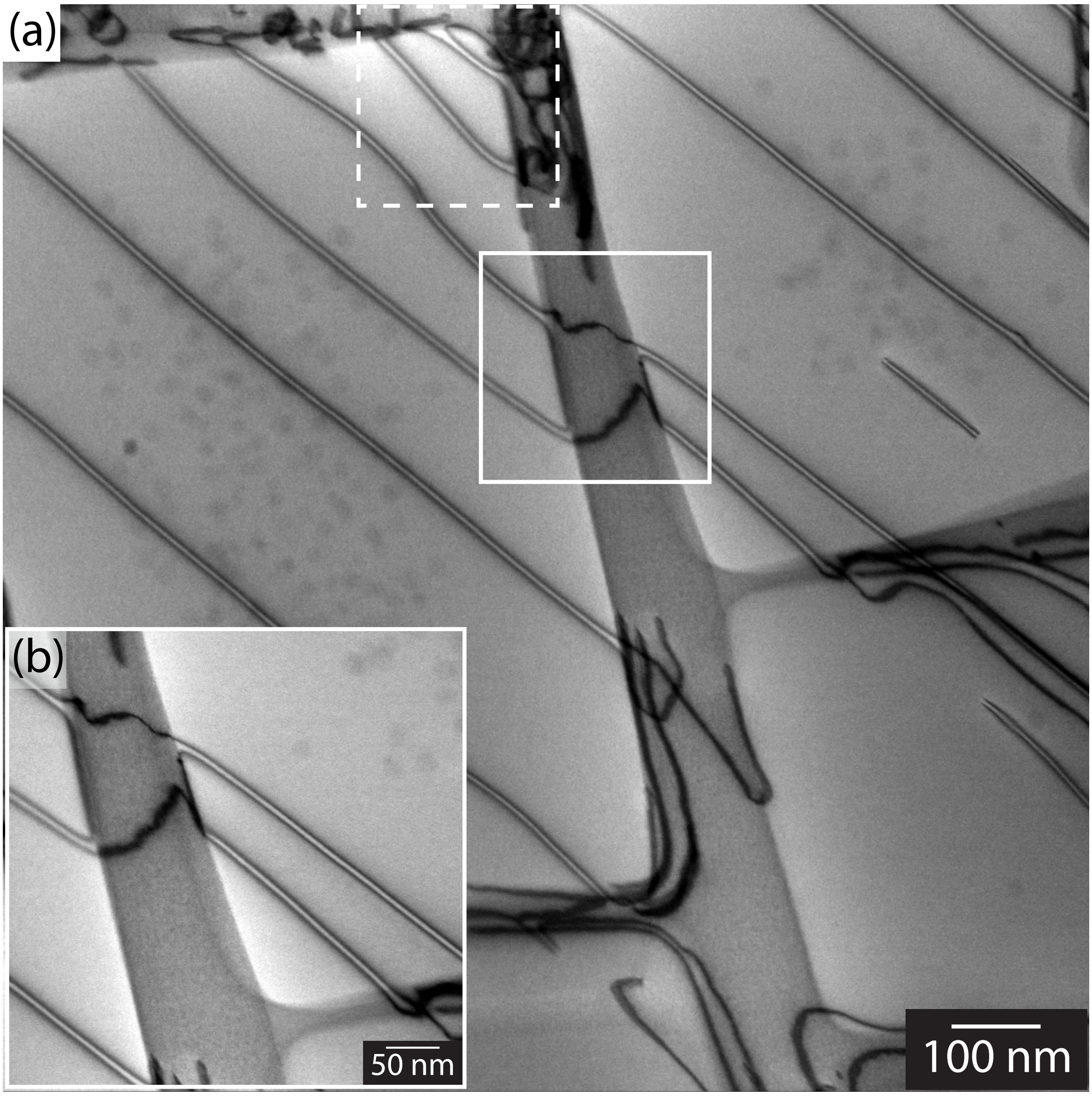

Figure 6.8 A STEM micrograph viewed down the [100] zone axis, taken from a CMSX-4 tensile specimen deformed at a strain rate of $10^{-4}\,\mathrm{s}^{-1}$, at 750 °C, interrupted at 3.3% strain, showing the interaction of two dislocation pairs that span across the γ channel. The dotted box shows two dislocation pairs forming a half loop. Inset (b) A higher magnification image of the dislocation structure highlighted in (a).

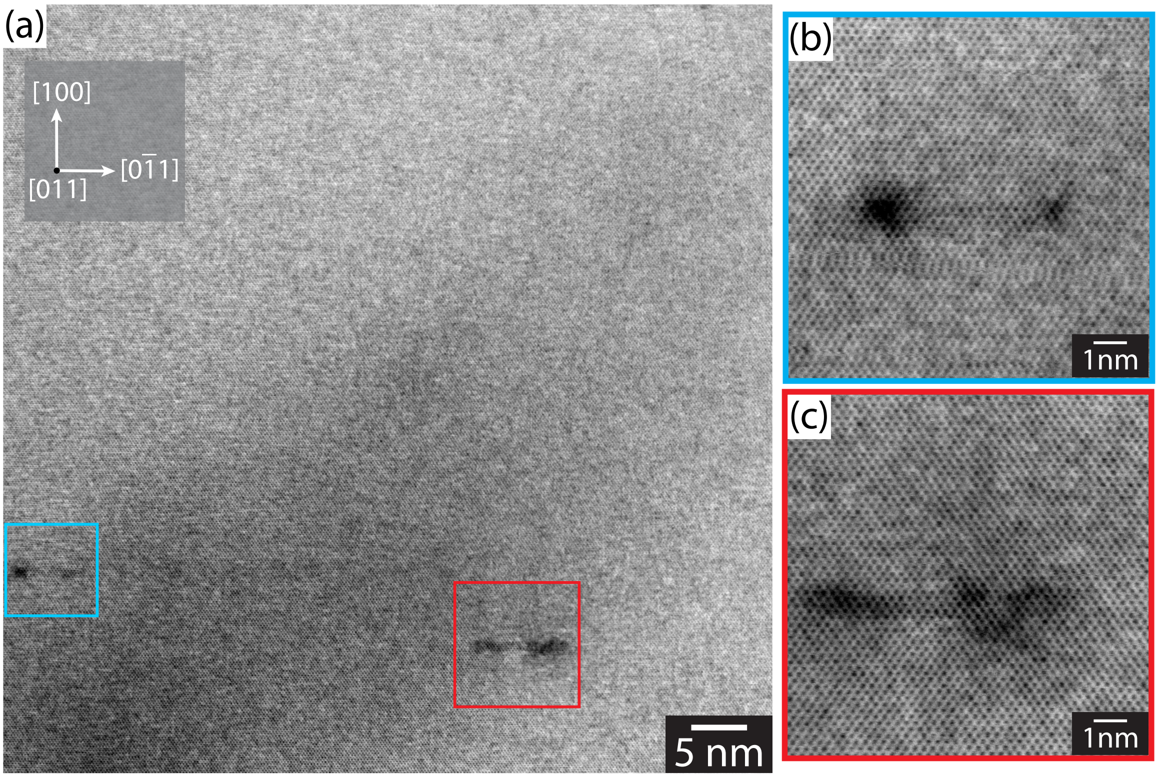

Figure 6.9 High resolution HAADF-STEM images of a CMSX-4 tensile specimen, deformed at a strain rate of of 10^{-4} s^{-1}, interrupted at 3.3% strain, cut and viewed down the [011] zone axis. (a) Dislocation pairs are visible down the dislocation line. (b)-(c) Higher magnification of the two visible dislocation pairs.

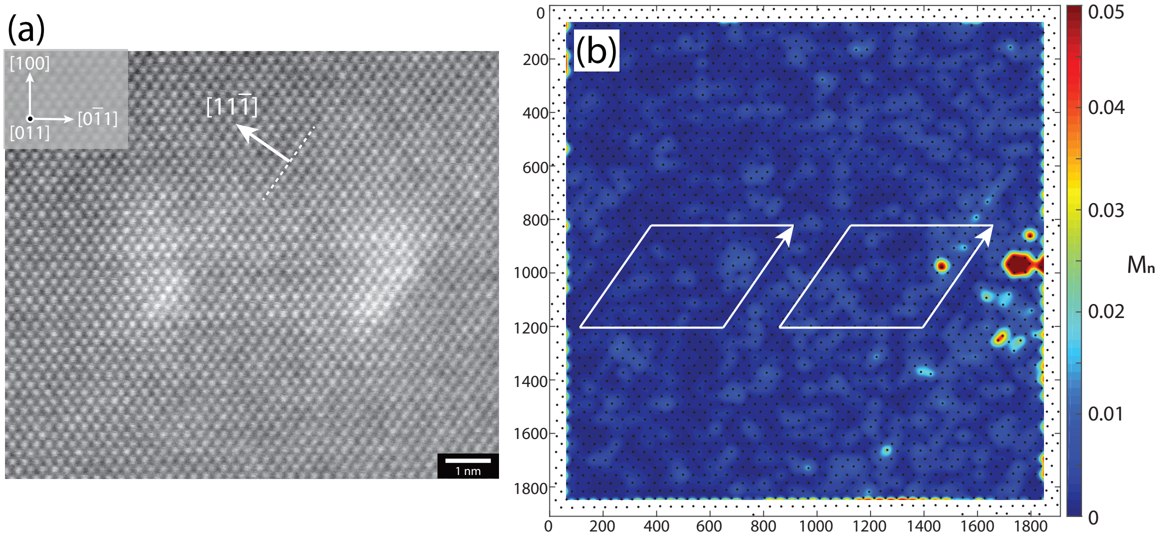

Figure 6.10 (a) A low magnification HRSTEM image of a dislocation pair at high resolution viewed down the [011] zone axis, taken from a tensile specimen of CMSX-4 tested at 750 °C at a strain rate $\dot{\varepsilon} = 10^{-4}\,\mathrm{s}^{-1}$, interrupted at 3.3% strain. Streaking is visible on the $(11\bar{1})$ plane, represented by the dashed line, (b) The corresponding Centre of Symmetry (CoS) mapping. Full Burgers circuits have been traced, highlighting the location of the dislocations.

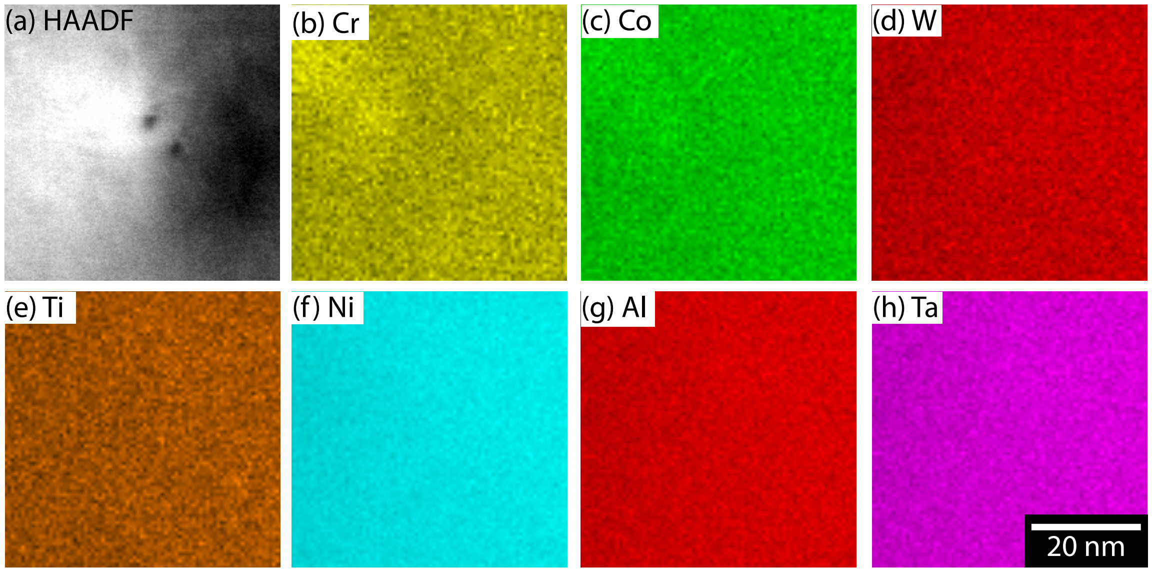

Figure 6.11 EDX maps showing spatial distributions of the elements Cr, Co, Al, W and Ni, taken from a region of the microstructure with a dislocation pair within the γ' phase from a sample of CMSX-4 deformed at 750 °C, at a strain rate of $10^{-4}\,\mathrm{s}^{-1}$ and interrupted at 3.3% strain. (a) A STEM-HAADF micrograph imaged down the [011] zone axis, showing a dislocation pair, viewed down the dislocation line, (b)-(h) show the compositional EDX maps of the HAADF imaged region for the elements Cr, Co, Al, W and Ti, Ni, Al and Ta respectively.

Taking γ_{APB} =180 mJ m^{-2}[18] yields:

$$\begin{aligned}\delta\tau_{APB} &= \frac{\gamma_{APB}}{2b} \\ &= \frac{180}{2\times 0.2565}\,\text{MPa} \\ &= 350\,\text{MPa}\end{aligned} \tag{6.3}$$

The APB hardening only applies to areas of the crystal containing the γ' precipitates. The γ' volume fraction, v_f, of single crystal CMSX-4 is approximately 75%, and therefore the contribution to APB hardening is scaled down to (350 × 0.75 =) 263 MPa. Finally, the contribution towards the yield stress from APB hardening can be determined. For an FCC single crystal undergoing tensile deformation in the [001] direction, the Schmid factor, m, for the primary slip system is 0.408. The contribution to the yield stress from APB hardening, denoted $\sigma_{y,APB}$, is calculated as:

$$\begin{aligned}\sigma_{y,APB} &= \frac{\tau_{APB}}{m} \\ &= \frac{263}{0.408}\,\text{MPa} \\ &= 645\,\text{MPa}\end{aligned} \tag{6.4}$$

The stress strain curves for single crystal CMSX-4 (Figure 6.1) show an overall yield stress around 975 MPa, so the contribution towards the yield stress from APB hardening is approximately 66%. This is of similar value to the APB hardening contribution to Mar-M200 calculated by Copley and Kear, of approximately two-thirds.[15]

6.3.2 The Yield Process for Single Crystal Ni-based Superalloys

The yield point in a two-phase single crystal, Ni-based superalloy represents the moment the stress is high enough for dislocations to enter the γ' precipitates from the narrow γ channels. This was shown in Chapter 4. Upon entry into the precipitates, dislocations glide as closely spaced pairs on the $\{111\}$ primary slip system, separated by a high energy APB. Figure 6.3(b) shows how tightly spaced the dislocation pairs are in the precipitate, and their separation in the γ channels.

As the dislocations glide, they create distinct slip bands as seen in Figure 6.3(a). The shearing dislocations have large Burgers vectors. Because of their large Burgers vectors, dislocations are repelled when within the vicinity. This leads to widening of the slip traces as shear progresses, which appear as slip bands. However, provided there is clean crystal for dislocations to move into, the stress required to move a dislocation through the microstructure is not affected. This is reflected macroscopically in the stress-strain curve as a plateau in stress after the yield point (Figure 6.1). A similar softening has been observed in three-dimensional (3D) discrete dislocation dynamics (DDD) modelling of a Ni-based single crystal superalloy.[80] The simulated stress-strain response is shown in Figure 6.12. It was suggested that shearing of the γ' precipitates by superdislocations reduced the resistance of the material to further slip and produced a softer mechanical response in the material.

As deformation continues, more of the slip planes are occupied by dislocations. Eventually dislocations will struggle to move, because of the repulsion force from sessile dislocations. A higher stress would be required to overcome this repulsion force. This causes the stress to rise after the stress plateau, at around 5% strain. A second slip system might become active. If so, dislocations would be free to glide on this system and the stress again plateaus. Eventually, dislocations fill the second slip system or dislocations on two slip systems interact and work hardening occurs, leading to a further increase in the stress until failure occurs.

Figure 6.13(a) shows a (111) glide plane relative to a cubic precipitate. There are six possible entry configurations for a dislocation to enter into the precipitate as shown in (b). For a dislocation pair to cross-slip, it needs to be oriented in the screw direction. However, only one in six interfaces encountered ($\sim$16.7%) would align the dislocation in the screw orientation and have the necessary external forces to enter the precipitate. This suggests around 15% of the dislocation segments cross-slip and become locked. The remaining dislocations move through both the γ' precipitates and γ channels rapidly and unhindered.

Further slip is prevented on the slip plane occupied by these locked dislocation pairs and closely adjacent slip planes because of the large repulsion forces from these large Burgers vectors. This leads to a widening of the slip traces as shear progresses because dislocations find it easier to glide in areas of the microstructure unoccupied by dislocations. This is reflected in the microstructure (Figure 6.3), with the initial deformation being concentrated within narrow slip bands, before widening. This suggests as long as there are clean areas of the microstructure to move into, the flow stress will remain unaffected, exhibited by the plateau of stress after the yield point.

6.3.3 The Formation of Dislocation Loops

Alongside the straight dislocation pairs, dislocation loops are also visible in the microstructure. A half loop is visible and highlighted in Figure 6.5. A full dislocation loop is also highlighted

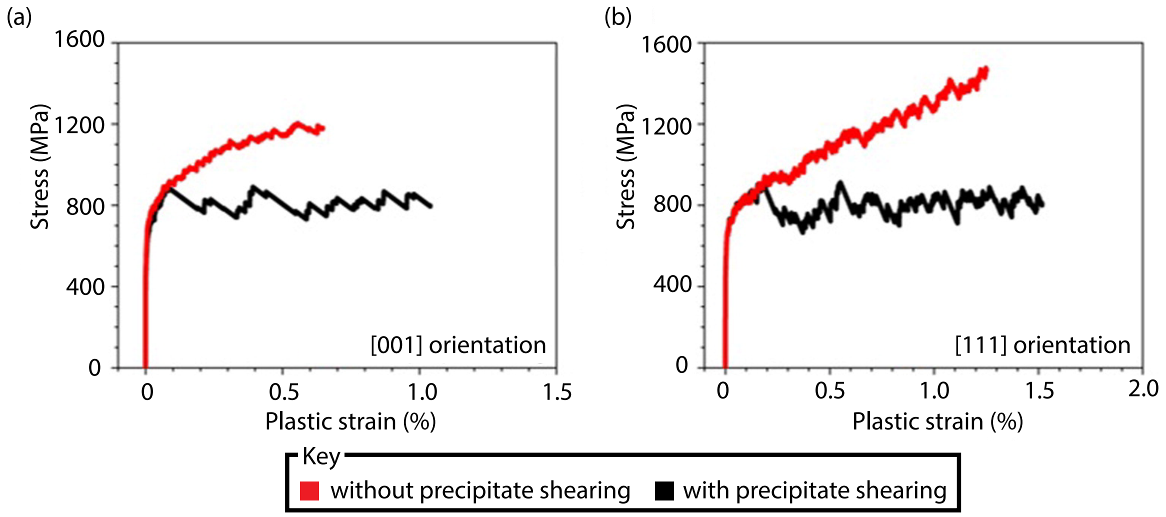

Figure 6.12 The simulated stress–strain response generated from three-dimensional (3D) discrete dislocation dynamics (DDD) modelling of a Ni-based single crystal superalloy, with (black) and without (red) precipitate shearing by dislocations for the (a) [001] and (b) [111] orientations.[80]

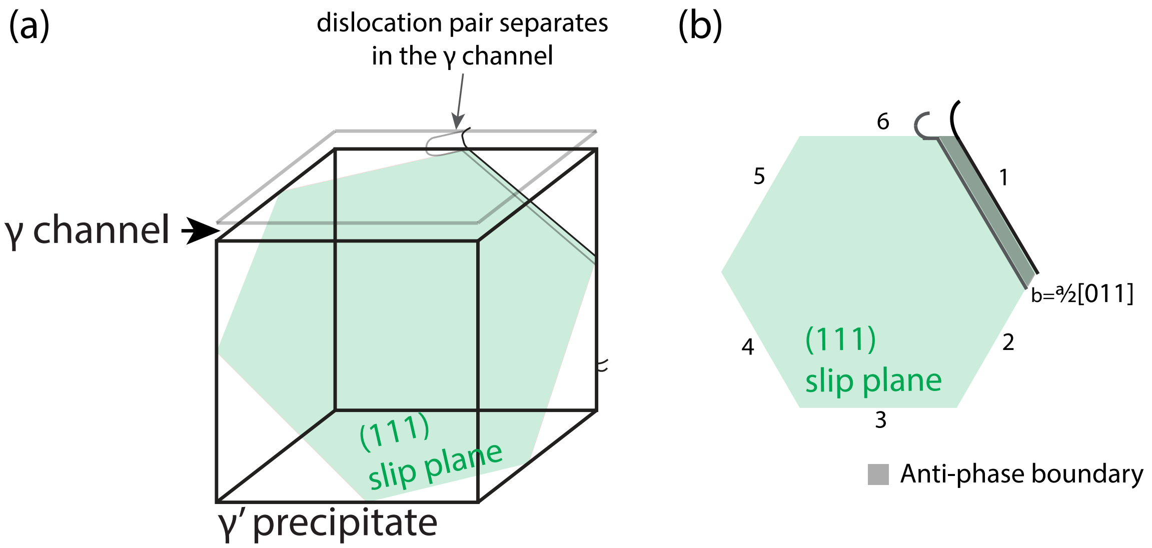

Figure 6.13 (a) A schematic illustration of dislocation motion on a (111) slip plane in relation to a cubic γ' precipitate. (b) A plane view of the (111) slip plane showing the six interfaces by which a dislocation pair can enter the precipitate from the γ channel. A pair of dislocations with Burgers vectors $\mathbf{b}=\frac{a}{2}[011]$ is shown entering from 'interface 1'.

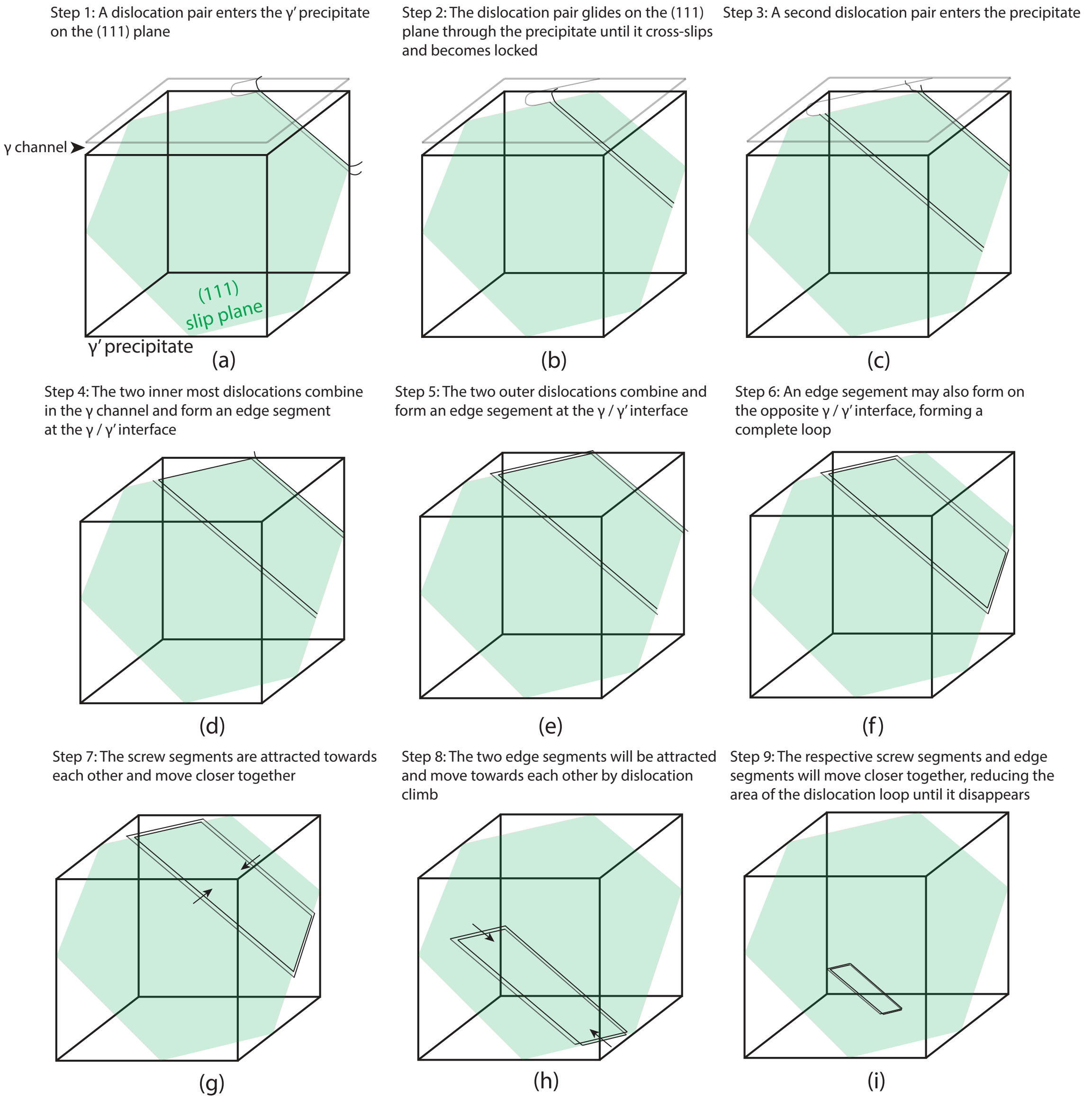

Step 1: A dislocation pair enters the γ′ precipitate on the (111) plane

Step 2: The dislocation pair glides on the (111) plane through the precipitate until it cross-slips and becomes locked

Step 3: A second dislocation pair enters the precipitate

Step 4: The two inner most dislocations combine in the γ channel and form an edge segment at the γ / γ′ interface

Step 5: The two outer dislocations combine and form an edge segement at the γ / γ′ interface

Step 6: An edge segement may also form on the opposite γ / γ′ interface, forming a complete loop

Step 7: The screw segments are attracted towards each other and move closer together

Step 8: The two edge segments will be attracted and move towards each other by dislocation climb

Step 9: The respective screw segments and edge segments will move closer together, reducing the area of the dislocation loop until it disappears

Figure 6.14 A schematic illustration of the mechanism to form a dislocation loop, starting with a pair of $\frac{a}{2}[011]$ dislocations entering a γ' precipitate on the (111) primary slip plane.

in Figure 6.6. To understand the make-up of these dislocation loops, a full loop was imaged down the [111] zone axis under six different two-beam conditions (see Figure 6.7). The dislocation loop is shown to be composed of four segments: two screw segments and two edge segments. The full loop is visible to varying degrees in all conditions except under the **g** = $(1\bar{1}1)$ condition (Figure 6.7(d)) where the screw segments are invisible. The visible tips in Figure 6.7(d) are the edge components of the loop and have been marked with the letter 'A' in Figure 6.7(d).

The make-up of these dislocation loops give an idea of how they might form. The complete suggested sequence to form a dislocation loop is illustrated in Figure 6.14. At the yield point, the stress is high enough for dislocation pairs to enter γ' precipitates. A dislocation pair will glide on the $(11\bar{1})$ plane through the precipitate and may cross-slip. As shown earlier, it is estimated that only 15% of the dislocations would be in the necessary orientation to cross-slip. Once locked, the adjacent dislocation line will continue to move through the microstructure. This is shown in Figure 6.3(b) where some segments of the dislocation line have become locked in the γ' precipitates.

Another dislocation may enter the precipitate and cross-slip. The two inner segments of the relative dislocation pairs combine through interaction in the γ channel. This is followed by the two outer dislocations. This forms an edge segment of the loop, which rests on the γ/γ' interface. A similar interaction can occur in the γ channel on the opposite side of the slip plane, resulting in the formation of a full loop. The edge and screw components of the loop are then attracted together and move by dislocation climb and APB reordering respectively. The loop shrinks and eventually disappears.

A potential clue to the interaction of the dislocation segments in the γ channels to form the edge components is captured in Figure 6.8. The STEM micrograph shows two dislocation pairs which span two adjacent precipitates, across a γ channel. The two inner dislocations have combined and pinched off, with two edge segments formed and resting on respective channel / precipitate interfaces, on opposite sides of the γ channel (see Figure 6.8(b)). If the two outer dislocations also combine, then two loops will be formed in two adjacent precipitates. A similar scenario has been captured at the top of Figure 6.8(a), where the dislocation segments from two dislocation pairs in the γ channel have combined to form a half-loop. If a similar set of steps were to occur at the other end of the two screw segments, a complete loop would form.

The driving force for the loop to shrink is large. Due to their close spacing, the screw segments can each be treated as superdislocations with Burgers vectors $\langle 110 \rangle$. The Peach Koehler equation (equation 6.5) can give a estimate of the attractive force between the two screw segments.

$$F = \frac{G b_1 b_2 r}{2\pi}(cos\theta + sin\theta) \tag{6.5}$$

Using Figure 6.8 as a reference, the distance between the dislocation pairs is approximately 100 nm. Both dislocation pairs are locked on the $(11\bar{1})$ plane and therefore lie 45° to each other. Taking θ = 45°, r = 100 nm, and $\mathbf{b}_1$ = $\mathbf{b}_2$ = $|\mathbf{b}_{110}|$, the attractive force between two dislocation pair screw segments was 0.016 N/m. For a precipitate of length 350 nm, the diagonal length is roughly 500 nm, equal to an attractive force of 8 nN. The edge components of a full loop also experience a similar attractive force. These values are high for a dislocation loop and suggest given sufficient time, the respective edge and screw segments will move towards each other (6.14(h)). The loop would keep shrinking until it disappears.

For the screw segments to come together, the APB between the dislocation pairs needs to be reordered as the dislocation pairs moves through the γ'. However, the APB energy is sufficiently high that the dislocation pairs will remain close together. The movement of the screw segments will therefore be limited by the rate of this APB reordering. Because the edge components have their Burgers vector perpendicular to the dislocation line, they move by climb. This is a diffusion-mediated process and therefore temperature dependent. The shape of the loops visible in the microstructure suggest the aspect ratio between the edge and screw segments remains fairly constant, This suggests dislocation climb and APB reordering happen at a similar rate under the test conditions of this chapter ($\dot{\varepsilon}$=10^{-4} s^{-1}, T=750 °C).

The loops shrinking would clear up areas of the crystal for further deformation. The relationship between the frequency of dislocation locking and annihilation would in turn affect the work hardening rate. Furthermore, a sample where dislocation locking occurs at a higher rate than dislocation annihilation should have a steeper work hardening rate compared to a sample where the dislocations annihilate at a similar rate to locking. Given the APB reordering for screw segments to move, and dislocation climb to move edge segments, the rate of loops shrinking would be expected to increase with temperature. A tensile test at a higher temperature should therefore have a lower work hardening rate.

6.3.4 Segregation on the Cross-slipped Plane

Figure 6.11 shows no compositional segregation between the dislocation pair, imaged down the [011] zone axis. This is in contrast to the segregation observed on the octahedral plane.[5, 27] The driving force for cross-slip is the anisotropy between the {111} and {001} planes. Segregation on the octahedral plane may lower the APB energy on the {111} plane, in turn reducing the driving force for cross-slip.

The driving force to cross-slip may have a strong effect on the yield stress. After the yield point, the stress was observed to stay flat at around 5% strain. If the driving force for cross-slip is reduced, fewer dislocations will become locked upon entering the precipitate. On the other hand, if a higher proportion of the dislocations cross-slip and become locked on entering the precipitate, they will occupy slip planes and the crystal will be filled with dislocations more quickly. The stress may then rise after yield instead of plateauing for such a large amount of strain.

6.4 Conclusion

Through analysis of the morphology of the dislocation structures, and relating them to the macroscopic stress-strain curve, the yield process for single crystal Ni-based superalloys has been outlined. The yield point corresponds to entry of $\frac{a}{2}\langle 110\rangle$ dislocation pairs into the γ' precipitates, separated by an APB. As dislocation pairs enter the γ' precipitates, the majority pass through rapidly and unhindered. Where pairs are aligned in the screw orientation relative to the γ/γ' interface, cross slip can occur, locking the pair. Due to orientation of the primary slip plane, only around 15% of the dislocations that enter the precipitate will cross-slip and become locked. Subsequent shearing dislocation pairs will seek non-deformed areas of the microstructure to move into due to the strong repulsion force of the locked dislocations and the fact that the slip plane has become occupied, widening the slip band but generally producing limited work hardening. Eventually more dislocation pairs become locked, and these fill the slip planes. A higher stress is then required to move further dislocations through the microstructure. This results in work hardening, and the stress rises. Locked dislocation pairs can interact to form dislocation loops. These loops were composed of two screw and two edge components. Due to the large magnitude of the Burgers vectors of the respective segments, these loops will eventually shrink and disappear by a diffusion-controlled process. This acts as a dynamic recovery mechanism. With increasing strain, the microstructure becomes filled with more dislocations and the sample work-hardens to failure.

Chapter 7

Conclusions and recommendations for further works

7.1 Conclusions

The dissertation has characterised the dislocation structures at and beyond the yield point as a function of temperature, alloy composition and strain rate by identifying the manner of dislocation and microstructure interactions with and within the γ' precipitates. Whilst the value of the APB energy and the volume fraction of the γ' phase remain the principal determinants of the yield stress, this dissertation lays the groundwork for including Kear-Wilsdorf locking of dislocation pairs and their transformation into stacking faults into the quantitative understanding of yield of single crystal, Ni-based superalloys and how it changes with composition and temperature.

The dissertation has established substantial dislocation activity takes place before the yield point, and that yield occurs when $\frac{a}{2}\langle 110\rangle$ dislocations enter the γ' precipitates. Subsequent passage through the γ' precipitates appears to occur rapidly and unhindered. However, where dislocation pairs are aligned in the screw orientation relative to the γ/γ' interface, upon entry into the precipitate, the dislocation pair can cross slip onto the $\{001\}$ plane, locking the dislocation pair. Two locked dislocations were also observed to form dislocation loops. The presence of locked dislocations on the slip plane impedes further flow on this plane, resulting in dislocations propagating adjacent un-deformed areas, widening the slip bands, but generally producing no work hardening.

The yield stress was affected by both temperature and alloy composition. The yield stress increased with increasing temperature for the two superalloys tested. For single crystal superalloy CMSX-4, the yield stress was highest for tensile deformation at 800 °C, dropping slightly at 850 °C. Single crystal superalloy TMS-138A exhibited the highest yield stress at 900 °C. The higher temperature made dislocations in the γ channels wavier and it is thought that these networks could act as a barrier to dislocations penetrating the γ' precipitates. In terms of alloy composition, single crystal, first generation superalloy SRR99 exhibited the highest yield stress of around 1025 MPa, and single crystal superalloy TMS-138A the lowest (850 MPa). Though the microstructure of deformed single crystal SRR99 was not analysed, comparison of single crystal CMSX-4 and TMS-138A showed dislocations in the γ matrix channel much more rigidly confined to the $\{111\}$ slip planes, even at the higher temperature of 900 °C when dislocation climb should be easier. It was hypothesised that this was due to the more negative lattice misfit of TMS-138A compared to CMSX-4.

The strain rate was found to have little effect on the yield stress at 750 °C for single crystal superalloy CMSX-4. However, it does have an effect on post-yield behaviour. At a sufficiently slow strain rate ($10^{-6}\,\mathrm{s}^{-1}$), a transition from APB shearing of precipitates to stacking fault shearing occurred. Because the stress required to propagate dislocations bound by stacking faults is lower than APB-bound dislocations, upon a sufficient number of dislocations shearing by stacking fault formation, the flow stress decreased after yield to values typical of creep deformation. The stacking fault features that form are similar to those that form during primary creep, suggesting there is a continuous relationship between tensile and creep deformation. Such stacking faults form through a reordering mechanism. The slow rate of deformation and temperature (750 °C) was sufficient to allow this reordering to occur. The fault was also found to be enriched with chromium and cobalt, and depleted in aluminium and nickel. This finding suggests alloy composition plays a role in the ease at which a superalloy can transition between APB shearing and SF shearing, with superalloys with low amounts of chromium and cobalt finding it difficult to induce stacking fault shear.

7.2 Recommendations for further works

To conclude this work, below is a list of potential avenues for further work. It is by no means a comprehensive list, instead work which naturally extends and builds upon the findings within this dissertation. The yield point corresponds to entry into precipitates within the two-phase γ/γ' microstructure whereas before, due to the nature of monolithic $L1_2$ compounds, more emphasis was placed on the cross-slip of dislocations. The interaction between dislocation and precipitate is therefore a two-step process, entry followed by potential cross-slip.

The yield stress was found to change with temperature suggesting entry into γ' is affected by temperature. It is currently unclear how the temperature controls precipitate entry. It has been hypothesised that composition and lattice misfit, and dislocation morphology could play a role. The lattice misfit is a difficult parameter to isolate and extensive work already exists within the literature on this topic. A systematic study of effect on the composition on the yield stress is worth considering, whereby certain elements are removed or added to a model two-phase alloy in weight-percentage increments, although this would also affect the lattice misfit. The yield stress is known to drop off rapidly beyond a certain temperature in all superalloys. In monolithic $L1_2$ compounds, this has traditionally been attributed to activation of cube slip. However, it has already been shown that the two-phase γ/γ' microstructure has different dislocation behaviour to monolithic $L1_2$ compounds. Conducting further interrupted tests at higher temperatures and analysing the resultant deformation structures would be fairly straightforward and provide further insight.

The cross-slip process still occurs. However, the findings of this dissertation show only $\sim$15% of the dislocation pairs cross-slip. Further investigation needs to be done to understand why a large percentage of the dislocation pairs are able to pass through the precipitates unhindered despite the lower APB energy on the (001) plane. The $\sim$15% quoted was empirically derived. Whether this value is specimen specific and how it changes with temperature or composition are still unclear. A similar analysis on CMSX-4 at different temperatures and on the fourth generation superalloy TMS-138A would be strong starting points.

The dual-phase γ/γ' microstructure allows for the formation of loops. These loops eventually annihilate, reducing the dislocation density. The temperature and composition can again be varied to understand how these two factors affect loop formation. Since climb is a thermally activated process it would be expected to occur more at higher temperatures. The edge segments of the loop would have more energy to move, perhaps changing the aspect ratio of the loop or increasing the rate of loop annihilation. Heat treatments on deformed specimens that contain dislocation loops may show a lower density of dislocations. Analysis of the dislocation structures formed from interrupted tensile tests at higher temperatures could improve our understanding of whether loop formation and annihilation is easier at higher temperature.

Since the two-phase structure allows for the formation of dislocation loops, there may be less of a need for cross-slipped dislocations to unlock to get dislocations moving and clearing areas of the microstructure for further deformation. However, can dislocations become unlocked or is forming dislocation loops the preferred mechanism to clear areas of the microstructure? It is debatable whether the cross-slip process is a thermal or athermal process and the initiation site of unlocking along the cross-slip dislocation line. Any model would also need to account for this difference between two-phase and intermetallic compounds.

Chemical segregation to stacking faults was another important feature of the slow strain rate tensile tests featured in Chapter 5. This segregation has previously been observed in primary creep specimens. A more comprehensive study of the compositional effects and in particular, whether a threshold wt.% value of cobalt or chromium exists would be of particular interest to further understand why the cobalt and chromium segregates to the fault. SRR99 did not show the drop in stress at low strain rate deformation suggesting there is also interplay between cobalt and chromium content in an alloy.

No segregation was observed between the $\{001\}$ anti-phase boundary linking the dislocation pair segments, which were the subject of Chapter 6. This lends further support to the suggestion that compositional segregation is an important step in the formation of stacking faults. The anti-phase boundary chemical arrangement is proposed to form by dynamic diffusion. A difference in contrast was observed between the dislocation pairs, suggesting they may be bound by complex stacking faults. Further high resolution TEM work may be able to clarify the cause of the contrast difference.

Nanometre sized tertiary precipitates of γ' were also imaged within the γ channels. These are on similar length scales to the APB width between the dislocation pairs in large γ' precipitates, featured in Chapter 6. It is currently not well understood how the nanometre-sized tertiary precipitates interact with dislocations and the effect that has on the macroscopic deformation and stress-strain behaviour. The size of the γ' precipitates themselves can also be changed by the pre-test heat treatment to see if a relationship exists between precipitate size and tensile behaviour.

The load orientation is another important factor that affects the deformation behaviour. Stringent quality control of maximum deviation off-axis exists in industry as a result. This factor was not extensively considered in this dissertation. A more systematic study of the effect of orientation would show whether the pseudo-creep deformation behaviour observed at slow strain rates is an effect of orientation, and more broadly the effect on the yield stress.

The final two studies proposed relate back to the understanding of the yield stress anomaly. The yield stress anomaly is known to be insensitive to strain rate and would be expected to show tension-compression asymmetry. Extensive work on monolithic $L1_2$ compounds has been done at various strain rates to understand the strain rate insensitivity and were the reasoning for conducting the experiments of Chapter 5. The strain rate can also be changed mid-test or even unloaded and re-tested at a different strain rate, which would further our understanding of the competition between APB shearing and stacking fault shear and the effect on stress strain behaviour. Finally, all of the work in this dissertation can also be conducted in compression instead of tension.

Bibliography

[1] Aoki, K. and Izumi, O. (1975). *Effect of Substitutional Solute Elements on the Strength of the Intermetallic Compound Ni$_3$Al at Elevated Temperature*, volume 39. The Japan Institute of Metals.

[2] Ardell, A. (1985). Precipitation Hardening. *Metallurgical Transactions A*, 16(12):2131–2165.

[3] Baluc, N., Schäublin, R., and Hemker, K. (1991). Methods for determining precise values of antiphase boundary energies in Ni$_3$Al. *Philosophical Magazine Letters*, 64(5):327–334.

[4] Barba, D., Alabort, E., Pedrazzini, S., Collins, D. M., Wilkinson, A. J., Bagot, P. A. J., Moody, M. P., Atkinson, C., Jérusalem, A., and Reed, R. C. (2017). On the microtwinning mechanism in a single crystal superalloy. *Acta Materialia*, 135:314–329.

[5] Barba, D., Smith, T., Miao, J., Mills, M., and Reed, R. (2018). Segregation-Assisted Plasticity in Ni-Based Superalloys. *Metallurgical and Materials Transactions A*, 49(9):4173—-4185.

[6] Beeley, P. and Smart, R. (1995). *Investment casting*. Institute of Materials London.

[7] Bhadeshia, H. (2003). Nickel Based Superalloys. https://www.phase-trans.msm.cam.ac.uk/2003/Superalloys/superalloys.html. Accessed: 2021-07-23.

[8] Bonneville, J. and Escaig, B. (1979). Cross-slipping process and the stress-orientation dependence in pure copper. *Acta Metallurgica*, 27(9):1477–1486.

[9] Bradley, A. and Taylor, A. (1938). An X-ray study of the iron-nickel-aluminium ternary equilibrium diagram. *Proceedings of the Royal Society of London. Series A, Mathematical and Physical Sciences*, pages 353–375.

[10] Chen, J., Feng, Q., and Sun, Z. (2010). Topologically close-packed phase promotion in a Ru-containing single crystal superalloy. *Scripta Materialia*, 63(8):795–798.

[11] Cheng, K., Jo, C., Jin, T., and Hu, Z. (2011). Precipitation behaviour of μ phase and creep rupture in single crystal superalloy CMSX-4. *Journal of Alloys and Compounds*, 509(25):7078–7086.

[12] Cheng, K., Jo, C., Kim, D., Jin, T., and Hu, Z. (2012). Unexpected precipitation of a Re-rich phase in single crystal superalloy CMSX-4 during thermal exposure. *Journal of Metallurgy*, 2012:1687–9465.

[13] Chou, C., Hirsch, P. B., McLean, M., and Hondros, E. (1982). Anti-phase domain boundary tubes in Ni_3Al. *Nature*, 300(5893):621–623.

[14] Clay, K., Jackson, J., Quested, P., and Morrell, R. (2009). Improving single-crystal orientation determination for advanced nickel-based alloys.

[15] Copley, S. and Kear, B. (1967). A dynamic theory of coherent precipitation hardening with application to nickel-base superalloys. *Transactions of the Metallurgical Society of AIME*, pages 984–992.

[16] Copley, S., Kear, B., and Rowe, G. (1972). The temperature and orientation dependence of yielding in Mar-M200 single crystals. *Materials Science and Engineering*, 10(Supplement C):87–92.

[17] Cottrell, A. H. and Bilby, B. (1949). Dislocation theory of yielding and strain ageing of iron. *Proceedings of the Physical Society. Section A*, 62(1):49.

[18] Crudden, D., Mottura, A., Warnken, N., Raeisinia, B., and Reed, R. (2014). Modelling of the influence of alloy composition on flow stress in high-strength nickel-based superalloys. *Acta materialia*, 75:356–370.

[19] Cui, C., Gu, Y., Yuan, Y., and Harada, H. (2011a). Dynamic strain aging in a new Ni-Co base superalloy. *Scripta Materialia*, 64(6):502–505.

[20] Cui, C., Gu, Y., Yuan, Y., and Harada, H. (2011b). Dynamic strain aging in a new Ni-Co base superalloy. *Scripta Materialia*, 64(6):502–505.

[21] Cui, C., Tian, C., Zhou, Y., Jin, T., and Sun, X. (2012). *Dynamic strain aging in Ni base alloys with different stacking fault energy*. Superalloys 2012.

[22] Dai, H., D'souza, N., and Dong, H. (2011). Grain selection in spiral selectors during investment casting of single-crystal turbine blades: Part I. Experimental investigation. *Metallurgical and Materials Transactions A*, 42(11):3430–3438.

[23] Davis, J. and Committee, A. (2000). *Nickel, Cobalt, and Their Alloys*. ASM specialty handbook. ASM International.

[24] Demura, M., Golberg, D., and Hirano, T. (2007). An athermal deformation model of the yield stress anomaly in Ni_3Al. *Intermetallics*, 15(10):1322–1331.

[25] Dixon, S. and Hall, C. (2013). Fluid mechanics and thermodynamics of turbomachinery: Seventh edition. *Fluid Mechanics and Thermodynamics of Turbomachinery: Seventh Edition*, pages 1–537.

[26] D'souza, N., Jennings, P., Yang, X., Lee, P., McLean, M., and Dong, H. (2005). Seeding of single-crystal superalloys — Role of constitutional undercooling and primary dendrite orientation on stray-grain nucleation and growth. *Metallurgical and Materials Transactions B*, 36(5):657–666.

[27] Eggeler, Y., Müller, J., Titus, M., Suzuki, A., Pollock, T., and Spiecker, E. (2016). Planar defect formation in the γ' phase during high temperature creep in single crystal CoNi-base superalloys. *Acta Materialia*, 113:335 – 349.

[28] Esaka, H., Shinozuka, K., and Tamura, M. (2005). Analysis of single crystal casting process taking into account the shape of pigtail. *Materials Science and Engineering: A*, 413:151–155.

[29] Escaig, B. (1968). Sur le glissement dévié des dislocations dans la structure cubique à faces centrées. *Journal de Physique*, 29(2-3):225–239.

[30] Eurich, N. and Bristowe, P. (2015). Segregation of alloying elements to intrinsic and extrinsic stacking faults in γ'-Ni_3Al via first principles calculations. *Scripta Materialia*, 102:87–90.

[31] Ezz, S. and Hirsch, P. (1994). The strain rate sensitivity of the flow stress and the mechanism of deformation of single crystals of $Ni_3(Al\,Hf)\,B$. *Philosophical Magazine A*, 69(1):105–127.

[32] Fang, J., Schulson, E. M., and Baker, I. (1994). The dislocation structure in $L1_2$ ordered alloy Ni_3Ge. *Philosophical Magazine A*, 70(6):1013–1025.

[33] Feller-Kniepmeier, M., Link, T., Poschmann, I., Scheunemann-Frerker, G., and Schulze, C. (1996). Temperature dependence of deformation mechanisms in a single crystal nickel-base alloy with high volume fraction of γ' phase. *Acta materialia*, 44(6):2397–2407.

[34] Fu, C., Reed, R., Janotti, A., and Krcmar, M. (2004). On the diffusion of alloying elements in the nickel-base superalloys. *Superalloys*, 2004:867–876.

[35] Fu, C., Ye, Y., and Yoo, M. (2006). Theoretical investigation of the elastic constants and shear fault energies of Ni_3Si. *Philosophical Magazine Letters*, 67(3):179–185.

[36] Fu, C. and Yoo, M. (1988). Stacking fault energies, crystal elasticity and their relation to the mechanical properties of $L1_2$-ordered alloys. *MRS Online Proceedings Library Archive*, 133.

[37] Fujita, A., Mishima, Y., and Suzuki, T. (1983). Temperature dependence of strength in a Cu_3Au-5% Ni alloy and its relevance to the APB morphology. *Journal of Materials Science*, 18(6):1881–1886.

[38] G. Wang, X., Liu, J., Jin, T., and Sun, X. (2014). The effects of ruthenium additions on tensile deformation mechanisms of single crystal superalloys at different temperatures. *Materials & Design*, 63:286–293.

[39] Galindo-Nava, E., Connor, L., and CMF, R. (2015). On the prediction of the yield stress of unimodal and multimodal γ' nickel-base superalloys. *Acta Materialia*, 98:377 – 390.

[40] Gialanella, S. and Malandruccolo, A. (2020). Superalloys. In *Aerospace Alloys*, pages 267–386. Springer.

[41] Glatzel, U. (1994). Neutron scattering experiments with a nickel base superalloy part II: Analysis of intensity profiles. *Scripta Metallurgica et Materialia*, 31(3):291 – 296.

[42] Glatzel, U. and Muller, A. (1994). Neutron scattering experiments with a nickel base superalloy part I: Material and experiment. *Scripta Metallurgica et Materialia*, 31(3):285 – 290.

[43] Golberg, D., Demura, M., and Hirano, T. (1998a). Effect of Al-rich off-stoichiometry on the yield stress of binary Ni_3Al single crystals. *Acta Materialia*, 46(8):2695–2703.

[44] Golberg, D., Demura, M., and Hirano, T. (1998b). Single crystal growth and characterization of binary stoichiometric and Al-rich Ni_3Al. *Journal of Crystal Growth*, 186(4):624–628.

[45] Goodfellow, A., Galindo-Nava, E., Christofidou, K., Jones, N., Martin, T., Bagot, P., Boyer, C., Hardy, M., and Stone, H. (2017). Gamma prime precipitate evolution during aging of a model nickel-based superalloy. *Metallurgical and Materials Transactions A*, pages 1–11.

[46] Goodfellow, A., Owen, L., Christofidou, K., Kelleher, J., Hardy, M., and Stone, H. (2019). The Effect of Temperature and Mo Content on the Lattice Misfit of Model Ni-Based Superalloys. *Metals*, 9(6):700.

[47] Gornostyrev, Y., Kontsevoi, O., Maksyutov, A., Freeman, A., Katsnelson, M., Trefilov, A., and Lichtenshtein, A. (2004). Negative yield stress temperature anomaly and structural instability of Pt_3Al. *Physical Review B*, 70:014102.

[48] Harris, C., Tedstrom, R., Daw, M., and Mills, M. (2006). Calculations of diffusion and diffusion-limited processes in Ni_3Al using accelerated molecular dynamics. *Computational Materials science*, 37(4):462–469.

[49] Heckl, A., Neumeier, S., Cenanovic, S., Göken, M., and Singer, R. (2011). Reasons for the enhanced phase stability of Ru-containing nickel-based superalloys. *Acta Materialia*, 59(17):6563–6573.

[50] Hegde, S., Kearsey, R., and Beddoes, J. (2008). Design of solutionizing heat treatments for an experimental single crystal superalloy. In *Proc. 11th. Int. Symp. On Superalloys*, pages 301–310.

[51] Heredia, F. and Pope, D. (1991). Effect of boron additions on the ductility and fracture behavior of Ni_3Al single crystals. *Acta Metallurgica et Materialia*, 39(8):2017–2026.

[52] Hirano, T., Demura, M., and Golberg, D. (1999). Compliance to Schmid's law in the stress anomaly regime of binary stoichiometric Ni_3Al. *Acta Materialia*, 47(12):3441–3446.

[53] Hirano, T. and Mawari, T. (1993). Unidirectional solidification of Ni_3Al by a floating zone method. *Acta Metallurgica et Materialia*, 41(6):1783–1789.

[54] Hirsch, P. (1992). A new theory of the anomalous yield stress in $L1_2$ alloys. *Philosophical Magazine A*, 65(3):569–612.

[55] Hobbs, R., Zhang, L., Rae, C., and Tin, S. (2008a). Mechanisms of topologically close-packed phase suppression in an experimental ruthenium-bearing single-crystal nickel-base superalloy at 1100°C. *Metallurgical and Materials Transactions A*, 39(5):1014–1025.

[56] Hobbs, R., Zhang, L., Rae, C., and Tin, S. (2008b). TCP suppression in a ruthenium-bearing single-crystal nickel-based superalloy. *The Journal of The Minerals, Metals & Materials Society (TMS)*, 60(7):37–42.

[57] Hobbs, R., Zhang, L., Rae, C., and Tin, S. (2008c). The effect of ruthenium on the intermediate to high temperature creep response of high refractory content single crystal nickel-base superalloys. *Materials Science and Engineering: A*, 489(1):65–76.

[58] Hou, L., Li, B., Wu, R., Cui, L., Ji, P., Long, R., Zhang, J., Li, X., Dong, A., and Sun, B. (2017). Microstructure and mechanical properties at elevated temperature of mg-al-ni alloys prepared through powder metallurgy. *Journal of Materials Science & Technology*, 33.

[59] Jackson, M. and Reed, R. (1999). Heat treatment of UDIMET 720Li: the effect of microstructure on properties. *Materials Science and Engineering: A*, 259(1):85–97.

[60] Janotti, A., Krcmar, M., Fu, C., and C Reed, R. (2004). Solute diffusion in metals: Larger atoms can move faster. *Physical Review Letters*, 92:085901.

[61] Jansson, B. and Melander, A. (1978). On the critical resolved shear stress from misfitting particles. *Scripta Metallurgica*, 12(6):497.

[62] Jarrett, R. and Tien, J. (1982). Effects of cobalt on structure, microchemistry and properties of a wrought nickel-base superalloy. *Metallurgical Transactions A*, 13(6):1021–1032.

[63] Jiang, C., Sordelet, D., and Gleeson, B. (2006). Site preference of ternary alloying elements in Ni_3Al: a first-principles study. *Acta Materialia*, 54(4):1147–1154.

[64] Jones, A. and Baxter, C. (1995). The rolls royce 'SCORPIO' system. *Measurement Science and Technology*, 6(1):131.

[65] Kamaraj, M. (2003). Rafting in single crystal nickel-base superalloys — an overview. *Sadhana*, 28(1-2):115–128.

[66] Karnthaler, H., Mühlbacher, E., and Rentenberger, C. (1996). The influence of the fault energies on the anomalous mechanical behaviour of Ni_3Al alloys. *Acta Materialia*, 44(2):547–560.

[67] Karunaratne, M., Carter, P., and Reed, R. (2000). Interdiffusion in the face-centred cubic phase of the Ni–Re, Ni–Ta and Ni–W systems between 900 and 1300 °C. *Materials Science and Engineering: A*, 281(1):229 – 233.

[68] Kear, B., Giamei, A., Leverant, G., and Oblak, J. (1969a). On intrinsic/extrinsic stacking fault pairs in the Ll_2 lattice. *Scripta Metallurgica*, 3(2):123–129.

[69] Kear, B., Giamei, A., Leverant, G., and Oblak, J. (1969b). Viscous slip in the $L1_2$ lattice. *Scripta Metallurgica*, 3(7):455–460.

[70] Kear, B. and HGF, W. (1962). Dislocation configurations in plastically deformed polycrystalline Cu_3Au alloys. *Transactions of the Metallurgical Society of AIME*, 224:382–386.

[71] Koizumi, Y., Kobayashi, T., Yokokawa, T., Zhang, J., Osawa, M., Harada, H., Aoki, Y., and Arai, M. (2004). Development of next-generation Ni-base single crystal superalloys. *Superalloys 2004*, pages 35–43.

[72] Koneva, N., Teplyakova, L., Starenchenko, V., and Kozlov, E. (1977). The effects of test temperature on the work-hardening characteristics of Ni_3Fe ordering single crystals oriented for multiple slip. *Soviet Physics Journal*, 20(10):1274–1278.

[73] Kovarik, L., Unocic, R., Li, J., and Mills, M. (2009a). The intermediate temperature deformation of ni-based superalloys: Importance of reordering. *JOM*, 61(2):42–48.

[74] Kovarik, L., Unocic, R., Li, J., Sarosi, P., and Shen, C. (2009b). Microtwinning and other shearing mechanisms at intermediate temperatures in Ni-based superalloys. *Progress in Materials*, 54(6).

[75] Kuriki, Y., Ochiai, S., Yodogawa, M., and Suzuki, T. (1985). The effect of zinc addition on the mechanical properties of Ni_3Al. *Transactions of the Japan institute of metals*, 26(3):213–214.

[76] Lall, C., Chin, S., and Pope, D. P. (1979). The orientation and temperature dependence of the yield stress of $Ni_3(Al, Nb)$ single crystals. *Metallurgical Transactions A*, 10(9):1323–1332.

[77] Laughin, D. and Hono, K. (2014). *Physical Metallurgy*. Elsevier, 5 edition.

[78] Leverant, G. and Kear, B. (1970). The mechanism of creep in gamma prime precipitation-hardened nickel-base alloys at intermediate temperatures. *Metallurgical and Materials Transactions B*, 1(2):491–498.

[79] Li, J. (2003). Central symmetry parameter.

[80] Lin, B., Huang, M., LG, Z., Roy, A., Silberschmidt, V., Barnard, N., Whittaker, M., and McColvin, G. (2018). 3D DDD modelling of dislocation–precipitate interaction in a nickel-based single crystal superalloy under cyclic deformation. *Philosophical Magazine*, 98(17):1550–1575.

[81] Llewelyn, S., Christofidou, K., Araullo-Peters, V., Jones, N., Hardy, M., Marquis, E., and Stone, H. (2017). The effect of Ni: Co ratio on the elemental phase partitioning in γ-γ' Ni-Co-Al-Ti-Cr alloys. *Acta Materialia*, 131:296–304.

[82] Louchet, F. (1995). Dislocation exhaustion and stress anomaly in $L1_2$ alloys: The 'E.L.U.' model. *Journal de Physique III*, 5(11):1803–1807.

[83] Maier, H., Niendorf, T., and Bürgel, R. (2015). *Handbuch Hochtemperatur-Werkstofftechnik: Grundlagen, Werkstoffbeanspruchungen, Hochtemperaturlegierungen und -beschichtungen*. Springer Fachmedien Wiesbaden.

[84] Marcinkowski, M., Brown, N., and Fisher, R. (1961). Dislocation configurations in $AuCu_3$ and AuCu type superlattices. *Acta Metallurgica*, 9(2):129–137.

[85] Matan, N., Cox, D., Carter, P., Rist, M., Rae, C., and Reed, R. (1999). Creep of CMSX-4 superalloy single crystals: effects of misorientation and temperature. *Acta materialia*, 47(5):1549–1563.

[86] McDonnell, B., Pascoe, R., Hancock, G., and Newey, C. (1967). The growth of single crystals of the intermediate phases NiAl and Ni_3Al. *Journal of Materials Science*, 2(4):365–370.

[87] McLean, M. (1983). *Directionally solidified materials for high temperature service*. London, Metals Society.

[88] Messé, O., Barnard, J., Pickering, E., Midgley, P., and Rae, C. (2014). On the precipitation of delta phase in ALLVAC® 718Plus. *Philosophical Magazine*, 94(10):1132–1152.

[89] Milligan, W. and Antolovich, S. (1987). Yielding and deformation behavior of the single crystal superalloy PWA 1480. *Metallurgical Transactions A*, 18(1):85–95.

[90] Milligan, W. and Antolovich, S. (1991). The mechanisms and temperature dependence of superlattice stacking fault formation in the single-crystal superalloy PWA 1480. *Metallurgical Transactions A*, 22(10):2309–2318.

[91] Mills, M. and Chrzan, D. (1992). Dynamical simulation of dislocation motion in $L1_2$ alloys. *Acta Metallurgica et Materialia*.

[92] Mishima, Y., Ochiai, S., Yodogawa, M., and Suzuki, T. (1986). Mechanical properties of Ni_3Al with ternary addition of transition metal elements. *Transactions of the Japan institute of metals*, 27(1):41–50.

[93] Moore, Z. (2008). *Life modeling of notched CM247LC DS nickel-base superalloy*. PhD thesis, Georgia Institute of Technology.

[94] Mottura, A., Finnis, M., and Reed, R. (2012). On the possibility of rhenium clustering in nickel-based superalloys. *Acta Materialia*, 60(6):2866–2872.

[95] Mottura, A., Miller, M., and Reed, R. (2008a). Atom probe tomography analysis of possible rhenium clustering in nickel-based superalloys. In *Proceedings of the International Symposium on Superalloys*, pages 891–900.

[96] Mottura, A., Wu, R., Finnis, M., and Reed, R. (2008b). A critique of rhenium clustering in Ni-Re alloys using extended X-ray absorption spectroscopy. *Acta Materialia*, 56(11):2669–2675.

[97] Mughrabi, H. (2014). The importance of sign and magnitude of γ / γ' lattice misfit in superalloys - with special reference to the new γ'-hardened cobalt-base superalloys. *Acta Materialia*, 81:21–29.

[98] Müller, L., Glatzel, U., and Feller-Kniepmeier, M. (1993). Calculation of the internal stresses and strains in the microstructure of a single crystal nickel-base superalloy during creep. *Acta Metallurgica et Materialia*, 41(12):3401–3411.

[99] Murakami, H., Harada, H., and Bhadeshia, H. (1994). The location of atoms in Re-and V-containing multicomponent nickel-base single-crystal superalloys. *Applied Surface Science*, 76:177–183.

[100] Murakumo, T., Kobayashi, T., Koizumi, Y., and Harada, H. (2004). Creep behaviour of Ni-base single-crystal superalloys with various γ' volume fraction. *Acta Materialia*, 52(12):3737–3744.

[101] Nabarro, F. and De Villiers, F. (1995). *Physics of creep and creep-resistant alloys*. CRC press.

[102] Ngan, A., Jones, I., and Smallman, R. (1992). The negative temperature dependence of yield strength in the $L1_2$ compound Fe_3Ge. *Materials Science and Engineering: A*, 153(1-2):387–391.

[103] Noguchi, O., Oya, Y., and Suzuki, T. (1981). The effect of nonstoichiometry on the positive temperature dependence of strength of Ni_3Al and Ni_3Ga. *Metallurgical Transactions A*, 12(9):1647–1653.

[104] Nosova, G. and Polyakova, N. (1980). The temperature dependence of the critical shear stresses in the ordered alloy ni 3 mn. *Fiz. Met. Metalloved.*, 50(6):1321–1323.

[105] Oblak, J., Paulonis, D., and Duvall, D. (1974). Coherency strengthening in Ni base alloys hardened by DO_{22} γ' precipitates. *Metallurgical Transactions*, 5(1):143.

[106] Ochiai, S., Mishima, Y., Yodogawa, M., and Suzuki, T. (1986). Mechanical properties of Ni_3Al with ternary addition of B-subgroup elements. *Transactions of the Japan institute of metals*, 27(1):32–40.

[107] O'Hara, K., Walston, W., Ross, W., and Darolia, R. (1994). Nickel base superalloy and article. US Patent 5,482,789.

[108] Okamoto, N., Hasegawa, Y., and Inui, H. (2014). Plastic deformation of single crystals of Pt_3Al with the $L1_2$ structure having a far Al-rich off-stoichiometric composition of Pt-29at.% Al. *Philosophical Magazine*, 94(12):1327–1344.

[109] Oni, A., Broderick, S., Rajan, K., and LeBeau, J. (2016). Atom site preference and γ'/γ mismatch strain in Ni Al Co Ti superalloys. *Intermetallics*, 73:72–78.

[110] Paidar, V., Pope, D., and Vitek, V. (1984). A theory of the anomalous yield behavior in $L1_2$ ordered alloys. *Acta Metallurgica*.

[111] Paidar, V., Yamaguchi, M., Pope, D., and Vitek, V. (1982). Dissociation and core structure of $\langle 110 \rangle$ screw dislocations in $L1_2$ ordered alloys II. Effects of an applied shear stress. *Philosophical Magazine A*, 45(5):883–894.

[112] Pollock, T. and Argon, A. (1992). Creep resistance of CMSX-3 nickel base superalloy single crystals. *Acta Metallurgica et Materialia*, 40(1):1–30.

[113] Pollock, T. and Field, R. (2002). Dislocations and high-temperature plastic deformation of superalloy single crystals. *Dislocations in Solids*, 11:547–618.

[114] Pollock, T. and Tin, S. (2006). Nickel-based superalloys for advanced turbine engines: chemistry, microstructure, and properties. *Journal of Propulsion and Power*, 22(2):361–374.

[115] Pope, D. (1972). The flow stress of Cu_3Au. *Philosophical Magazine*, 25(4):917–927.

[116] Rae, C., Matan, N., and Reed, R. (2001). The role of stacking fault shear in the primary creep of [001]-oriented single crystal superalloys at 750°C and 750 MPa. *Materials Science and Engineering: A*, 300(1-2):125–134.

[117] Rae, C. and Reed, R. (2007). Primary creep in single crystal superalloys: Origins, mechanisms and effects. *Acta Materialia*, 55(3):1067–1081.

[118] Rawlings, R. and Staton-Bevan, A. (1975). The alloying behaviour and mechanical properties of polycrystalline Ni_3Al (γ' phase) with ternary additions. *Journal of Materials Science*, 10(3):505–514.

[119] Reed, R. (2008). *The superalloys: fundamentals and applications.* Cambridge university press.

[120] Rosengaard, N. and Skriver, H. (1994). Ab initio study of antiphase boundaries and stacking faults in $L1_2$ and DO_{22} compounds. *Physical Review B*, 50(7):4848.

[121] Ru, Y., Li, S., Zhou, J., Pei, Y., Wang, H., Gong, S., and Xu, H. (2016). Dislocation network with pair-coupling structure in $\{111\}$ γ/γ' interface of Ni-based single crystal superalloy. *Scientific Reports*, 6:29941.

[122] Ru, Y., Zhao, H., Zhang, H., Pan, X., Zhao, W., Pei, Y., Li, S., and Gong, S. (2019). Design for anomalous yield in γ'-strengthening superalloys. *Materials & Design*, 183:108082.

[123] Saburi, T., Hamana, T., Nenno, S., and Pak, H. (1977). Temperature and orientation dependence of the yield strength of Ni_3(Al, W). *Japanese Journal of Applied Physics*, 16(2):267–272.

[124] Sass, V., Glatzel, U., and Feller-Kniepmeier, M. (1996). Anisotropic creep properties of the nickel-base superalloy CMSX-4. *Acta Materialia*, 44(5):1967–1977.

[125] Schoeck, G., Kohlhammer, S., and Fahnle, M. (1999). Planar dissociations and recombination energy of $[110]$ superdislocations in Ni_3Al: generalized Peierls model in combination with ab initio electron theory. *Philosophical Magazine Letters*, 79(11):849–857.

[126] Sengupta, A., Putatunda, S., Bartosiewicz, L., Hangas, J., Nailos, P., Peputapeck, M., and Alberts, F. (1994). Tensile behavior of a new single crystal nickel-based superalloy (CMSX-4) at room and elevated temperatures. *Journal of Materials Engineering and Performance*, 3(5):664–672.

[127] Sestak, B. (1979). Plasticity and crystal structure. In *Proceedings of the 5th International Conference on Strength of Metals and Alloys, Aachen, Hrsg.: Haasen, P., Gerold, V., Kostorz, G*, volume 3, pages 1461–1482.

[128] Shah, D. and Duhl, D. (1984). The effect of orientation, temperature and gamma prime size on the yield strength of a single crystal nickel base superalloy. In *Proceedings of the fifth international symposium on superalloys, ASM, Metals Park, Ohio*.

[129] Shi, Z., Liu, S., and Li, J. (2015). Rejuvenation heat treatment of the second-generation single-crystal superalloy DD6. *Acta Metallurgica Sinica (English Letters)*, 28(10):1278–1285.

[130] Sims, C. T. (1984). A history of superalloy metallurgy for superalloy metallurgists. *Superalloys 1984*, pages 399–419.

[131] Smith, F. (1999). *Industrial applications of X-ray diffraction.* CRC Press.

[132] Smith, T., Esser, B., Antolin, N., Carlsson, A., Williams, R., Wessman, A., Hanlon, T., Fraser, H., Windl, W., McComb, D., et al. (2016a). Phase transformation strengthening of high-temperature superalloys. *Nature communications*, 7:13434.

[133] Smith, T. M., Unocic, R. R., Deutchman, H., and Mills, M. J. (2016b). Creep deformation mechanism mapping in nickel base disk superalloys. *Materials at High Temperatures*, 33(4-5):372–383.

[134] Spätig, P., Bonneville, J., and Martin, J. (1993). A new method for activation volume measurements: application to Ni_3(Al, Hf). *Materials Science and Engineering: A*, 167(1-2):73–79.

[135] Staton Bevan, A. and Rawlings, R. (1975). The deformation behaviour of single crystal Ni_3(Al, Ti). *Physica Status Solidi (a)*, 29(2):613–622.

[136] Sun, Y. and Hazzledine, P. (1988). A TEM weak-beam study of dislocations in γ' in a deformed Ni-based superalloy. *Philosophical Magazine A*, 58(4):603–617.

[137] Suzuki, K., Ichihara, M., and Takeuchi, S. (1979). Dissociated structure of superlattice dislocations in Ni_3Ga with the $L1_2$ structure. *Acta Metallurgica*, 27(2):193–200.

[138] Suzuki, T., Mishima, Y., and Miura, S. (1989). Plastic behaviour in Ni_3(Al,X) single crystal - Temperature, strain-rate, orientation and composition. *ISIJ International*, 29(1):1–23.

[139] Suzuki, T. and Oya, Y. (1981). The temperature dependence of the strength of pseudo-binary platinum-based $L1_2$ alloys with B-subgroup elements. *Journal of Materials Science*, 16(10):2737–2744.

[140] Suzuki, T., Oya, Y., and Ochiai, S. (1984). The mechanical behavior of nonstoichiometric compounds Ni_3Si, Ni_3Ge, and Fe_3Ga. *Metallurgical and Materials Transactions A*, 15(1):173–181.

[141] Suzuki, T., Oya, Y., and Wee, D. (1980). Transition from positive to negative temperature dependence of the strength in Ni_3Ge-Fe_3Ge solid solution. *Acta Metallurgica*, 28(3):301–310.

[142] Takasugi, T., Izumi, O., and Yoshida, M. (1991). Mechanical properties of recrystallized $L1_2$-type Ni_3(Si, Ti) intermetallics. *Journal of Materials Science*, 26(5):1173–1178.

[143] Takasugi, T., Nagashima, M., and Izumi, O. (1990). Strengthening and ductilization of Ni_3Si by the addition of Ti elements. *Acta Metallurgica Et Materialia*, 38(5):747–755.

[144] Takasugi, T. and Yoshida, M. (1992). Strength anomaly and dislocation structure at 4.2 K in Ni_3(Si, Ti) single crystals. *Philosophical Magazine A*, 65(3):613–624.

[145] Takeuchi, S. and Kuramoto, E. (1971). Anomalous temperature dependence of the yield stress in Ni_3Ga. *Journal of the Physical Society of Japan*, 31(4):1282–1282.

[146] Takeuchi, S. and Kuramoto, E. (1973). Temperature and orientation dependence of the yield stress in Ni_3Ga single crystals. *Acta Metallurgica*, 21(4):415–425.

[147] Tan, X., Liu, J., Jin, T., Hu, Z., Hong, H., Choi, B., Kim, I., Jo, C., and Mangelinck, D. (2014). Variation of microstructure by Ru additions in a single crystal Ni based superalloy. *Materials Science and Technology*, 30(3):289–300.

[148] Thornton, P., Davies, R., and Johnston, T. (1970). The temperature dependence of the flow stress of the γ' phase based upon Ni_3Al. *Metallurgical Transactions*, 1(1):207–218.

[149] Tien, J. and Jarrett, R. (1982). Effects of cobalt in nickel-base superalloys. In *High Temperature Alloys for Gas Turbines 1982*, pages 423–446. Springer.

[150] Umakoshi, Y., Pope, D., and Vitek, V. (1984). The asymmetry of the flow stress in Ni_3(Al, Ta) single crystals. *Acta Metallurgica*, 32(3):449–456.

[151] Veyssiere, P., Douin, J., and Beauchamp, P. (1985). On the presence of super lattice intrinsic stacking faults in plastically deformed Ni_3Al. *Philosophical Magazine A*, 51(3):469–483.

[152] Veyssière, P. and Morris, D. (1993). Comment on 'transmission electron microscopy of dislocation structures in iron-doped Al_3Ti with the $L1_2$ structure'. *Philosophical Magazine A*, 67(2):491–495.

[153] Victoria, M. and Vidoz, A. (1968). Tensile Behavior upon Ordering of Ni_3Fe Single Crystals. *physica status solidi (b)*, 28(1):131–144.

[154] Viguier, B., Martin, I., and Bonneville, J. (2002). Work hardening in some ordered intermetallic compounds. *Dislocations in Solids*, 11:459–545.

[155] Viswanathan, G., Shi, R., Genc, A., Vorontsov, V., Kovarik, L., Rae, C., and Mills, M. (2015). Segregation at stacking faults within the γ' phase of two ni-base superalloys following intermediate temperature creep. *Scripta Materialia*, 94:5–8.

[156] Vitek, V. (1974). *Crystal Lattice Defects*, 5.

[157] Vorontsov, V. (2011). *Phase Field Modelling of Dislocations in Nickel Base Superalloys*. PhD thesis, University of Cambridge.

[158] Vorontsov, V., Kovarik, L., Mills, M., and Rae, C. (2012a). High-resolution electron microscopy of dislocation ribbons in a CMSX-4 superalloy single crystal. *Acta Materialia*, 60(12):4866–4878.

[159] Vorontsov, V., Shen, C., Wang, Y., Dye, D., and Rae, C. (2010). Shearing of γ' precipitates by $a\langle 112\rangle$ dislocation ribbons in Ni-base superalloys: A phase field approach. *Acta Materialia*, 58(12):4110–4119.

[160] Vorontsov, V., Voskoboinikov, R., and Rae, C. (2012b). Shearing of γ' precipitates in Ni-base superalloys: a phase field study incorporating the effective γ-surface. *Philosophical Magazine*, 92(5):608–634.

[161] Vorontsov, V., Voskoboinikov, R., and Rae, C. M. (2011). Prediction of mechanical behaviour in Ni-base superalloys using the phase field model of dislocations. In *Advanced Materials Research*, volume 278, pages 150–155. Trans Tech Publ.

[162] Voskoboynikov, R. and Rae, C. (2009). A new γ-surface in $\{111\}$ plane in $L1_2$ Ni_3Al. *Iop Conference Series: Materials Science and Engineering*, 3.

[163] Wagner, A., Shollock, B., and McLean, M. (2004). Grain structure development in directional solidification of nickel-base superalloys. *Materials Science and Engineering: A*, 374(1-2):270–279.

[164] Wahl, J., Harris, K., and Moore, T. (2002). Grain boundary strengthened single crystal superalloys. *Advanced Materials and Processes for Gas Turbines*, pages 129–135.

[165] Wang, N., Liu, L., Gao, S., Zhao, X., Huang, T., Zhang, J., and Fu, H. (2014a). Simulation of grain selection during single crystal casting of a Ni-base superalloy. *Journal of alloys and compounds*, 586:220–229.

[166] Wang, W., Jin, T., Liu, J., Sun, X., Guan, H., and Hu, Z. (2008). Role of Re and Co on microstructures and γ' coarsening in single crystal superalloys. *Materials Science and Engineering: A*, 479(1-2):148–156.

[167] Wang, X., Liu, J., Jin, T., and Sun, X. (2014b). The effects of ruthenium additions on tensile deformation mechanisms of single crystal superalloys at different temperatures. *Materials & Design*, 63:286–293.

[168] Wee, D., Noguchi, O., Oya, Y., and Suzuki, T. (1980). New $L1_2$ ordered alloys having the positive temperature dependence of strength. *Transactions of the Japan Institute of Metals*, 21(4):237–247.

[169] Wee, D., Pope, D., and Vitek, V. (1984). Plastic flow of Pt_3Al single crystals. *Acta Metallurgica*, 32(6):829–836.

[170] Wee, D. and Suzuki, T. (1979). The temperature dependence of hardness of $L1_2$ ordered alloys. *Transactions of the Japan Institute of Metals*, 20(11):634–646.

[171] Weertman, J. (1963). Interstitial producing extended jogs in face-centred cubic lattices. *Philosophical Magazine*, 8(90):967–975.

[172] Wu, X., Makineni, S., Liebscher, C., Dehm, G., Mianroodi, J., Shanthraj, P., Svendsen, B., Bürger, D., Eggeler, G., and Raabe, D. (2020). Unveiling the Re effect in Ni-based single crystal superalloys. *Nature Communications*, 11(1):1–13.

[173] Yamaguchi, M., Paidar, V., and Pope, D. (1982). Dissociation and core structure of $\langle 110 \rangle$ screw dislocations in $L1_2$ ordered alloys I. core structure in an unstressed crystal. *Philosophical Magazine*.

[174] Yang, W., Hu, S., Huo, M., Sun, D., Zhang, J., and Liu, L. (2019). Orientation controlling of Ni-based single-crystal superalloy by a novel method: grain selection assisted by un-melted reused seed. *Journal of Materials Research and Technology*, 8(1):1347–1352.

[175] Yeh, A., Kawagishi, K., Harada, H., Yokokawa, T., Koizumi, Y., Kobayashi, T., Ping, D., Fujioka, J., and Suzuki, T. (2008). Development of Si-bearing 4th generation Ni-base single crystal superalloys. In *Proceedings of the International Symposium on Superalloys*, pages 619–628.

[176] Zhang, J., Murakumo, T., Harada, H., Koizumi, Y., Kobayashi, T., et al. (2004). Creep deformation mechanisms in some modern single-crystal superalloys. *Superalloys*, 2004:189–195.

[177] Zhang, J., Murakumo, T., Koizumi, Y., and Harada, H. (2003). The influence of interfacial dislocation arrangements in a fourth generation single crystal TMS-138 superalloy on creep properties. *Journal of Materials Science*, 38(24):4883–4888.

[178] Zhang, J., Wang, J., Harada, H., and Koizumi, Y. (2005). The effect of lattice misfit on the dislocation motion in superalloys during high-temperature low-stress creep. *Acta Materialia*, 53(17):4623–4633.

[179] Zhou, H., Ro, Y., Harada, H., Aoki, Y., and Arai, M. (2004). Deformation microstructures after low-cycle fatigue in a fourth-generation Ni-base SC superalloy TMS-138. *Materials Science and Engineering: A*, 381(1-2):20–27.

[180] Zietara, M., Neumeier, S., Göken, M., and Czyrska-Filemonowicz, A. (2017). Characterization of γ and γ' phases in 2nd and 4th generation single crystal nickel-base superalloys. *Metals and Materials International*, 23(1):126–131.

Appendix A

Appendix

A.1 The Thompson Tetrahedron

To explain dislocation interactions and defects possible within FCC structures, vector notation is used as opposed to the more conventional Miller indices notation. The Thompson reference tetrahedron, illustrated in Figure A.1, offers an efficient framework to discuss dislocations in FCC lattices and their potentially complex reactions. For this reason, it has been selected as the preferred notation system. The tetrahedron consists of four atoms at its vertices, A, B, C and D, each of which is touching the other three. ABCD is made up of four $\{111\}$ planes: (111), $(\overline{11}1)$, $(\bar{1}1\bar{1})$ and $(1\overline{11})$. The atoms define three non-coplanar primitive vectors and thus the FCC lattice. If the midpoints of the faces are labelled α, β, γ and δ, all the dislocation Burgers vectors are represented. The edges AB, BC,CA, etc. correspond to the $\langle 110\rangle$ directions in these planes. The edges correspond to the normal slip vectors $\frac{a}{2}\langle 110\rangle$. The Shockley partials into which these are dissociated have Burgers vectors $\frac{a}{6}\langle 112\rangle$ and are represented by Roman-Greek symbols Aγ, Bγ, Dγ, etc, or Greek-Roman symbols γA, γB, γD, etc. In addition, the notation of Weertman[171] is used, whereby a bar is placed over the dislocation vectors that are associated with an extrinsic stacking fault.

A.2 Blueprint of the tensile specimen

All tensile specimens within this dissertation were machined to the specifications outlined in Figure A.2. The gauge length for Chapter 4 was shorter (12 mm) and eventually increased to 25 mm to increase the number of slices obtainable from one tensile specimen.

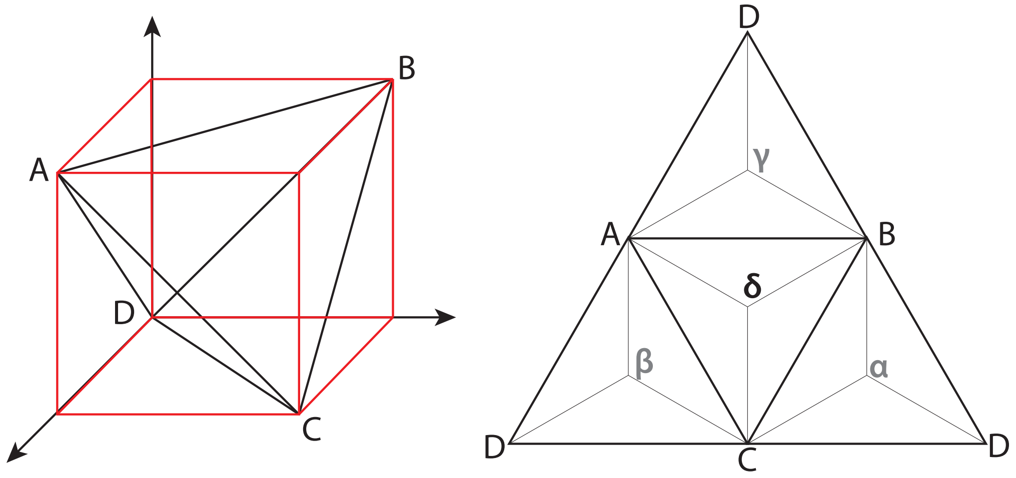

Figure A.1 Unfolded net of the Thompson tetrahedron, used to describe slip in FCC crystals. Triangles ABC, ACD, BCD and ABD represent (111), $(1\bar{1}\bar{1})$, $(\bar{1}1\bar{1})$ and $(\bar{1}\bar{1}1)$ respectively.

A.3 Imaging and analysis of HAADF images through Centre of Symmetry (COS) analysis

It is difficult to identify planar faults in HAADF images. One method that has been successfully used is called centre of symmetry analysis. Each bright spot on a HAADF image represents an atom column viewed directly down a crystallographic direction. The distances to the six nearest, neighbouring atom columns are measured. These are then compared to determine the symmetry of the atom column relative to it's neighbours. At the location of a planar fault, the neighbouring atoms are no longer equidistant to the central atom column, resulting in asymmetry. The vary degrees of asymmetry across a HAADF image will highlight planar faults.

Digital HAADF images were subject to a number of processing steps and numerical analysis in order to enhance and emphasise the observed features. The purpose of this analysis was to locate and identify the symmetry of each atom column and thus any faults in the stacking sequence. All stages of the processing sequence were performed using MATLAB® with the imaging processing toolbox. They are described as follows:

i. Load the original image, i.e. read the intensity magnitudes for each of the pixels.

ii. Perform a fast Fourier transform (FFT) on the image. The underlying periodicity of the atomic columns and the symmetry of heir positions in space mean that a Fourier transform of the image gives a pseudo diffraction pattern.

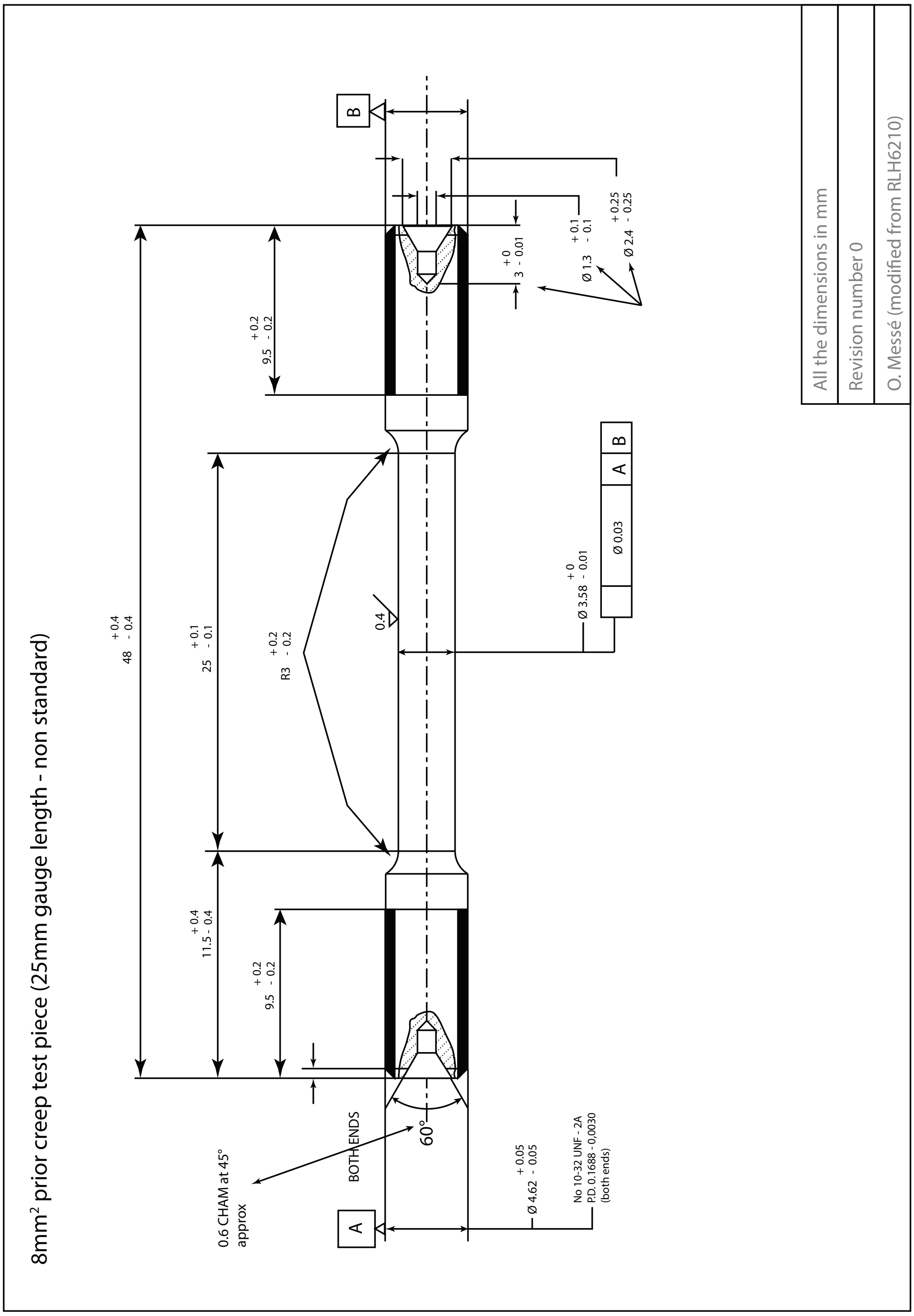

Figure A.2 A blue-print to which the tensile specimen were machined with dimensions in mm.

iii. The central 000 spot of the pattern is quite diffuse. This is a result of the noise in the original image and makes the atomic column positions less distinguishable from one another. To remove some of the noise signal, the area between the 000 spot and the nearest set of diffracted spots must be masked out and assume zero intensity. The inverse FFT is then performed to produce a filtered image.

iv. To aid the algorithm that determines the positions of the atomic columns in the last step, one must make their geometric appearance and spatial distribution appear more uniform. Assume, the intensity of each atomic function is a convolution of a 2D Gaussian distribution basis and some underlying second function. One can perform a discrete de-convolution of this underlying function from the Gaussian of some width. The value of σ is approximately equal to the apparent average width (in pixels) of an atomic column. The de-convolution yields an image in which the underlying crystal lattice is very clearly defined. The FFT of the de-convoluted image produces a much better pseudo diffraction pattern showing second and third order spots. There is a limit to how large or small the chosen value of σ can be. Too large a value leads to a loss of the underlying periodic lattice and the FFT yields no spots. Too small a value does not define the lattice points as well.

v. Re-convolute the image with a Gaussian function that has some smaller value of σ. This makes the atomic columns appear rounder and more distinct from their nearest neighbours. The image is now ready for the algorithm that located the atomic column positions.

vi. Measure the average size of each atomic column (diameter) and average distance to nearest neighbours in pixels in the re-convoluted image using ImageJ software. Now, using these estimates, one can run an algorithm that searches for the intensity maxima corresponding to the atomic columns and refines their positions relative to one another. The x,y positions of the atomic columns are then tabulated in a text file that can now be used in the centre-of-symmetry analysis. The resultant array of points are plotted in .

Once the tabulated spatial coordinates of the atomic columns are obtained, centre of symmetry analysis is performed. When reading in the x,y positions of each atomic column, a unique sequence number n is assigned. In a perfect crystal, each atomic column (and each point n) will be surrounded by six nearest neighbour columns. The centre of symmetry analysis used in this study is based on the procedure outlined by Li.[79] It is carried out using the following sequence of steps:

i. Calculate the distances between each atomic column and all other neighbours.

ii. Identify the six nearest neighbours.

iii. Rank the neighbours 1 to 6 in order of increasing distance. Let the rank be donated by r.

iv. Taking the central point n, as the origin, calculate the relative coordinates of each of the six neighbours. This gives the position vector, d_1, of each neighbour.

v. Take the position vector of the first neighbour, d_r, and search among the remaining five neighbours to find the smallest difference in the position vector $D = |d_1 + d_j|^2$. Call this minimum D_1. Given the hexagonal arrangement of the nearest neighbours in a perfect crystal, the d_j that gives the smallest D will be on the opposite corner of the hexagonal to d_1. In fact, in a perfect crystal D will be zero, since d_j will lie on the straight line running through d_1 and the origin at point n.

vi. Repeat the previous step with each of the remaining five neighbours to obtain the full set of minimum vector sums D_1 to D_6.

vii. Calculate the centre of symmetry parameter, M_n, as given by the following equation:

$$\mathrm{M}_n = \frac{\frac{1}{2}\sum_{r=1}^{6} D_r}{2\sum_{r=1}^{6} |d_r|^2} \tag{A.1}$$

It can be seen from the equation that the crystal deviates from centro-symmetry when a stacking fault is present and the origin hexagonal arrangement is lost. This gives non-zero values of M_n for the atomic columns in the fault.

The points on the edges of the images do not have six neighbours. Therefore, an exclusive zone must be specified around the edge so that only points with six neighbours are considered in the centre of symmetry analysis. In addition, to obtain a 2D density plot of M_n, the points were meshed and the data within each mesh element was interpolated using MATLAB®'s cubic algorithm.

A.4 Stress-strain curves of interrupted tests

To analyse the development of the microstructure in Chapter 4, interrupted tensile tests were run for which the stress-strain curves are shown in Figures A.3,A.4 and A.5. Where the

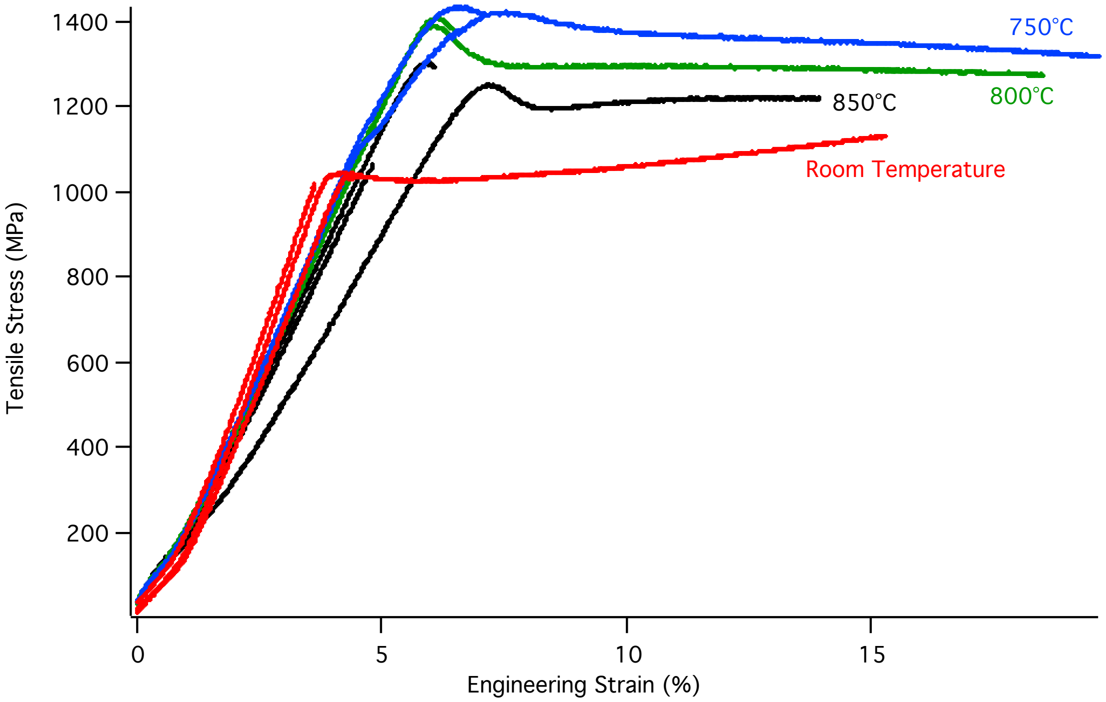

Figure A.3 Stress versus engineering-strain plots of all interrupted tensile tests for CMSX-4 at four different temperatures. The engineering stress is used because the extensometer slipped during testing.

extensometer was unable to record the strain, a plot of stress versus engineering stain is provided.

A.5 Volume fraction calculation

The γ' volume fraction was calculated from the model and equation in Figure A.6. Measurements for the ’s’ and ’w’ values were taken from an SEM image viewed down the [100] zone axis. The volume fraction was found to be around 70 %.

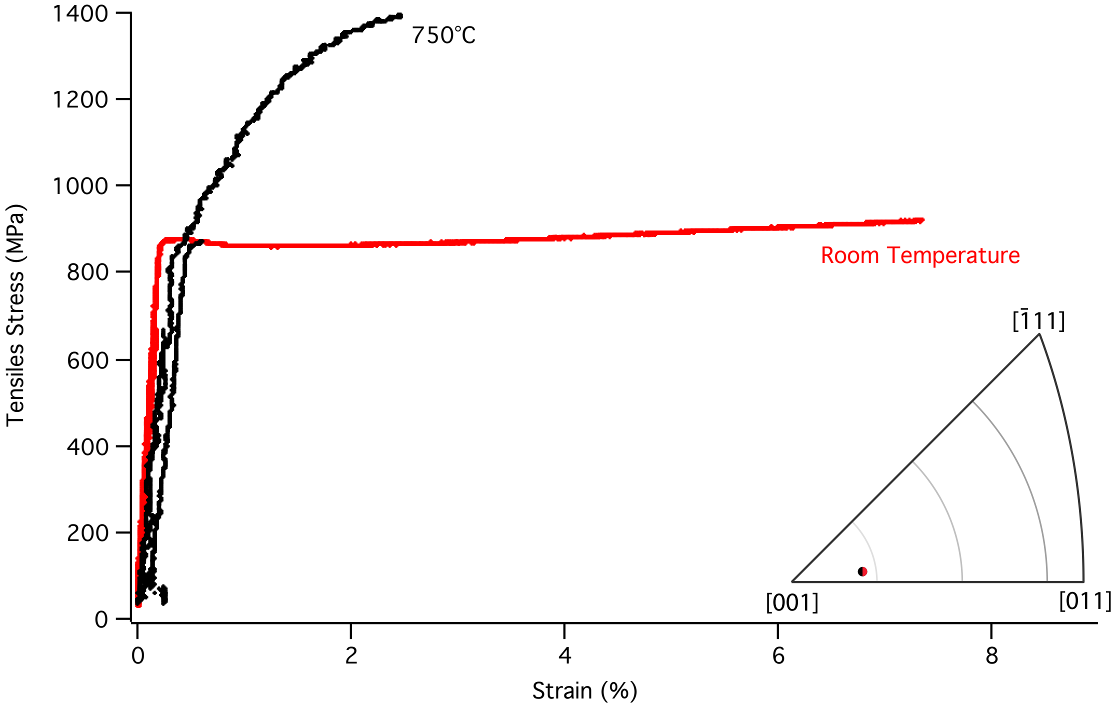

Figure A.4 Stress versus strain plots of all interrupted tensile tests for TMS-138A at room temperature and 750 °C.

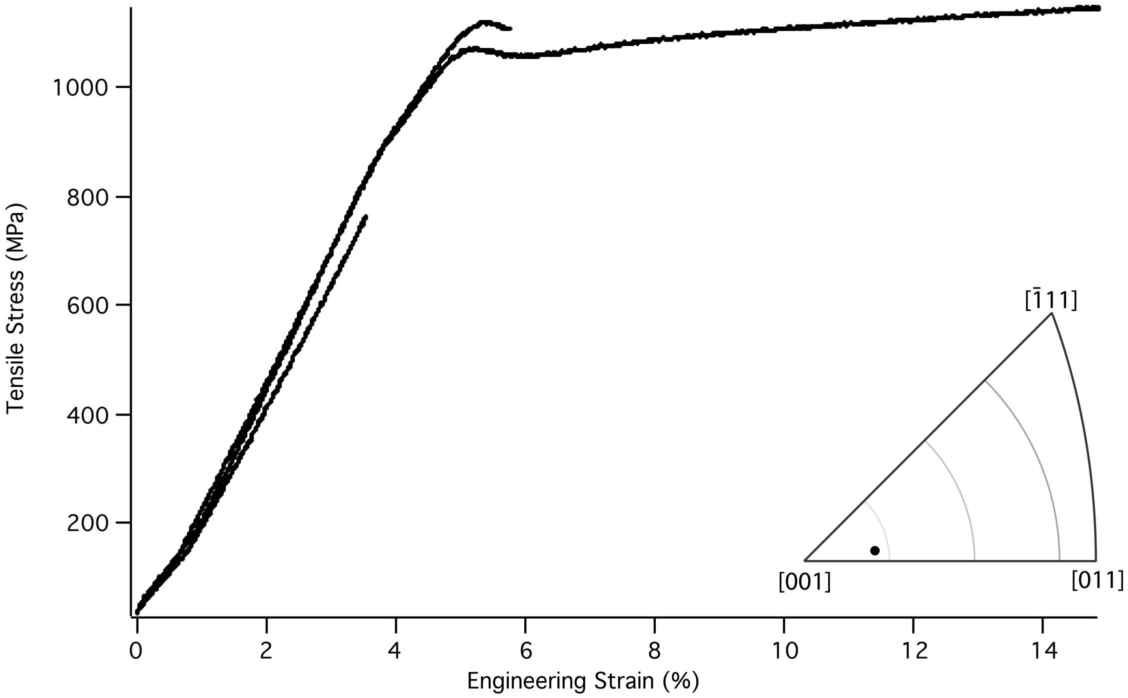

Figure A.5 Stress versus engineering-strain plots of all interrupted tensile tests for TMS-138A at 900 °C. The engineering stress is used because the extensometer slipped during testing.

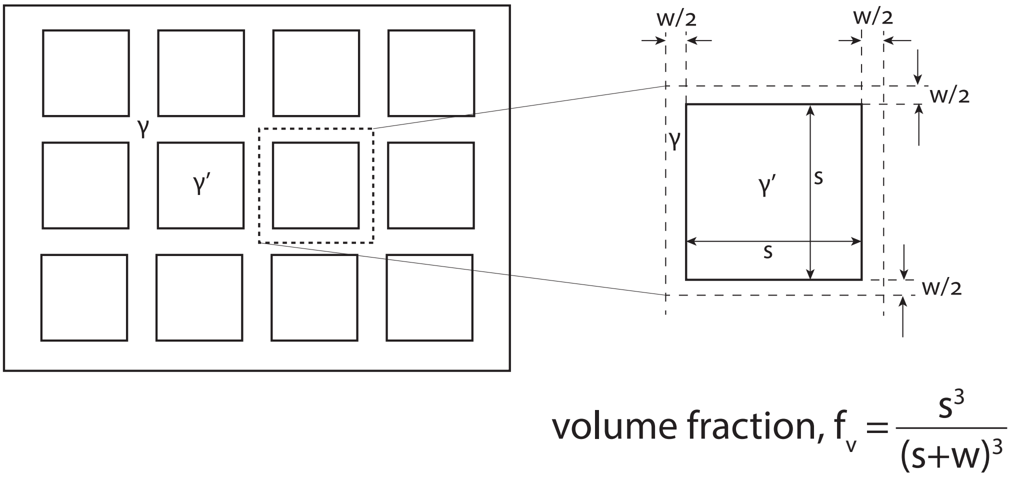

Figure A.6 Model of a regular structure with cubic precipitates in a {100} cut section and the equation used to find the γ' volume fraction. Adapted from Burgel.[83]